Passivation of the HAYNES® 214® Nickel-base Superalloy via Pulsed Laser Deposition of Alumina and Chromia Nanocoatings for Degradation Resistance at Elevated Temperatures

by

Eric Stowe

B.S. Chemical Engineering, University of Massachusetts Amherst, 2015

Submitted to the Graduate Faculty of the

Swanson School of Engineering in partial fulfillment

of the requirements for the degree of

Master of Science in Materials Science and Engineering

University of Pittsburgh

2021

UNIVERSITY OF PITTSBURGH

SWANSON SCHOOL OF ENGINEERING

This thesis was presented

by

Eric Stowe

It was defended on

July 16, 2021

and approved by

Brian Gleeson, Ph.D., Professor
Department of Mechanical Engineering and Materials Science

Jung-Kun Lee, Ph.D., Professor
Department of Mechanical Engineering and Materials Science

Markus Chmielus, Ph.D., Associate Professor
Department of Mechanical Engineering and Materials Science

Thesis Advisor: Jung-Kun Lee, Ph.D., Professor
Department of Mechanical Engineering and Materials Science

Passivation of the HAYNES® 214® Nickel-base Superalloy via Pulsed Laser Deposition of Alumina and Chromia Nanocoatings for Degradation Resistance at Elevated Temperatures

Eric Stowe, M.S.

University of Pittsburgh, 2021

HAYNES® 214® is a nickel-base superalloy that forms a protective alpha alumina (α-Al_2O_3) scale at temperatures above 950°C, which is necessary for oxidation and corrosion protection. At temperatures lower than 950°C, the formation of a protective α-Al_2O_3 layer is very difficult due to the significantly slower diffusion of aluminum from within the bulk alloy compared to the faster inward diffusion of oxygen. Due to this, internal precipitates of α-Al_2O_3 are routinely observed within the subsurface region of the alloy and these precipitates can negatively impact the alloy's mechanical strength and other material properties.

This thesis investigates the role of using pulsed laser deposited Al_2O_3 and chromia (Cr_2O_3) nanocoatings as a means to apply a passivation layer on the surface of the HAYNES® 214® alloy in an effort to provide oxidation and corrosion resistance at a temperature as low as 800°C. Through the use of various material characterization techniques, the use of a Cr_2O_3 nanocoating about 150 nanometers in thickness is capable of promoting and sustaining the formation of a protective α-Al_2O_3 scale for durations of at least 100 hours of exposure to air. The Cr_2O_3-coated alloy also provides superior protection under thermal cycling and hot corrosion conditions. The Al_2O_3-coated alloy provided intermediate results compared to the uncoated alloy in all isothermal oxidation tests performed; however, when exposed to hot corrosion conditions, the Al_2O_3-coated alloy performed similarly to the uncoated alloy. The Al_2O_3-coated alloy did appear to provide some benefit under thermal cycling conditions.

Table of Contents

List of Tables

List of Figures

Preface

The author would like to thank and acknowledge Dr. Jung-Kun Lee for his guidance and encouragement throughout the research and thesis writing process. Dr. Lee demonstrated a commitment to my professional growth and success through the continuous feedback and suggestions he provided. As a part time student pursuing and completing an unconventional research-based master's degree, Dr. Lee exhibited an excellent balance of patience relative to my less than full time schedule availability and motivation with regard to the pace and advancement of the research and thesis progression.

The author would also like to thank and acknowledge Seongha Lee, Matthew Kovalchuk, Preston Nguyen, Haiming Ma, Jakub Toman, and Rocco Cerchiara for their help and support throughout various phases of the experimentation, sample preparation, and characterization process. Their help and guidance significantly aided in the success of this thesis.

Lastly, the author would also like to thank and acknowledge Tres Harriman and Don Lucca at the Oklahoma State University for performing Raman spectroscopy and photoluminescence characterization on numerous oxidized samples. The characterization they performed helped confirm the results of this thesis.

1.0 Introduction

Superalloys, by definition, are either of the nickel, iron-nickel, or cobalt base and contain a multitude of other alloying elements designed to provide the demanding material properties needed for service. One key aspect of superalloys is that they are capable of operating at temperatures up to, and in excess of, about 70% of their absolute melting temperatures (T_m). Nickel-base superalloys are primarily used in applications that are subjected to high temperatures and oxidizing conditions (e.g., furnaces, gas turbines, jet engines, etc.) due to their excellent high temperature strength and oxidation resistance. The high temperature strength arises from the formation of nickel aluminide (Ni_3Al) precipitates (also known as the gamma prime (γ') phase) dispersed throughout the primary gamma (γ) phase matrix which consists of face centered cubic (FCC) nickel (Ni). The microstructure of a typical nickel-base superalloy showing the primary γ and γ' phases is shown in Figure 1.

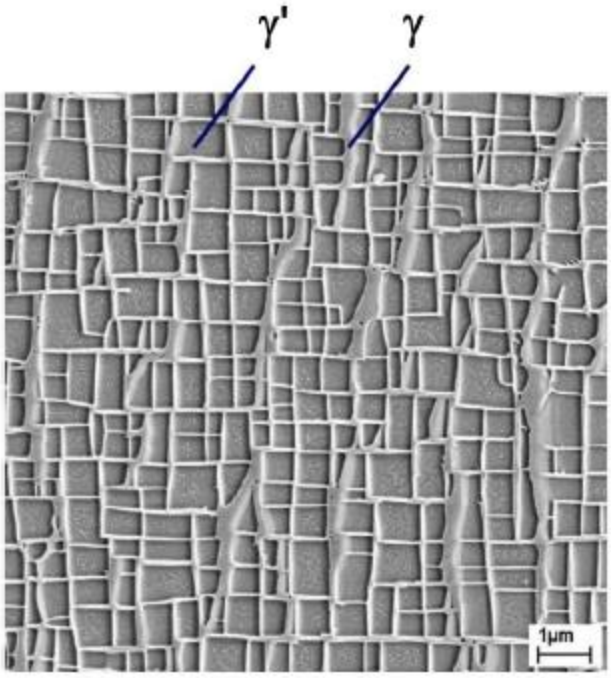

Figure 1: Microstructure of a Typical Nickel-base Superalloy Showing the Primary γ and γ' Phases (Figure Reproduced from [1])

The oxidation resistance occurs due to the alloy's slow formation of a continuous and protective external oxide scale during use. Depending on the alloy composition, some are designated as alumina or chromia formers owing to the fact that the protective external oxide scale that forms during high temperature exposure is either aluminum oxide (Al_2O_3) or chromium oxide (Cr_2O_3), respectively. Cr_2O_3 forming nickel-base superalloys have limitations in high temperature applications (i.e., greater than 1000°C) due to the volatilization of Cr_2O_3 which is described by the chemical reactions in Equations (1-1) and (1-2).

$$Cr_2O_3(s) + \frac{3}{2}O_2(g) \leftrightarrow 2\,CrO_3\,(g) \quad (1\text{-}1)$$

$$Cr_2O_3(s) + \frac{3}{2}O_2(g) + 2H_2O\,(g) \leftrightarrow 2\,CrO_2(OH)_2\,(g) \quad (1\text{-}2)$$

At temperatures above 1000°C, protective Cr_2O_3 scales that may be present on the surface can volatize into gases meaning the alloy's protection against oxidation can be compromised. Furthermore, if other metal-oxide scales are on the alloy surface (e.g., oxide products formed during transient oxidation, as described in Section 2.1.2.1), depending on the location of the Cr_2O_3 scale, the generation of gases from the volatilization reaction can build up pressure and lead to spallation. Spallation causes the oxide scale to become discontinuous and this causes the alloy to form additional metal-oxide. The repeated formation and spallation of the oxide scale results in depletion of the reactive metals in the alloy (i.e., chromium (Cr)) ultimately leading to complete exhaustion. Once the alloy can no longer form a protective Cr_2O_3 scale, further oxidation or attack can result in failure. Unlike Cr_2O_3 chromia which can volatilize at high temperatures, Al_2O_3 does not suffer from any volatilization which makes it a much more protective oxide at temperatures 1000°C and higher.

While Al_2O_3 scales are more protective, Al_2O_3 scale formation at lower temperatures (i.e., 800°C or 900°C) are very difficult due to the much slower diffusion of aluminum (Al) from within the bulk alloy compared to the faster inward diffusion of oxygen from the environment. As a result, if the Al_2O_3 forming nickel-base superalloy is dilute in Al content, internal precipitates of Al_2O_3 will form when exposed to lower temperatures. Internal oxide precipitates are undesirable because they change the mechanical properties of the superalloy, introduce stress in the subsurface region,

and can be an initiator for intergranular fracture since brittle oxides are preferentially located at grain boundaries.

HAYNES® 214® is a nickel-base superalloy which is comprised of Ni-Cr-Al-Fe and a small amount of yttrium (Y). This superalloy is an Al_2O_3 former and it is intended to be used in oxidizing environments where the temperature exceeds 955°C (1750°F) due to the alloy's formation of a continuous, protective, and slow growing external alpha Al_2O_3 (α- Al_2O_3) scale [2]. Table 1 below lists the nominal compositions of the HAYNES® 214® nickel-base superalloy with the primary components and compositions identified in italics.

Table 1: Nominal Composition of the HAYNES® 214® Nickel-base Superalloy (Data Reproduced from [2])

Element	Weight Percent (wt %)
Nickel	*75 Balance*
Chromium	*16*
Aluminum	*4.5*
Iron	*3*
Cobalt	2 max.
Manganese	0.5 max.
Molybdenum	0.5 max.
Titanium	0.5 max.
Tungsten	0.5 max.
Niobium	0.15 max.
Silicon	0.2 max.
Zirconium	0.1 max.
Carbon	0.04
Boron	0.01 max.
Yttrium	*0.01*

A few applications where the HAYNES® 214® superalloy has been used commercially is in clean firing (mesh belts, trays and fixtures for firing of pottery and fine china, and the heat treatment of electronic devices and technical grade ceramics), the gas turbine industry (foil construction honeycomb seals, combustor splash plates, and other static oxidation – limited parts), automotive industry (catalytic converter internals and used as a burner cup material in auxiliary heaters for military vehicles), and industrial heating markets (refractory anchors, furnace flame hoods, and rotary calciners for processing chloride compounds) [2]. Figure 2 below shows several images of parts and components made from the HAYNES® 214® nickel-base superalloy.

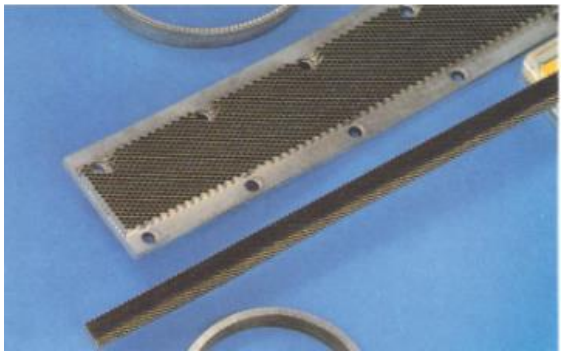

Honeycomb Seals

Flamehood

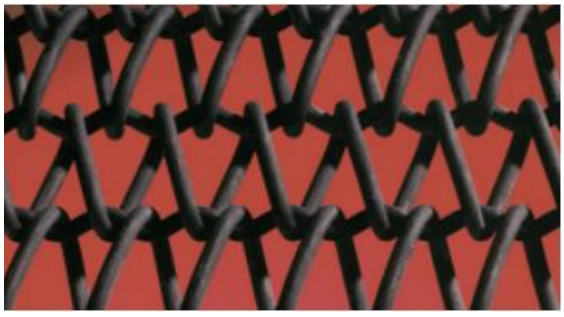

Belt in a Chinaware Decorating Kiln

Burner Assembly

Figure 2: Example of Parts and Components Fabricated from the HAYNES® 214® Nickel-base Superalloy (Figure Reproduced from [2])

As mentioned above, the HAYNES® 214® superalloy is intended to be used above 955°C where the alloy is capable of forming a protective external α-Al_2O_3 scale. However, below 955°C, the HAYNES® 214® superalloy forms oxides that are much less protective and are composed of a mixture of Ni, Cr, and Al. Thus, at low temperatures (i.e., 800°C or 900°C), the HAYNES® 214® superalloy has limitations for its use.

2.0 Background and Theory

2.1 Oxidation

2.1.1 Fundamentals of Metal Oxidation

Oxidation is a naturally occurring phenomenon where pure metals and oxygen chemically react to form metal-oxide according to the generic chemical reaction shown in Equation (2-1) [3]

$$\frac{2x}{y}M + O_2 \leftrightarrow \frac{2}{y}M_xO_y \tag{2-1}$$

where x and y are integers associated with the stoichiometry of the chemical reaction, M is the metal, and O/O_2 is oxygen. According to chemical reaction kinetics, equilibrium of the metal and oxygen reaction can be described by Equation (2-2)

$$K_{eq} = \frac{a_{Products}}{a_{Reactants}} = \frac{a_{M_xO_y}{}^{2/y}}{\left(a_M{}^{2x/y}\right)\left(a_{O_2}\right)} \tag{2-2}$$

where K_{eq} is the temperature dependent equilibrium constant for the chemical reaction, $a_{products}$ is the chemical activity of the reaction products, $a_{reactants}$ is the chemical activity of the reactants, $a_{M_xO_y}{}^{2/y}$ is the chemical activity of the metal-oxide, $a_M{}^{2x/y}$ is the chemical activity of the pure metal, and a_{O_2} is the chemical activity of oxygen. The solid materials (i.e., the metal and metal-

oxide shown in Equation (2-1)) are always assumed to be in their pure standard state, therefore the chemical activities are equal to one as long as the metal and metal-oxide are immiscible in each other. As a result, the equilibrium equation can be reduced to the following (Equation (2-3))

$$K_{eq} = \frac{1}{a_{O_2}} = \frac{1}{P_{O_2}} \tag{2-3}$$

where K_{eq} and a_{O_2} are defined above, and P_{O_2} is the oxygen partial pressure.

Due to the thermodynamic driving force dictated by the change in Gibbs free energy (GFE), ΔG, a chemical reaction can be spontaneous or non-spontaneous. For a spontaneous reaction, ΔG is negative and the reaction occurs in the forward direction (i.e., reactants to products) without external influence until equilibrium is established. For a non-spontaneous reaction, ΔG is positive and the reaction will naturally occur in the reverse direction (i.e., products to reactants) until equilibrium is established. A non-spontaneous reaction can occur in the forward direction (i.e., reactants to products) only if an external input such as heat is added.

The change in GFE for a chemical reaction can be found by Equation (2-4)

$$\Delta G = \Delta G^{O} + RT\ln K_{eq} \tag{2-4}$$

where ΔG is the change in GFE, ΔG^{O} is the standard state change in GFE, R is the universal gas constant, T is temperature, and K_{eq} is defined above. By combining Equations (2-3) and (2-4), an expression for the change in GFE as a function of the oxygen partial pressure can be achieved (Equation (2-5))

$$\Delta G = \Delta G^{O} - RT\ln P_{O_2} \tag{2-5}$$

where all variables have been defined previously. The definition of the standard state change in GFE for a chemical reaction is given by Equation (2-6)

$$\Delta G^{O} = \Delta H^{O} - T\Delta S^{O} \tag{2-6}$$

where ΔG^{O} and T are defined above, ΔH^{O} is the standard state change in enthalpy, and ΔS^{O} is the standard state change in entropy. As shown in Equation (2-6), the GFE is a combination of three thermodynamic state variables; enthalpy, temperature, and entropy.

Once the equilibrium of a chemical reaction is established, the change in GFE is equal to zero. Thus, Equation (2-5) can be rewritten in terms of equilibrium conditions (Equation (2-7))

$$0 = \Delta G^{O} - RT\ln {P_{O_2}}^{Eq} \rightarrow \Delta G^{O} = RT\ln {P_{O_2}}^{Eq} \tag{2-7}$$

where ΔG^{O}, R, and T are defined above, and ${P_{O_2}}^{Eq}$ is the equilibrium oxygen partial pressure. As a result of Equation (2-7), the equilibrium oxygen partial pressure for a metal-oxygen reaction can be calculated by Equation (2-8)

$${P_{O_2}}^{Eq} = e^{\left(\frac{\Delta G^{O}}{RT}\right)} \tag{2-8}$$

where all variables have been defined above.

Since the change in GFE of formation for a system follows a linear relationship ($y = mx + b$), a useful diagram which relates the GFE of formation and temperature for numerous metal-oxygen reactions is the Ellingham diagram shown in Figure 3. The y-axis of the Ellingham diagram shows the change in standard state GFE of formation for various metal-oxygen reactions whereas the x-axis shows the temperature that the reaction takes place at. Based on the linear relationship, the standard state change in enthalpy, ΔH^O, for a specific metal-oxygen reaction can be determined via the y-intercept of the given metal-oxygen line on the Ellingham diagram. Furthermore, the standard state change in entropy, ΔS^O, for a specific metal-oxygen reaction can be determined via the slope of the given metal-oxygen line on the Ellingham diagram.

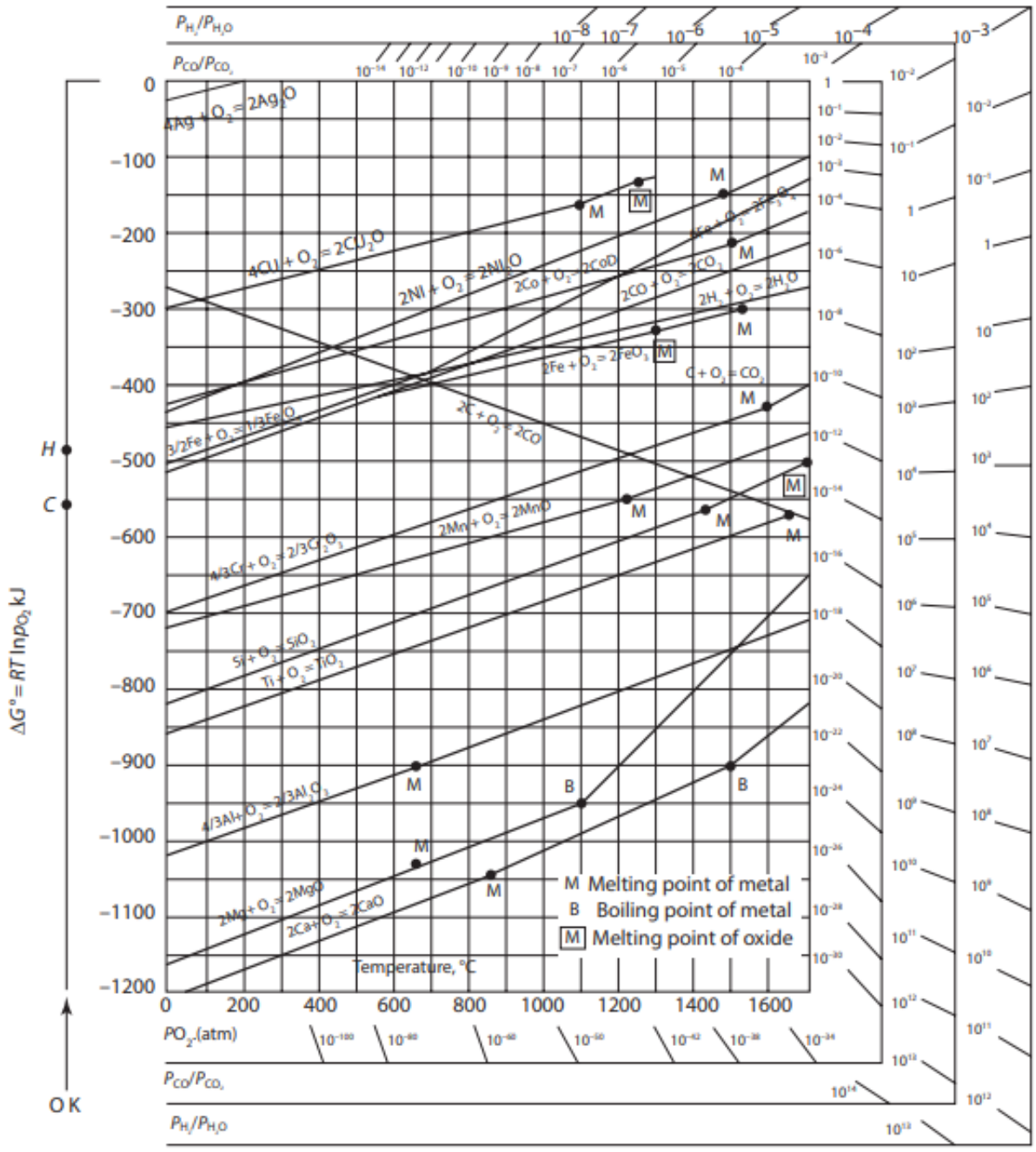

Figure 3: Ellingham Diagram Showing the GFE, Temperature, and Equilibrium Oxygen Partial Pressure for the Formation of Various Metal Oxides (Figure Reproduced from [4])

The Ellingham diagram also contains a third axis which shows oxygen partial pressures over a range of $1 - 10^{-100}$ atmospheres (atm). This axis is particularly useful to determine the oxygen partial pressure that is in equilibrium with a metal at a specific temperature (i.e., the dissociation partial pressure from Equation (2-8)). The oxygen partial pressure that is in equilibrium with a metal can dictate whether or not metal-oxide will form. If the oxygen partial pressure is above the equilibrium oxygen partial pressure, the reaction will proceed in the forward direction to form more metal-oxide. If the oxygen partial pressure is below the equilibrium oxygen partial pressure, the reaction will not occur and metal-oxide formation is prevented.

The Ellingham diagram is constructed in a way that the more negative the change in standard state GFE is on the Ellingham diagram, the more stable the metal-oxide is, and the greater the thermodynamic driving force is for the pure metal to react with oxygen. At 800°C, the equilibrium partial pressure for the formation of Al_2O_3 and Cr_2O_3 is about 10^{-48} atm and 10^{-33} atm, respectively. These very small oxygen partial pressures, in combination with the large negative change in standard state GFE, signify the extreme difficulty in keeping pure Al or Cr in the unoxidized state. Thus, the oxides of common alloying components such as Cr, titanium (Ti), and Al are among the most stable and thermodynamically favorable metal-oxides.

2.1.2 Oxidation of Alloys and Superalloys

Alloys and superalloys often contain two, three, or four or more metallic elements that are added to achieve unique material properties depending on the intended end-use. The addition of metallic elements into alloys and superalloys results in microstructural changes via solid solution strengthening and precipitate hardening, and the resulting material properties cannot be obtained by using any single metallic element from the alloy. While the addition of different metallic

elements improves the material properties, it also makes the oxidation process and mechanism much more complex than pure metals, as was described in Section 2.1.1. The complexity arises from the following [3]:

- Each metallic element has its own affinity for oxygen (i.e., thermodynamic driving force) as shown in the Ellingham diagram in Figure 3
- Additional oxides can form such as ternary or higher oxides (e.g., spinel which has the generic chemical formula of AB_2O_4)
- Oxides in contact with each other may have some level of solubility
- Metal ions have different mobilities within the oxide phases
- Metal ions have different diffusivities within the alloy
- Each additional metallic element added to an alloy increases the allowable degrees of freedom as dictated by the Gibbs phase rule and this introduces the possibility for internal oxidation (i.e., subsurface oxide precipitation) to occur

With respect to the oxidation of alloys and superalloys, there are five key phenomena; transient and steady state oxidation, internal oxidation, transition from internal to external oxidation, the third element (gettering) effect, and surface condition. Each of these phenomena are discussed in the succeeding sections. For simplicity, the oxidation discussions below are presented relative to a binary (i.e., two component) alloy of Ni and Al (Ni-Al) where Ni is the solvent and more noble metal while Al is the solute and more reactive metal. When exposed to oxygen, the more reactive metal, in this case Al, will undergo selective oxidation since the standard state GFE of formation is more negative (i.e., more thermodynamically favorable) and Al_2O_3 is more stable

at significantly smaller oxygen partial pressures. The role of a third element, in this case Cr for the ternary (i.e., three component) alloy of Ni-Cr-Al, is discussed in Section 2.1.2.4.

2.1.2.1 Transient and Steady-State Oxidation

Transient oxidation is referred to as the early stages of alloy oxidation where base metal oxides (e.g., nickel oxide (NiO) in the case of a binary Ni-Al alloy) form on the surface. During this transient stage, the alloy undergoes rapid weight gain until the surface is completely oxidized and a continuous, external oxide scale is formed. Once this continuous, external oxide scale is formed on the surface, further metal-oxide formation becomes a diffusion-controlled process where the rate limiting step is the transport of oxygen through the scale. When this occurs, steady state conditions are achieved and the growth of the protective Al_2O_3 scale follows the general kinetic rate law shown in Equation (2-9)

$$W = kt^{1/n} \tag{2-9}$$

where W is the weight gain (in units of mass per unit area), k is the rate constant, t is time, and n is an integer. This kinetic rate law is applicable to any alloy that undergoes oxidation; however, each alloy system may have different values of n such as 1 for an alloy that follows linear kinetics, 2 for an alloy that follows parabolic kinetics, or 3 and higher for an alloy that follows sub-parabolic kinetics.

Many alloys, including nickel-base superalloys, follow parabolic oxidation kinetics which can be described by Equation (2-9) above and inserting the value 2 for the integer n. The resulting parabolic rate law is shown in Equation (2-10)

$$W^2 = k_p t \tag{2-10}$$

where W and t are defined above, and k_p is the parabolic rate constant. Figure 4 below shows a plot of parabolic rate constants at different temperatures for some common oxide scales that form on various metals or alloys. Additionally, Figure 5 below shows a typical weight gain curve for the high temperature oxidation of the HAYNES® 214® nickel-base superalloy at 1100°C and 1200°C.

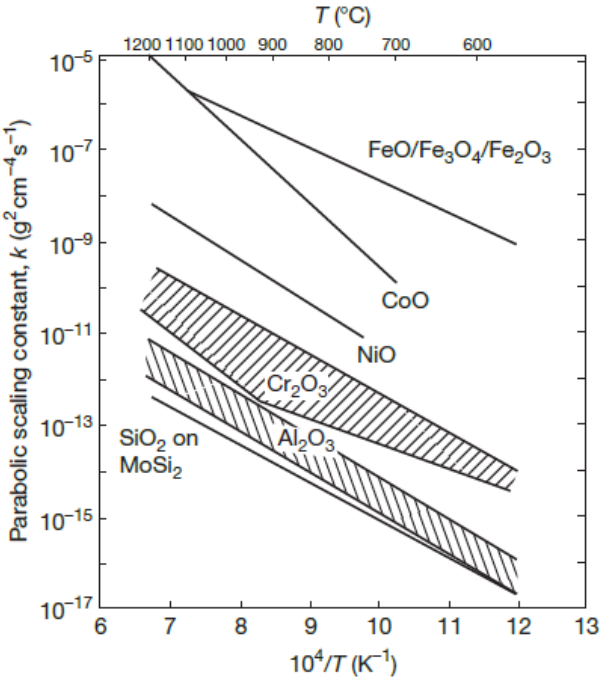

Figure 4: Parabolic Rate Constants as a Function of Temperature for Various Oxide Scale Formations (Figure Reproduced from [3])

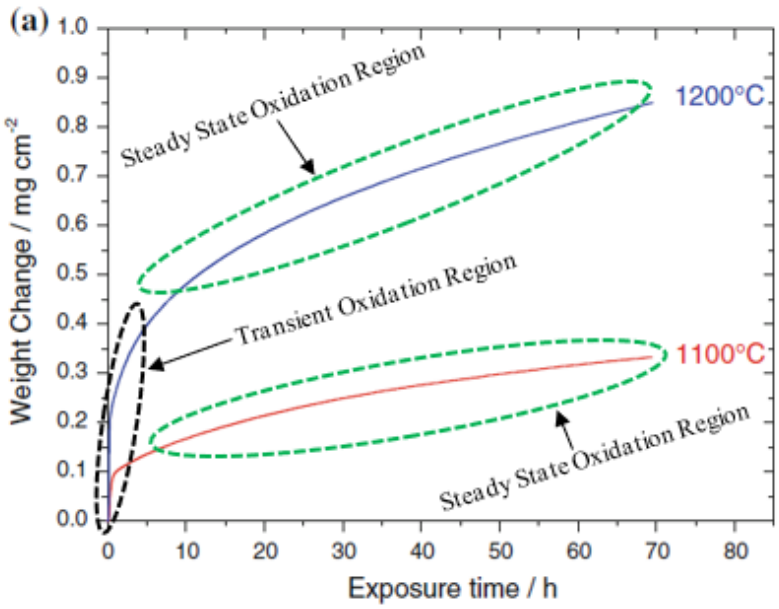

Figure 5: Weight Gain Kinetics Showing the Transient and Steady State Oxidation Regions for the HAYNES® 214® Nickel-base Superalloy at 1100°C and 1200°C (Figure Reproduced from [5])

As seen in Figure 4, the three primary metal oxide scales that form on the HAYNES® 214® nickel-base superalloys (NiO, Cr_2O_3, and Al_2O_3) follow parabolic kinetics. More importantly, the rate constants indicate the order of scale formation; first NiO is formed, followed by Cr_2O_3, and finally Al_2O_3. Because diffusion follows an Arrhenius type of relationship (i.e., is exponentially dependent on temperature), Figure 4 shows that the scaling constant of Al_2O_3 at low temperature (e.g., 800°C) could be one or two magnitudes slower than at higher temperature (e.g., 1000°C). This is a direct result of the slower bulk diffusion of Al from within the alloy. The detailed process and mechanism for the formation of these three oxide scales is further describe in the succeeding sections. Additionally, Figure 5 shows that the transient oxidation region for the HAYNES® 214®

nickel-base superalloy is rapid (on the order of about an hour (hr) at both 1100°C and 1200°C) and the steady state oxidation region is very slow and becomes slower over time, indicative of diffusion-controlled kinetics.

2.1.2.2 Internal Oxidation

Internal oxidation is a diffusion-controlled process which results in precipitates of metal-oxide (e.g., Al_2O_3 in the case of a binary Ni-Al alloy) forming in the subsurface region of the alloy. With regards to alloys and superalloys used in high temperature and oxidizing conditions, internal oxidation should be avoided as this can detrimentally affect the mechanical strength and other material properties required for use. In order for Al_2O_3 to precipitate internally, there are two criteria that must be met. First, the mole fraction of the more reactive solute metal (i.e., Al) must be below the critical mole fraction required for the transition from internal to external oxidation (discussed in Section 2.1.2.3 below), and second, the solubility product of the metal-oxide (i.e., Al_2O_3) within the primary alloy matrix (i.e., Ni) must be exceeded [6]. The solubility product criteria can be understood via Equation (2-11) [6]

$$N_B N_O > K_{SP} \tag{2-11}$$

where N_B is mole fraction of the solute metal (Al) in the alloy, N_O is mole fraction of oxygen in the alloy, and K_{SP} is the equilibrium solubility product for a dilute alloy.

The amount that the solubility product must be exceeded before precipitation of internal oxides occurs (i.e., how much the alloy must become supersaturated) is an alloy specific parameter [3]. Factors affecting the relationship between supersaturation and precipitation include oxide

stability, oxide composition, and oxide crystal structure, and it is generally understood that the more thermodynamically stable the metal-oxide is, the less supersaturation is needed before precipitation of the internal oxide occurs [3]. Thus, as depicted by the Ellingham diagram in Figure 3, internal oxides of Al and Cr are the most common and this has been observed in many previous studies [7, 8, 9, 10].

For a binary alloy of Ni-Al that undergoes no external oxidation (i.e., if there were no external NiO formation), Wagner derived an expression for the depth of the internal oxidation zone assuming there is negligible metal recession. This expression is shown in Equation (2-12) [3]

$$\varepsilon = \left(\frac{2N_O{}^S D_O t}{v N_B{}^0}\right)^{\frac{1}{2}} \tag{2-12}$$

where ε is the depth of the internal oxidation zone, $N_O{}^S$ is the solubility of oxygen in the alloy, D_O is the diffusivity of oxygen in the alloy, t is time, v is the stoichiometric factor for Al_2O_3, and $N_B{}^0$ is the mole fraction of the more reactive solute metal in the bulk alloy (i.e., Al). In the event that there is external oxidation (e.g., NiO formation) and the oxidation process becomes controlled by the diffusion of oxygen through the outer NiO scale, the oxygen solubility ($N_O{}^S$) is no longer fixed by the oxygen partial pressure of the environment the alloy is exposed to, but instead is dependent upon the equilibrium oxygen partial pressure at the alloy-oxide interface ($N_O{}^I$) [3]. In practice, most or all alloys will form some type of external oxide scale, thus relative to Equation (2-12), the oxygen solubility ($N_O{}^S$) would be taken as the equilibrium oxygen partial pressure at the alloy-oxide interface ($N_O{}^I$).

As Equation (2-12) shows, internal oxidation relies on two primary factors; the product of $N_O{}^{S/I}D_O$ which is referred to as the oxygen permeability into the alloy, and $N_B{}^0$ which is the mole fraction of the more reactive solute metal (Al) in the alloy (e.g., 2 wt%, 5 wt%, etc.). The oxygen solubility ($N_O{}^{S/I}$) follows Sievert's law [4] as shown in Equation (2-13)

$$N_O{}^{S/I} \propto (P_{O_2})^{\frac{1}{2}} \tag{2-13}$$

where all variables have been defined previously. Since the oxygen solubility has a square root dependence on the oxygen partial pressure, and the depth of the internal oxidation zone has a square root dependence on the oxygen solubility, this means the depth of the internal oxidation zone is proportional to the fourth root of the oxygen partial pressure, as shown in Equation (2-14)

$$\varepsilon \propto (P_{O_2})^{\frac{1}{4}} \tag{2-14}$$

where all variables have been defined previously. As a result of Equations (2-12), (2-13), and (2-14), there are two ways to control internal oxidation; reduce the oxygen partial pressure at the alloy surface or alloy-oxide interface (which subsequently affects the oxygen permeability into the alloy ($N_O{}^{S/I}D_O$)) or increase the amount of solute metal (Al) in the alloy.

2.1.2.3 Transition from Internal to External Oxidation

Wagner proposed that the transition between internal and external oxidation occurs when a critical volume fraction of metal-oxide is obtained within the internal oxidation zone. When this

occurs, the inward diffusion of oxygen becomes so restricted that the oxygen partial pressure within the alloy becomes too low to form additional metal-oxide and extend the internal oxidation zone (i.e., the oxygen partial pressure is less than the equilibrium partial pressure from Equation (2-8) where the chemical reaction does not proceed in the forward direction) [3, 6]. When this occurs, the lateral growth of the metal-oxide precipitates within the internal oxidation zone becomes kinetically favorable because the oxygen partial pressure in this region is still sufficient to cause metal-oxide formation and thus the alloy will eventually develop a continuous oxide scale that covers the entire surface [3, 6]. The schematic in Figure 6 illustrates this phenomenon (for simplicity, the schematic assumes that the more noble metal (i.e., Ni) does not form an external oxide scale).

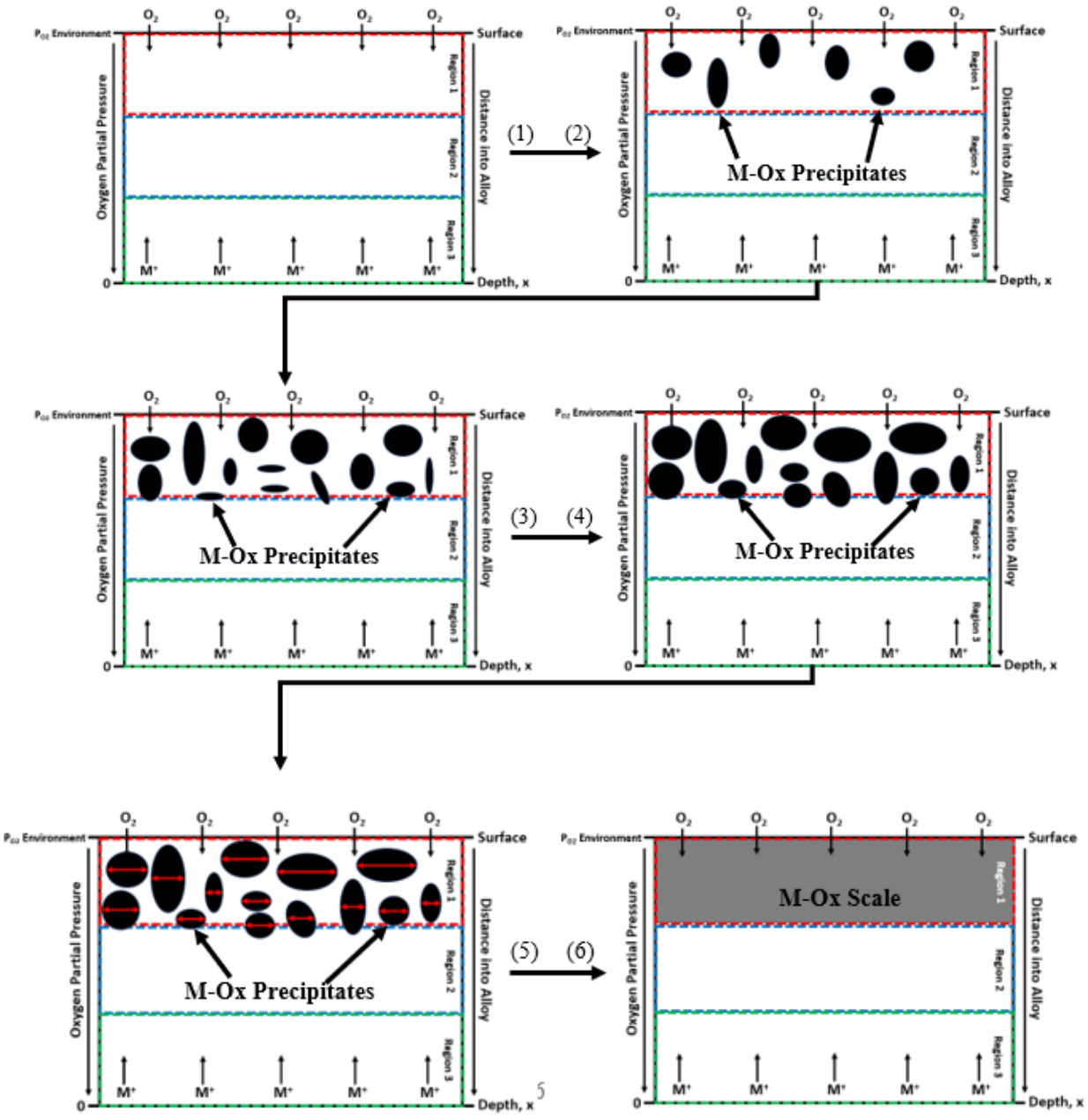

Figure 6: Schematic of the Time Dependent Process for the Transition Between Internal and External Oxidation

In Figure 6, the six schematics show the time dependent process for the transition from internal to external oxidation. In phase 1, the alloy is exposed to a high temperature oxidizing environment where the inward diffusion of oxygen into the alloy and the outward diffusion of the more reactive solute metal cations (i.e., Al) from within the bulk alloy begins. In phase 2, the oxygen partial pressure in the subsurface zone (region 1) has increased due to the inward diffusion of oxygen, and the more reactive solute metal cations have reached this area of the alloy due to outward diffusion. The oxygen partial pressure in region 1 is above the equilibrium partial pressure for the formation of Al_2O_3, thus if the subsurface zone is supersaturated, internal precipitation of Al_2O_3 will occur. In phases 3 and 4, the inward and outward diffusion of oxygen and solute metal cations, respectively, continues resulting in either the formation of new internal precipitates of Al_2O_3 or growth of existing precipitates. In these two phases, the oxygen partial pressure has increased further into the alloy (i.e., beginning to extend into region 2) and therefore the depth of the internal oxidation zone extends into this area.

During phase 5, the volume fraction of internal precipitates of Al_2O_3 in region 1 has become so large that the continued inward diffusion of oxygen becomes severely restricted. When this restriction occurs, the oxygen partial pressure at larger depths of the alloy (i.e., in the middle of region 2) is too low to form internal oxide precipitates, thus the solute metal cations continue to diffuse upwards without precipitation (i.e., the internal oxidation zone does not extend deeper). The continued supply of solute metal cations within region 1 and at the boundary of regions 1 and 2 reacts with the oxygen in this subsurface zone to precipitate more internal oxides. Because the partial pressure of oxygen in region 1 is large enough to form internal oxide precipitates but is insufficient in region 2, the continued growth of internal oxide switches from being kinetically favorable in the downward (vertical) direction to being more kinetically favorable in the lateral

(horizontal) direction. As oxidation continues, the lateral growth of internal oxide precipitates eventually joins together to form a continuous and external oxide scale as seen in phase 6. Once a continuous external oxide scale has been formed, the alloy would be protected and further oxidation would follow steady state, diffusion-controlled growth as described in Section 2.1.2.1.

Wagner also derived an expression to determine the critical mole fraction of the more reactive solute metal that is required to be in the alloy before the transition from internal to external oxidation can occur. This expression is shown in Equation (2-15) [3, 6]

$$N_{B^*}{}^{0} \geq \left(f^{*} \left(\frac{V_M}{V_{OX}} \right) \pi \frac{N_O{}^{S} D_O}{2 v D_B} \right)^{\frac{1}{2}} \tag{2-15}$$

where $N_O{}^{S}$, D_O, and v are defined above, and $N_{B^*}{}^{0}$ is the critical mole fraction of the more reactive solute metal in the alloy (Al), f^{*} is a constant typically taken as 0.3, V_M is the molar volume of the alloy, V_{OX} is the molar volume of the oxide, and D_B is the diffusion coefficient of the more reactive solute metal (Al) in the alloy. Equation (2-15) assumes there is no external oxide scale formation of the solvent metal (Ni) as this results in a much more complex equation. As with the phenomenon of internal oxidation, if there is an external oxide scale formation of the solvent metal (Ni), the oxygen solubility ($N_O{}^{S}$) is no longer fixed by the oxygen partial pressure of the environment the alloy is exposed to, but instead is dependent upon the equilibrium oxygen partial pressure at the alloy-oxide interface ($N_O{}^{I}$) [6]. Similar to the expression for internal oxidation in Equation (2-12), Equation (2-15) also relies on two primary factors; the oxygen permeability into the alloy (the product of $N_O{}^{S/I} D_O$) and the diffusivity of the more reactive solute metal from within the bulk

alloy (D_B). One way to affect the diffusivity of the more reactive solute metal (D_B) within the alloy is through the alteration of the alloy surface finish, as discussed in Section 2.1.2.5 below.

In binary Ni-Al alloys, the amount of Al needed to form a continuous external scale can be extensive at low temperatures. Hayashi [9] studied the oxidation performance of three different Ni-Al alloys at 800°C; Ni-3Al, Ni-6Al, and Ni-10Al. In all three alloys, it was found that an internal oxidation zone was developed, showing that the Al content needed to form a continuous external Al_2O_3 scale must be at least greater than 10 wt%.

2.1.2.4 Gettering Effect (Third Element Effect)

One of the most prominent discoveries of alloy oxidation is the phenomena of the third element effect, also called the gettering effect. In order for the gettering effect to occur, a metallic element must be added to an alloy which has an intermediate affinity to oxygen compared to the most noble solvent metal (e.g., Ni) and most reactive solute metal (e.g., Al). One example of this is the addition of Cr to the binary alloy of Ni-Al to form a ternary alloy of Ni-Cr-Al and this drastically affects the oxidation mechanism. This is because Cr_2O_3 has a standard state GFE of formation in between that of NiO and Al_2O_3 and is more thermodynamically stable at lower oxygen partial pressures than NiO. As a result, it is found that adding Cr to a binary alloy of Ni-Al requires less Al content in order to form a continuous and protective external Al_2O_3 scale on the surface of the alloy [11, 12].

The primary reason less Al is needed when Cr is added to the alloy is due to the formation of Cr_2O_3 which aids in lowering the oxygen partial pressure and oxygen activity at the alloy-oxide interface and within the subsurface region of the alloy. If the amount of Cr added to the alloy lowers the oxygen partial pressure or oxygen activity to a value below what is needed to form Al_2O_3, formation and precipitation cannot occur. Preventing the formation and precipitation of

internal Al_2O_3 allows the bulk Al to diffuse to the alloy-oxide interface where it can form a continuous and external scale.

In a study done by Zhang [11], a binary alloy of Ni-10Al (atomic percent (at%)) was oxidized at 900°C for 24-hrs in 1 atm of pure oxygen. The binary alloy formed an outer layer of NiO and contained an extensive internal oxidation zone of Al_2O_3 precipitates. Zhang found that by adding 10 at% of Cr to the binary alloy of Ni-10Al, the ternary alloy of Ni-10Cr-10Al was able to form a continuous and external Al_2O_3 scale on the surface of the alloy. Niu [12] further expanded upon this finding by lowering the at% of Al to 7. In this experiment, a binary alloy of Ni-7Al was oxidized at 900°C for 24-hrs in 1 atm of pure oxygen. As was the case with the binary alloy of Ni-10Al, the binary alloy of Ni-7Al also formed an outer layer of NiO and contained an extensive internal oxidation zone of Al_2O_3 precipitates. Similar to Zhang's findings, when adding 10 at% of Cr to the binary alloy of Ni-7Al, the ternary alloy of Ni-10Cr-7Al formed a continuous and external scale of Al_2O_3. This is an excellent example of how the addition of Cr can act as an oxygen getter and allow an alloy to form a continuous and external scale of Al_2O_3 compared to a binary alloy that contains the same amount of Al but experiences internal oxidation only.

In the classical experiments performed by Giggins and Pettit [7], 21 alloys containing varying compositions (wt%) of Ni, Cr, and Al were studied at temperatures of 1000°C, 1100°C, and 1200°C. All of the alloys were oxidized in 0.1 atm of oxygen for 20-hrs to develop and understand the detailed mechanisms of oxidation. Of the 21 alloys, 19 were ternary alloys of Ni-Cr-Al, while one was a binary alloy of Ni-Cr and the last was a binary alloy of Ni-Al.

Giggins and Pettit found that the oxidation mechanisms of the alloys could be classified into three separate groups; the formation of an external NiO scale and internal oxidation of Cr_2O_3 and Al_2O_3 (Region I), the formation of an external Cr_2O_3 scale and internal oxidation of Al_2O_3

(Region II), and the formation of an external Al_2O_3 scale with no internal oxidation (Region III). The ternary isothermal diagrams showing the compositions of all 21 alloys and the three distinct regions for the different oxidation mechanisms at 1000°C, 1100°C, and 1200°C are shown in Figure 7, Figure 8, and Figure 9 below.

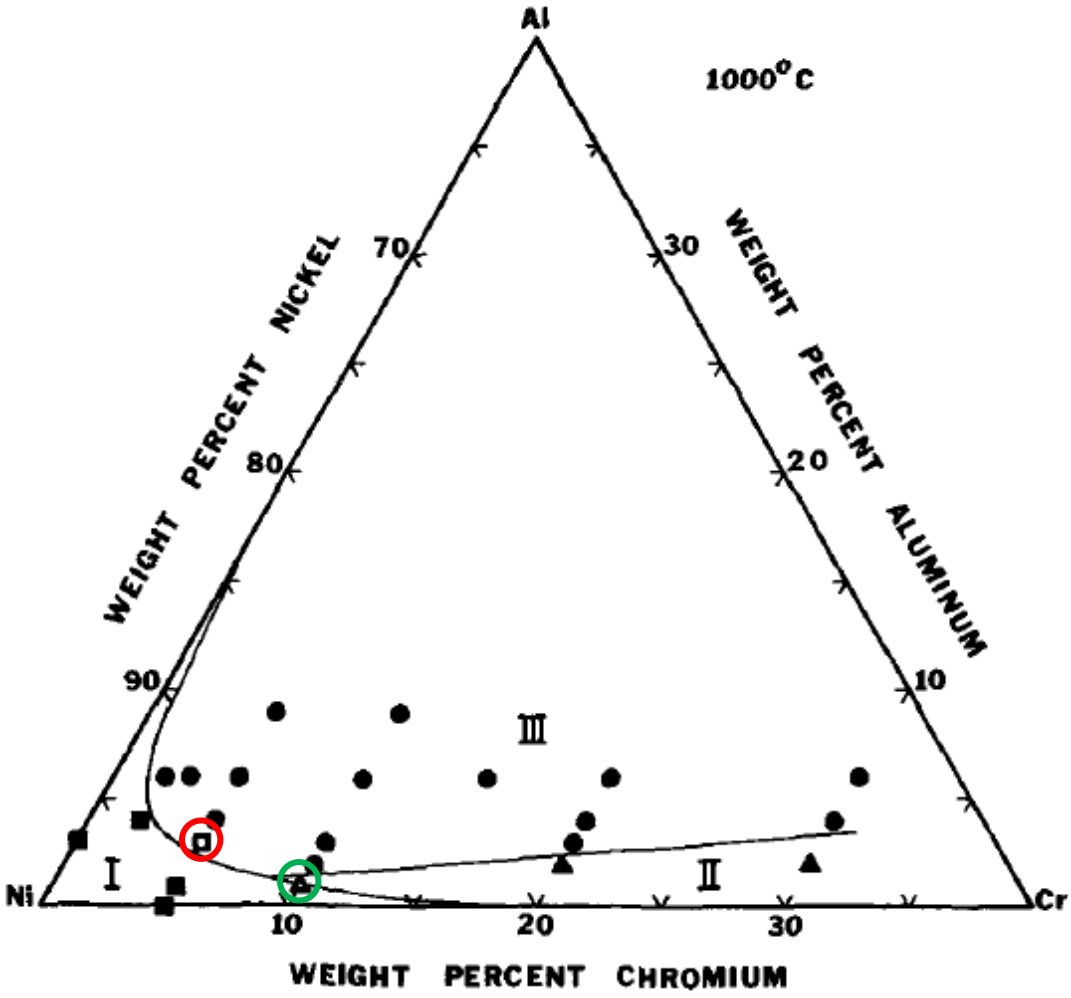

Figure 7: Ternary Isothermal Diagram Showing the Compositions of All 21 Alloys and the Three Distinct Regions Corresponding to the Three Different Oxidation Mechanisms at 1000°C (Figure Reproduced from [7])

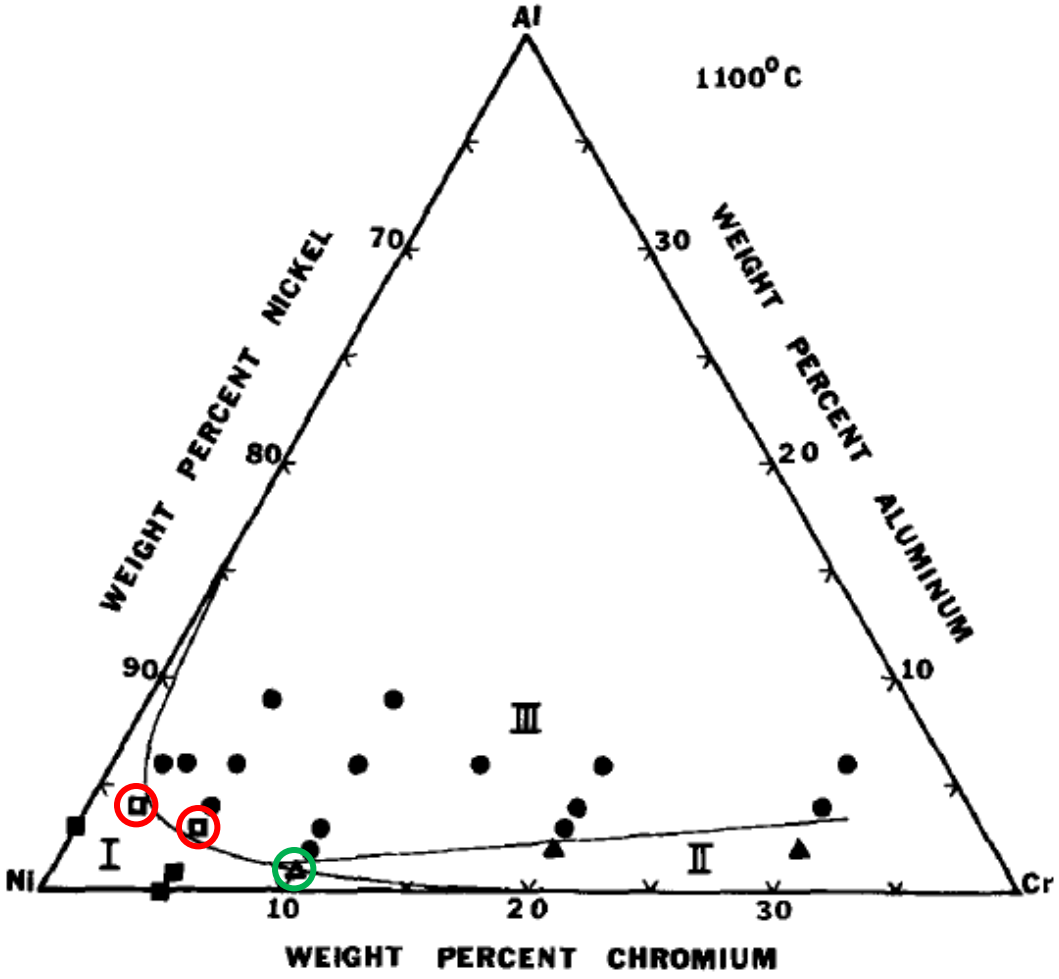

Figure 8: Ternary Isothermal Diagram Showing the Compositions of All 21 Alloys and the Three Distinct Regions Corresponding to the Three Different Oxidation at 1100°C (Figure Reproduced from [7])

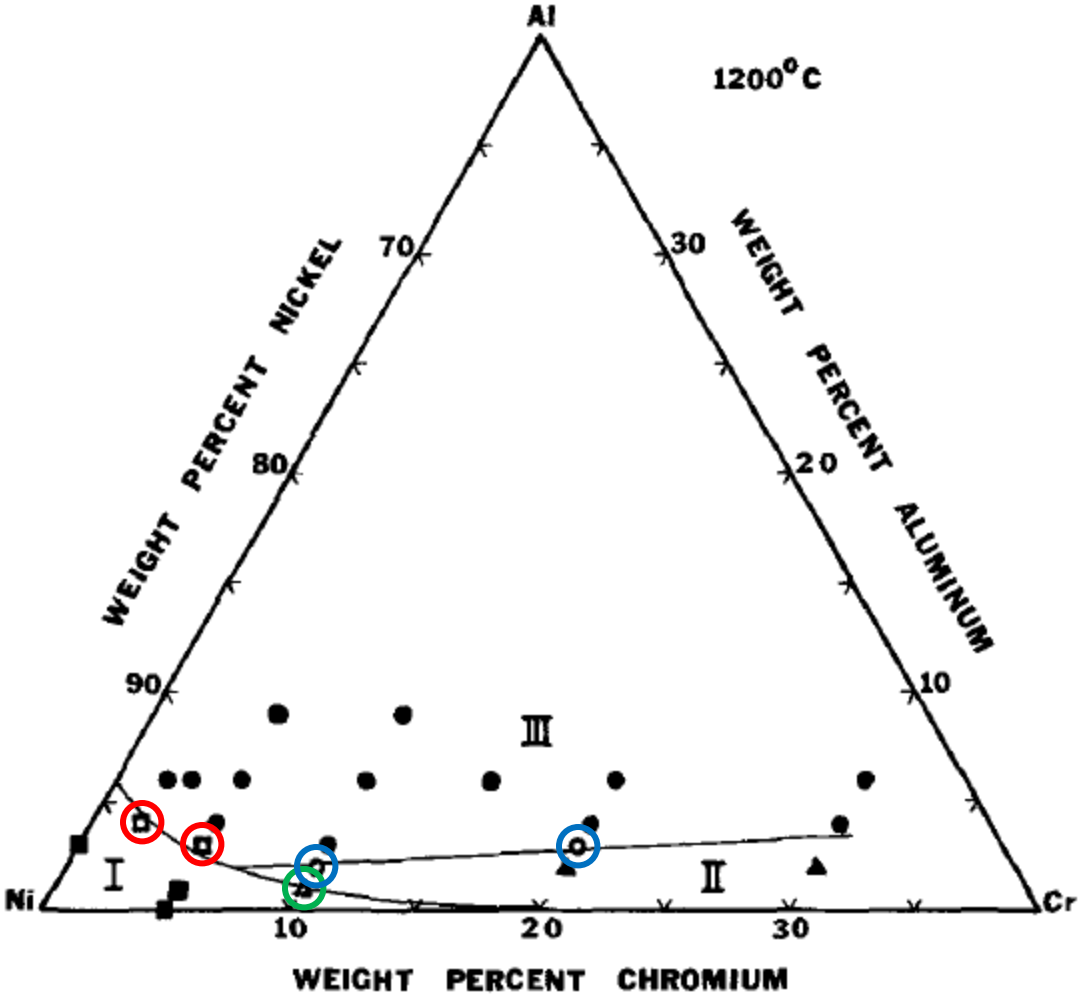

Figure 9: Ternary Isothermal Diagram Showing the Compositions of All 21 Alloys and the Three Distinct Regions Corresponding to the Three Different Oxidation at 1200°C (Figure Reproduced from [7])

To understand the three different oxidation mechanisms of the ternary Ni-Cr-Al alloys, Giggins developed a schematic showing the complete time dependent oxidation process from transient oxidation to continuous scale formation depending on which mechanism (Region I, II, or III) the alloy follows. The time dependent oxidation process is shown in Figure 10 below.

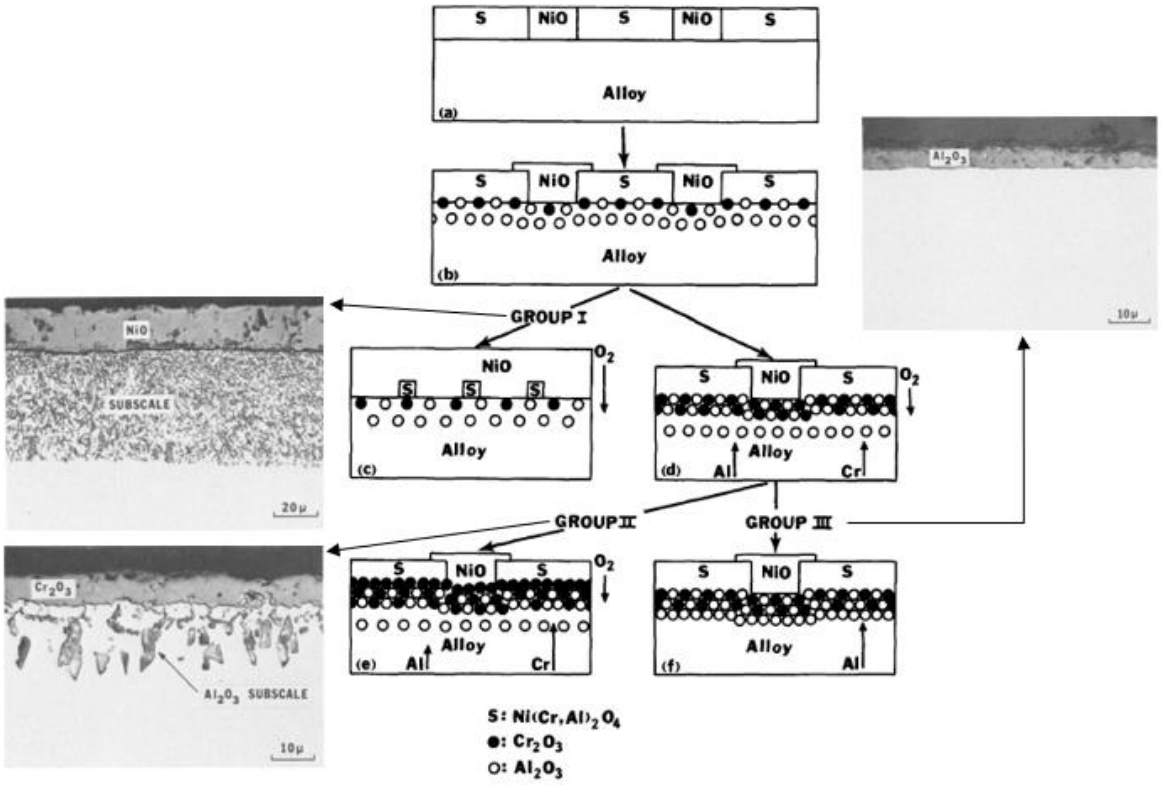

Figure 10: Schematic of the Three Different Oxidation Mechanisms (Group I, Group II, and Group III) For the Ni-Cr-Al Alloys (Figure Reproduced from [7])

In step (a), the alloy undergoes transient oxidiation (as described in 2.1.2.1) where base metal oxides NiO, Cr_2O_3, and some Al_2O_3 form on the surface. The NiO reacts with some of the Cr_2O_3 and Al_2O_3 to form a spinel oxide of nickel chromate ($NiCr_2O_4$) or nickel aluminate ($NiAl_2O_4$) or a mixed spinel structure ($Ni(Cr,Al)_2O_4$). In step (b), the oxidation process continues and diffusion of the more reactive solute metals (Cr and Al) occurs from within the bulk alloy towards the alloy/oxide interface. Both steps (a) and (b) are identical for all three oxidation mechanisms and it isn't unil after step (b) where the oxidation mechanisms change depending on the bulk alloy composition.

If the Ni content is very high and the alloy is very dilute in Cr and Al content, step (c) shows that the alloy will form a thick external oxide scale of NiO whereas the subsurface region of the alloy will contain an extensive internal oxidation zone of Cr_2O_3 and Al_2O_3. An example of an alloy that followed this mechanism contained compositions of Ni-2Cr-4Al. In step (d), if the Ni content is much lower and the Cr and Al contents are increased, the alloy will form an outer layer comprised of primarily $Ni(Cr,Al)_2O_4$ with a continuous mixed oxide of Al and Cr ($(Al,Cr)_2O_3$) underneath. This step is consistent for alloys that either follow mechanism II or III.

In step (e), if the Cr content in the alloy is large enough combined with the oxygen partial pressure below the mixed oxide of $(Al,Cr)_2O_3$ being high enough to form Al_2O_3 precipitates and the diffusion of Al from within the bulk alloy being slow enough, the alloy will form a continuous scale of Cr_2O_3 with a subsurface region containing internal Al_2O_3 precipitates. An example of an alloy that followed this mechanism contained compositions of Ni-20Cr-2Al.

In step (f), if the alloy has increased Al content (compared to those alloys from step (e)) and the diffusion of Al from within the bulk alloy is fast enough, a continuous and external Al_2O_3 scale will form with no internal Al_2O_3 precipiates. Because Al_2O_3 scales provide the best oxidation

resistance and are slow growing, combined with the absence of any internal oxidation occurring, alloys that follow this mechanism are always preferred. An example of an alloy that followed this mechanism contained compositions of Ni-20Cr-4Al.

While most alloys followed one of the three oxidation mechanisms (i.e., regions I, II, or III), Giggins discovered that several alloys (circled in red, green, and blue in Figure 7, Figure 8, and Figure 9) oxidized following two of the mechanisms simultaneously (termed transition alloys). This was due to the compositions falling on or immediately near the lines separating regions I and III (square data points circled in red), regions I and II (triangular data points circled in green), or regions II and III (circular data points circled in blue) in the ternary isothermal diagrams. Cross-sectional scanning electron microscopy (SEM) images of alloys that exhibited mixed oxidation mechanisms for each scenario are shown in Figure 11, Figure 12, and Figure 13 below.

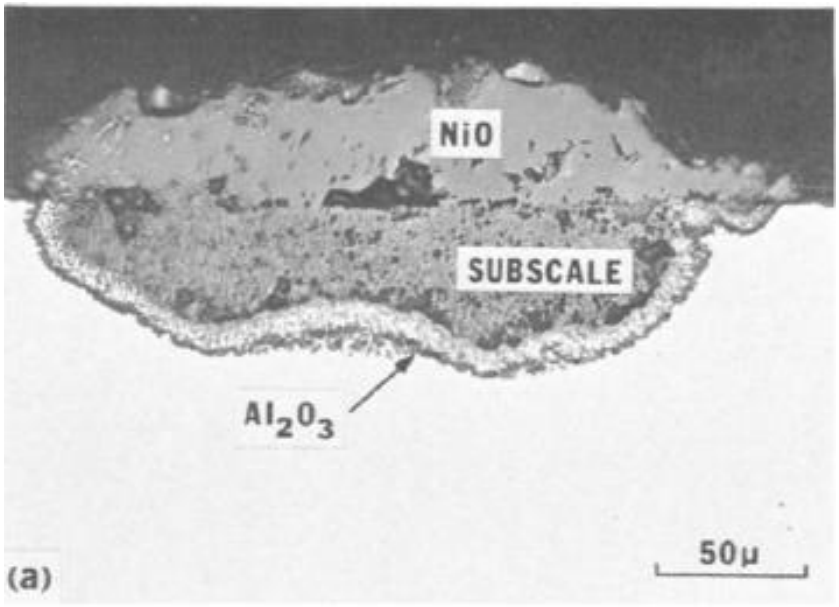

Figure 11: Cross-Sectional SEM Image of a Ni-Cr-Al Alloy Exhibiting a Mixed Oxide Growth Mechanism from Regions I and III (Figure Reproduced from [7])

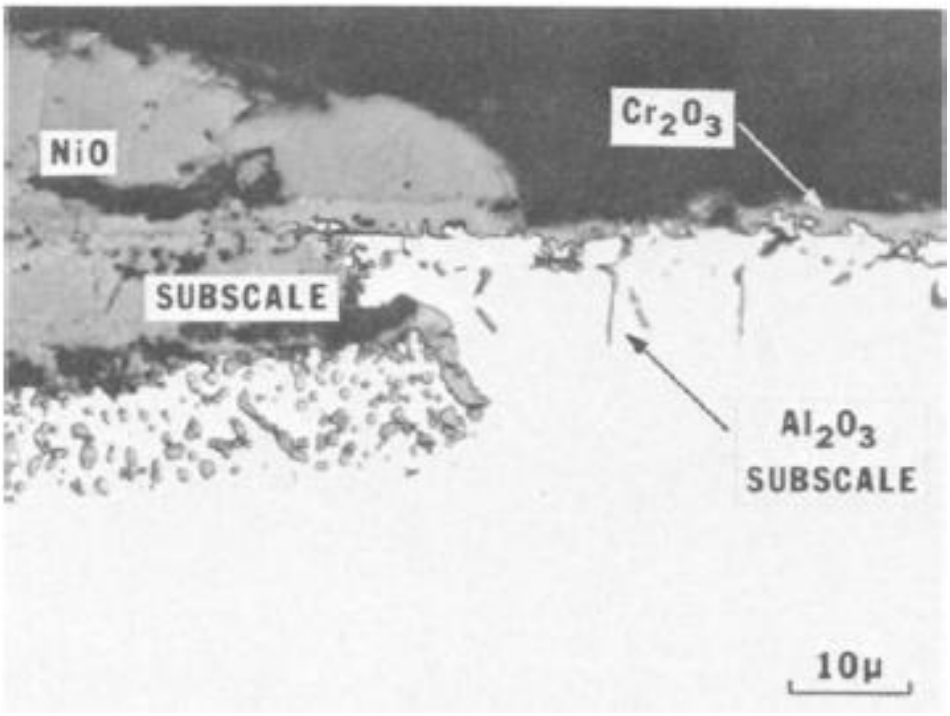

Figure 12: Cross-Sectional SEM Image of a Ni-Cr-Al Alloy Exhibiting a Mixed Oxide Growth Mechanism from Regions I and II (Figure Reproduced from [7])

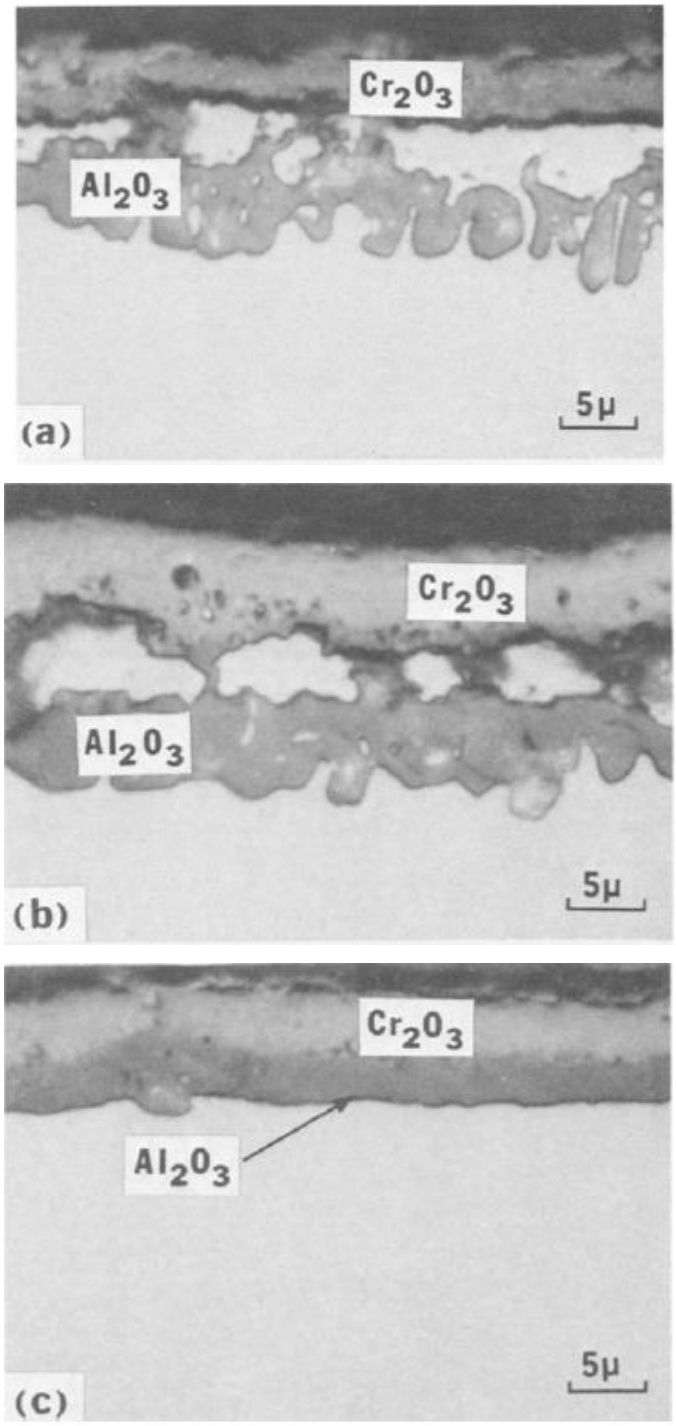

Figure 13: Cross-Sectional SEM Image of a Ni-Cr-Al Alloy Exhibiting a Mixed Oxide Growth Mechanism from Regions II and III (Figure Reproduced from [7])

Giggins claims that the alloys that exhibited mixed oxide growth (i.e., followed two mechanisms simultaneously) performed in such a way due to localized differences in surface preparation or impurity content.

2.1.2.5 Effects of Surface Finish

As seen in Equation (2-15) in Section 2.1.2.3, one way to lower the critical mole fraction required to initiate the transition from internal to external oxidation is through increasing the diffusivity of the more reactive solute metal from within the bulk alloy (D_B). Past research [13, 14] has shown that the diffusivity of the more reactive solute metal can be increased through changes in the surface finish of the alloy (e.g., abrasion, sand blasting, or other mechanisms which introduce surface deformation). By introducing deformation within the subsurface region of the alloy, there is stress and strain that that gets generated. When the alloy undergoes high temperature oxidation, the stress and strain get relieved via recrystallization. The recrystallization process is shown in Figure 14.

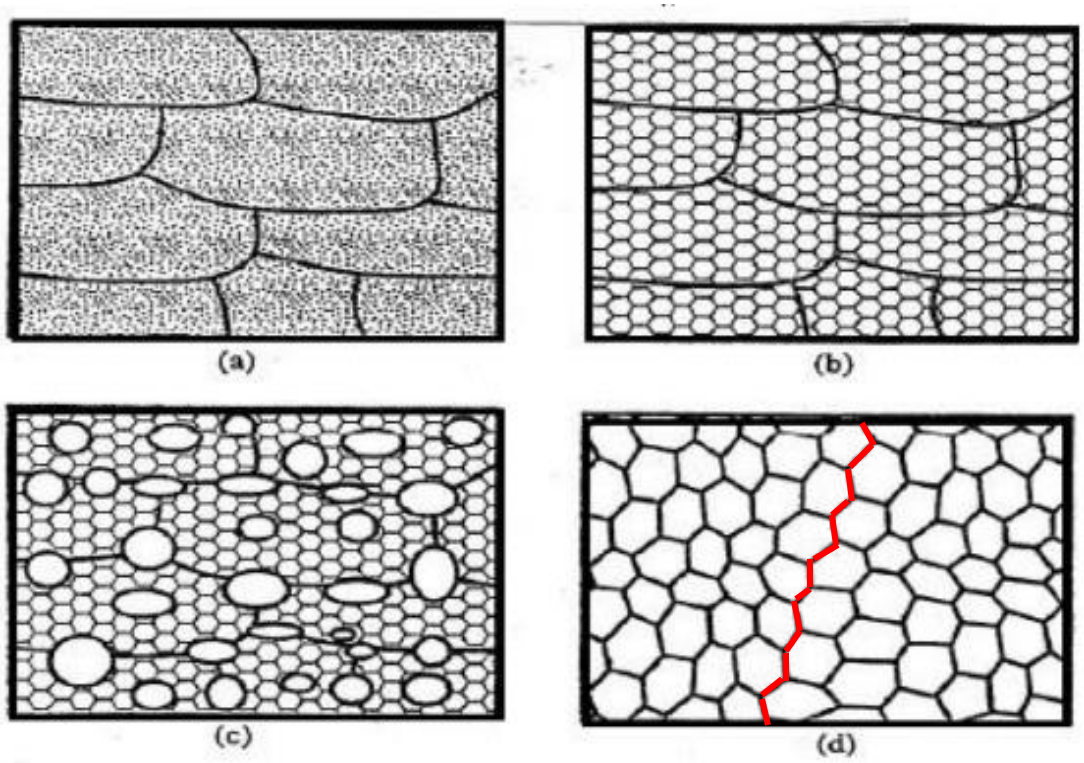

Figure 14: Schematic for Recovery, Nucleation, and Growth During the Recrystallization Process (Figure Reproduced from [15])

During recrystallization, the nucleation and initial growth of new crystals provides significantly more grain boundaries which facilitates faster diffusion of reactive species (also called short circuit diffusion). These short circuit diffusion paths (example outlined in red above) allow Al from within the immediate subsurface region to reach the alloy surface faster, more easily promoting the formation of a protective external Al_2O_3 scale. Kang [13] demonstrated that this phenomenon was exhibited on a Ni-6Cr-8Al alloy by utilizing two separate surface finishes; polished with colloidal silica and abraded to 1200 grit using silicon carbide (SiC) paper. The effect of polishing with colloidal silica is that the surface of the alloy does not contain any deformation whereas the alloys abraded to 1200 grit contain a surface deformation layer from the grinding

process. Kang found that the alloys polished with colloidal silica showed no external formation of Al_2O_3 but rather internal precipitates of Al_2O_3 in the subsurface zone. Conversely, alloys abraded to 1200 grit exclusively showed external Al_2O_3 formation and no internal oxide precipitates.

Since the alloys polished with colloidal silica contained no surface deformation, no recrystallization occurred and short circuit diffusion was not possible. Without short circuit diffusion, the bulk Al diffusion was too slow compared to the inward diffusion of oxygen and thus only internal precipitates of Al_2O_3 formed. On the other hand, the alloys abraded to 1200 grit did contain a surface deformation layer, thus upon high temperature exposure, a recrystallization zone developed and this facilitated short circuit diffusion paths for faster Al diffusion along grain boundaries. It is clear that the short circuit diffusion phenomena in the 1200 grit alloys promoted the formation of a continuous external scale of Al_2O_3 instead of internal precipitates as was experienced with the non-surface deformed alloys polished with colloidal silica.

This short circuit diffusion phenomenon was also demonstrated using the HAYNES® 214® nickel-base superalloy [14] which was oxidized at 800°C. In this work, coupons containing two different surface finishes were utilized; abraded to 1200 grit and vapor honed. House found that coupons abraded to 1200 grit primarily formed a continuous and external scale comprised of an Al_2O_3-Cr_2O_3-Al_2O_3 sandwich structure. Analysis of the subsurface zone via TEM showed a sizable recrystallization zone where the alloy relieved the stress and strain induced from the abrasion process. It was deduced that the recrystallization process upon high temperature exposure provided short circuit diffusion paths for Al to reach the alloy surface and form a continuous external scale. However, House also found that localized areas of the alloy surface formed a duplex oxide structure containing an outer layer of a Ni-Cr rich oxide on top of a layer of coarsened Al_2O_3 precipitates in the subsurface zone. The vapor honed alloy coupons showed similar oxidation

performance where an Al_2O_3-Cr_2O_3-Al_2O_3 sandwich structure was also developed, however unlike the 1200 grit abraded coupons, the middle Cr_2O_3 layer was found to be discontinuous. Based on these results, it was clear that the short circuit diffusion phenomenon was the primary factor in allowing the HAYNES® 214® nickel-base superalloy to form an external scale of Al_2O_3 at low temperatures.

2.2 Hot Corrosion

Hot corrosion is a form of accelerated, deposit-induced corrosion that results from the presence of salt contaminants such as sodium sulfate (Na_2SO_4), magnesium sulfate ($MgSO_4$), potassium sulfate (K_2SO_4), calcium sulfate ($CaSO_4$), sodium chloride (NaCl), or vanadium oxide (V_2O_5) that can be present in some of the service environments that nickel-base superalloys are used in [16]. In addition to salt contaminants, the environment must also contain sulfur dioxide (SO_2) and sulfur trioxide (SO_3) to provide a partial pressure sufficient to sustain the corrosion process. If salt contaminants are present during high temperature exposure, they can deposit onto the surface of the alloy and significantly alter the oxidation performance. If the temperature is high enough, some salts can melt (i.e., liquify) and the molten salt deposits can attack, damage, or degrade the protective oxide scale that is necessary for the alloy to maintain its high temperature strength and oxidation resistance over time [16]. If the protective oxide scale is destroyed, this can lead to the inward diffusion of sulfur (S) which can combine with the more reactive metal cations in the alloy to form internal metal-sulfide precipitates such as chromium sulfide (Cr_2S_3) or aluminum sulfide (Al_2S_3). The formation of internal metal-sulfide precipitates will consume the reactive metal in the alloy (i.e., Cr or Al) and thus the alloy can no longer form a protective external oxide scale. Without being able to reform a protective external oxide scale, the alloy is more

susceptible to rapid attack. This negatively impacts the mechanical performance and integrity of the alloy and can ultimately lead to failure. Hot corrosion is classified into two categories; type 1 and type 2.

Type 1 hot corrosion, also referred to as high temperature hot corrosion (HTHC), occurs in the temperature range of 850°C to 950°C and is a primary concern if there are salt deposits that are capable of melting on the alloy surface thus attacking the protective oxide layer. Type 2 hot corrosion, also referred to as low temperature hot corrosion (LTHC), occurs in the temperature range of 650°C to 800°C. One primary difference between HTHC and LTHC is that the partial pressure of SO_3 must be higher for LTHC than HTHC. The hot corrosion testing performed as part of this thesis did not include Type 2 conditions, thus the detailed description for its occurrence is not discussed herein. However, the process of Type 2 hot corrosion is discussed extensively in the literature [16, 17, 18].

2.3 Pulsed Laser Deposition

Pulsed laser deposition (PLD) is a physical vapor deposition (PVD) technique that is used to grow thin films and coatings on substrate surfaces. PLD is performed in a vacuum chamber and a pulsed laser is used to ablate or vaporize the surface of a target material that is desired to be deposited on the substrate surface. The pulsed laser is directed and focused onto the target material using a series of mirrors and lenses, and the laser is rastered across the target surface so that uniform ablation occurs, burning in a single location is avoided, and film uniformity on the substrate surface occurs. When the target surface is ablated, a vapor plume is generated and this

plume provides the upward material flux for thin film growth on the substrate surface. A schematic showing the PLD process within the vacuum chamber is shown in Figure 15.

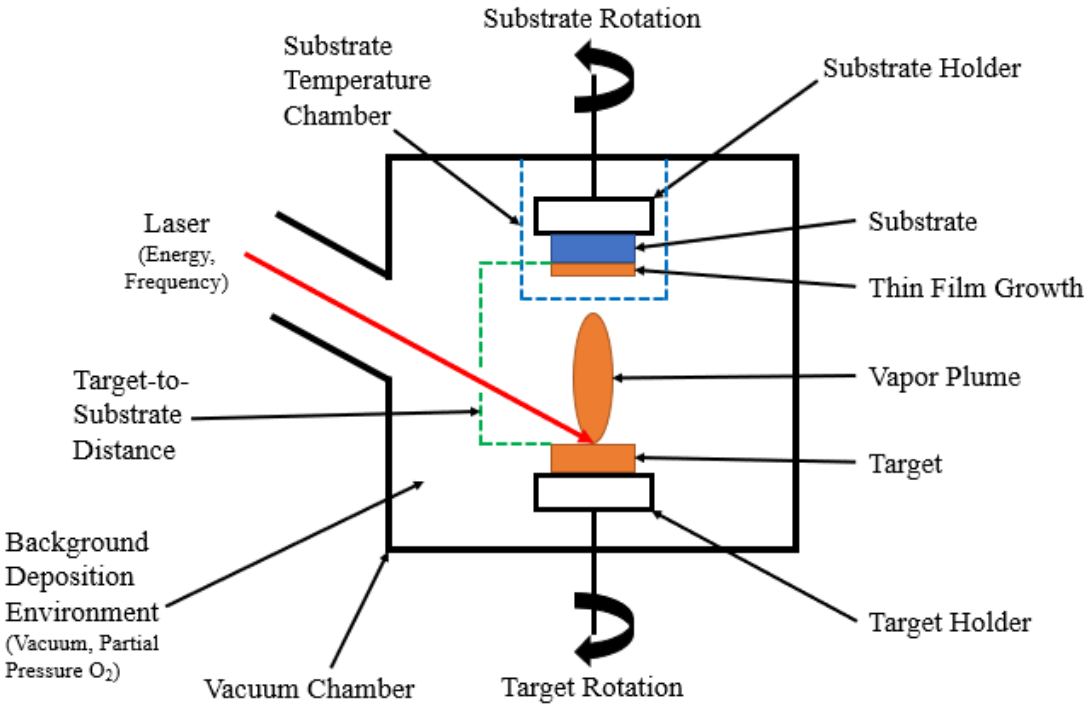

Figure 15: Schematic of the PLD Process

The PLD system has a variety of user selectable and instrument configurable process parameters that can be altered and tuned based on the deposition experiment being performed. The variable PLD process parameters include substrate temperature, target-to-substrate distance, background deposition environment, laser energy, laser frequency, and deposition duration. Each of these six variable process parameters can affect the structure (i.e., crystalline or amorphous),

morphology (uniform, columnar, etc.), density (dense, semi-porous, porous, etc.) and thickness (nanometers, micrometers, etc.) of the coating being deposited. Of the six variable PLD process parameters mentioned above, the most influential one with respect to the PLD film's morphology and density on the substrate surface is the background deposition environment utilized.

The relationship between film morphology and density with respect to background deposition environment is best understood by looking at a study that was done by Di Fonzo et. al [19]. In this experiment, Al_2O_3 was deposited on silicon (Si) (100) substrates using PLD at various oxygen partial pressures and fixed target-to-substrate distances, and subsequently characterizing the effect on film morphologies and densities. In the aforementioned study, fixed target-to-substrate distances of 26 millimeters (mm) and 70 mm were utilized with oxygen partial pressures ranging from 0.5 Pascals (Pa) to 100 Pa. In all experiments performed, a nanosecond (ns) Nd:YAG laser containing a wavelength of 266 nanometers (nm) was directed onto a polycrystalline Al_2O_3 target at an angle of 40°. The incident laser contained a fixed energy and frequency of 140 millijoules (mJ) and 10 Hertz (Hz), respectively. Under these deposition conditions, Al_2O_3 films of at least 3 micrometers (μm) in thickness were grown. Figure 16 and Figure 17 show the resulting PLD film morphologies on the surfaces of the Si substrates.

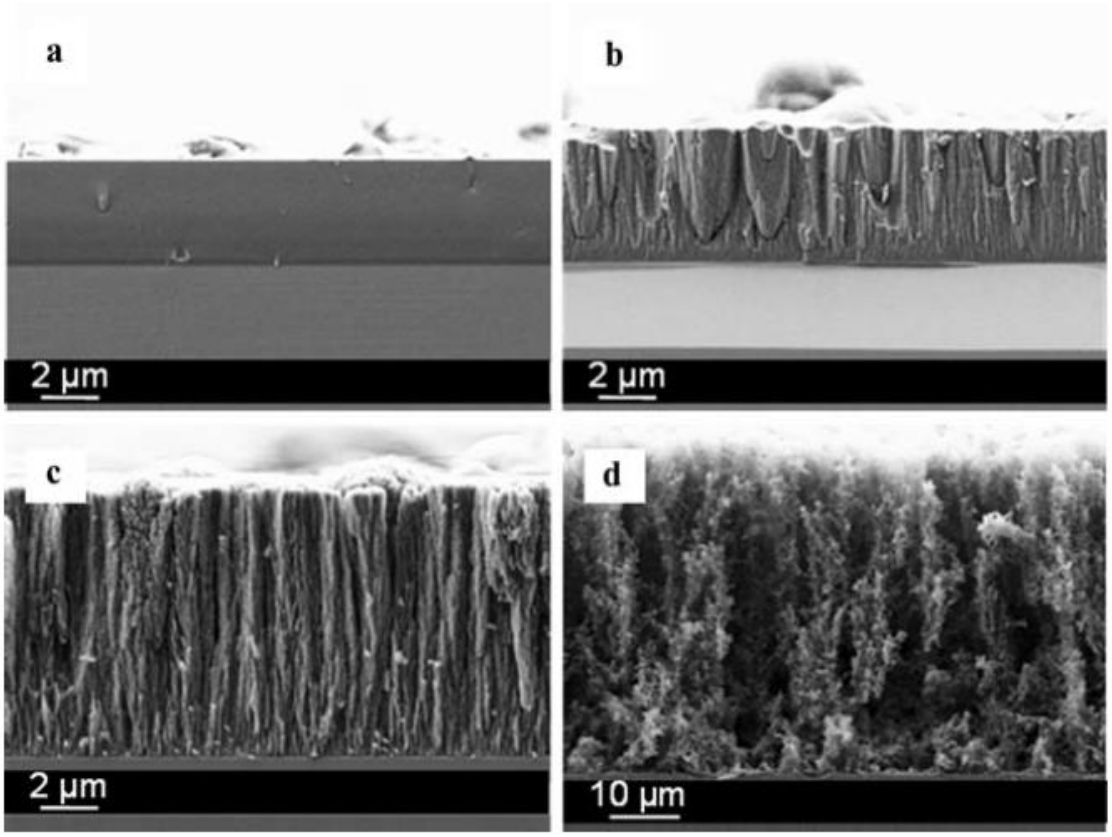

Figure 16: SEM Cross Section Images Showing the Variation of PLD Film Morphologies Produced via Changes in the Background Deposition Environment Containing Different Oxygen Partial Pressures at a Fixed Target-to-Substrate Distance of 70 mm. Images (a) – (d) Shown in Increasing Oxygen Partial Pressures from 0.5, 5, 25, and 100 Pa. Figure Reproduced from [19].

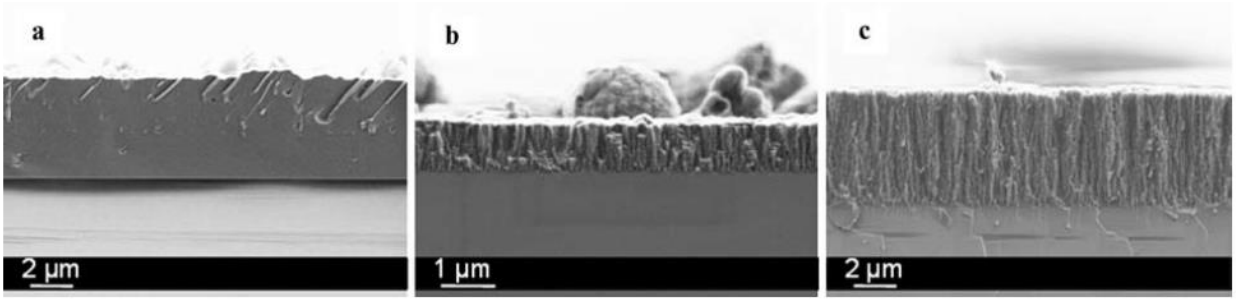

Figure 17: SEM Cross Section Images Showing the Variation of PLD Film Morphologies Produced via Changes in the Background Deposition Environment Containing Different Oxygen Partial Pressures at a Fixed Target-to-Substrate Distance of 26 mm. Images (a) – (c) Shown in Increasing Oxygen Partial Pressures from 5, 25, and 100 Pa. Figure Reproduced from [19].

As seen in Figure 16 and Figure 17, the PLD films deposited on the Si substrates range from highly uniform and dense to columnar grains to very porous and spongelike. The latter is more exemplified in the Al_2O_3 PLD films deposited at 100 Pa using a target-to-substrate distance of 70 mm. These two figures are just one example of how a single PLD process parameter can directly influence the types of films that are deposited on the substrate surface.

The PLD instrumentation also allows the substrate rotation speed, target rotation speed, and laser voltage to be changed; however, these parameters do not affect the coating structure, morphology, or thickness. The laser voltage and laser energy are linked with one another, thus whichever laser energy is chosen, the laser voltage is adjusted accordingly. The substrate and target rotation speeds are used for different purposes; substrate rotation helps to ensure film uniformity during the deposition process while target rotation, in combination with laser rastering, helps

ensure uniform target ablation. Due to these reasons, both the target and substrate rotation speeds are rarely used as tunable parameters during PLD experiments.

2.4 Literature Reviews

2.4.1 Oxidation of the HAYNES® 214® Nickel-base Superalloy

The high temperature (i.e., 1000°C to 1200°C) oxidation performance of the HAYNES® 214® nickel-base superalloy has been studied to a limited extent, and there is less research done on the performance at low temperatures (e.g., 800°C to 900°C). In a study done by Allam et. al [8], the carburization and oxidation behavior of the HAYNES® 214® nickel-base superalloy was examined using two different mixtures of methane (CH_4) and hydrogen (H_2); commercial grade 2% CH_4 – 98% H_2 and 10% CH_4 – 90% H_2 (nominal compositions) at temperatures ranging from 800°C to 1100°C. The CH_4 – H_2 mixtures also contained an impurity oxygen content of less than 100 parts per million (ppm). The important findings in this research are that the surface region of the alloy after short term isothermal exposure (30 minutes (min), 3-hrs, 10-hrs, and 50-hrs) at 1000°C in the 10% CH_4 – 90% H_2 gas mixture showed an enrichment of Al, and upon energy dispersive spectroscopy (EDS) analysis, it was found to contain concentrations of Al that were in excess of the original alloy composition (4.5 wt%). The author's also report that the Al concentration near the surface increases with increasing exposure durations, however it increases more prominently with increasing temperatures. These two observations indicate that during oxidation, Al cations from the bulk alloy diffuse outwardly toward the alloy-gas interface.

The HAYNES® 214® coupons were then thermally cycled in the 2% CH_4 – 98% H_2 gas mixture at 800°C, 900°C, 1000°C, and 1100°C for a total of 500-hrs using 50-hr cycles (10 cycles total). Figure 18 shows the surface and cross-sectional SEM images for the thermally cycled HAYNES® 214® coupons at 800°C, 900°C, 1000°C, and 1100°C.

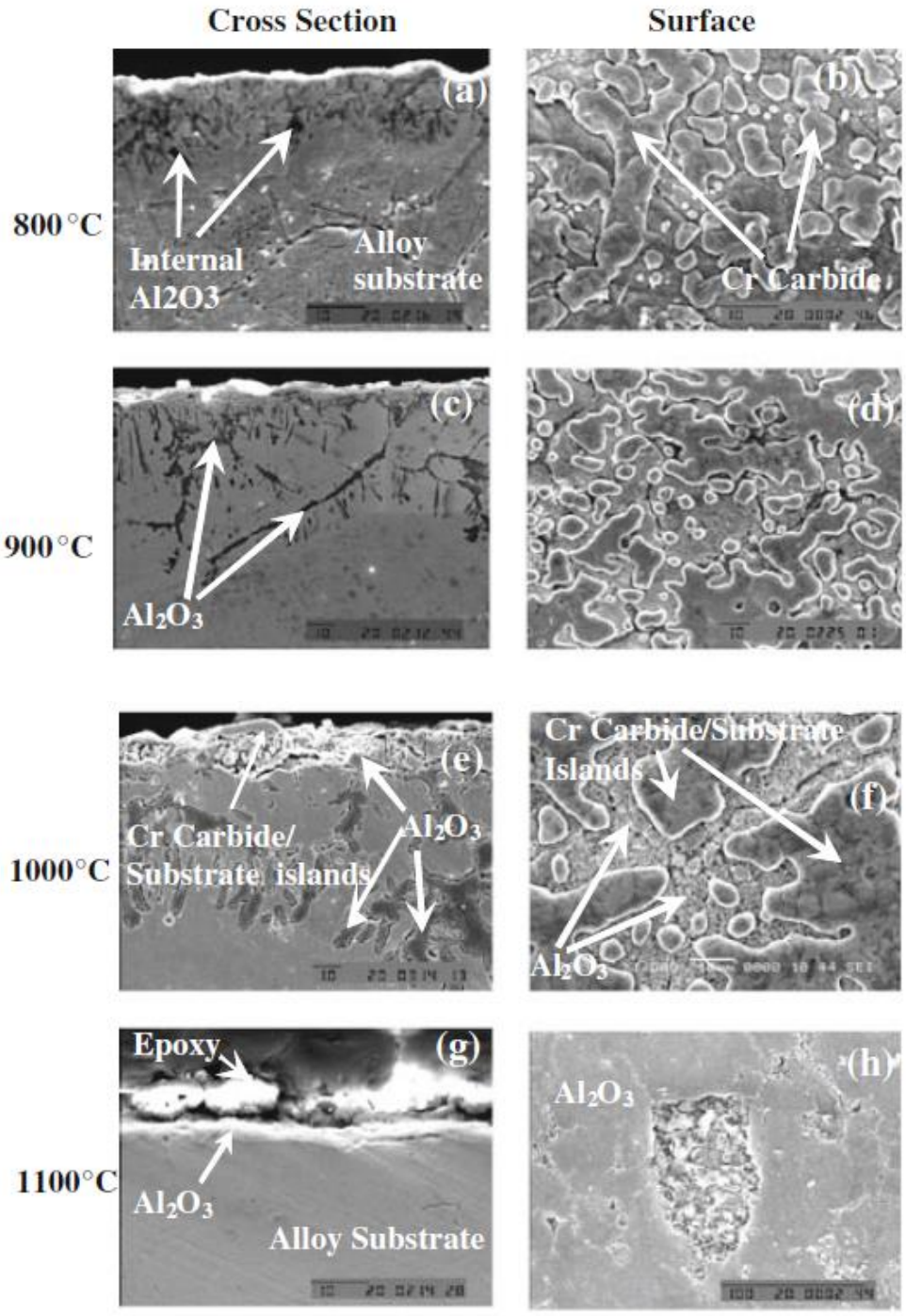

Figure 18: Cross-Sectional and Surface SEM Images of the Thermally Cycled HAYNES® 214® Alloy After Exposure to the 2% CH_4 – 98% H_2 Gas Mixture at 800°C, 900°C, 1000°C, and 1100°C for a Duration of 500-hrs (50-hrs per Cycle, 10 Total Cycles) (Figure Reproduced from [8])

At 800°C, SEM analysis of the surface of the HAYNES® 214® samples showed the presence of small chromium carbide (Cr_3C_2) islands on top of the underlying alloy whereas cross-sectional SEM analysis showed the presence of significant platelet and lamellar shaped internal oxide precipitates extending into a zone of about 15 μm beneath the alloy surface. Upon EDS analysis, these internal oxide precipitates were found to be α-Al_2O_3, and the alloy surface showed no external oxide formation. At 900°C, the Cr_3C_2 islands on the alloy surface grew laterally and began merging together to form larger islands. The alloy cross section still showed no external oxide formation and the internal α-Al_2O_3 precipitates extended deeper into the alloy. The internal α-Al_2O_3 precipitates formed at 900°C were found to extend to an average depth of about 50 to 80 μm. At low temperatures (i.e., 800°C to 900°C), Allam hypothesized that the formation of internal precipitates of Al_2O_3 were a result of the alloy containing an insufficient amount of Al to cause the transition between internal and external oxidation as described in Section 2.1.2.3. Due to this, the Al diffusion from within the bulk alloy was much slower than the inward diffusion of oxygen, therefore a continuous scale could not be formed.

At 1000°C, the Cr_3C_2 islands on the alloy surface continued their lateral growth and the alloy cross section still exhibited internal α-Al_2O_3 precipitates, although significant coarsening occurred (i.e., lateral growth was more kinetically favorable) compared to the internal oxides formed during oxidation at 800°C and 900°C. Additionally, at 1000°C, a semi-continuous surface layer of Al_2O_3 was present indicating that the criteria for the transition from internal to external oxidation were met. When the temperature was increased to 1100°C, the diffusion of Al from within the bulk alloy was fast enough where a continuous and protective external α-Al_2O_3 scale was formed on the alloy surface. This scale subsequently protected the alloy surface from any Cr_3C_2 formation. Furthermore, no internal Al_2O_3 precipitates were found. The formation of an

external α-Al_2O_3 scale at 1100°C matches other literature results where the oxidation performance of the HAYNES® 214® nickel-base superalloy was also studied at high temperatures [5, 20].

The findings from Allam et. al can be compared with those observed by Deodeshmukh [21] who also studied the oxidation performance of the HAYNES® 214® nickel-base superalloy at low temperatures (871°C and 982°C). Figure 19, Figure 20, and Figure 21 below show surface and cross-sectional SEM images of HAYNES® 214® coupons after various durations of oxidation in flowing air.

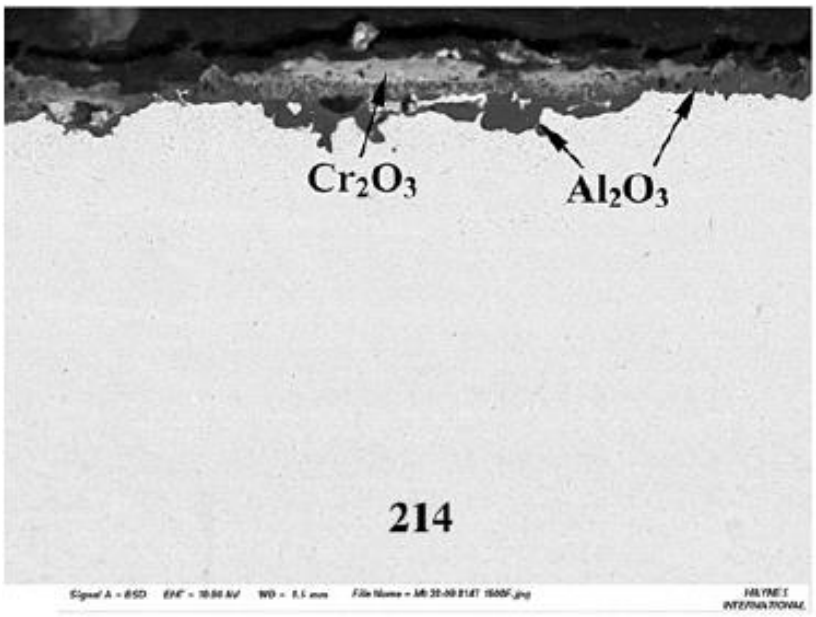

Figure 19: Cross-Sectional SEM Image of a HAYNES® 214® Coupon After 1008-hrs of Thermal Cycling in Flowing Air at 871°C (Figure Reproduced from [21])

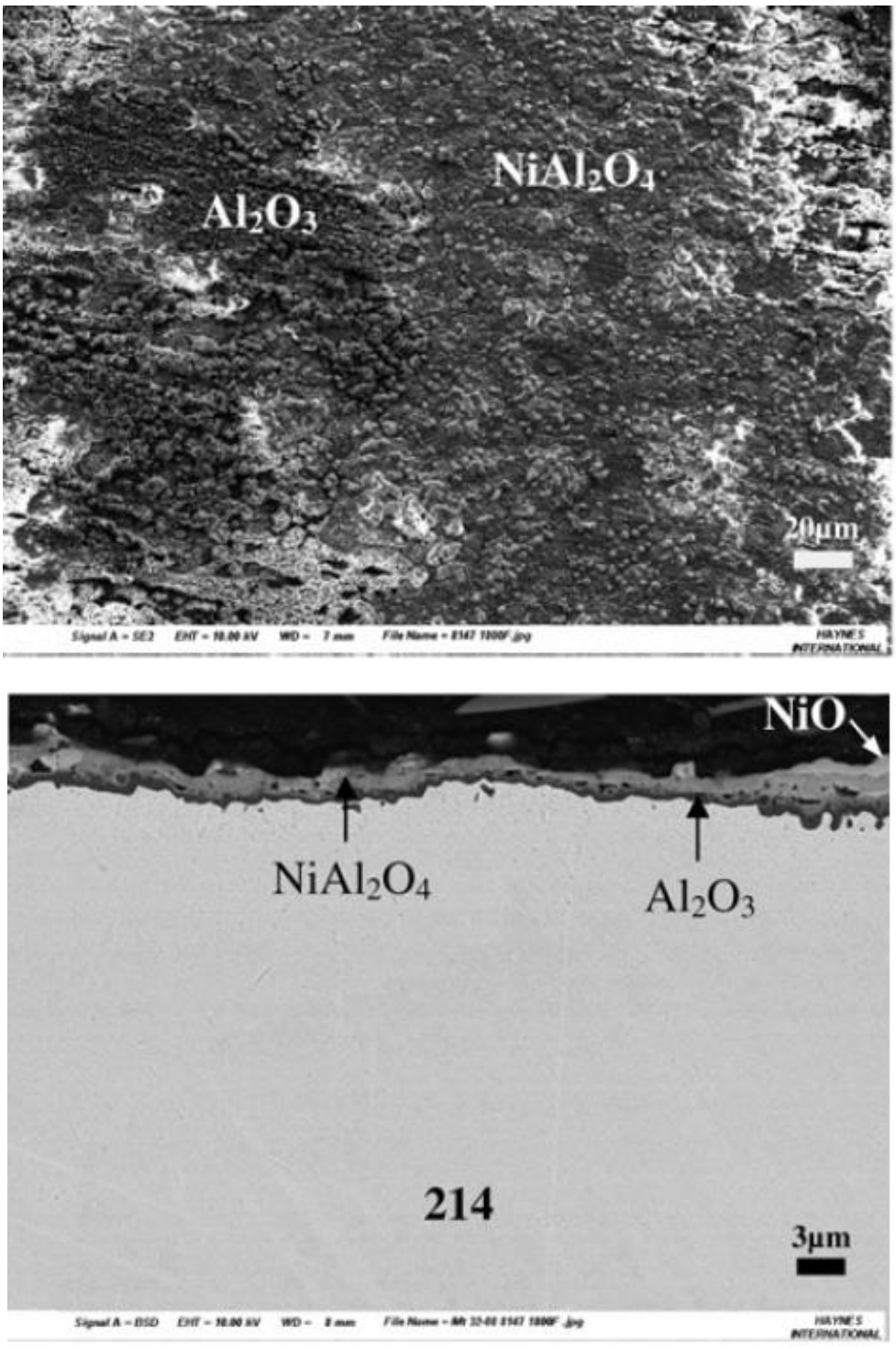

Figure 20: Surface and Cross-Sectional SEM Images of a HAYNES® 214® Coupon After 100-hrs of Isothermal Oxidation at 982°C (Figure Reproduced from [21])

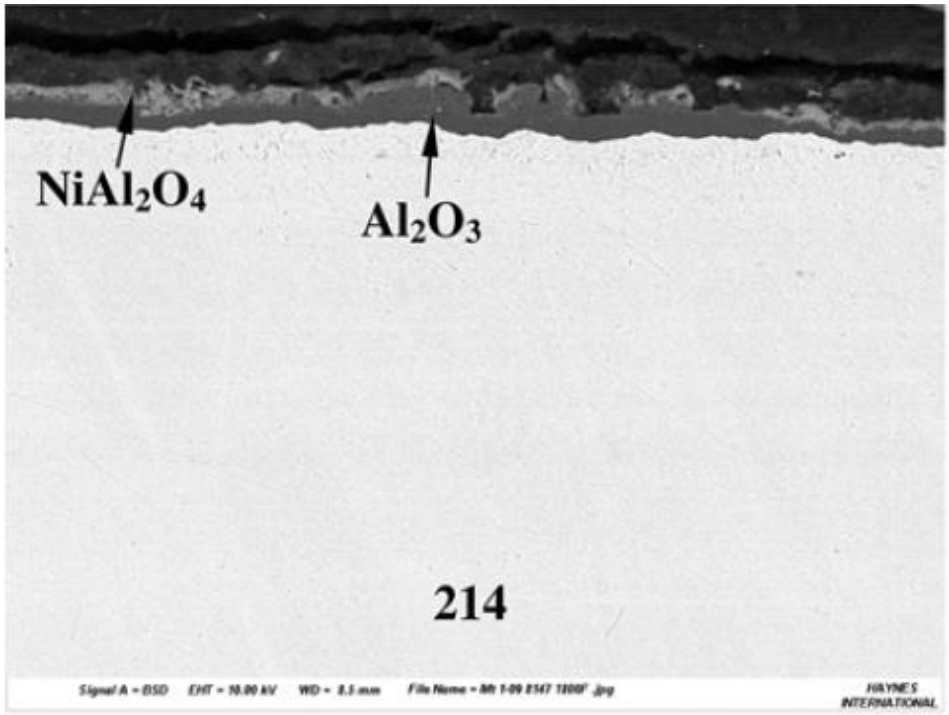

Figure 21: Cross-Sectional SEM Image of a HAYNES® 214® Coupon After 1008-hrs of Thermal Cycling in Flowing Air at 982°C (Figure Reproduced from [21])

At 871°C, the HAYNES® 214® coupon experienced a mixed oxidation mechanism similar to that described by Giggins and Pettit [7] where regions of the surface contained an outer Cr_2O_3 scale on top of coarse internal precipitates of Al_2O_3 which have formed a semi-continuous layer. However, other regions of the surface solely formed an external scale of Al_2O_3. When increasing the temperature to 982°C, both isothermal oxidation and thermal cycling conditions resulted in the HAYNES® 214® alloy forming a continuous external Al_2O_3 scale. This protective Al_2O_3 layer was formed underneath a layer of transient oxidations products comprised of NiO and $NiAl_2O_4$.

2.4.2 Pulsed Laser Deposition of Al_2O_3 Coatings for Corrosion Protection

PLD has been widely used as a means to deposit uniform and dense films of Al_2O_3 on various substrate surfaces in order to successfully protect against corrosion. The use of a dense and external Al_2O_3 film that has been deposited on the substrate surface via PLD effectively provides an isolation barrier between the substrate to be protected and the environment that can detrimentally impact the substrate material.

In a study done by Singh et. al [22], PLD was used to deposit Al_2O_3 coatings on stainless steel (SS) substrates to investigate the corrosion protection against liquid uranium (U) in an effort to improve its containment and handling. The Al_2O_3 coatings were a maximum of 75 μm in thickness resulting from a cumulative deposition duration of 7-hrs. The substrates used were surface roughened SS discs about 5 to 6 mm in diameter. To roughen the discs (substrates), the surfaces were sand blasted so that the mechanical adhesion of the Al_2O_3 coating to the substrate surface could be improved.

The PLD system used in this study employed a focused beam of a ns Nd:YAG laser which had a wavelength of 532 nm, a pulse energy in the region of 18 to 20 mJ, a pulse duration of 6 ns, and a 10 Hz pulse repetition rate. With PLD, the material flux that comes from ablating the target occurs primarily normal to the target surface, thus the laser beam used in PLD experiments is usually incident to the target at an angle of 45°, as was done in this study.

The PLD experiments performed in this study occurred at room temperature and, unlike more conventional PLD experiments which utilizes high vacuum conditions as the background environment, Singh et. al used atmospheric air. However, the use of atmospheric air as the background means that there will be atomic or molecular collisions between the vapor plume of the ablated PLD target and the gas particles present in the background. These collisions will impact

the film structure and morphology, as was described in Section 2.3, therefore in order to deposit dense films for corrosion protection, there is a maximum allowable separation between the PLD target and the substrate to minimize particle-particle collisions. The average distance between particle-particle collisions can be described by the relationship shown in Equation (2-16)

$$\lambda \propto \frac{1}{P \text{ (or } n_V)} \tag{2-16}$$

where λ is the mean free path between gas particle collisions, P is pressure, and n_V is the number of atoms or molecules per unit volume.

Based on the relationship between collision distance and pressure, in order to obtain dense films of Al_2O_3 and minimize particle-particle collisions prior to the vapor plume depositing onto the substrate surface, Singh et. al configured the target and substrate surfaces to be parallel to each other with the separation between the two being about 3 mm. Figure 22 shows a representative cross-sectional SEM image of the Al_2O_3 coating on the SS substrate prior to corrosion testing.

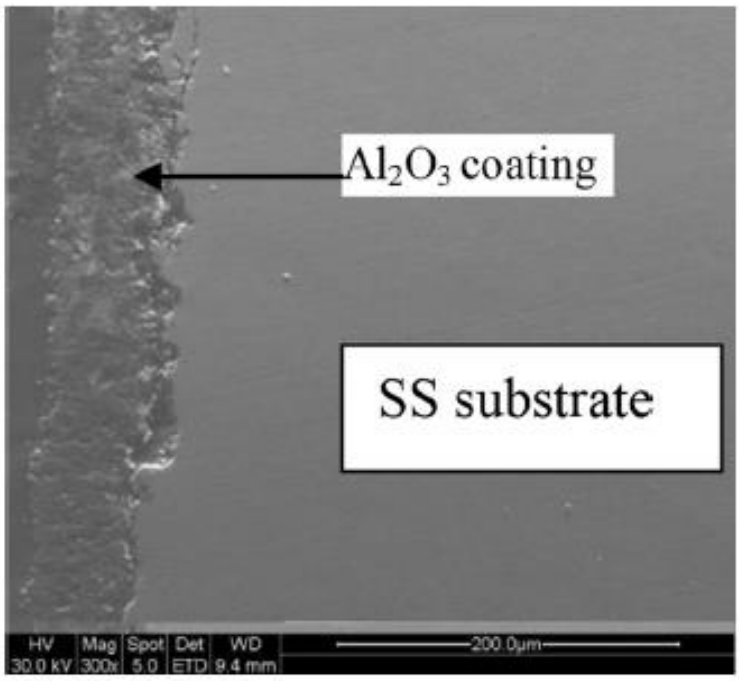

Figure 22: Cross-Sectional SEM Image of the Al_2O_3 Coated SS Substrate Prior to Corrosion Testing (Figure Reproduced from [22])

To test the corrosion resistance of the SS discs coated with Al_2O_3 against molten U, differential thermal analysis (DTA) was used. The DTA signal that was collected was a measure of the temperature difference between a reference sample and the test sample when subjected to identical thermal cycles. Solid U was placed on the surface of an uncoated SS coupon and a coupon containing an Al_2O_3 film deposited by PLD, and then both coupons were placed in a furnace to undergo a single thermal cycle. For the thermal cycle, the temperature was steadily increased to 1165°C so that the solid U would melt on the coupon surface (the melting temperature of U is 1132°C). Once the temperature reached 1165°C, the coupons were held there for 2-hrs which allowed the liquid U to interact with the Al_2O_3 coated and uncoated coupons. After 2-hrs, the

furnace was then gradually decreased back to room temperature. Figure 23 shows the DTA signals for the Al_2O_3 coated and uncoated SS coupons over the course of the single thermal cycle performed.

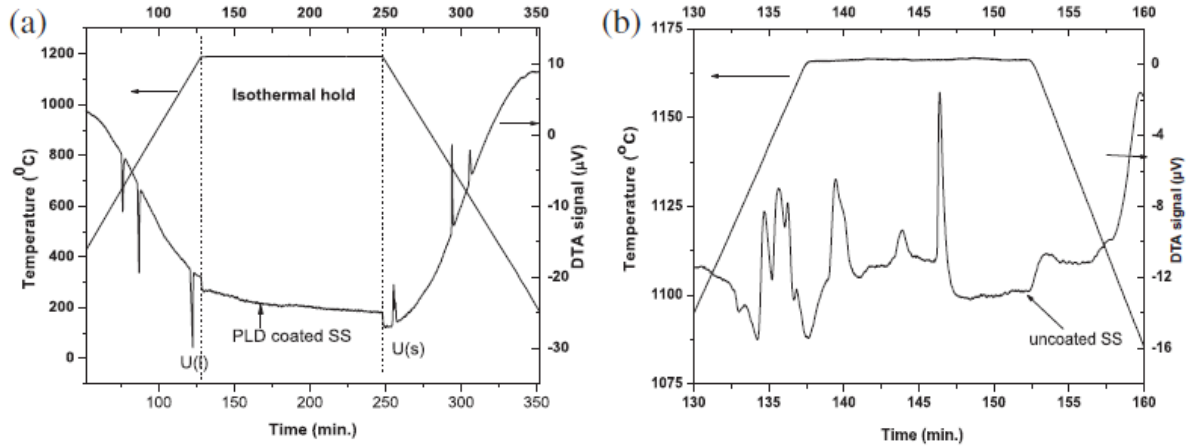

Figure 23: DTA Signal for the Al_2O_3 Coated SS Substrate (a) and Uncoated SS Substrate (b) When Exposed to Molten U at 1165°C for 2-hrs (Figure Reproduced from [22])

In this study, Singh et. al describes that the observed peaks and dips in the DTA signal indicate the occurrence of exothermic and endothermic reactions where phase transitions or chemical reactions in the test specimen are taking place. As Figure 23 shows, during the isothermal hold phase of the test, there are no peaks or dips in the DTA signal of the SS coupon that is coated with Al_2O_3 which implies there is no reaction between the liquid U on the surface and the underlying SS substrate. However, during the heat up and cool down phases, there are several

sharp peaks and dips in the DTA signal which is expected since the temperature increase or decrease is causing the U to either liquify or solidify, respectively.

In comparison, the uncoated SS coupon showed significant peaks and dips throughout the entire heat up, isothermal hold, and cool down phases of the experiment. This exemplifies that chemical reactions and phase changes were taking place between the liquid U on the surface and the SS substrate in contact with it. These interactions led to significant corrosion of the SS which proves uncoated SS is not a suitable material for the handling and containment of liquid U.

The findings from Singh et. al's experiments are also consistent with other studies which used Al_2O_3 coatings deposited by PLD to protect against corrosion. In a study done by García Ferré et. al [23], PLD was used to deposit Al_2O_3 coatings on as-received Steel-9Cr-1Mo substrates to protect against corrosion from heavy liquid metals (HLMs). The steel substrates used in this experiment contained dimensions of 10 x 20 x 1 mm^3 and the surfaces were ground to a 2000-grit finish using SiC paper.

In this experiment, the Al_2O_3 PLD films were deposited in a SS vacuum chamber containing a low oxygen pressure and were grown at three different temperatures; room temperature, 400°C, and 600°C. The laser energy and frequency were fixed at 250 mJ and 20 Hz, respectively. Under these conditions, Al_2O_3 films approximately 2 to 8 μm in thickness were deposited onto the surfaces of the steel substrates where the variation in film thickness was a result of different deposition durations (i.e., the number of laser pulses).

To test the corrosion performance between the Al_2O_3 coated and uncoated steel samples, a single test was performed in a tubular furnace for 500-hrs at 550°C in an atmosphere containing extra pure nitrogen (N_2) with a sufficient amount of water (H_2O) and oxygen present to be considered oxidizing. A total of 15 steel coupons, 3 uncoated and 12 coated with Al_2O_3, were

subjected to the corrosion test. Of the 12 Al_2O_3 coated steel coupons, 6 coupons had films grown at room temperature where 3 coupons had film thicknesses of 2 μm and the remaining 3 coupons had film thicknesses of 8 μm. Another 3 Al_2O_3 coated steel coupons had films grown at 400°C which contained film thicknesses of 8 μm while the last 3 Al_2O_3 coated steel coupons had films grown at 600°C also containing film thicknesses of 8 μm. All 15 steel coupons were placed into their own Al_2O_3 crucible for the corrosion test.

In the experiments performed by García Ferré et. al, the HLM used was molten lead (Pb), thus grains cut from an as-received 99.99% pure Pb slab were loaded into the individual Al_2O_3 crucibles containing the steel coupons. Once the corrosion test concluded, the molten Pb was poured out of the Al_2O_3 crucibles and the coupons were left to cool in air. A thin layer of Pb melt that was adherent on the uncoated faces of the steel coupons was not removed but allowed to solidify. Figure 24 and Figure 25 show the surface and cross section of the uncoated steel coupon following the completion of the test.

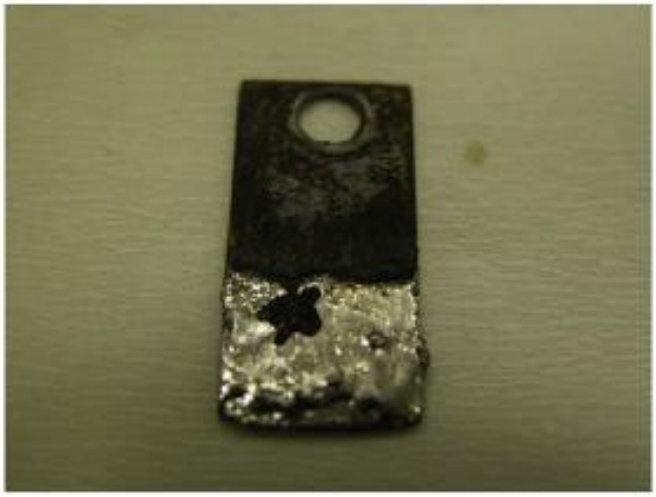

Figure 24: Surface Image of the Uncoated Steel Coupon After Exposure to Molten Pb for 500-hrs at 550°C (Figure Reproduced from [23])

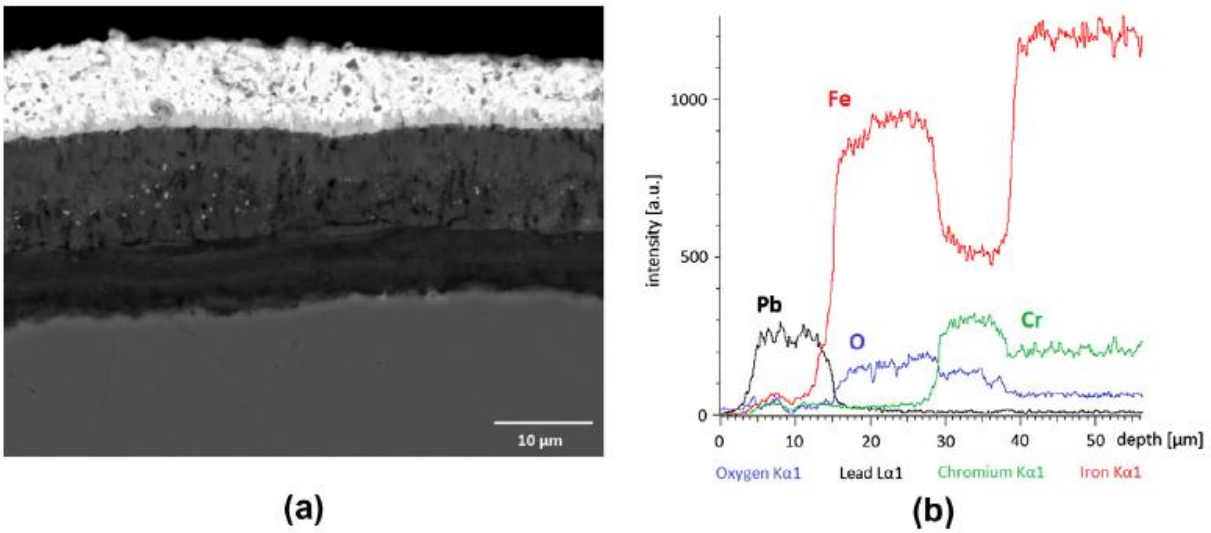

Figure 25: Cross-Sectional SEM Image of the Uncoated Steel Coupon (a) and EDS Line Scan Identifying the Elements in each Corrosion Product Layer (b) (Figure Reproduced from [23])

As shown in Figure 24 and Figure 25, the uncoated steel coupon suffered significant corrosion which is evident by the formation of various layers of corrosion products beneath the solidified melt of pure Pb. The production of these corrosion layers indicates that there is an interaction between the steel coupon and the liquid Pb (containing oxygen from the atmosphere) because the iron (Fe) and Cr from the bulk alloy has formed outer layers of iron oxide (Fe_2O_3) and Cr_2O_3, respectfully.

To determine if coating the steel coupon with a thick Al_2O_3 film via PLD prevents an interaction with the liquid Pb (and thus provides protection against corrosion), the test was repeated. Figure 26 shows surface images of the Al_2O_3 coated steel coupon before and after

corrosion testing while Figure 27 shows a cross-sectional SEM image and EDS elemental map of the Al_2O_3 coated steel coupon after corrosion testing.

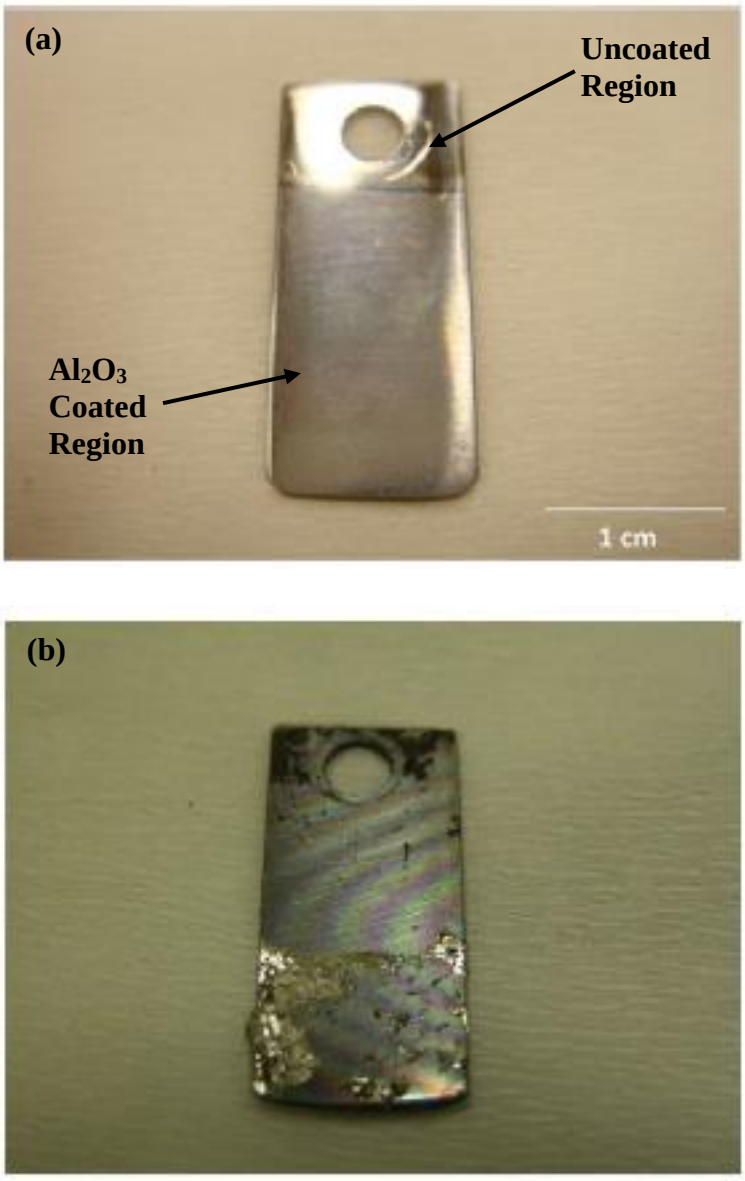

Figure 26: Surface Images of the Al_2O_3 Coated Steel Coupon Before Corrosion Testing (a) and After Corrosion Testing (b) (Figure Reproduced from [23])

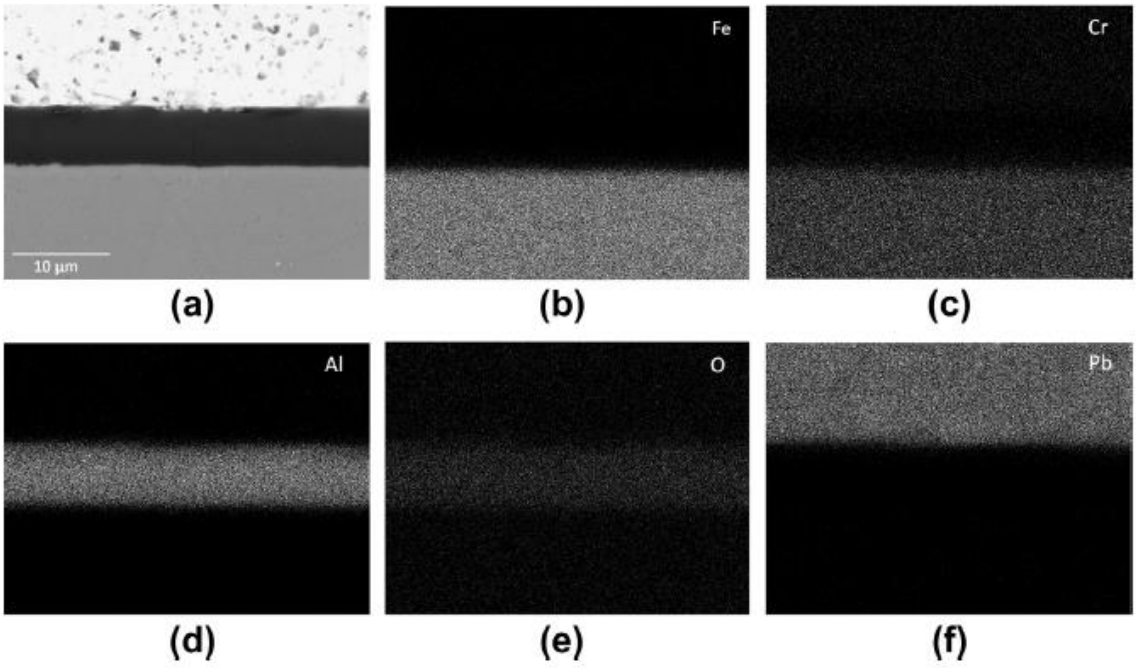

Figure 27: Cross-Sectional SEM Image of the Al_2O_3 Coated Steel Coupon (a) and EDS Elemental Maps Identifying Each Element in the Cross Section ((b) – (f)) (Figure Reproduced from [23])

As seen in Figure 26, the top portion of the steel coupon (approximately one fourth of the surface) was not coated with Al_2O_3 whereas the remaining areas were. The Al_2O_3 coated and uncoated areas can be seen visually by looking at the differences in reflection of light on the surface. It is obvious that when the steel coupon contains a thick coating of Al_2O_3 that has been deposited via PLD, the steel is completely protected from any interaction with the liquid Pb (containing oxygen) and thus corrosion is prevented. This can be seen via the EDS elemental map in Figure 27 where the cross-sectional image of the steel coupon is shown in image (a) and the elements of Fe, Cr, Al, oxygen (O), and Pb are shown in images (b) through (f), respectively.

By looking at the elemental maps, the outer layer (image (f)) is completely comprised of the Pb melt which had solidified on the coupon surface. Beneath the solidified Pb melt was the Al_2O_3 coating (images (d) and (e)) showing the presence of only Al and O. Lastly, beneath the Al_2O_3 coating was the steel coupon (images (b) and (c)) which is primarily composed of Fe and Cr. As the elemental maps show, besides the Al_2O_3 coating, there are no other oxidation products present. This indicates there is no chemical reactions or interaction between the steel and the liquid Pb which contains oxygen. If there was an interaction, the EDS elemental maps would indicate the presence of Fe_2O_3 and Cr_2O_3 as the Fe and Cr from the steel would have reacted with the oxygenated liquid Pb. Thus, the results of this study show that by applying a thick Al_2O_3 coating on the surface of the steel coupon via PLD, a barrier is created that effectively isolates the substrate from the liquid Pb. This shows that this material system is capable of handling and containing HLMs.

3.0 Research Description

3.1 Hypothesis Statement

The hypothesis of this thesis is that the oxidation and corrosion performance of the HAYNES® 214® nickel-base superalloy at temperatures of 800°C to 900°C can be favorably altered by applying nanoscale surface coatings of Al_2O_3 and Cr_2O_3 that act as a passivation or barrier layer.

3.2 Objectives

The objective of this research is to use PLD to deposit nanoscale coatings of Al_2O_3 and Cr_2O_3 on small coupons of the HAYNES® 214® nickel-base superalloy and then subject these coupons to a series of tests including isothermal oxidation, thermal cycling, and hot corrosion. By characterizing the oxidation and corrosion products on the alloy surface and within the subsurface zone, we will be able to obtain a fundamental understanding of the coatings' roles during the oxidation and hot corrosion process.

3.3 Tasks

The first part of this thesis was to prepare a series of alloy coupons containing three different conditions; uncoated, Al_2O_3 coated, and Cr_2O_3 coated. The alloy coupons were then

placed into furnaces and exposed to oxidizing and hot corrosion environments. The second part of this thesis was to use a wide variety of materials characterization techniques to determine the composition, morphology, structure, and thickness of the oxidation and corrosion products on the alloy coupon surfaces. The material characterization techniques used as part of this research include optical microscopy (OM), SEM, EDS, transmission electron microscopy (TEM), x-ray diffraction (XRD), Raman spectroscopy, and Photoluminescence spectroscopy (PL).

4.0 Experimental Methods

4.1 HAYNES® 214® Sample Preparation

Plates of HAYNES® 214® supplied by Haynes International were mechanically sectioned into square coupons containing nominal dimensions of 1 centimeter (cm) by 1 cm (surface area of 1 cm^2). The top and bottom surfaces of each coupon were chemically cleaned using Ethanol and wiped dry. The top surfaces of all HAYNES® 214® coupons were then either vapor honed or abraded prior to undergoing isothermal oxidation, thermal cycling, or hot corrosion testing. The bottom surfaces of all coupons were not subjected to vapor honing or abrasion and were left as the wrought as-received alloy.

4.1.1 Vapor Honed Surface Condition

To prepare vapor honed samples, a VAPOR BLAST™ Liquid Honing machine was used to induce deformation on the top surfaces of clean and dry HAYNES® 214® coupons. During the vapor honing process, each coupon was securely clamped in vise-grip pliers and the top surface was aligned with the running vapor hone stream for approximately 15 seconds (s). Once vapor honed, the coupons were removed from the machine and the top and bottom surfaces were again cleaned with Ethanol to remove any vapor hone residue remaining and then dried.

4.1.2 Abraded Surface Condition

To prepare abraded samples, a Struers LaboForce-100 containing a standard rotating grinding wheel equipped with SiC paper was used to polish the top surfaces of clean and dry HAYNES® 214® coupons to a 1200-grit finish. To ensure the entire surface was polished, the coupons were ground using a uniform force in several different directions. Once the coupons were polished, the top and bottom surfaces were again cleaned with Ethanol to remove any residue remaining and then dried.

4.1.3 Pulsed Laser Deposition of Al_2O_3 and Cr_2O_3 Nanocoatings

Coatings of Al_2O_3 and Cr_2O_3 approximately 150 to 175 nm in thickness were deposited onto the surfaces of half of the vapor honed and abraded HAYNES® 214® coupons using the PVD Products PLD-3000 system shown in Figure 28.

Figure 28: PVD Products PLD-3000 System Used to Deposit Al_2O_3 and Cr_2O_3 Nanocoatings on the Surfaces of the HAYNES® 214® Coupons (Figure Reproduced from [24])

To understand the deposition rate of the Al_2O_3 coatings, systematic depositions were performed on Si substrates for various durations. The Si substrates were then destructively sectioned and the cross sections were analyzed using an SEM to determine the PLD coating thickness. Table 2 below shows the relationship between deposition duration and the resulting Al_2O_3 coating thickness.

Table 2: Relationship Between Deposition Duration and Al_2O_3 Coating Thickness

Deposition Duration[1]	Al_2O_3 Coating Thickness
10 min	~ 175 nm
30 min	~ 500 nm
60 min	~ 1 μm

[1] All other deposition conditions were held constant as seen below:

- Room Temperature
- 85 mm Target-to-Substrate Distance
- 150 mJ Laser Energy
- 40 Hz Laser Frequency
- Vacuum Environment

Based on the PLD parameters used, it was found that the deposition rate was about 17 nm/min and the relationship between thickness and duration was approximately linear. Prior to performing oxidation (isothermal and thermal cycling) and hot corrosion tests, the mechanical adhesion of the Al_2O_3 and Cr_2O_3 coatings to the alloy surface was investigated. Because the goal of the coating is to act as a passivation or barrier layer, the coating must remain adherent during the high temperature oxidation process.

During the PLD process, the coating grows via high velocity impingement of molecules on the alloy surface. Thus, the impingement of the molecules must be sufficient to form and grow a coating that has enough strength to withstand the forces generated from several different types of stresses that may occur at the alloy-PLD coating interface. First, thermal stresses will be generated at this interface due differences in the coefficients of thermal expansion between the metallic alloy and the ceramic oxide. Second, mechanical stresses may be generated at this interface due to the possibility for the formation of a thermally grown oxide layer immediately below the PLD coating.

If either of these stresses are significant enough to exceed the mechanical adhesion strength of the PLD coating on the alloy surface, the coating could crack (oxides are brittle), spall off of the surface (portions of the coating are completely removed), or become detached (coating is no longer adherent to the alloy surface).

Should any of these phenomena occur, passivation of the alloy surface would be compromised as oxygen would either have unrestricted access to the surface (in the case of spalling) or oxygen would be capable of easily diffusing to the surface through any cracks that formed (in the case of cracking). Thus, in order to understand the limitations on coating thickness relative to the mechanical adhesion on the alloy surface, two HAYNES® 214® coupons were isothermally oxidized at 800°C for a 3-hrs. Both coupons contained a different coating thickness; one had a thickness of roughly 1 μm (60-min PLD duration) and one had a thickness of about 175 nm (10-min PLD duration). Figure 29 and Figure 30 below show the surface and cross-sectional SEM images of the coupon containing the 1 μm thick coating before and after 3-hrs of isothermal oxidation in air at 800°C.

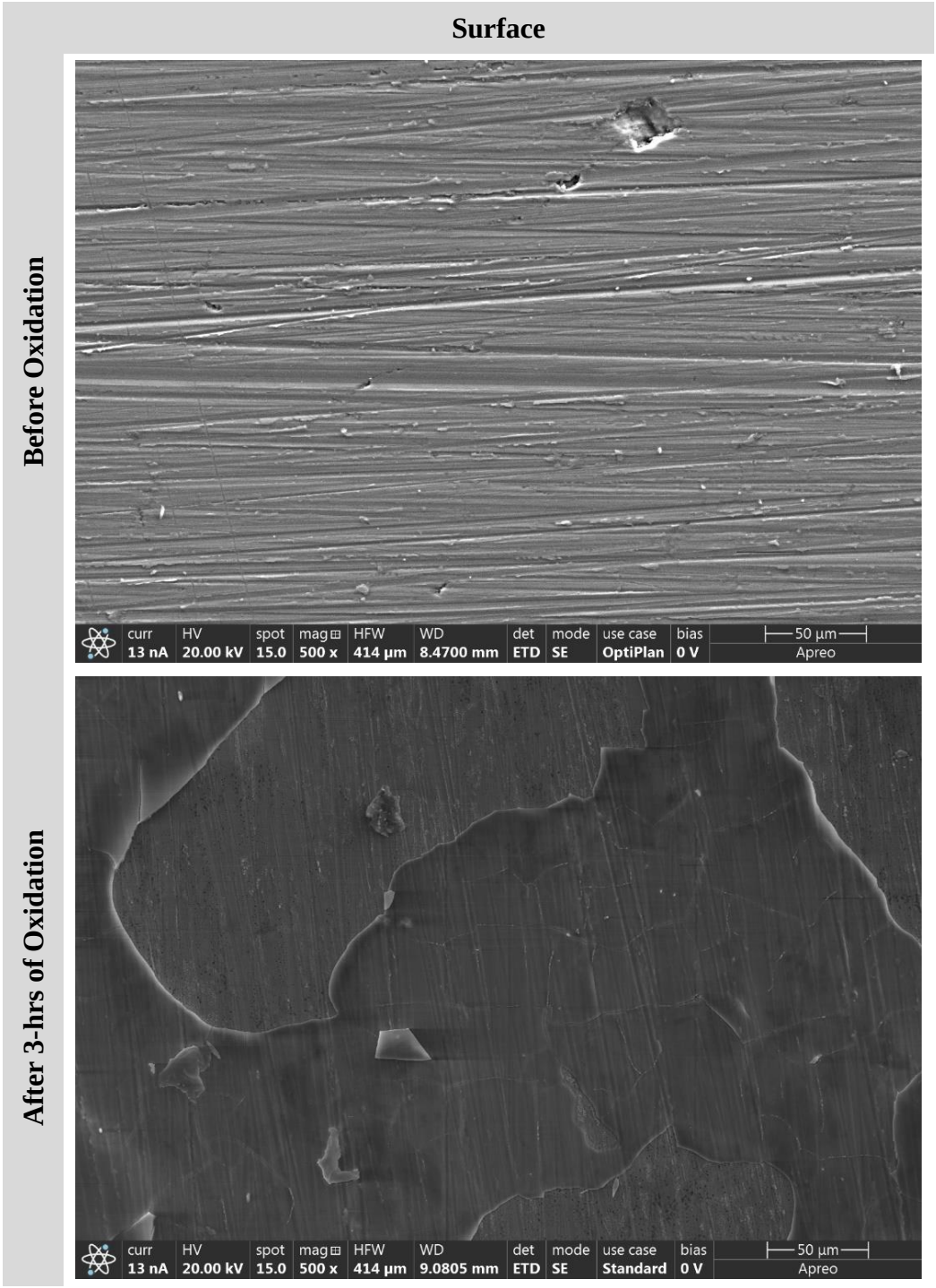

Figure 29: Surface SEM Image of a HAYNES® 214® Coupon Containing a 1 µm Thick Al_2O_3 Coating Before Oxidation and After 3-hrs of Isothermal Oxidation in Air at 800°C

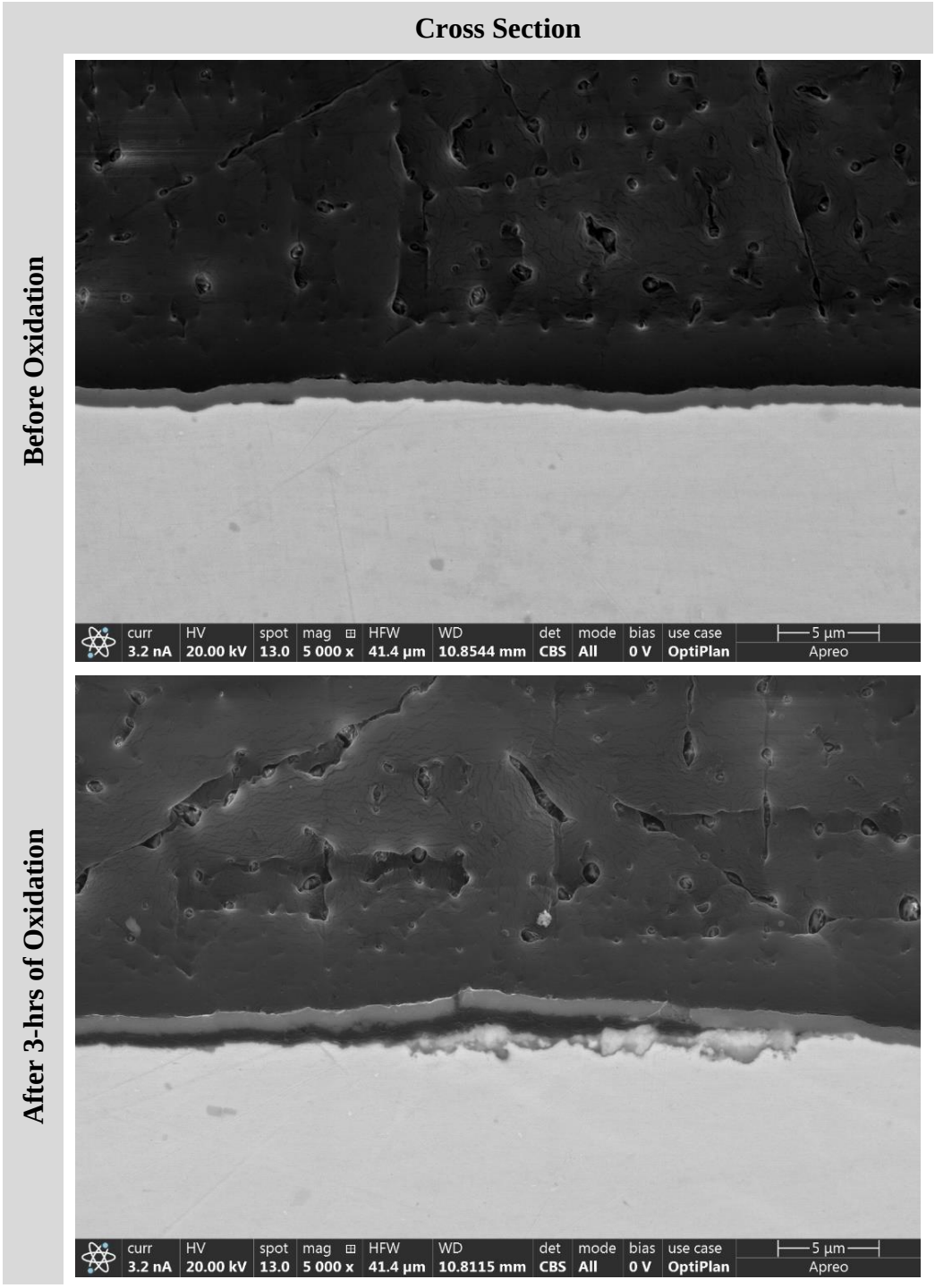

Figure 30: Cross-Sectional SEM Image of a HAYNES® 214® Coupon Containing a 1 µm Thick Al_2O_3 Coating Before Oxidation and After 3-hrs of Isothermal Oxidation in Air at 800°C

As seen in Figure 29 and Figure 30, after only 3-hrs of isothermal oxidation in air, the coating showed significant cracking and breakaway from the alloy surface. In some locations, large areas of the alloy were completely exposed leaving the surface susceptible to oxidation attack. In this case, a 1 μm thick coating would not suffice as a passivation layer because oxygen would have unrestricted access to the exposed alloy surface and oxygen diffusion through the cracks in the coating would be rapid. Both of these scenarios are undesirable, and for this reason, a 1 μm thick coating served as an estimation for the upper bound of film thickness for this thesis.

For the coupon containing the 175-nm thick coating, it was found that the coating remained completely adherent to the alloy surface after 3-hrs of isothermal oxidation in air at 800°C. SEM images of the surface and cross section are not shown here because this coating thickness was used for all of the tests performed as part of this research. Thus, the effect of using this coating thickness relative to the oxidation and corrosion performance of the HAYNES® 214® nickel-base superalloy can be found in Section 5.0.

Once an understanding of the deposition rate and mechanical adhesion for Al_2O_3 and Cr_2O_3 coatings were achieved, a complete set of PLD parameters to be used for coating the HAYNES® 214® coupons were developed. Table 3 lists the PLD conditions used for depositing the Al_2O_3 and Cr_2O_3 nanocoatings onto the surfaces of the vapor honed and abraded HAYNES® 214® coupons. The primary PLD parameters used for the film deposition are identified in italics.

Table 3: PLD Conditions Used to Deposit the Al_2O_3 and Cr_2O_3 Nanocoatings onto the Surfaces of the Vapor Honed and Abraded HAYNES® 214® Coupons

Deposition Parameter	Value/Condition
Substrate Temperature [1]	*Room Temperature*
Target-to-Substrate Distance [2]	*85 mm*
Substrate Rotation Speed	10 revolutions per min (RPM)
Target Rotation Speed	30 RPM
Background Deposition Environment [3]	*Vacuum (No Oxygen Flow)*
Laser Energy [4]	*150 mJ*
Laser Voltage	20.0 kilovolts (kV)
Laser Frequency [4]	*40 Hz*
Deposition Duration [5]	*10 min*

1 Room temperature conditions were chosen because this reduced the total deposition time as additional time was not needed to allow the alloy coupon to cool within the load chamber of the PLD system.

2 Vacuum conditions were used due to the need for a dense coating. Section 2.3 above described the role of using a background oxygen environment and how increasing the oxygen partial pressure can result in more porous coatings.

3 The duration was chosen due to the mechanical adhesion aspects discussed above. This duration resulted in a coating the remained adherent after oxidation at 800°C.

4 The target to substrate distance was chosen because this was the load position of the PLD system and thus additional substrate movement was not required.

5 The laser energy and frequency were chosen based on previous literature that deposited Al_2O_3 coatings via PLD.

4.2 Oxidation of the HAYNES® 214® Nickel-base Superalloy

4.2.1 Isothermal Oxidation

To investigate the isothermal oxidation performance of the HAYNES® 214® alloy, vapor honed and abraded coupons with and without Al_2O_3 and Cr_2O_3 nanocoatings deposited on the surface were isothermally oxidized in a Daihan Scientific WISD atmospheric box furnace for 3- and 100-hrs at 800°C. A ramp rate of 5°C/min was utilized resulting in a total heat up duration of 2-hrs and 40-min. The furnace was then held at 800°C for 3- and 100-hrs before undergoing a natural convection cool down. Once the furnace was cooled, the HAYNES® 214® coupons were removed and characterized as described in Section 4.5. Figure 31 shows the schematic of the isothermal oxidation process used.

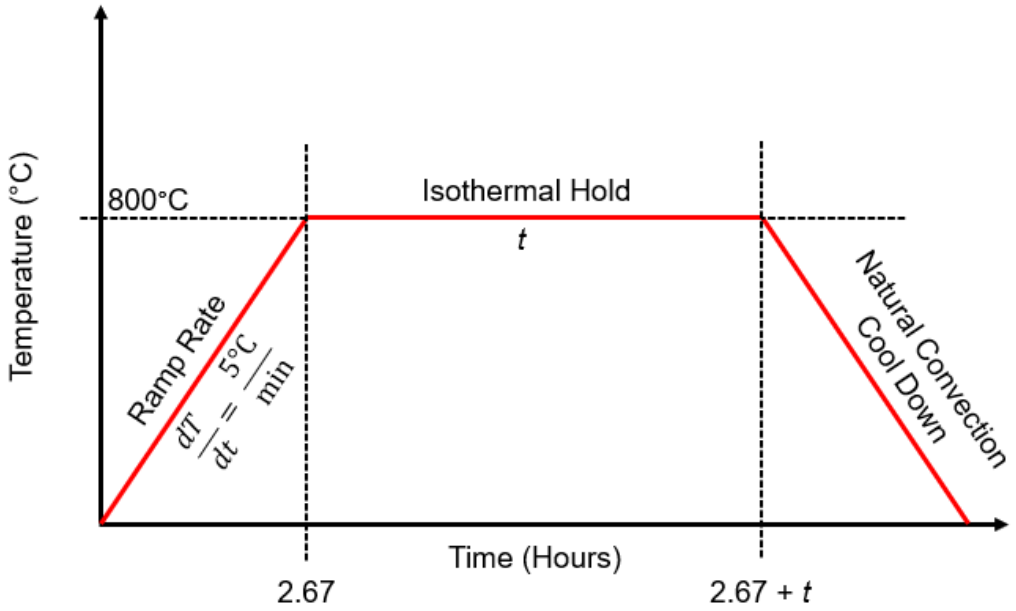

Figure 31: Isothermal Oxidation Process Used for the HAYNES® 214® Coupons

4.2.2 Thermal Cycling

To understand the thermal cycling performance of the HAYNES® 214® alloy, abraded HAYNES® 214® coupons with and without Al_2O_3 and Cr_2O_3 nanocoatings deposited on the surface were subjected to thermal cycling in a Mellen NACCI tube furnace at 800°C. Prior to inserting the coupons into the furnace, each coupon was weighed to determine the starting weight. The tube furnace was initially heated to 800°C, thus no wait time was required to allow the furnace to reach the test temperature. The coupons were placed inside an Al_2O_3 crucible and the crucible was rapidly slid into the hot zone of the furnace (i.e., the location where the temperature inside the tube was 800°C) and left there for the cycle duration.

Each HAYNES® 214® coupon was thermally cycled for a total of 100-hrs (5 cycles for 20-hrs each), and after each cycle the crucible was removed from the tube furnace and the coupons were allowed to cool in ambient air. Additionally, after each thermal cycle, the HAYNES® 214® coupons were reweighed to determine the interim weight gain. For the furnace environment used in the thermal cycling tests, the test gas used was always air containing 0.001% of SO_2 (10 ppm of SO_2) supplied at a flow rate of 30 milliliters (mL)/min. Additionally, an upstream platinum (Pt) catalyst was used to establish an O_2-SO_2-SO_3 equilibrium in the flowing gas.

4.3 Hot Corrosion Testing

4.3.1 Single Salt Hot Corrosion of Na_2SO_4

To understand the hot corrosion performance of the HAYNES® 214® alloy, abraded HAYNES® 214® coupons with and without Al_2O_3 and Cr_2O_3 nanocoatings deposited on the surface were subjected to thermally cycled hot corrosion testing in a Mellen NACCI tube furnace at 900°C. Prior to inserting the coupons into the tube furnace, approximately 3 milligrams (mg)/cm^2 of Na_2SO_4 was placed on each alloy surface, and then the coupons were weighed to determine the starting weight. The tube furnace was initially heated to 900°C, thus no wait time was required to allow the furnace to reach the test temperature. The coupons were placed inside an Al_2O_3 crucible and the crucible was rapidly slid into the hot zone of the furnace (i.e., the location where the temperature inside the tube was 900°C) and left there for the cycle duration.

Each HAYNES® 214® coupon was thermally cycled for a total of 100-hrs (5 cycles for 20-hrs each), and after each cycle the crucible was removed from the tube furnace and the coupons

were allowed to cool in ambient air. Since the melting point of Na_2SO_4 is 884°C, using a test temperature of 900°C means the salt will melt on the coupon surface and maximize the potential for hot corrosion to occur. After each hot corrosion thermal cycle, the HAYNES® 214® coupons were reweighed to determine the interim weight gain. For the furnace environment used in the hot corrosion thermal cycling tests, the test gas used was always air containing 0.001% of SO_2 (10 ppm of SO_2) supplied at a flow rate of 30 mL/min. Additionally, an upstream Pt catalyst was used to establish an O_2-SO_2-SO_3 equilibrium in the flowing gas.

4.4 Electrochemical Corrosion Testing

To test the electrochemical corrosion resistance of the HAYNES® 214® coupons, potentiodynamic polarization experiments were performed on the uncoated, Al_2O_3 coated, and Cr_2O_3 coated alloy surfaces. Figure 32 shows the experimental setup for the potentiodynamic polarization experiments.

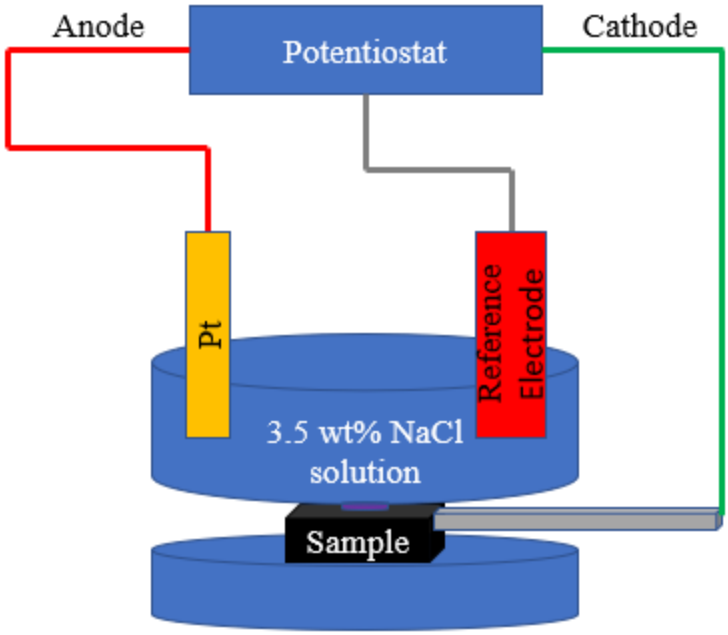

Figure 32: Test Setup for the Potentiodynamic Polarization Experiments

To perform the electrochemical corrosion resistance tests, a conductive strip was secured to each coupon surface using a conductive silver (Ag) paste, and the coupons were then clamped into an apparatus where a small circular area of the coupon surface was exposed to the inside of a container filled with a 3.5 wt% solution of sodium chloride (NaCl). A Pt wire and reference electrode were inserted into the container and a cathodic positive current was utilized where the Pt wire was the anode (red cable) and the alloy coupon was the cathode (working electrode, green cable). The potential was swept from an initial voltage of -1 volts (V) to a final voltage of 0 V, using increments of 0.00017 V/s. As the voltage was varied, the resulting current was plotted to generate a Tafel curve.

4.5 Material Characterization

4.5.1 Optical Microscopy

The top surfaces of the HAYNES® 214® coupons with and without Al_2O_3 and Cr_2O_3 nanocoatings were analyzed and imaged using a Zeiss SmartZoom OM at 100X and 500X magnifications. OM was primarily used to investigate the macroscopic oxidation performance of the alloy coupons in addition to identifying areas on the surfaces to examine further using SEM.

4.5.2 X-ray Diffraction (XRD)

4.5.2.1 Powder XRD

The top surfaces of the HAYNES® 214® coupons with and without Al_2O_3 and Cr_2O_3 nanocoatings were analyzed using the Bruker D8 Discover XRD at an operating voltage and current of 40 kV and 40 milliamps (mA), respectively. The XRD was arranged in a powder configuration where the incident x-rays and detector were simultaneously scanned over a 2-theta (θ) angle range of 30° to 95° using an increment of 0.02°/step and a scan speed of 0.25 s/step. Based on these parameters, the total scan time was about 13.5 min. For all powder XRD analyses, copper (Cu) K-alpha (K_α) radiation containing a wavelength of 1.5406 angstroms (Å) was utilized.

4.5.2.2 Glancing Angle XRD

The top surfaces of the HAYNES® 214® coupons with and without Al_2O_3 and Cr_2O_3 nanocoatings were analyzed using the Bruker D8 Discover XRD at an operating voltage and current of 40 kV and 40 mA, respectively. The XRD was arranged in a glancing angle

configuration where the incident x-ray rays were fixed at a 2θ angle of 5° while the detector was scanned over a 2θ angle range of 8° to 50° using an increment of 0.02°/step and a scan speed of 0.1 s/step. Based on these parameters, the total scan time was 3.5 min. For all glancing angle XRD analyses, Cu K_α radiation containing a wavelength of 1.5406 Å was utilized.

4.5.3 Scanning Electron Microscopy

4.5.3.1 Sample Preparation

To prepare the oxidized HAYNES® 214® coupons for cross-sectional SEM analysis, an Allied High Tech Products Techcut 4™ Precision Low Speed Saw equipped with a diamond coated wafer blade was used to cut the coupons in half. Once sectioned, half of the coupon was mounted with the cut surface placed face down in a mixture of an epoxy resin and hardener and allowed to cure overnight. The hardened resin, including the mounted HAYNES® 214® coupon inside, was then ground to a 1200-grit finish using a Struers LaboForce-100 apparatus and a sequence of 500- and 1200-grit SiC paper and water. Following grinding at both 500- and 1200-grit, an OM was used to examine the cross section to ensure that all scratches were uniform and no deeper scratches were present.

For the HAYNES® 214® coupons that were subjected to hot corrosion testing, due to the possibility of the corrosion products being loosely attached on the surface, a slightly different mounting approach was utilized. For these coupons, the entire coupon was mounted in a mixture of an epoxy resin and hardener with the corrosion surface facing upwards. By first mounting the coupon in this way, all corrosion products will remain attached to the coupon surface during subsequent sample preparation steps. Once the epoxy resin and hardener cured, the circular mount was ground into a square configuration which outlined the shape of the coupon. The square mount

was then placed in a rotating blade saw and the coupon (and square mount) was cut in half to expose the cross section. Once sectioned, half of the coupon (and square mount) was then mounted again in the epoxy resin and hardener mixture, however this time the cut surface was placed face down so that the cross section could be analyzed. Once the epoxy resin and hardener cured, the hardened resin (including the mounted HAYNES® 214® coupon inside) was then ground to a 1200-grit finish using the Struers LaboForce-100 apparatus and a sequence of 320-, 500-, and 1200-grit SiC paper and ethanol. Because the corrosion products formed during hot corrosion testing are water soluble, the fluid used during the grinding process had to be ethanol which would not dissolve the corrosion products.

After the coupons had been ground to a 1200-grit, the resin and mounted coupon were polished to a 0.25 μm finish using the same Struers LaboForce-100 apparatus and a sequence of 3-, 1-, and 0.25 μm polishing pads containing a diamond suspension and lubricant. After each polishing increment, an OM was used again to examine the cross section to ensure that all scratches were eliminated and the cross section appeared completely smooth. After the coupons were polished to a 0.25 μm finish, to prevent charge buildup during SEM and EDS analysis, a thin coating of palladium (Pd) was applied on the resin and polished coupon using a Cressington 108 Auto Pd sputter coater.

4.5.3.2 Electron Imaging

The top surfaces and cross sections of the HAYNES® 214® coupons with and without Al_2O_3 and Cr_2O_3 nanocoatings were analyzed using a high-resolution FEI Apreo Hi-Vac field-emission gun (FEG) SEM. For all surface images, secondary electrons were utilized which better illustrate topography, texture, and surface features. Conversely, for all cross-sectional images, backscatter electrons were utilized which interact with individual elements differently and thus

can more easily distinguish the oxidation products on the alloy surface or within the subsurface zone.

4.5.3.3 Energy Dispersive Spectroscopy

The cross sections of the HAYNES® 214® coupons with and without Al_2O_3 and Cr_2O_3 nanocoatings were analyzed using the FEI Apreo SEM equipped with an EDAX Octane Elite EDS system. All EDS analyses were collected and processed using the APEX EDS software. While EDS can be used in a variety of ways (e.g., point analysis, line scans, etc.), EDS was used in this thesis to generate elemental maps of the alloy cross sections to show the oxidation products on the alloy surface or within the subsurface region.

4.5.4 Transmission Electron Microscopy

4.5.4.1 Sample Preparation

To prepare an oxidized coupon for cross-sectional TEM analysis, the coupon was cut into two separate pieces using the Allied High Tech Products Techcut 4™ Precision Low Speed Saw equipped with a diamond coated wafer blade. Each coupon piece contained dimensions of about 2 mm (length) by 2.5 mm (width) by 2.5 mm (depth) (2 mm x 2.5 mm x 2.5 mm (L x W x D)). The oxidized surfaces of the two coupon pieces were then epoxied together such that the oxidized region was located at the center line, creating a sandwich sample. The sandwich sample contained a total dimension of roughly 4 mm x 2.5 mm x 2.5 mm (L x W x D).

Next, a K.D. UNIPRESS WS-22B high precision wire saw equipped with a thin tungsten (W) wire and lubricated with boron carbide (B_4C) mixed in a glycerin slurry was used to trim the epoxied sandwich sample to total dimensions of approximately 2 mm (length) (1 mm on each side

of the epoxy line) by 2.5 mm (width) by 250 μm (depth) (2 mm x 2.5 mm x 250 μm (L x W x D)). Once these dimensions were obtained, with the epoxy line vertical, one surface of the sandwich sample was polished to a 1 μm finish while the opposite surface was dimple grinded using a Fischione Instruments Model 200 Dimpling Grinder to thin the area around the epoxy line to a thickness of about 30 μm. The dimple grinded surface was then argon (Ar) ion milled using a Fischione Instruments Model 1050 TEM Mill until the epoxy line had just been perforated, giving four locations for TEM imaging and analysis.

4.5.4.2 High Angle Annular Dark Field Imaging

The cross section of a Cr_2O_3 coated HAYNES® 214® coupon that had undergone 100-hrs of isothermal oxidation in air at 800°C was analyzed using the FEI Titan Themis G2 200 Probe Cs Corrected TEM. The FEI Titan TEM was used to generate high angle annular dark field (HAADF) images of the Cr_2O_3 coated coupon cross section. HAADF images are similar to backscatter electron images in an SEM due to electrons interacting with individual elements differently. Thus, HAADF images can easily distinguish the different oxidation products on the coupon surface or within the subsurface region.

4.5.4.3 Energy Dispersive Spectroscopy

The cross section of a Cr_2O_3 coated HAYNES® 214® coupon after 100-hrs of isothermal oxidation was analyzed using the FEI Titan TEM equipped with a Windowless Super-X EDS system. All EDS analyses were collected and processed using the Velox software.

4.5.5 Raman Spectroscopy and Photoluminescence

The top surfaces of the HAYNES® 214® coupons with and without Al_2O_3 and Cr_2O_3 nanocoatings were analyzed using a WITec Alpha Scanning Near-Field OM (SNOM) which generated both Raman images and Raman spectra. Table 4 below provides the equipment settings used for the Raman analysis.

Table 4: Settings and Parameters for the WITec Alpha SNOM Relative to Generating Raman Images and Raman Spectra

Setting	Value/Condition
Excitation Source	532 nm Nd:YAG Laser
Confocal Pinhole	50 μm Diameter Optical Fiber
Microscope Objective	100x / 0.9NA
Excitation Spot Diameter	Approximately 0.5 μm
Spectrometer	0.3-meter (m) Monochromator with a Thermoelectrically Cooled Charge Coupled Device (CCD)

The Raman spectra were collected using an 1800 groove/mm grating and each spectrum was collected in a single location. Additionally, the spectrum collected is the average of 4 accumulations with each accumulation having an integration time of 10 s. The PL spectra (which also contains the Raman modes) were collected using a 150 groove/mm grating and each spectrum was also collected in a single location. Additionally, the spectrum collected is the average of 10

accumulations with each accumulation having an integration time of 1 s. All data files have had cosmic rays removed and the background was subtracted using a 0-order polynomial.

5.0 Results and Discussion

5.1 Isothermal Oxidation

5.1.1 Abraded Surface Condition

The abraded HAYNES® 214® coupons ground to a 1200-grit were first analyzed using OM to determine the macroscopic oxidation performance of the alloy surfaces. Figure 33, Figure 34, and Figure 35 show the OM images of the uncoated, Al_2O_3 coated, and Cr_2O_3 coated HAYNES® 214® coupon surfaces before, after 3-hrs, and after 100-hrs of isothermal oxidation in air at 800°C.

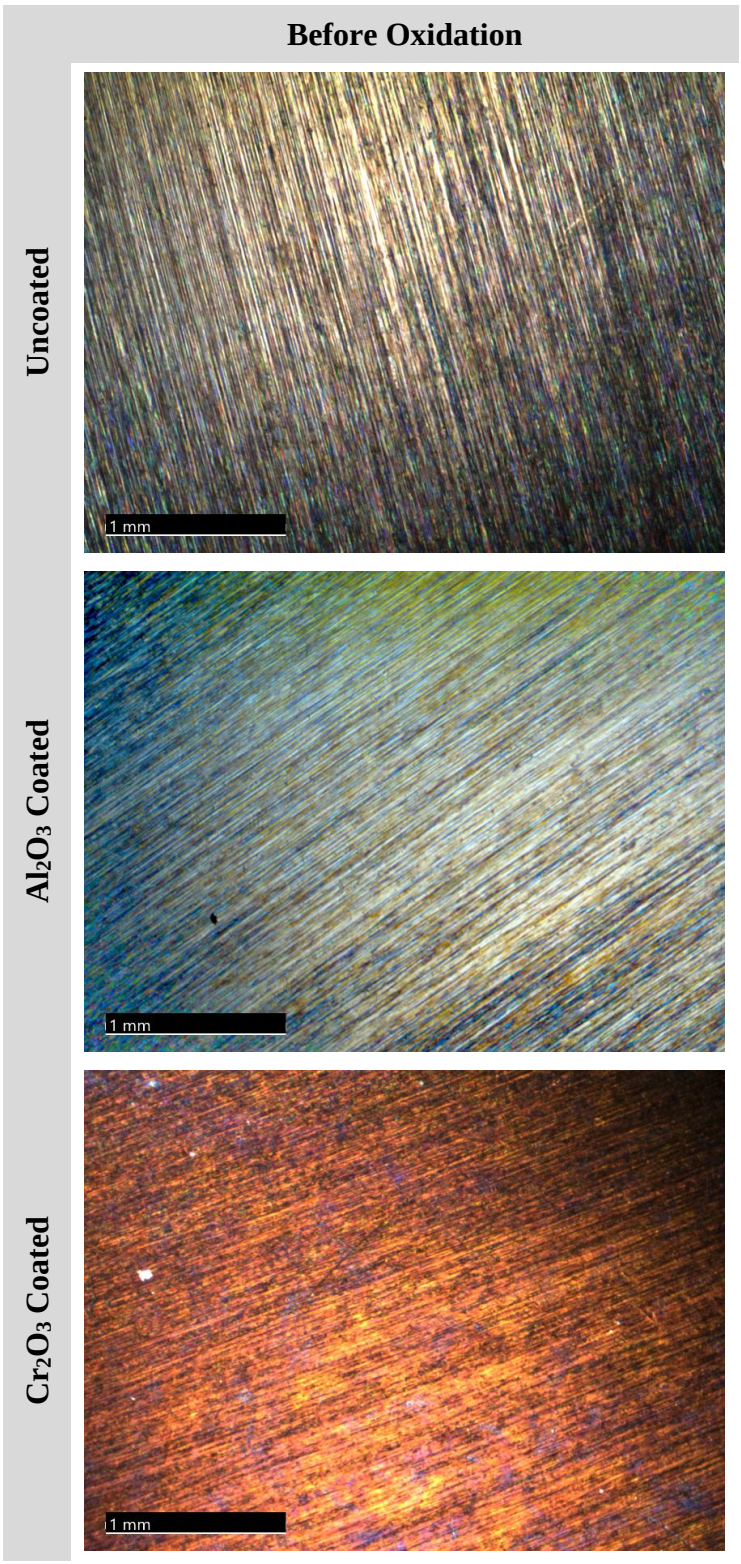

Figure 33: OM Images of the Uncoated, Al_2O_3 Coated, and Cr_2O_3 Coated 1200-Grit HAYNES® 214® Coupons Before Oxidation

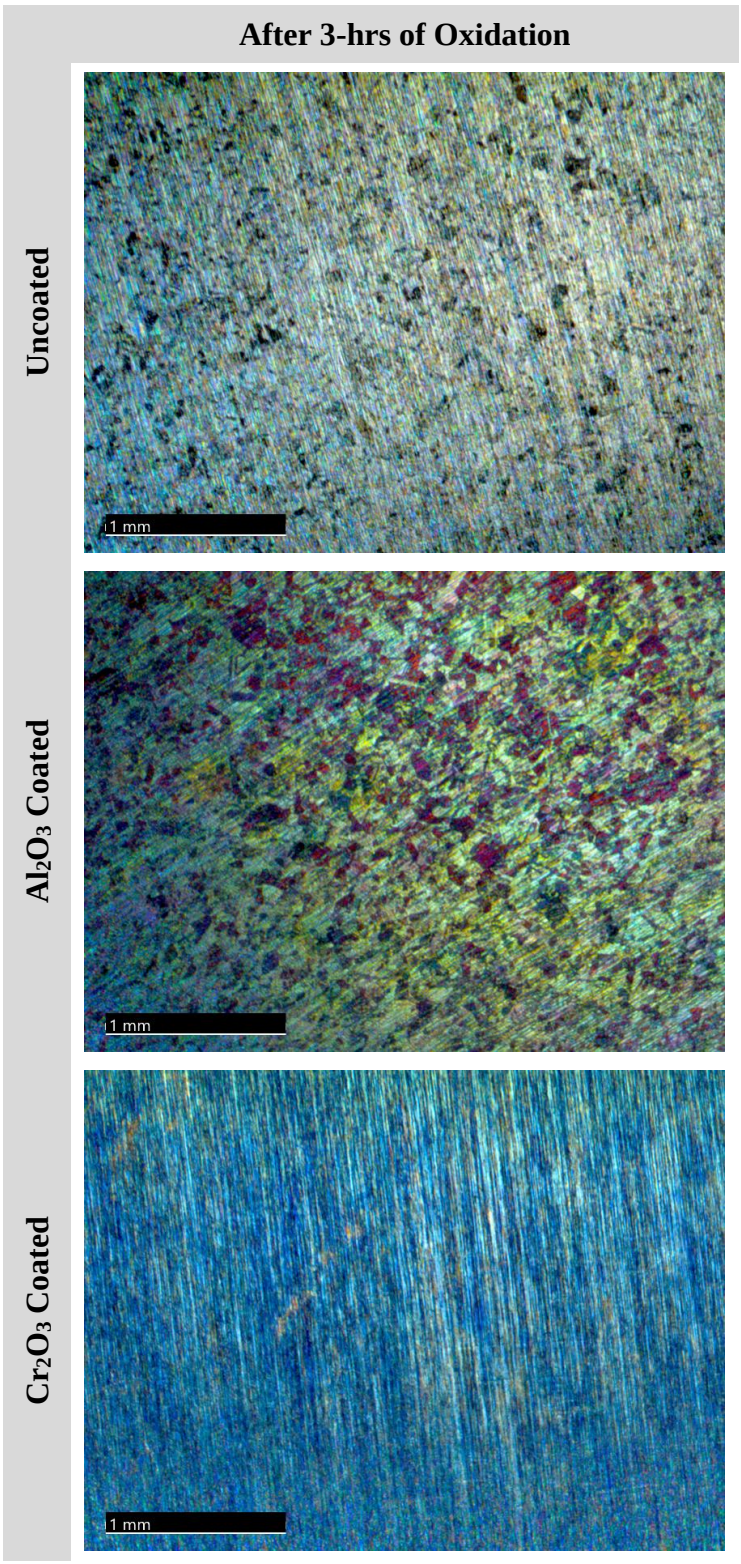

Figure 34: OM Images of the Uncoated, Al_2O_3 Coated, and Cr_2O_3 Coated 1200-Grit HAYNES® 214® Coupons After 3-hrs of Isothermal Oxidation in Air at 800°C

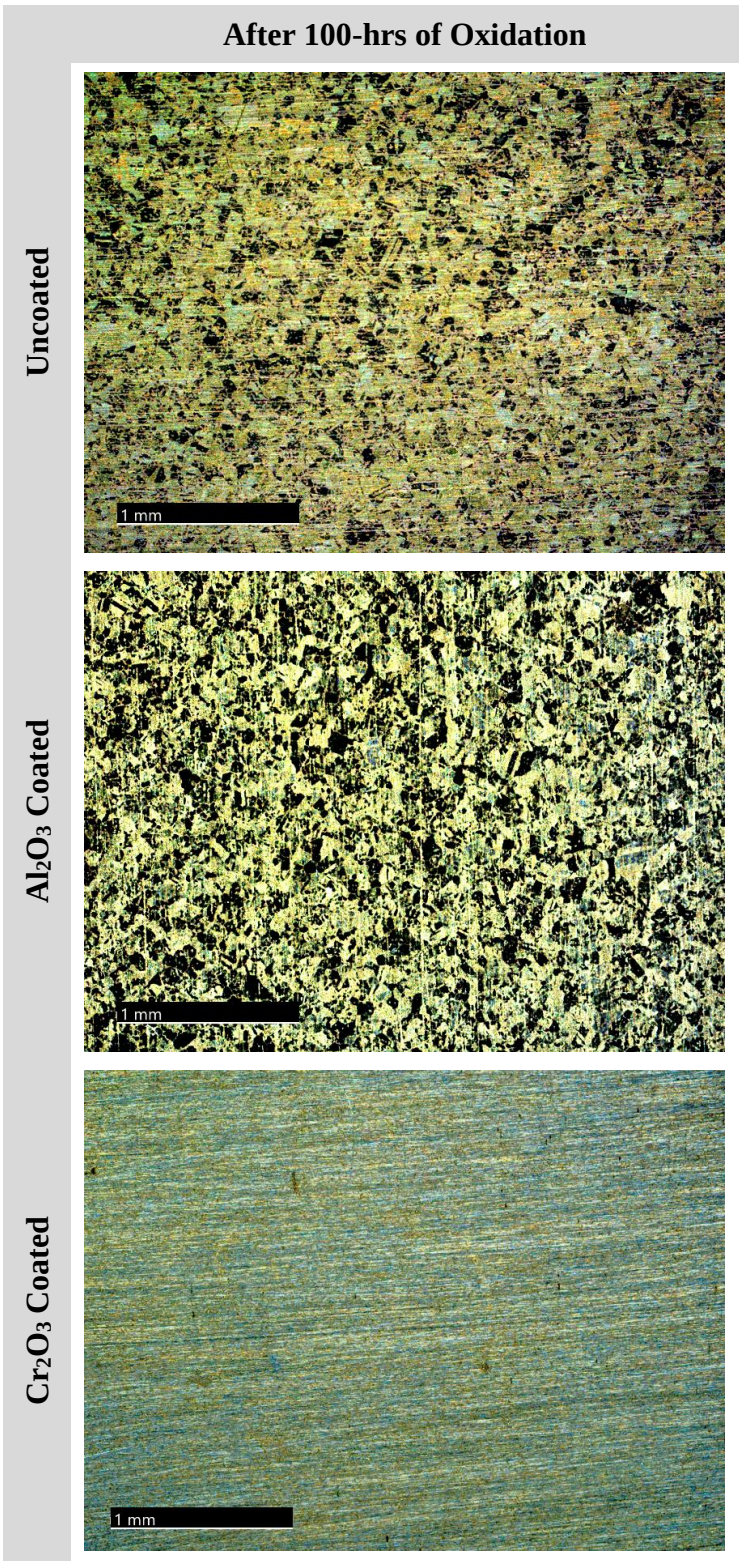

Figure 35: OM Images of the Uncoated, Al_2O_3 Coated, and Cr_2O_3 Coated 1200-Grit HAYNES® 214® Coupons After 100-hrs of Isothermal Oxidation in Air at 800°C

As the figures above show, before exposing the three coupon types to high temperature oxidizing conditions, the uncoated coupon exhibits a silver hue which resembles the pure metallic surface of the alloy. Conversely, the Al_2O_3 coated and Cr_2O_3 coated coupons show a light blue and red-orange-purple color, respectively. Once the coupons have been oxidized for 3-hrs, the surfaces begin to show different macroscopic oxidation performances as indicated by a color change. The surface of the uncoated coupon shows two distinct regions; a large portion of the surface is a light blue color whereas other localized areas appear gray-black. The areas appearing gray-black indicate the presence of some sort of external oxide feature since the light is either being absorbed or scattered in these regions. Conversely, the areas appearing light blue indicate the presence of a conformal oxide as the light is being reflected off of the surface. Additionally, the grooves from the abraded alloy surface can be seen in these regions.

Similar to the uncoated coupon, the Al_2O_3 coated coupon also shows two distinct regions on the surface. The majority of the surface appears a blue-green-yellow shade, however there are also localized areas of gray-black and red-purple. As described with the uncoated coupon, the areas appearing gray-black signify that there is some external oxide feature in these locations. However, the red-purple regions also appear to be an external oxide formation (see Figure 82 in Appendix A for a closer magnification OM image of the gray-black and red-purple areas of the uncoated and Al_2O_3 coated coupons). Unlike the uncoated and Al_2O_3 coated alloy coupons, the surface of the Cr_2O_3 coated coupon appears a uniform navy-blue color and there are no gray-black areas on the alloy surface. This means that the oxide on the surface is entirely conformal as the light is being completely reflected and no external oxide features are absorbing or scattering any light. Furthermore, the fact that the color of the surface has changed from a red-orange-purple color to a

navy-blue color indicates that there is a thickness or compositional change as the interaction with the light is different.

When increasing the high temperature oxidation duration to 100-hrs, the uncoated and Al_2O_3 coated alloy coupons show comparable oxidation results in that there are still two different and distinct regions; about half of the surface area appears solid black, and the other half of the surface area appears a yellow-gold color. Since the black areas mean that light is being absorbed or scattered, this means about half of the uncoated and Al_2O_3 coated coupon surfaces are covered in an external oxide growth (e.g., a nodule or island) whereas the other half of the surfaces are covered by a conformal oxide (due to the reflection of light). As was the case after 3-hrs of high temperature oxidation, the Cr_2O_3 coated alloy surface differs significantly from the uncoated and Al_2O_3 coated coupons. Rather than have a large fraction of the surface be covered in an external oxide growth, the Cr_2O_3 coated coupon still shows a completely conformal oxide as exemplified by the absence of black regions and the presence of a light blue-yellow color.

Based on the OM images of the oxidized coupon surfaces which showed both external oxide features and conformal oxide products, the alloy surfaces were examined closer using SEM. Figure 36, Figure 37, and Figure 38 show the surface SEM images of the uncoated, Al_2O_3 coated, and Cr_2O_3 coated coupon surfaces before, after 3-hrs, and after 100-hrs of isothermal oxidation in air at 800°C.

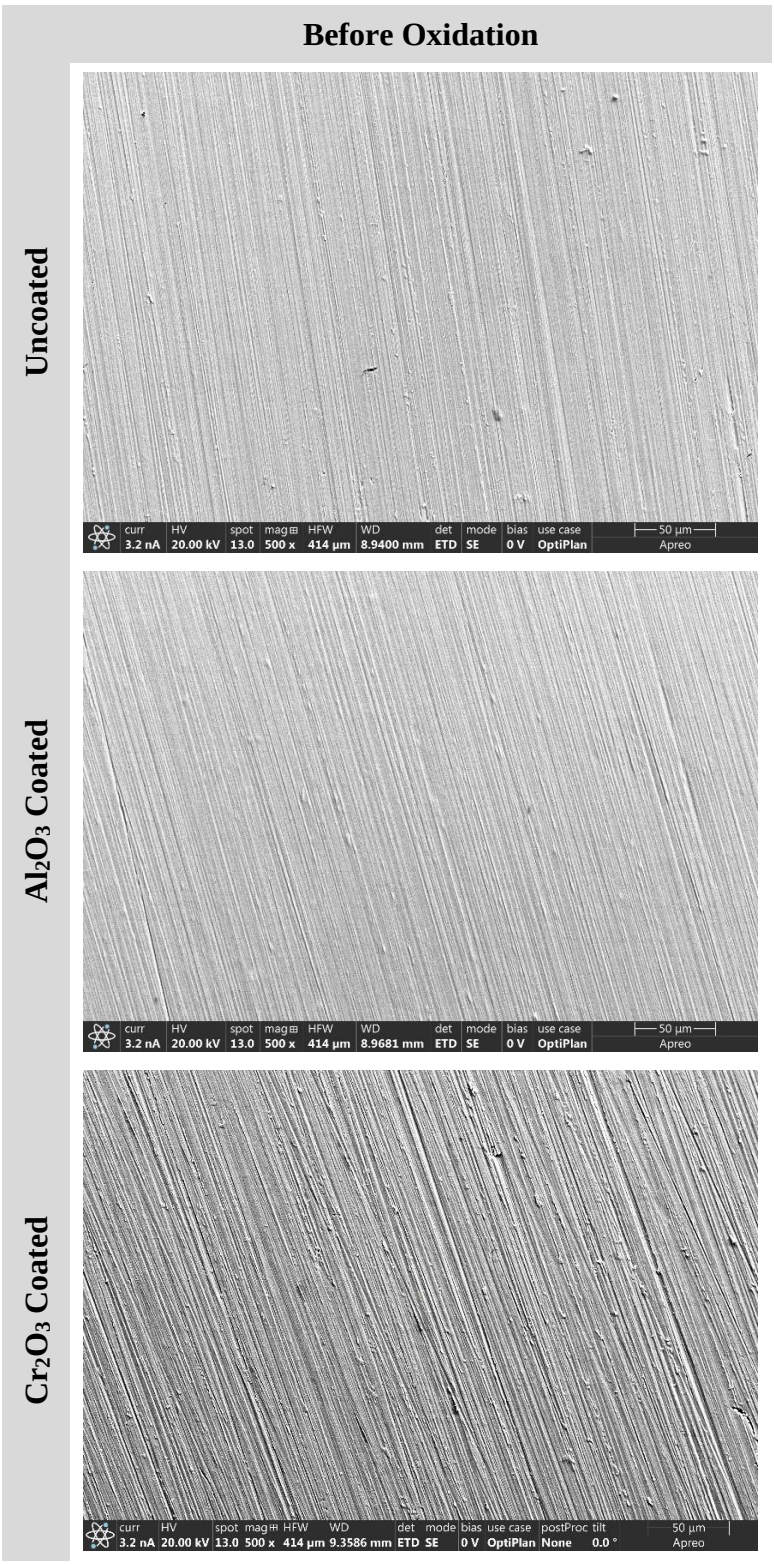

Figure 36: Surface SEM Images of the Uncoated, Al_2O_3 Coated, and Cr_2O_3 Coated 1200-Grit HAYNES® 214® Coupons Before Oxidation

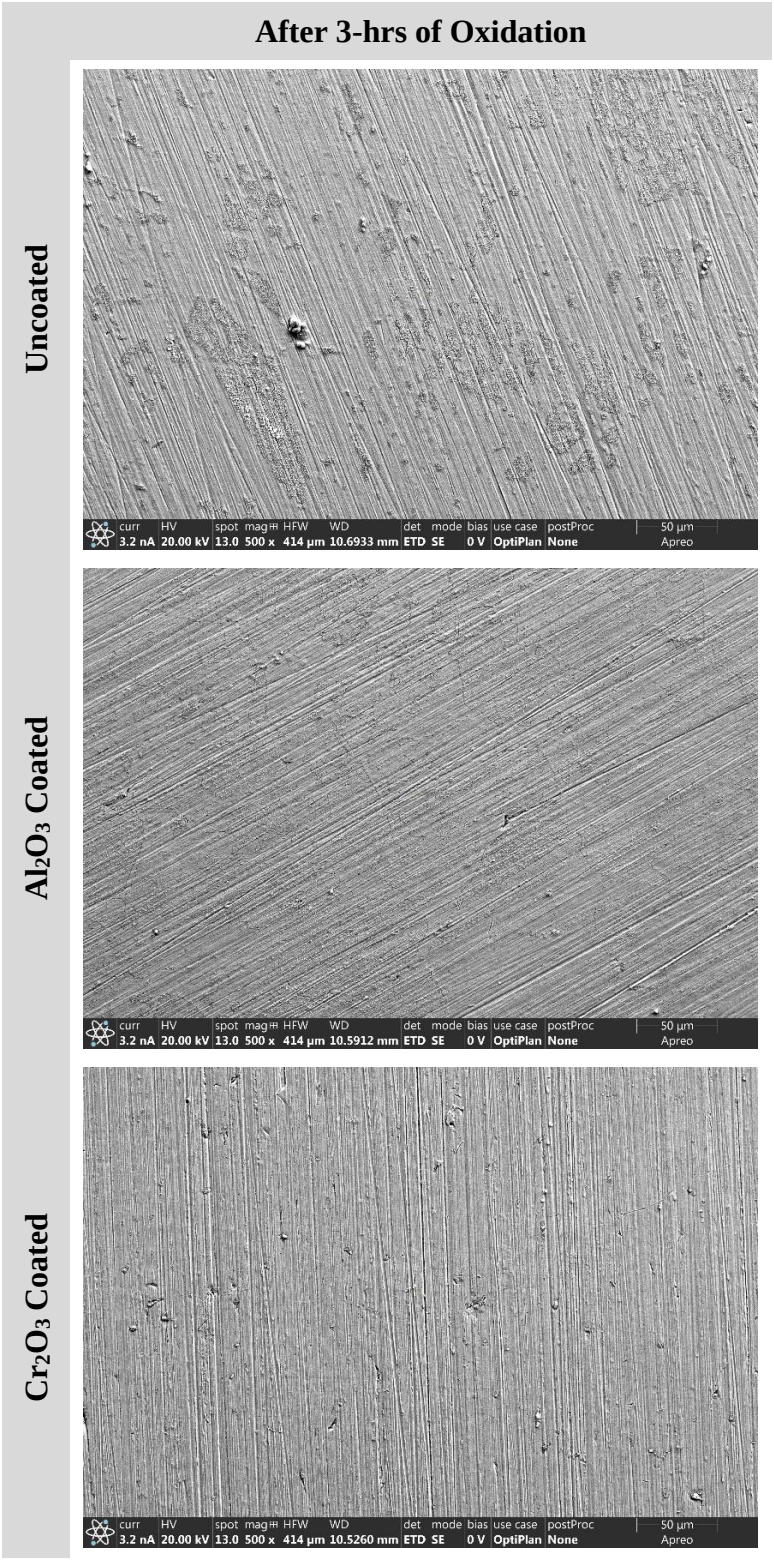

Figure 37: Surface SEM Images of the Uncoated, Al_2O_3 Coated, and Cr_2O_3 Coated 1200-Grit HAYNES® 214® Coupons After 3-hrs of Isothermal Oxidation in Air at 800°C

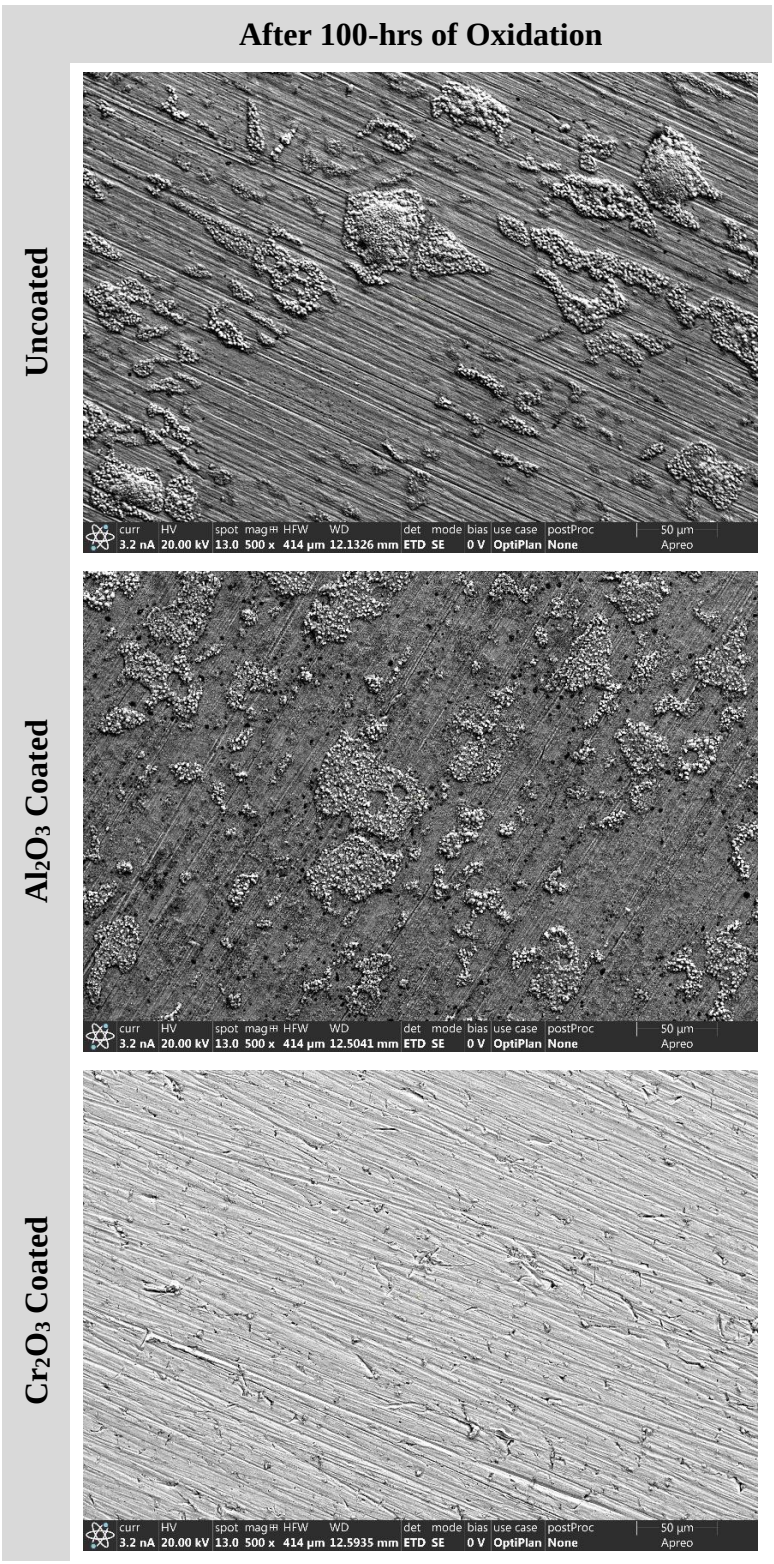

Figure 38: Surface SEM Images of the Uncoated, Al_2O_3 Coated, and Cr_2O_3 Coated 1200-Grit HAYNES® 214® Coupons After 100-hrs of Isothermal Oxidation in Air at 800°C

As expected before oxidation, the surfaces of all three coupon types are smooth and the grooves on the 1200-grit abraded surface can be clearly seen. Using the SEM and taking a closer look at the coupon surfaces that were oxidized for 3-hrs, it can be seen that the gray-black areas shown in the 3-hr OM image of the uncoated alloy are in fact nodules or islands of external oxide growth. These oxide nodules or islands can be seen all over the surface in localized areas. For the Al_2O_3 coated coupon, distinct oxide nodules or islands cannot be found; however, there are regions that show slightly outlined areas which may be the start of some external oxide growth (see Figure 83 in Appendix A for backscatter electron images of the external oxide growth on the uncoated and Al_2O_3 coated coupons). Lastly, consistent with what was shown in the OM images, SEM analysis of the Cr_2O_3 coated coupon surface shows no external oxide growth (nodules or islands) and any oxide that is on the surface appears entirely conformal. Furthermore, the grooves from mechanical abrasion (polishing) of the alloy surface during sample preparation can still be seen.

When increasing the oxidation duration to 100-hrs, the surface of the uncoated alloy coupon shows more extensive external oxide growth, and the nodules or islands that had formed after 3-hrs of oxidation grew in size (both height and width) and quantity (i.e., fraction of the surface covered). Relative to the Al_2O_3 coated coupon, an interesting phenomenon has taken place in between the 3- and 100-hr durations where the alloy surface now shows the formation of external oxide nodules and islands identical to the uncoated alloy surface. Furthermore, these external oxide islands and nodules appear of the same size (height and width) compared to the uncoated alloy. Upon closer examination of the Cr_2O_3 coated alloy, SEM analysis confirms that the surface is smooth, the oxide is conformal, and there are no external oxide formations (islands or nodules).

To determine the compositions and morphology of the oxides on the alloy surfaces (and any internal oxidation that may be present), the cross sections of each alloy coupon were analyzed

using SEM and EDS. The cross-sectional SEM images of the uncoated, Al_2O_3 coated, and Cr_2O_3 coated coupons after 3-hrs of isothermal oxidation in air at 800°C are shown in Figure 39, Figure 40, and Figure 41. Accompanying each cross-sectional SEM image is an EDS map showing the compositions of the oxidation products on the alloy surfaces or within the subsurface zone.

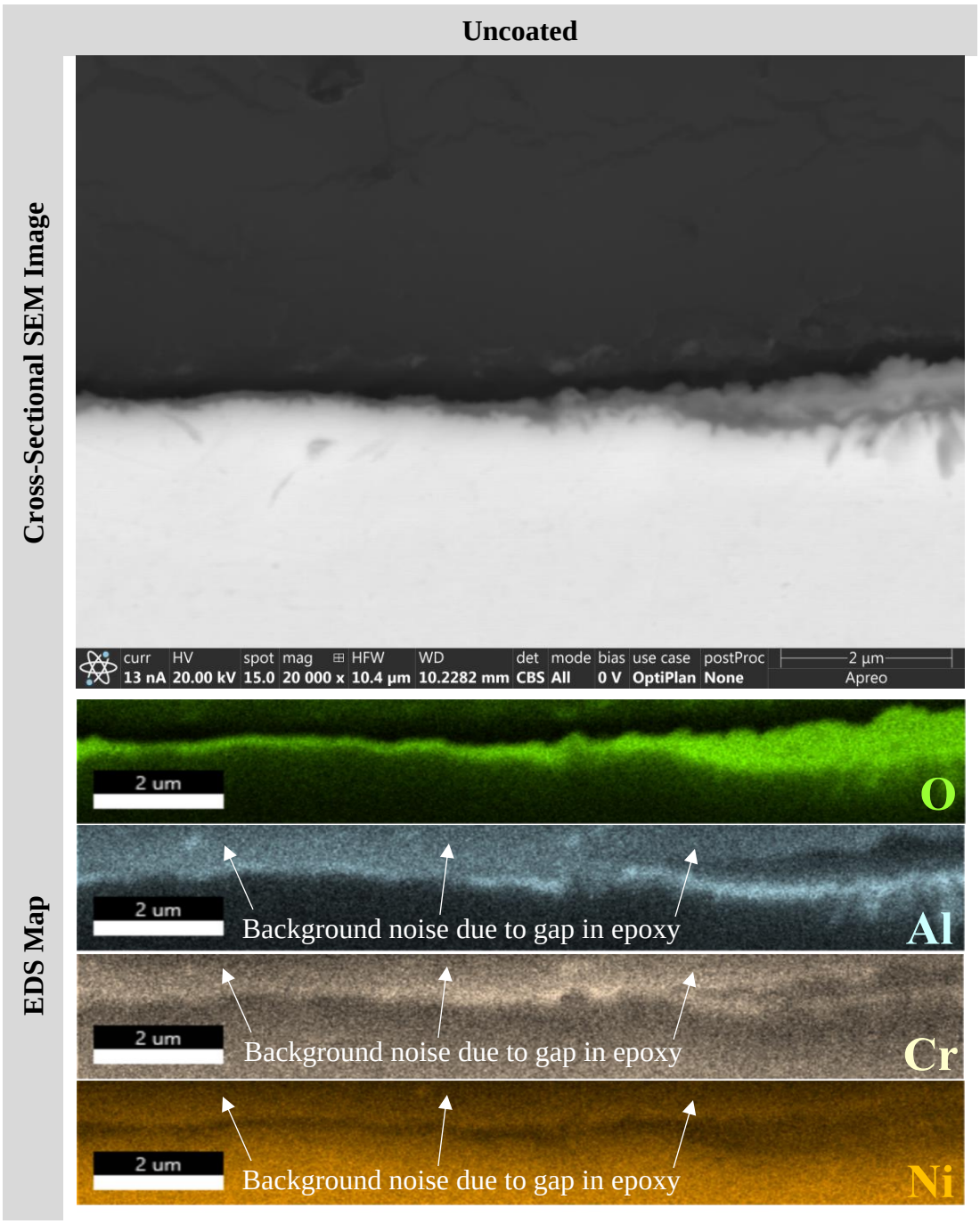

Figure 39: Cross-Sectional SEM Image and EDS Map of the Uncoated 1200-Grit HAYNES® 214® Coupon After 3-hrs of Isothermal Oxidation in Air at 800°C

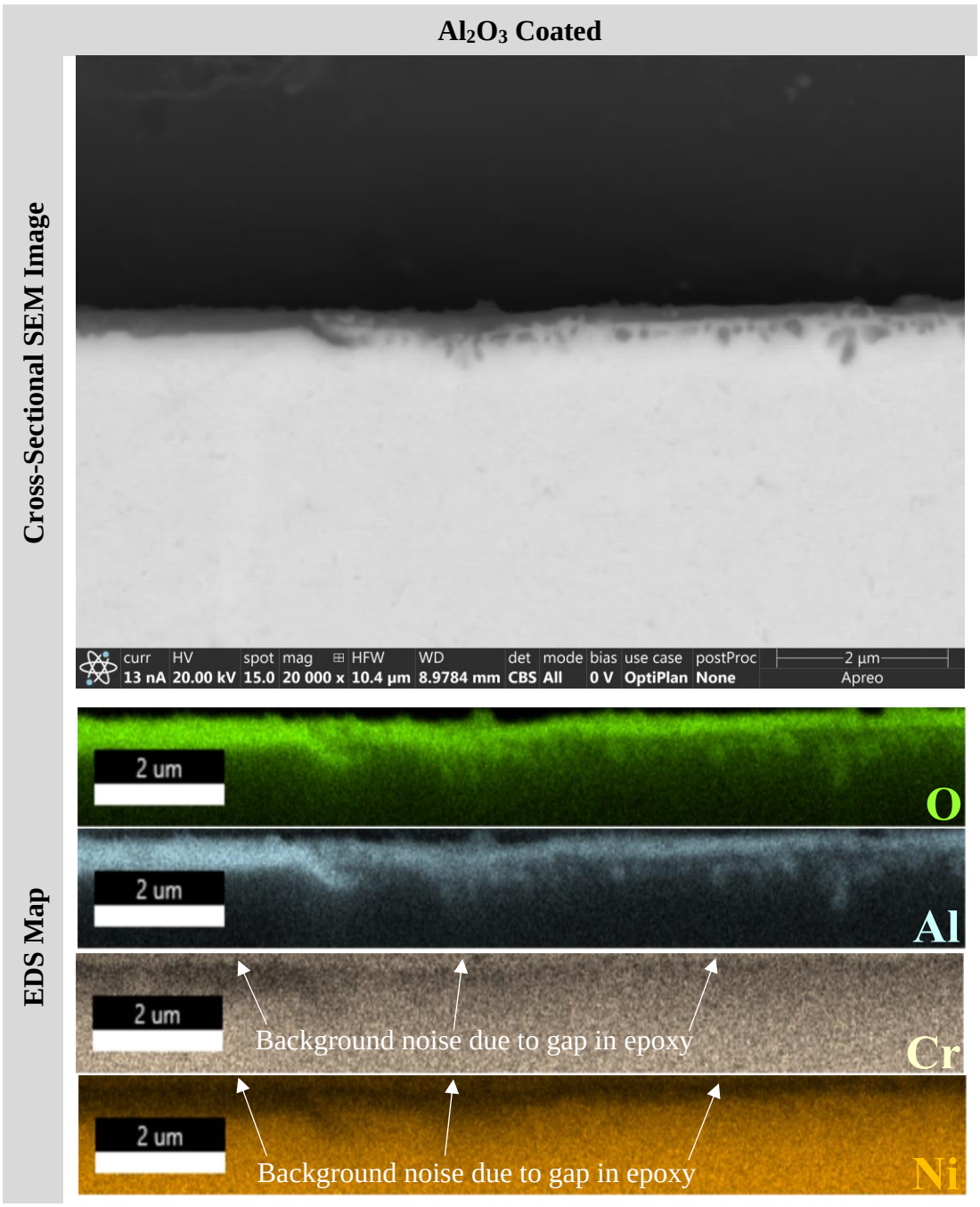

Figure 40: Cross-Sectional SEM Image and EDS Map of the Al_2O_3 Coated 1200-Grit HAYNES® 214® Coupon After 3-hrs of Isothermal Oxidation in Air at 800°C

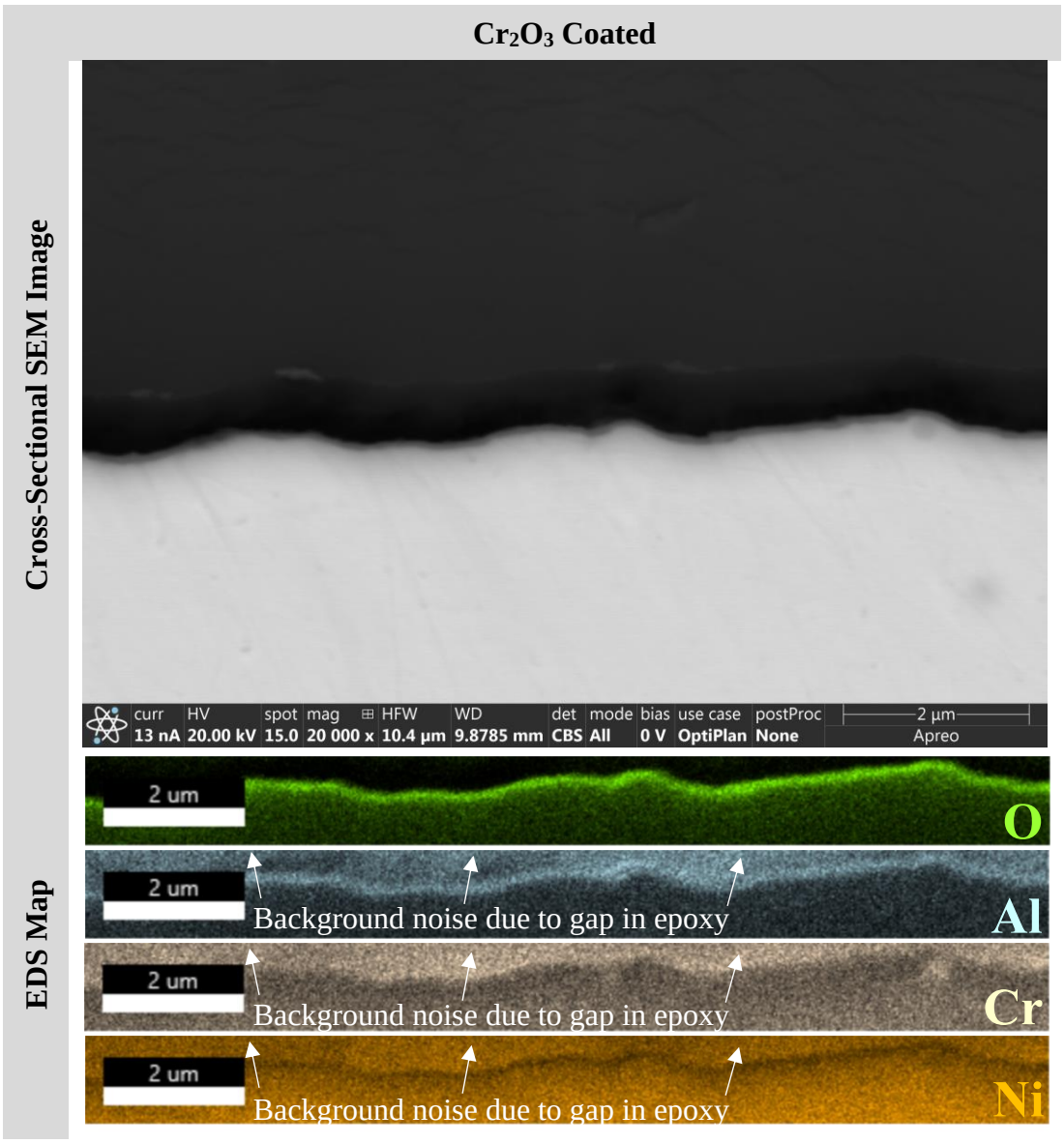

Figure 41: Cross-Sectional SEM Image and EDS Map of the Cr_2O_3 Coated 1200-Grit HAYNES® 214® Coupon After 3-hrs of Isothermal Oxidation in Air at 800°C

After 3-hrs of oxidation, the uncoated coupon exhibits a dual oxidation growth where regions of the surface are covered in a thin, conformal, and external oxide scale approximately 100 nm in thickness whereas other regions contain a much thicker oxide scale that has grown both inward (into the alloy subsurface) and outward (on top of the alloy surface). This dual oxidation growth was expected based on the OM and SEM images of the surface. The EDS maps generated indicate that the regions of the alloy where the thinner, external scale has formed is an Al-rich oxide and regions where the thicker oxide has formed contains an outer layer of a Ni/Cr-rich oxide and an inner layer of an Al-rich oxide that has formed within the subsurface region.

Since abrading the alloy coupons to a 1200-grit introduces a surface deformation layer, it is clear that the regions where an external Al-rich oxide scale has formed experienced short circuit diffusion where the Al was capable of diffusing to the alloy surface fast enough to form an external scale. However, in localized regions of the alloy surface, the Al diffusion was not fast enough compared to the inward diffusion of oxygen, and instead internal precipitates were formed. This mixed oxide growth mechanism is very similar to the phenomenon Giggins and Pettit [7] noted in their classical experiments described in Section 2.1.2.4 where localized differences in surface preparation or impurities of Ni-Cr-Al alloys containing compositions near the boundary regions were found to follow two mechanisms simultaneously.

With respect to the Al_2O_3 coated coupon after 3-hrs of oxidation, a dual oxidation growth mechanism was also exhibited. However, unlike the uncoated coupon which showed regions where an exclusive external scale had formed and other regions containing layers of both an inner and outer oxide, the Al_2O_3 coated alloy shows no outer oxide layer. Instead, some areas of the surface show a thicker external scale of an Al-rich oxide about 250 nm in thickness and other areas

of the surface show a thinner external scale of an Al-rich oxide about 150 nm in thickness on top of internal Al_2O_3 precipitates.

Based on this formation, it appears that the thicker scale regions are a combination of the Al_2O_3 PLD coating applied to the alloy surface (about 150 nm in thickness) and a layer of thermally grown Al-rich oxide underneath (about 100 nm in thickness). Thus, two important things happened in these regions; the short circuit diffusion phenomenon was sufficient to provide an Al supply to the alloy-PLD coating interface and oxygen diffusion through the Al_2O_3 PLD coating was slow enough to prevent the formation of internal oxides, allowing the Al to form a continuous oxide layer beneath the PLD coating. In the other regions where internal oxidation was observed, either the inward oxygen diffusion through the Al_2O_3 PLD coating was faster resulting in an oxygen partial pressure and oxygen activity large enough to precipitate internal Al_2O_3 or the short circuit diffusion of Al to the alloy-PLD coating interface was slower to the extent that external scale growth was unachievable. In comparison to the uncoated coupon, it appears that applying an Al_2O_3 coating on the alloy had some effect as it was capable of suppressing the outward diffusion of Ni and Cr as indicated by the lack of any Ni/Cr-rich oxide formation on the surface.

For the Cr_2O_3 coated alloy, no internal oxidation of any kind was observed and instead, the alloy had formed a thin external scale of an Al-rich oxide that was approximately 100 nm in thickness. The significance of this is two-fold. First, it is obvious that applying a Cr_2O_3 coating to the alloy surface was able to suppress any outward diffusion of Ni and Cr to the surface, thus preventing the formation of less protective Ni/Cr-rich oxides (e.g., NiO, Cr_2O_3, $NiCr_2O_4$) as was seen in the uncoated coupon. Second, the Cr_2O_3 coating was very effective in slowing down the inward diffusion of oxygen such that the oxygen partial pressure and oxygen activity within the subsurface zone never reached the threshold or critical value required for the formation of internal

Al_2O_3 precipitates (unlike the uncoated and Al_2O_3 coated alloy). By slowing down the inward diffusion of oxygen, combined with the short circuit diffusion of Al from within the recrystallization zone, the alloy was capable of only forming an external scale.

To determine how the different coupons performed in the longer-term oxidation tests, the cross-sectional SEM images of the uncoated, Al_2O_3 coated, and Cr_2O_3 coated alloy after 100-hrs of isothermal oxidation in air at 800°C are shown in Figure 42, Figure 43, and Figure 44. Accompanying each cross-sectional SEM image is an EDS map showing the compositions of the oxidation products on the alloy surfaces or within the subsurface zone.

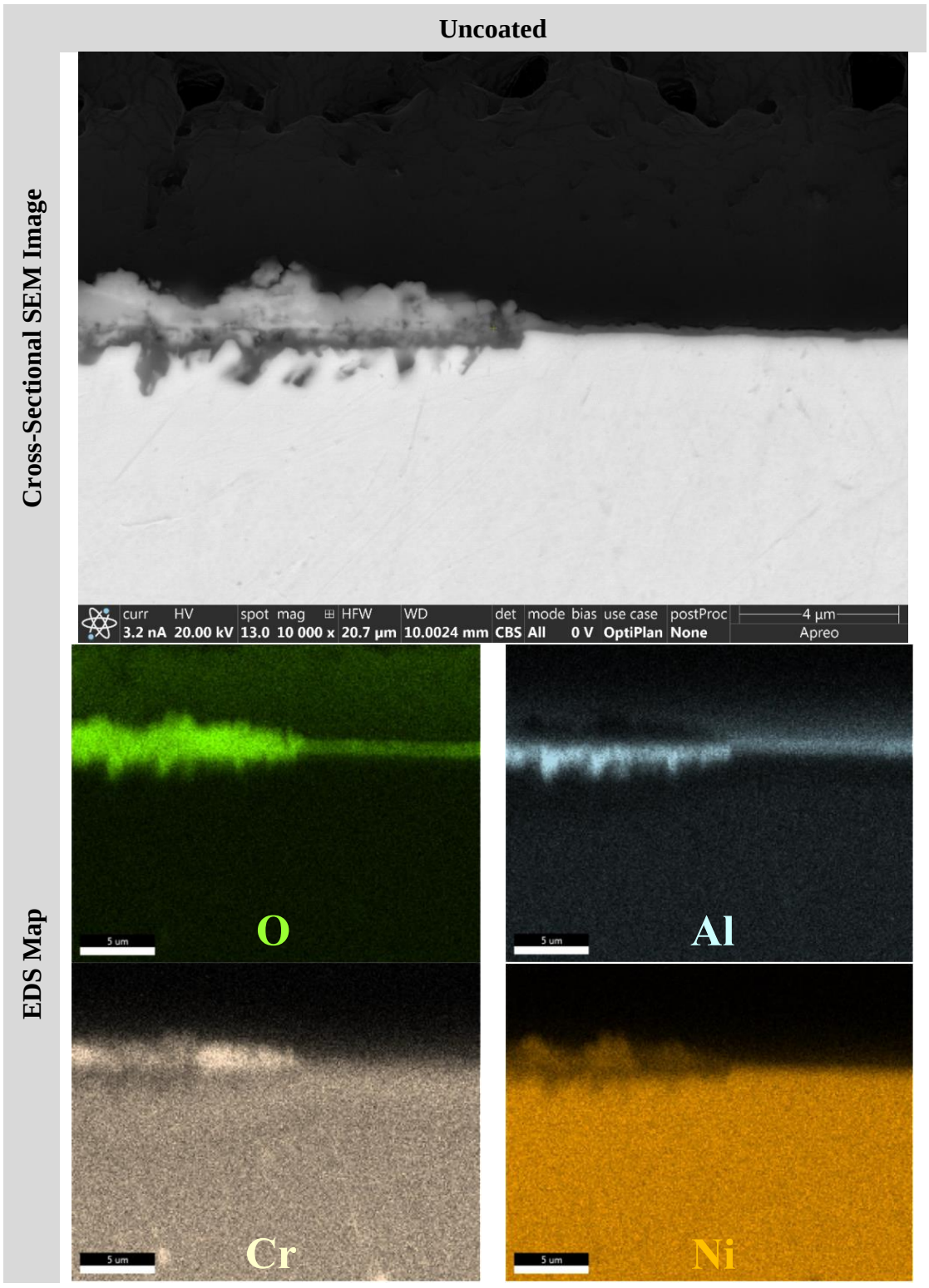

Figure 42: Cross-Sectional SEM Image and EDS Map of the Uncoated 1200-Grit HAYNES® 214® Coupon After 100-hrs of Isothermal Oxidation in Air at 800°C

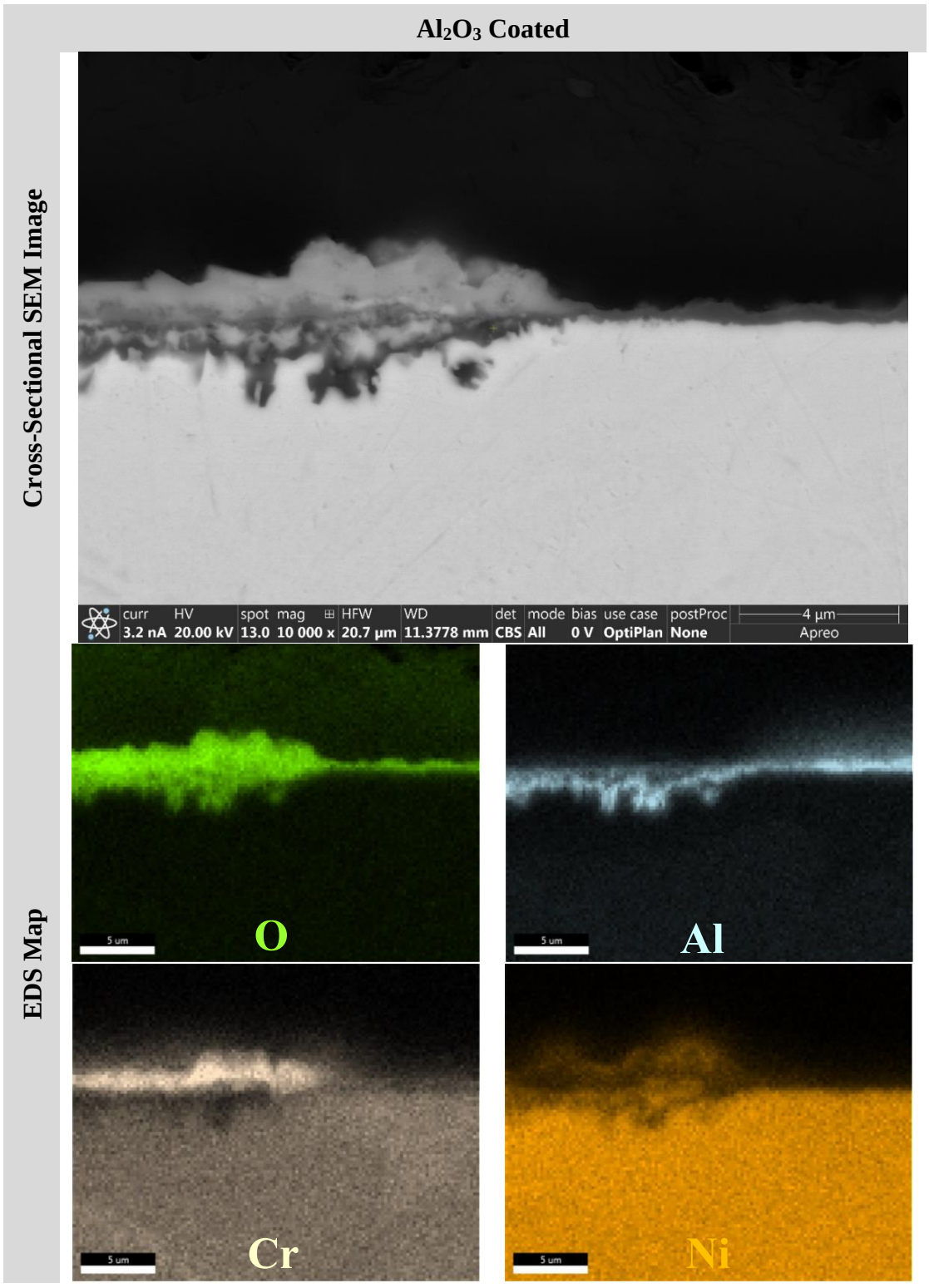

Figure 43: Cross-Sectional SEM Image and EDS Map of the Al_2O_3 Coated 1200-Grit HAYNES® 214® Coupon After 100-hrs of Isothermal Oxidation in Air at 800°C

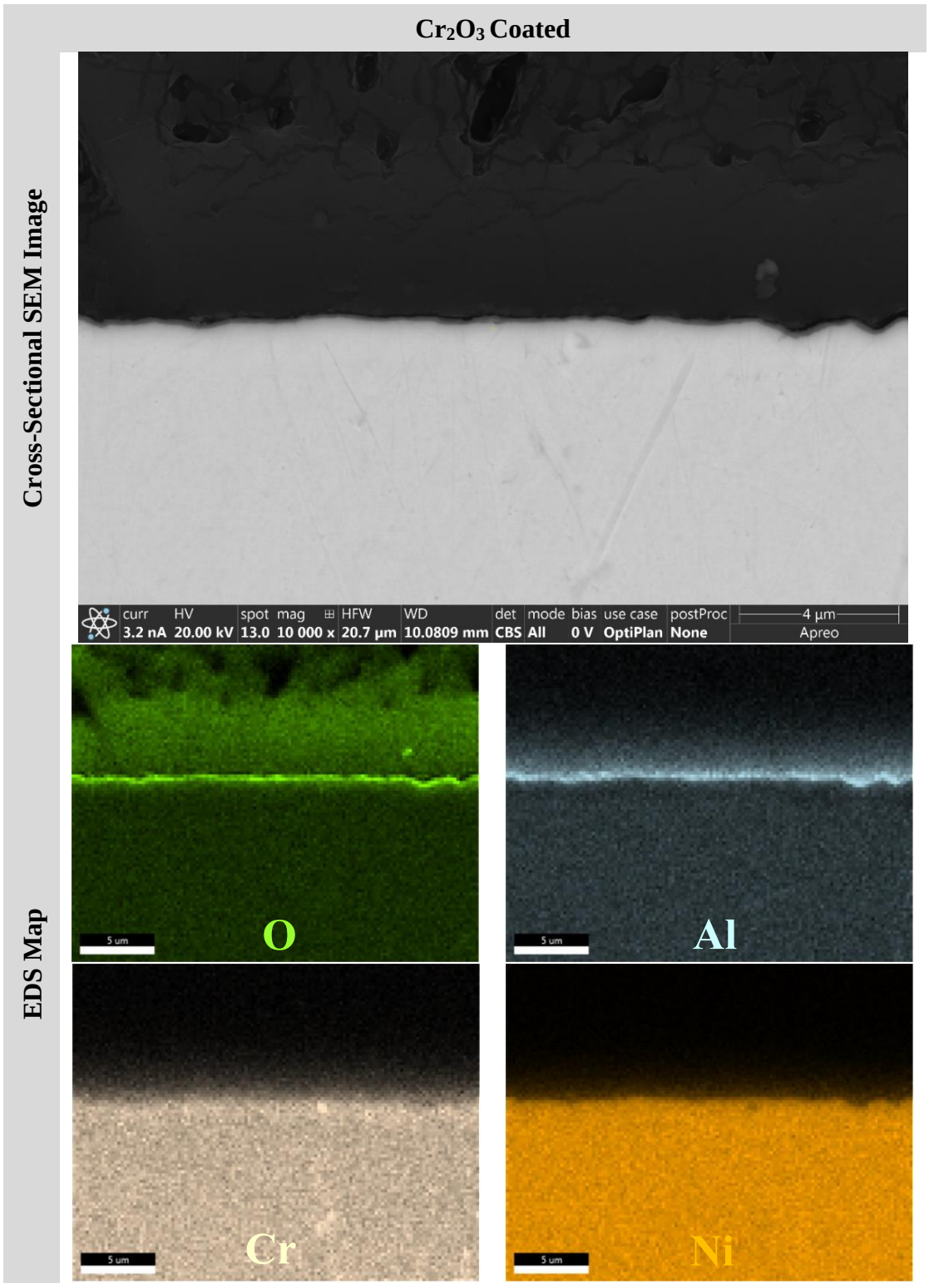

Figure 44: Cross-Sectional SEM Image and EDS Map of the Cr_2O_3 Coated 1200-Grit HAYNES® 214® Coupon After 100-hrs of Isothermal Oxidation in Air at 800°C

When increasing the oxidation duration to 100-hrs, the uncoated alloy shows the same type of oxidation growth as the 3-hr coupon, however the thicknesses of both oxidation regions have increased. In the areas where the external Al-rich oxide scale had formed after 3-hrs of oxidation, the scale had thickened to about 250 nm and still remained an Al-rich layer. This indicates that steady state, diffusion-controlled kinetics were obtained in these regions. In the areas where an outer Ni/Cr-rich oxide has formed on top of a region of internal Al_2O_3 precipitates, the outer layer has grown about an additional 1 μm in thickness (height) and the inner layer has begun penetrating further into the alloy subsurface (about 500 nm for the 3-hr coupon and about 1 μm for the 100-hr coupon).

The fact that the oxide growth for both coupon durations were identical means that the ability for an external Al-rich oxide scale to form upon the very initial high temperature exposure will dictate how the oxide growth occurs as the oxidation process continues. As was seen with the uncoated coupon, regions of the alloy surface that were initially capable of forming an external Al-rich oxide continued to form that same layer as the oxidation process carried on. Conversely, regions of the alloy surface that formed internal precipitates of Al_2O_3 beneath a Ni/Cr-rich oxide scale continued to form additional Ni/Cr-rich oxide on top of the internal precipitates which grew further into the subsurface region.

With respect to the Al_2O_3 coated alloy, a similar but not identical oxide growth has occurred between the 3-hr and 100-hr durations. After 3-hrs of oxidation, the coupon had showed regions of both a thicker and thinner external Al-rich scale and the areas where the thinner scale was present was accompanied by the formation of internal Al_2O_3 precipitates. When the oxidation duration increased to 100-hrs, the Al_2O_3 coated alloy now shows an outer layer comprising of a Ni/Cr-rich oxide on top of a semi-continuous layer of Al_2O_3 which has formed within the

subsurface region of the alloy (i.e., internal oxidation). Thus, between 3- and 100-hrs of oxidation, the Al_2O_3 coating that was still present on the surface of the alloy after 3-hrs was no longer there. Instead, these areas of the alloy surface were replaced with a Ni/Cr-rich oxide. Additionally, it appears that the regions where internal Al_2O_3 precipitates had formed after 3-hrs of oxidation had grown into a semi-continuous layer in the subsurface zone. As was the case for the uncoated alloy, the oxide scales that formed on the Al_2O_3 coated alloy upon initial high temperature exposure (i.e., short term for 3-hrs) appear to dictate the growth after longer term (i.e., 100-hrs). Areas that formed an external scale of Al-rich oxide continued to grow that scale as the coupon was further oxidized. However, regions that formed internal Al_2O_3 precipitates oxidized very differently. These regions appeared to grow into a semi-continuous layer and the Ni and Cr metal trapped above this area then oxidized into a Ni/Cr-rich oxide scale.

For the Cr_2O_3 coated alloy, the oxidation performance for the 3-hr and 100-hr coupons are identical where the entire surface had formed an external scale of an Al-rich oxide. The only difference between the two durations is the scale thickness which had increased from 100 nm after 3-hrs of oxidation to about 175 nm after 100-hrs of oxidation. Based on this, it is clear that steady-state, diffusion controlled kinetics for the formation of a protective Al-rich oxide scale were achieved for the Cr_2O_3 coated alloy. To more clearly show the external scale of the Al-rich oxide that has formed on the surface of the Cr_2O_3 coated alloy, higher magnification SEM images were taken. Figure 45 below shows the higher magnification SEM images for the Cr_2O_3 coated coupons that were isothermally oxidized in air for 3- and 100-hrs at 800°C.

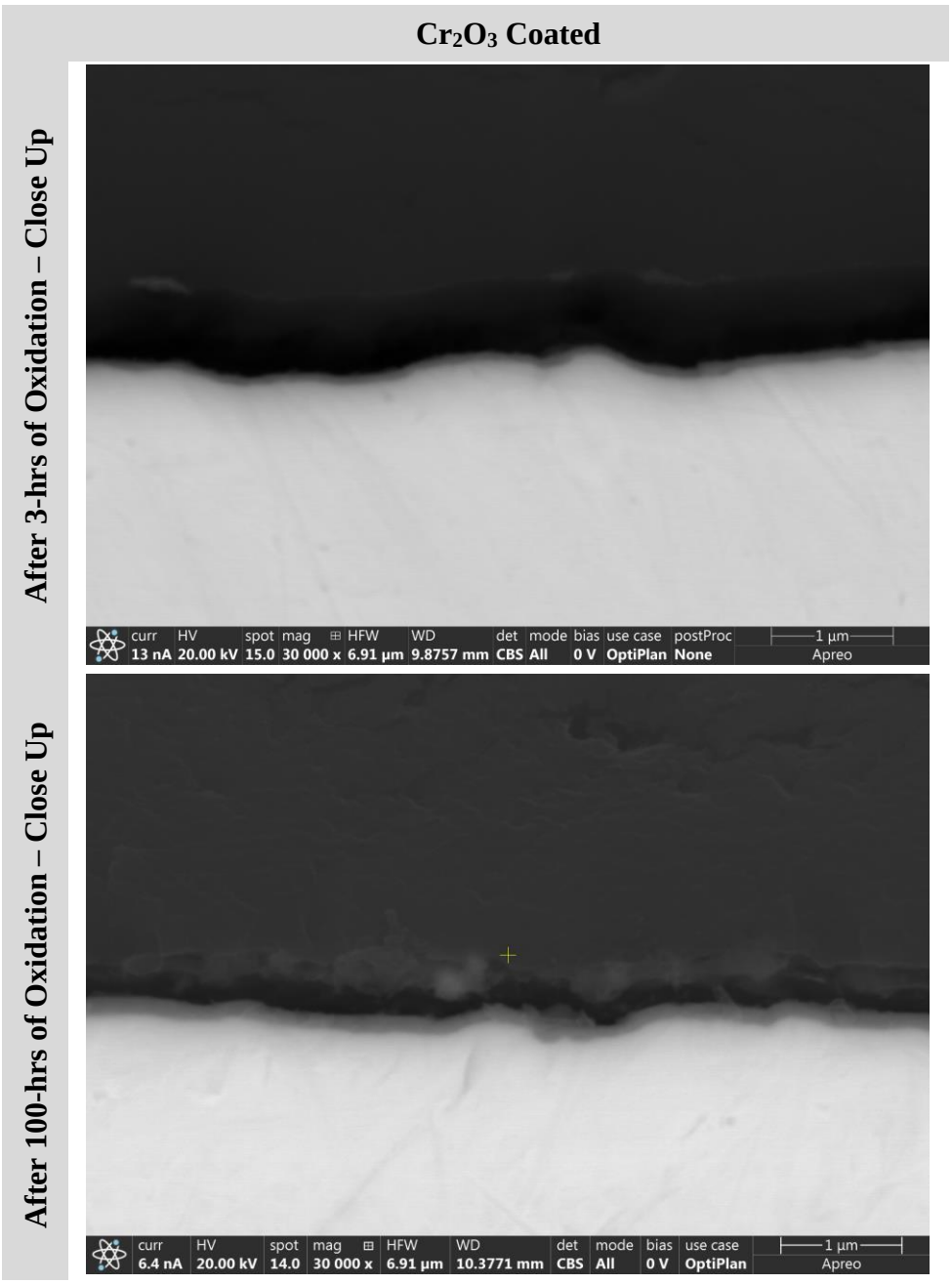

Figure 45: Increased Magnification Cross-Sectional SEM Images of the Cr_2O_3 Coated 1200-Grit HAYNES® 214® Coupons After 3- and 100-hrs of Isothermal Oxidation in Air at 800°C

One primary question that arises from the SEM and EDS analysis of the Cr_2O_3 coated alloy that only shows the presence of an external Al-rich oxide scale is where the Cr_2O_3 PLD coating that was applied on the surface prior to oxidation went. Thus, to get a better understanding of the composition of the external scale, the cross section of the Cr_2O_3 coated coupon that had been isothermally oxidized in air for 100-hrs at 800°C was examined using TEM, as shown in Figure 46. Accompanying the cross-sectional image is an EDS map showing the compositions of the oxidation products on the alloy surface.

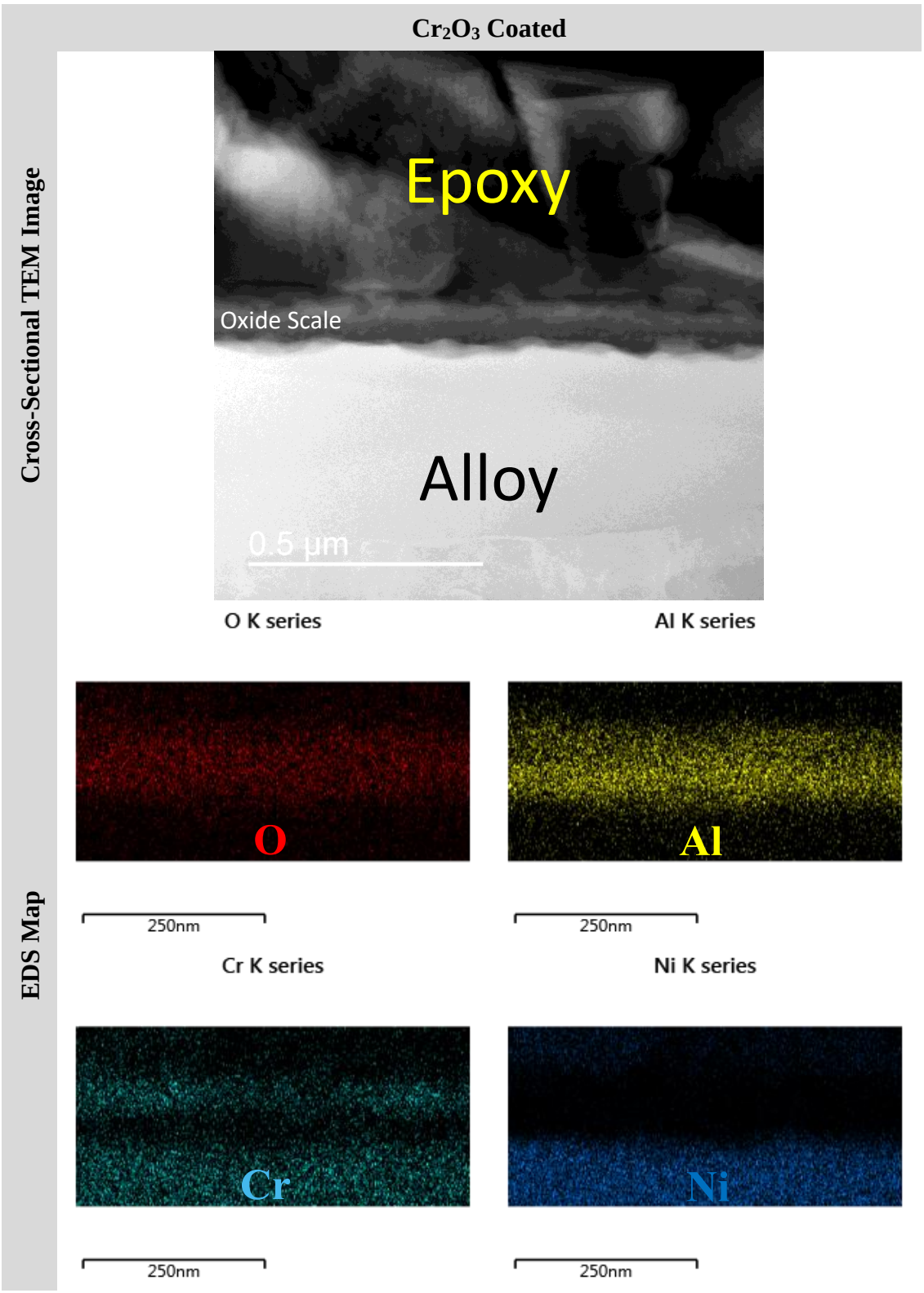

Figure 46: Cross-Sectional TEM Image and EDS Map of the Cr_2O_3 Coated 1200-Grit HAYNES® 214® Coupon After 100-hrs of Isothermal Oxidation in Air at 800°C

Using TEM, a higher magnification image and better resolution EDS map were able to be obtained and these provided a better understanding of the external oxide scale on the Cr_2O_3 coated alloy. While SEM and EDS showed the external scale to be Al-rich, TEM confirms this but shows two distinct oxide regions. The outer layer is a mixture of an Al/Cr oxide about 50 nm in thickness whereas the inner layer is solely Al_2O_3 about 60 nm in thickness. Thus, it can be inferred that the outer Al/Cr oxide layer was created due to some solubility between the Cr_2O_3 PLD coating that was applied on the surface and the formation of thermally grown Al_2O_3 below the PLD coating. It is important to note that the crystal structures of α-Cr_2O_3 and α-Al_2O_3 are the same (part of the hexagonal crystal structure family) which means that the interface between these oxides can be coherent and aid in allowing some solubility.

Since the EDS map shows what the oxide scales and products are compositionally, to confirm the structure of these oxides, powder XRD and glancing angle XRD were utilized. Glancing angle XRD is sensitive to thin surface layers, coatings, and films, thus this technique would be able to clearly identify the structure of the oxide scales that were determined via SEM/TEM and EDS. Figure 47 below shows the glancing angle XRD spectra for the uncoated, Al_2O_3 coated, and Cr_2O_3 coated alloy after 100-hrs of isothermal oxidation in air at 800°C. Conversely, Figure 84, Figure 85, and Figure 86 in Appendix B shows the powder XRD spectra for the uncoated, Al_2O_3 coated, and Cr_2O_3 coated alloy before, after 3-hrs, and after 100-hrs of isothermal oxidation in air at 800°C.

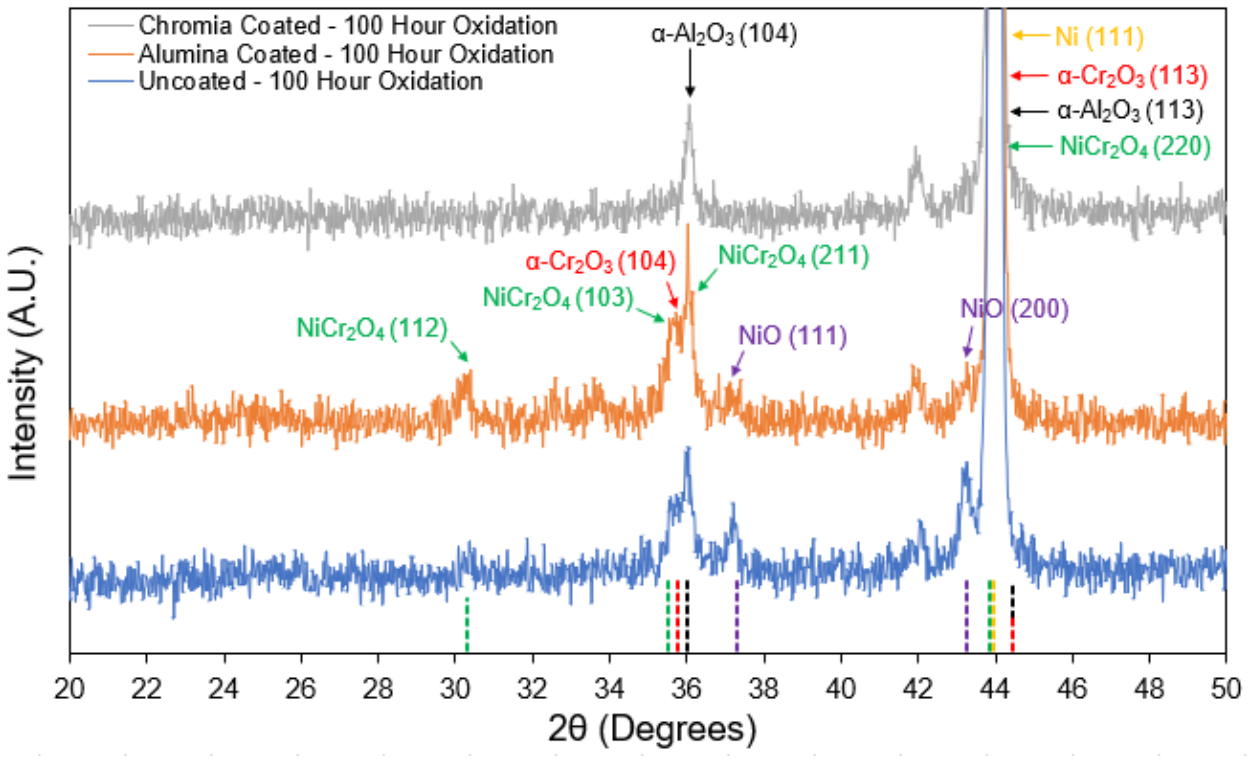

Figure 47: Glancing Angle XRD Spectra for the Uncoated, Al_2O_3 Coated, and Cr_2O_3 Coated 1200-Grit HAYNES® 214® Coupons After 100-hrs of Isothermal Oxidation in Air at 800°C

Since glancing angle XRD is a surface sensitive technique, the diffraction peaks generated are representative of the oxide scales and layers on the surfaces of the alloy coupons. As seen above, the glancing angle XRD spectra of the uncoated and Al_2O_3 coated alloy show the presence of NiO, α-Cr_2O_3, α-Al_2O_3, and the more complex $NiCr_2O_4$ spinel structure. Additionally, the intense primary peak for the γ alloy phase (FCC Ni) can be detected. The XRD spectra confirms the results found from the cross-sectional SEM and EDS analysis where the uncoated and Al_2O_3 coated coupons were found to contain two distinct and different oxidation regions; areas where a

thinner external scale of an Al-rich oxide had grown and areas where a thicker scale containing an outer layer of a Ni/Cr-rich oxide on top of internal precipitates of Al_2O_3 had formed. Combining the SEM and EDS results with the obtained XRD spectra, it can be deduced that the areas of the surface where the thin external Al-rich oxide scale has formed is α-Al_2O_3, and the areas where a thicker scale containing an outer layer of a Ni/Cr-rich oxide is a mixture of NiO, α-Cr_2O_3, and $NiCr_2O_4$.

For the Cr_2O_3 coated alloy, the glancing angle XRD spectra only shows the presence of α-Al_2O_3 in addition to the intense primary peak for the γ alloy phase (FCC Ni). No peaks belonging to NiO, α-Cr_2O_3, or $NiCr_2O_4$ were detected. The XRD spectra confirms the results found from the cross-sectional SEM/TEM and EDS analysis where the Cr_2O_3 coated alloy was only found to contain a thin external scale of Al-rich oxide. Thus, combining the SEM/TEM and EDS results with the obtained XRD spectra, it can be deduced that the surface which has formed an external Al-rich oxide scale is α-Al_2O_3.

Additionally, the XRD spectra shows a peak for all three coupons at a 2θ angle of about 42°. This peak does not belong to any oxides of Ni, Cr, or Al. Table 5 below summarizes the obtained XRD spectra compared to the reference data gathered via Joint Committee on Powder Diffraction Standards (JCPDS).

Table 5: Summary of Obtained Glancing Angle XRD Spectra Compared to Reference XRD Spectra for the Uncoated, Al_2O_3 Coated, and Cr_2O_3 Coated 1200-Grit HAYNES® 214® Coupons After 100-hrs of Isothermal Oxidation in Air at 800°C

$NiCr_2O_4$				
Obtained Spectra		JCPDS Card [00-023-0432]		
Plane (hkl)	Peak Location (2θ)	Plane (hkl)	Peak Location (2θ)	Intensity
(112)	30.33°	(112)	30.326°	70
(103)	35.65°	(103)	35.496°	90
(211)	36.13°	(211)	36.011°	100
(220)	43.76°	(220)	43.872°	70
NiO				
Obtained Spectra		JCPDS Card [00-002-1216]		
Plane (hkl)	Peak Location (2θ)	Plane (hkl)	Peak Location (2θ)	Intensity
(111)	37.20°	(111)	37.281°	70
(200)	43.32°	(200)	43.254°	100
α-Al_2O_3				
Obtained Spectra		JCPDS Card [01-070-3319]		
Plane (hkl)	Peak Location (2θ)	Plane (hkl)	Peak Location (2θ)	Intensity
(104)	36.05°	(104)	36.019°	100
(113)	44.34°	(113)	44.436°	95.5
α-Cr_2O_3				
Obtained Spectra		JCPDS Card [01-082-3804]		
Plane (hkl)	Peak Location (2θ)	Plane (hkl)	Peak Location (2θ)	Intensity
(104)	35.83°	(104)	35.738°	100
(113)	44.32°	(113)	44.432°	27
γ Phase (Ni)				
Obtained Spectra		JCPDS Card [01-077-3085]		
Plane (hkl)	Peak Location (2θ)	Plane (hkl)	Peak Location (2θ)	Intensity
(111)	44.18°	(111)	43.937°	100

In addition to glancing angle XRD, Raman spectroscopy [25] and PL spectroscopy [25] were performed on the oxidized alloy coupons to aid in characterizing the structure and composition of the surface oxide layers. In addition to collecting the individual Raman and PL spectra, Raman mapping was also performed where a region of the alloy surface was examined and intensity maps were generated for specific Raman shift values. Figure 48, Figure 49, and Figure 50 show the OM images taken, the reduced area where the Raman mapping was performed, and the intensity maps for a specific Raman shift. Figure 51 then plots the Raman spectra for specific points based on areas of interest (i.e., different oxide growth regions) from the OM image and Raman intensity maps.

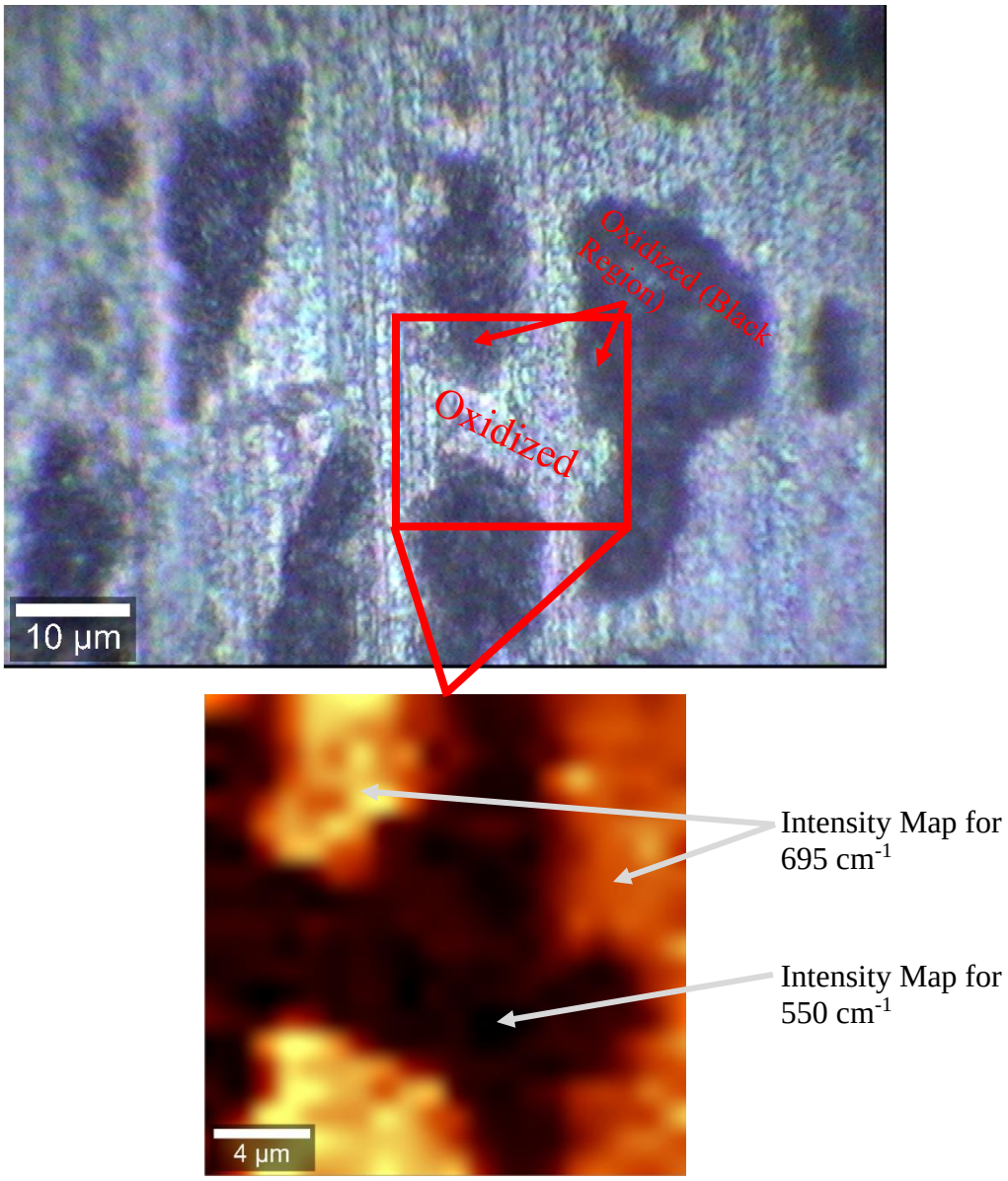

Figure 48: OM Image, Reduced Area for Raman Mapping, and Raman Intensity Map for the Uncoated 1200-Grit HAYNES® 214® Coupon After 100-hrs of Isothermal Oxidation in Air at 800°C

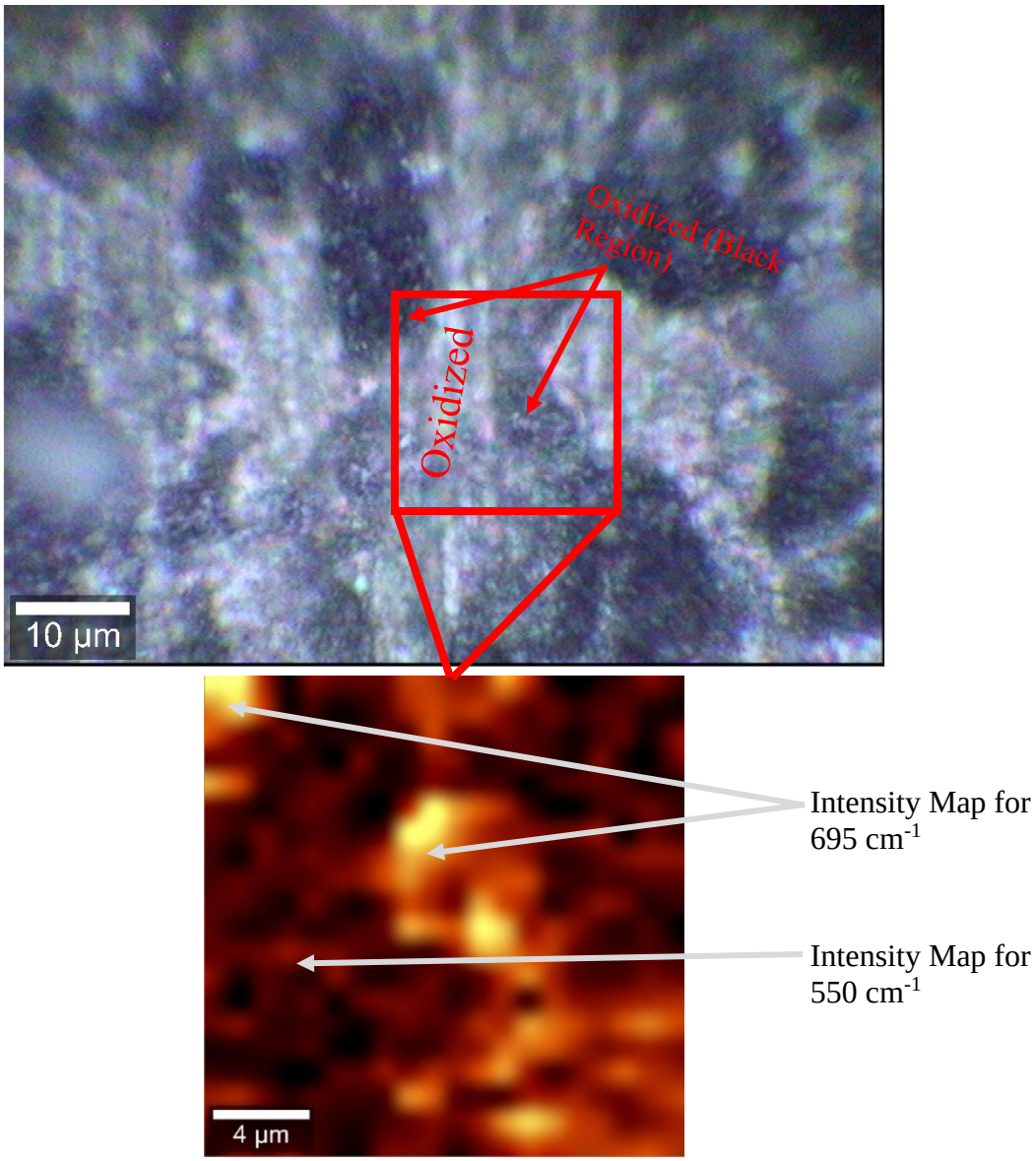

Figure 49: OM Image, Reduced Area for Raman Mapping, and Raman Intensity Map for the Al_2O_3 Coated 1200-Grit HAYNES® 214® Coupon After 100-hrs of Isothermal Oxidation in Air at 800°C

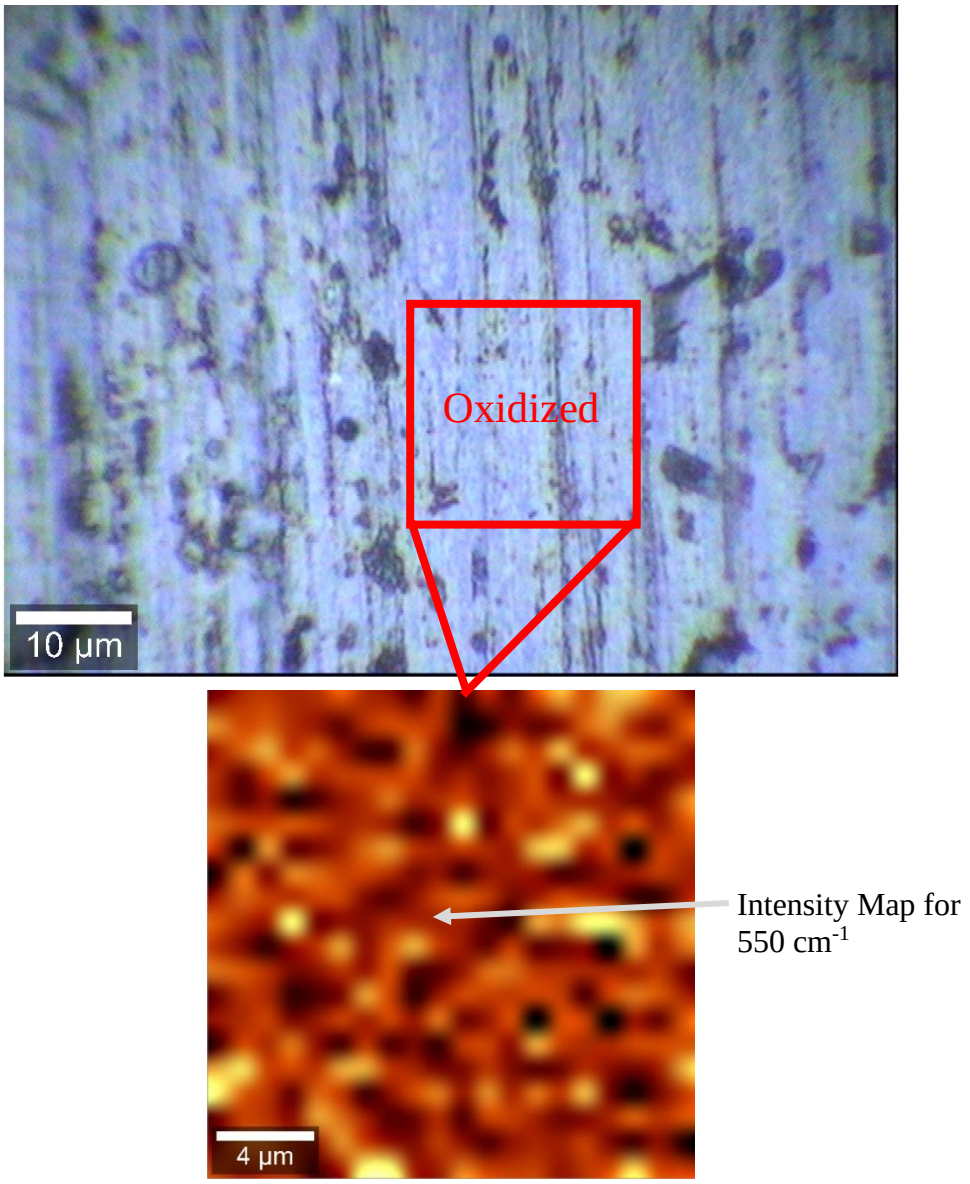

Figure 50: OM Image, Reduced Area for Raman Mapping, and Raman Intensity Map for the Cr_2O_3 Coated 1200-Grit HAYNES® 214® Coupon After 100-hrs of Isothermal Oxidation in Air at 800°C

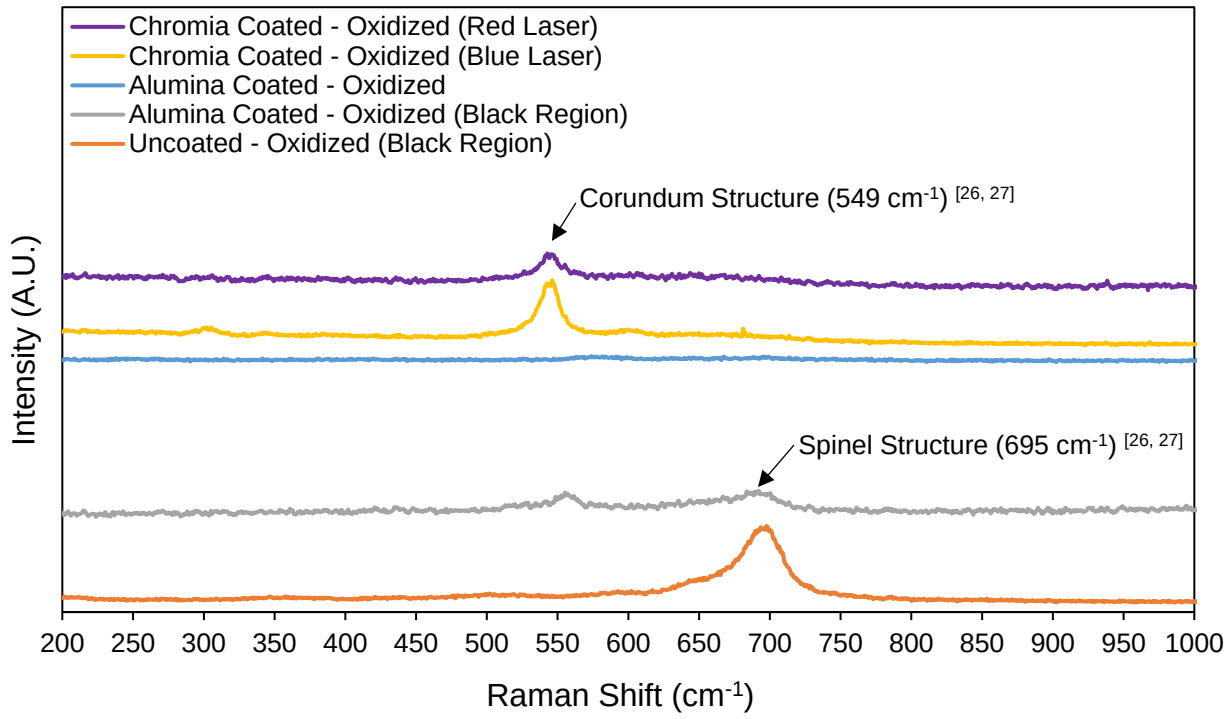

Figure 51: Raman Spectra of the Uncoated, Al_2O_3 Coated, and Cr_2O_3 Coated 1200-Grit HAYNES® 214® Coupons After 100-hrs of Isothermal Oxidation in Air at 800°C

The Raman spectra plotted above matches the results found from the glancing angle XRD spectra. In the spectra that were collected from the black oxidized regions of the uncoated and Al_2O_3 coated alloy surfaces, the Raman spectra show a peak belonging to the spinel structure at a Raman shift of about 695 cm^{-1} [26, 27]. The previous OM, SEM, and EDS data showed that the black regions on the surface of the uncoated and Al_2O_3 coated alloy corresponded to areas where an external Ni/Cr-rich oxide growth had formed. XRD measurements deduced that these regions contained a mixture of NiO, α-Cr_2O_3, and $NiCr_2O_4$ (which takes the form of a spinel structure). Thus, when the Raman spectra was collected in this same black oxidized region, confirmation with respect to the presence of a spinel structure is obtained.

For the Cr_2O_3 coated coupon, since no black oxidized regions were observed, a peak for the spinel structure is not seen. However, the Raman spectra does show a peak belonging to the corundum structure at a Raman shift of 550 cm^{-1} [26, 27]. In the Raman spectra, there are two spectrums for the Cr_2O_3 coated coupon, one where an incident red laser was used and one where an incident blue laser was used. Even though these colors have different wavelengths and energies associated with them, both spectrums still show the corundum structure at a Raman shift of 550 cm^{-1}. The previous OM, SEM, and EDS data showed that the colored, flat, and conformal regions on the surface of the Cr_2O_3 coated alloy corresponded to areas where an external Al-rich oxide layer had formed. XRD measurements deduced that this layer was α-Al_2O_3 which has the corundum structure. Thus, when the Raman spectra was collected in this same colored, flat, and conformal region, confirmation with respect to the presence of a corundum structure is obtained.

In addition to Raman spectra, PL spectra were obtained for the same regions on the uncoated, Al_2O_3 coated, and Cr_2O_3 coated alloy surfaces, as seen in Figure 52. PL is a useful characterization technique for oxides because colors can be emitted from oxides that are doped with very small amounts of impurity cations. This is especially true for Al_2O_3 where small amounts of Cr can create a ruby (red) color or small amounts of Fe, Ti, Cr, vanadium (V), or magnesium (Mg) can result in a sapphire (blue) color. Thus, this technique provides an additional method to determine the presence of α-Al_2O_3 on the surface of the oxidized alloy coupons.

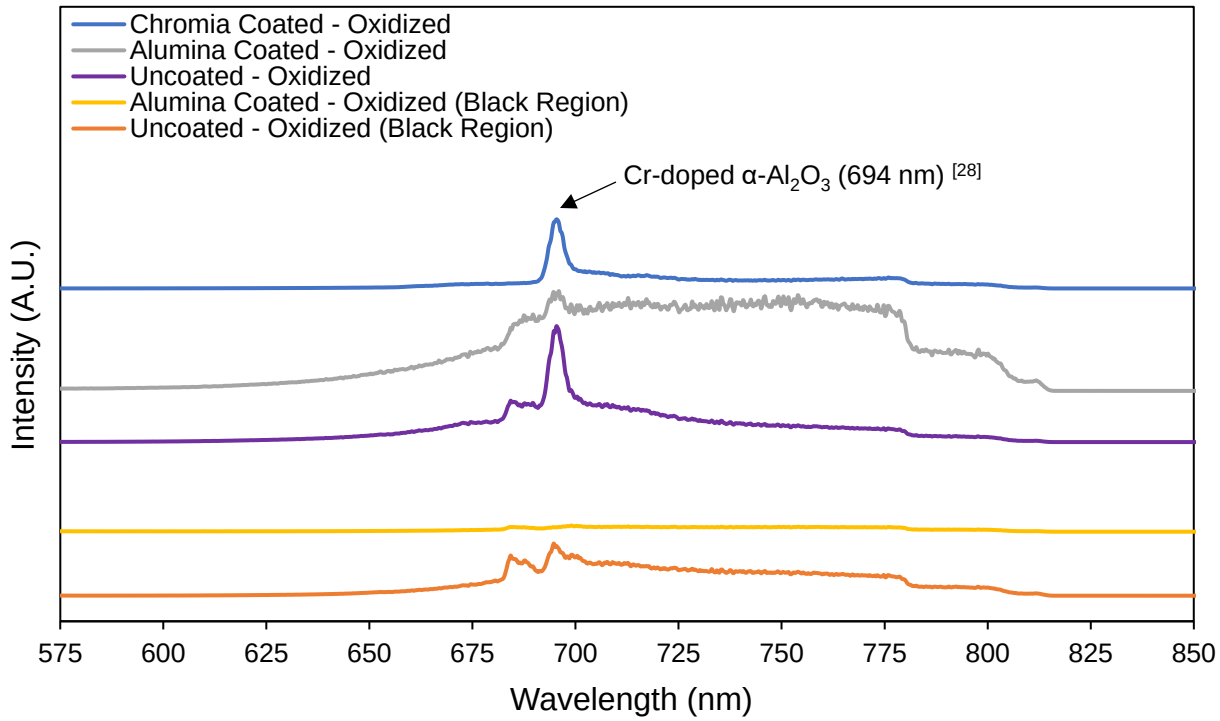

Figure 52: PL Spectra of the Uncoated, Al_2O_3 Coated, and Cr_2O_3 Coated 1200-Grit HAYNES® 214® Coupons After 100-hrs of Isothermal Oxidation in Air at 800°C

As the PL spectra shows, a peak belonging to the wavelength of 694 nm is detected for all of the locations where the PL spectra was collected with the exception of the "black region" on the Al_2O_3 coated all. The significance of the 694 nm peak is that it belongs to the ruby color [28] where ruby is a mineral of α-Al_2O_3 that has the corundum structure. Within the corundum lattice, Cr ions can replace the Al ions to create a very dilute Cr-doped α-Al_2O_3 structure. The effect of doping is that when light illuminates the Cr-doped α-Al_2O_3, it is absorbed where after a very brief moment of time, a photon containing an energy that is equivalent to the wavelength of the ruby color is emitted. The presence of the peak belonging to the ruby color in all of the PL spectra

provides further confirmation of the formation of α-Al_2O_3 on the oxidized surfaces of the uncoated, Al_2O_3 coated, and Cr_2O_3 coated coupons.

In addition to surface characterization, to understand whether the surfaces of the alloy coupons containing different oxide growths resulted in different electrochemical corrosion resistances, potentiodynamic polarization tests were run. These tests generate Tafel curves for the anodic and cathodic reactions of each alloy coupon to determine the corrosion current (I_{corr}) and corrosion potential (E_{corr}). Figure 53 below shows the potentiodynamic polarization plots for the uncoated, Al_2O_3 coated, and Cr_2O_3 coated coupons before oxidation.

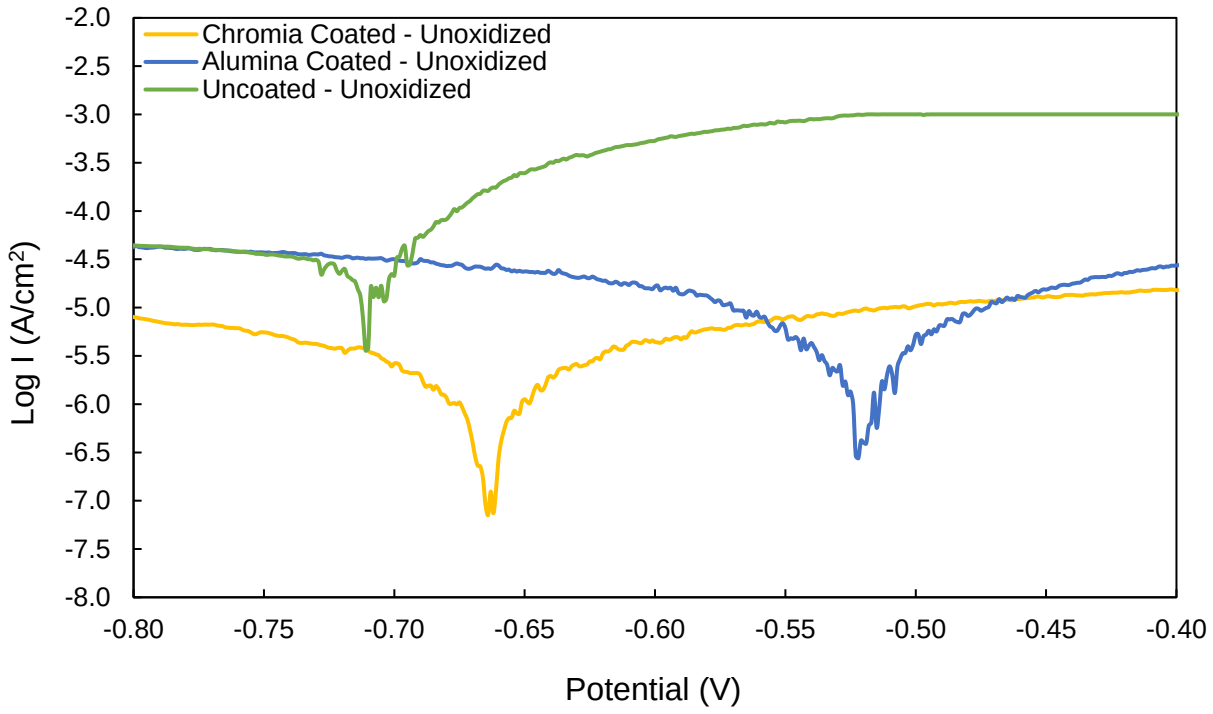

Figure 53: Potentiodynamic Polarization Plots of the Uncoated, Al_2O_3 Coated, and Cr_2O_3 Coated 1200-Grit HAYNES® 214® Coupons Before Oxidation

Based on the Tafel plots, I_{corr} for the three coupons were different which is evident based on where curves switch from the anodic region to the cathodic region (where the dip in current occurs). To determine I_{corr}, linear lines are drawn in the regions immediately before and after the dip in the current (forms a "V" shape). Then, the x- and y-values of the point at which the linear lines intersect are deemed E_{corr} and I_{corr}. Once I_{corr} is known, the polarization resistance (R_p) of the alloy surfaces can be determined using Equation (5-1) [29]

$$R_P = \left(\frac{1}{2.3}\right)\left(\frac{b_a b_c}{b_a + b_c}\right)\left(\frac{1}{I_{corr}}\right) \tag{5-1}$$

where R_p is the polarization resistance, b_a is the linear slope of the anodic reaction, b_c is the linear slop of the cathodic reaction, and I_{corr} is the corrosion current which was determined using the technique described above. Using R_p, the protection efficiency (P_{EF}) can then be calculated by using Equation (5-2) [30]

$$P_{EF} = \frac{{R_{P_{Uncoated}}}^{-1} - {R_{P_{Coated}}}^{-1}}{{R_{P_{Uncoated}}}^{-1}} \tag{5-2}$$

where P_{EF} is the protection efficiency, $R_{P_{Uncoated}}{}^{-1}$ is the inverse of the polarization resistance for the uncoated alloy coupon, and $R_{P_{Coated}}{}^{-1}$ is the inverse of the polarization for the coated alloy coupon (either Al_2O_3 or Cr_2O_3 coated). The P_{EF} determines how well the coated alloy surface resists polarization, or corrosion, compared to the uncoated alloy surface. Table 6 below lists the E_{corr} and I_{corr} determined from the Tafel curves in Figure 53, in addition to the calculated R_P and P_{EF} for the uncoated, Al_2O_3 coated, and Cr_2O_3 coated alloys before oxidation.

Table 6: E_{corr}, I_{corr}, R_P, and P_{EF} of the Uncoated, Al_2O_3 Coated, and Cr_2O_3 Coated 1200-Grit HAYNES® 214® Coupons Before Oxidation

	E_{Corr} (V)	I_{Corr} (μA/cm^2)	R_P (kΩ)	P_{EF} (%)
Uncoated	-0.7068	17.806	321.64	N/A
Al_2O_3 Coated	-0.5177	2.349	10535	96.94
Cr_2O_3 Coated	-0.6619	0.595	65227	99.50

According to the P_{EF}, the Al_2O_3 and Cr_2O_3 coated coupons provide significantly more protection against electrochemical corrosion which is expected given an oxide coating has been deposited on the surfaces of the alloy. Since the P_{EF} of the Al_2O_3 and Cr_2O_3 coated coupons are very close to each other (97% and 99.5%), a distinction between whether the Al_2O_3 or Cr_2O_3 coating provided better protection cannot be made.

With the characterization of the oxide growth on the uncoated and Al_2O_3 coated coupons differing from the Cr_2O_3 coated coupon, it was thought that the oxidized alloy surfaces may show different electrochemical corrosion results. The reason that this was thought is because the Ni/Cr-

rich oxide layer that was present on regions of the uncoated and Al_2O_3 coated coupon surfaces is less protective from an oxidation standpoint, these regions may also be less protective with respect to electrochemical corrosion and thus result in very different Tafel curves. Therefore, additional potentiodynamic polarization tests were run for the uncoated, Al_2O_3 coated, and Cr_2O_3 coated coupons that had been oxidized for 3- and 100-hrs. The resulting Tafel curves are shown in Figure 54 and Figure 55.

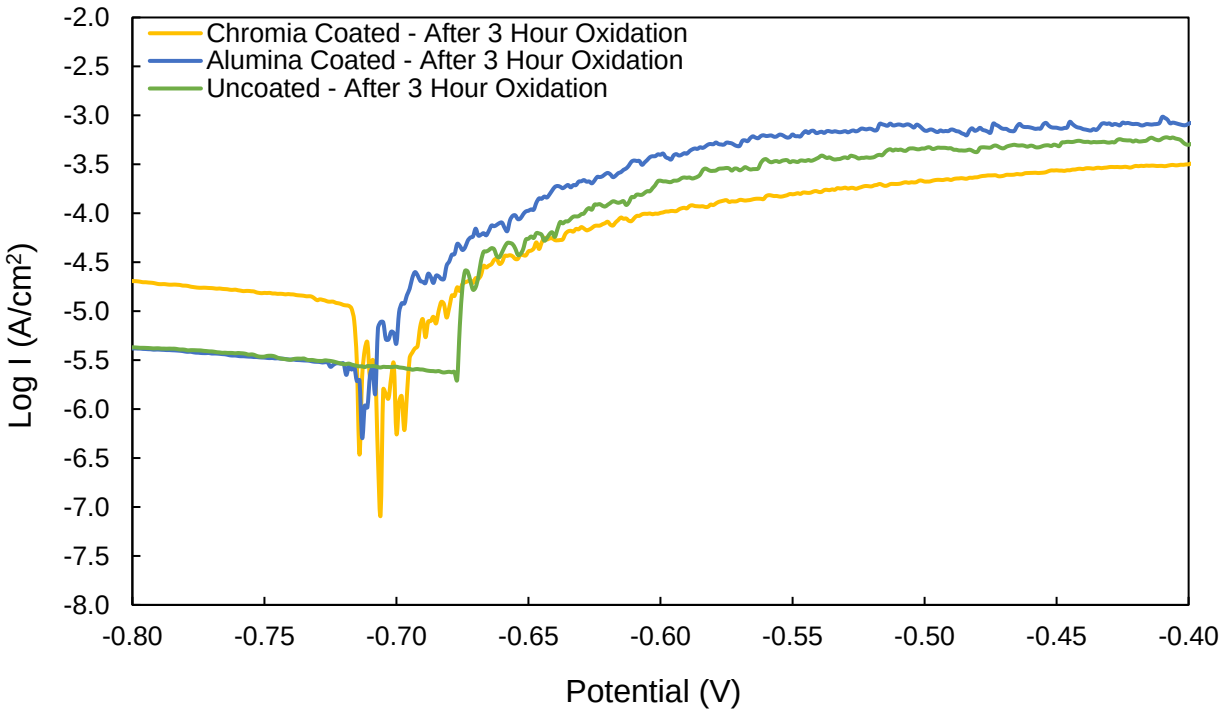

Figure 54: Potentiodynamic Polarization Plots of the Uncoated, Al_2O_3 Coated, and Cr_2O_3 Coated 1200-Grit HAYNES® 214® Coupons After 3-hrs of Isothermal Oxidation in Air at 800°C

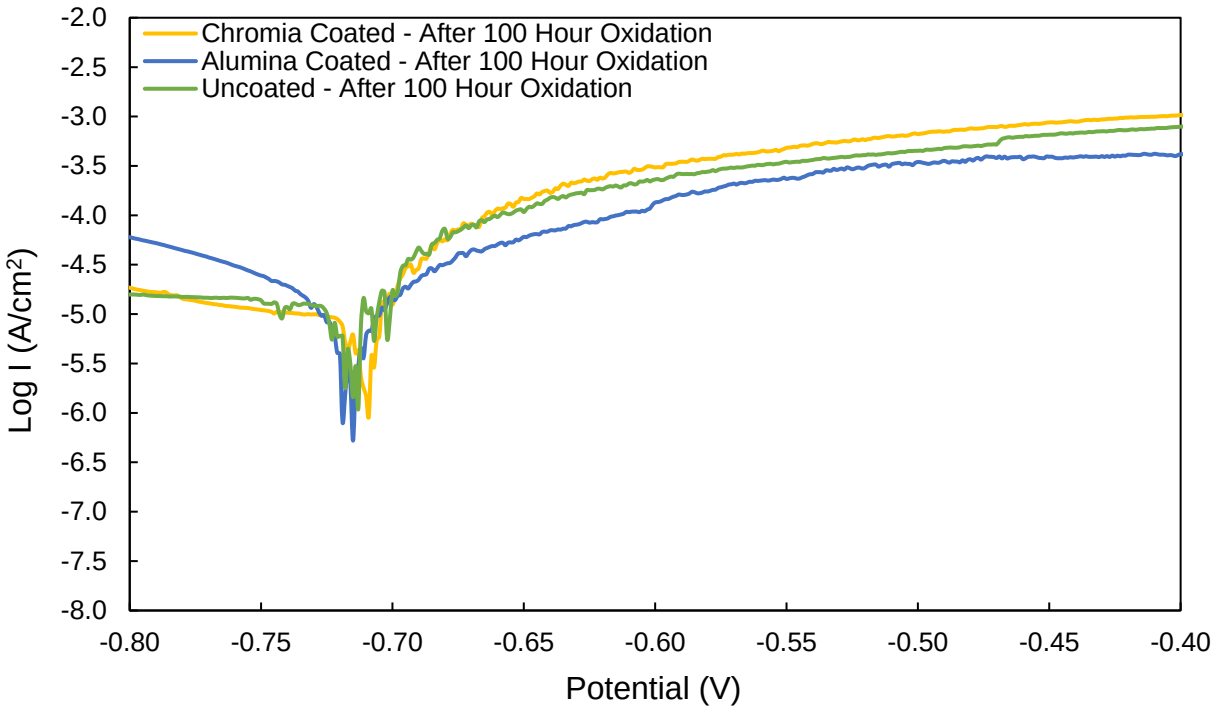

Figure 55: Potentiodynamic Polarization Plots of the Uncoated, Al_2O_3 Coated, and Cr_2O_3 Coated 1200-Grit HAYNES® 214® Coupons After 100-hrs of Isothermal Oxidation in Air at 800°C

All three coupons that were oxidized for 3- and 100-hrs roughly show the same Tafel curves for the anodic and cathodic regions of the corrosion reaction. Because the dip in current occurs in about the same location for all three coupons at both 3- and 100-hours, this means that I_{corr} would be about the same for all of the coupons. If I_{corr} is the same, then according to Equations (19) and (20), there would be no P_{EF} gains. As a result, the R_P and P_{EF} values were not calculated for the alloy coupons oxidized for 3- and 100-hrs. The key result for these tests is that even though the regions of the uncoated and Al_2O_3 coated surfaces contain a less oxidation resistant Ni/Cr-rich

oxide layer, these areas are still effective in preventing electrochemical corrosion thus resulting in the same surface protection.

5.1.1.1 Analysis of the Role of the Al_2O_3 and Cr_2O_3 PLD Coatings

According the results presented above, it is clear that the PLD have a direct impact on the oxidation mechanism of the HAYNES® 214® alloy. The role of the PLD coatings can be understood by referring back to Wagner's theory on the transition from internal to external oxidation, as was discussed in Section 2.1.2.3. Equation (2-15) described the relationship between the critical mole fraction of the most reactive metal (i.e., Al) needed to cause the transition between internal and external oxidation. This relationship was a function of several important factors including the oxygen solubility at the alloy-PLD coating interface ($N_O^{S/I}$), the diffusivity of oxygen (D_O), and the diffusivity of Al from within the bulk alloy (D_B). Since the oxygen solubility follows Sievert's law (Equation (2-13)), this means there is a relationship between the critical mole fraction of Al needed to cause the transition between internal and external oxidation and the oxygen partial pressure. An example plot of how the oxygen partial pressure affects the critical mole fraction is shown in Figure 56 below. In this plot, the regions where the alloy would be expected to experience internal and external oxidation are shown, and the areas where the transition between internal and external oxidation starts and completes is outlined.

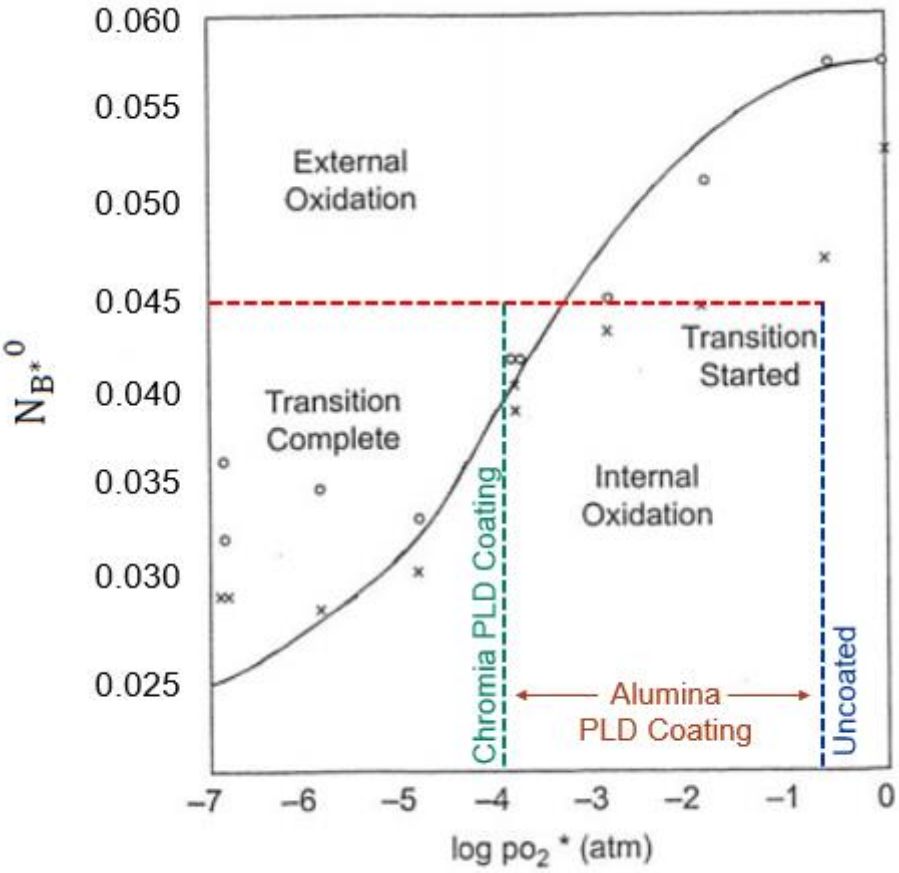

Figure 56: Schematic for the Role of the Al_2O_3 and Cr_2O_3 PLD Coatings with Respect to the 1200-Grit HAYNES® 214® Coupons After Isothermal Oxidation in Air at 800°C

The figure shown above is not specifically for the HAYNES® 214® alloy but the shape of the curve is the same. The Al composition (4.5 wt%) is outlined here with a red dashed line drawn horizontally across the entire range of oxygen partial pressures. Under atmospheric oxygen pressure (0.21 atm, as outlined in the blue dashed line) at 800°C, the uncoated alloy would fall within the internal oxidation region but the transition between internal and external oxidation would have started. This would explain why the oxidation results of the uncoated alloy showed

regions where an external α-Al_2O_3 scale had formed and other regions where Al_2O_3 had precipitated internally.

Since the Cr_2O_3 coated alloy showed no internal oxidation and only showed the formation of an external α-Al_2O_3 scale, it is hypothesized that the Cr_2O_3 PLD coating that was applied on the surface of the alloy effectively reduced the oxygen partial pressure at the alloy-PLD coating interface such that the Al content in the HAYNES® 214® alloy (4.5 wt%) is more than the critical mole fraction required for the alloy to complete the transition between internal and external oxidation. This interpretation can be seen on Figure 56 by the use of the green dashed line which intersects the x-axis at a much lower oxygen partial pressure than the uncoated alloy which was exposed to atmospheric oxygen pressure (0.21 atm). When the green dashed line, which represents the reduced oxygen partial pressure, intersects the line representing the amount of Al in the alloy, the intersection lies in the region of the curve where exclusive external oxidation occurs and the transition from internal to external oxidation is complete.

For the Al_2O_3 coated alloy, which showed intermediate but comparable results to the uncoated alloy, it is probable that the Al_2O_3 PLD coating falls somewhere in between the uncoated alloy and the Cr_2O_3 PLD coating. If the Al_2O_3 coated alloy is in between, the oxygen partial pressure at the alloy surface would not be as reduced as the Cr_2O_3 PLD coating. Thus, the intersection with the line representing the amount of Al in the alloy would still lie in the region where the alloy undergoes internal oxidation but the transition between internal and external oxidation has started. This would explain the oxidation results of the Al_2O_3 coated alloy because there were regions where an external α-Al_2O_3 scale had formed and other regions where Al_2O_3 had precipitated internally.

To determine what the oxygen partial pressure was at the interface between the alloy and Cr_2O_3 PLD coating (i.e., the boundary condition), the parabolic rate law (Equation (2-10)) can be used and adjusted for scale thickness instead of weight gain, as shown in Equation (5-3)

$$X^2 = k_p t \tag{5-3}$$

where k_p and t have been defined previously, and X is the scale thickness. Since the α-Al_2O_3 scale thickness that was formed on the uncoated and Cr_2O_3 coated alloys after the same time duration (i.e., 100-hrs) is known, and because k_p has a $\frac{3}{16}$ dependence on the oxygen partial pressure, a ratio can be created to determine what the oxygen partial pressure was at the interface between the alloy and Cr_2O_3 PLD coating. This ratio can be seen in Equation (5-4) below

$$\left(\frac{X_{Al2O3}{}^{Cr2O3\ Coated}}{X_{Al2O3}{}^{Uncoated}}\right)^2 = \left(\frac{P_{O2}{}^{alloy-Cr2O3\ coating}}{P_{O2}{}^{alloy}}\right)^{\frac{3}{16}} \tag{5-4}$$

where $X_{Al2O3}{}^{Cr2O3\ Coated}$ is the α-Al_2O_3 scale thickness on the Cr_2O_3 coated alloy, $X_{Al2O3}{}^{Uncoated}$ is the α-Al_2O_3 scale thickness on the uncoated alloy, $P_{O2}{}^{alloy-Cr2O3\ coating}$ is the oxygen partial

pressure at the alloy-Cr_2O_3 PLD coating interface, and $P_{O2}{}^{alloy}$ is the oxygen partial pressure at the uncoated alloy surface.

In this ratio, the only unknown is the oxygen partial pressure at the alloy-Cr_2O_3 PLD coating interface, thus Equation (5-5) solves for this unknown.

$$\left(\frac{110\text{ nm}}{275\text{ nm}}\right)^2 = \left(\frac{P_{O2}{}^{\text{alloy}-\text{Cr2O3 coating}}}{0.21\text{ atm}}\right)^{\frac{3}{16}} \quad (5\text{-}5)$$

Thus, it is found that oxygen partial pressure at the alloy-Cr_2O_3 PLD coating interface is equal to 1.2 x 10^{-5} atm. Therefore, when compared to the uncoated alloy that was exposed to atmospheric oxygen pressure (0.21 atm), the Cr_2O_3 PLD coating reduces the oxygen partial pressure by about 4 orders of magnitude.

5.1.2 Vapor Honed Surface Condition

As Section 5.1.1 above presents the results for the 1200-grit abraded alloy coupons, coupons prepared with a vapor honed surface condition were also isothermally oxidized in air at 800°C to determine whether the oxidation performance and mechanism would be the same or different. First, the macroscopic oxidation performance was examined using OM and the surface images of the uncoated, Al_2O_3 coated, and Cr_2O_3 coated coupons before and after 100-hrs of isothermal oxidation in air at 800°C are shown in Figure 57 and Figure 58 below.

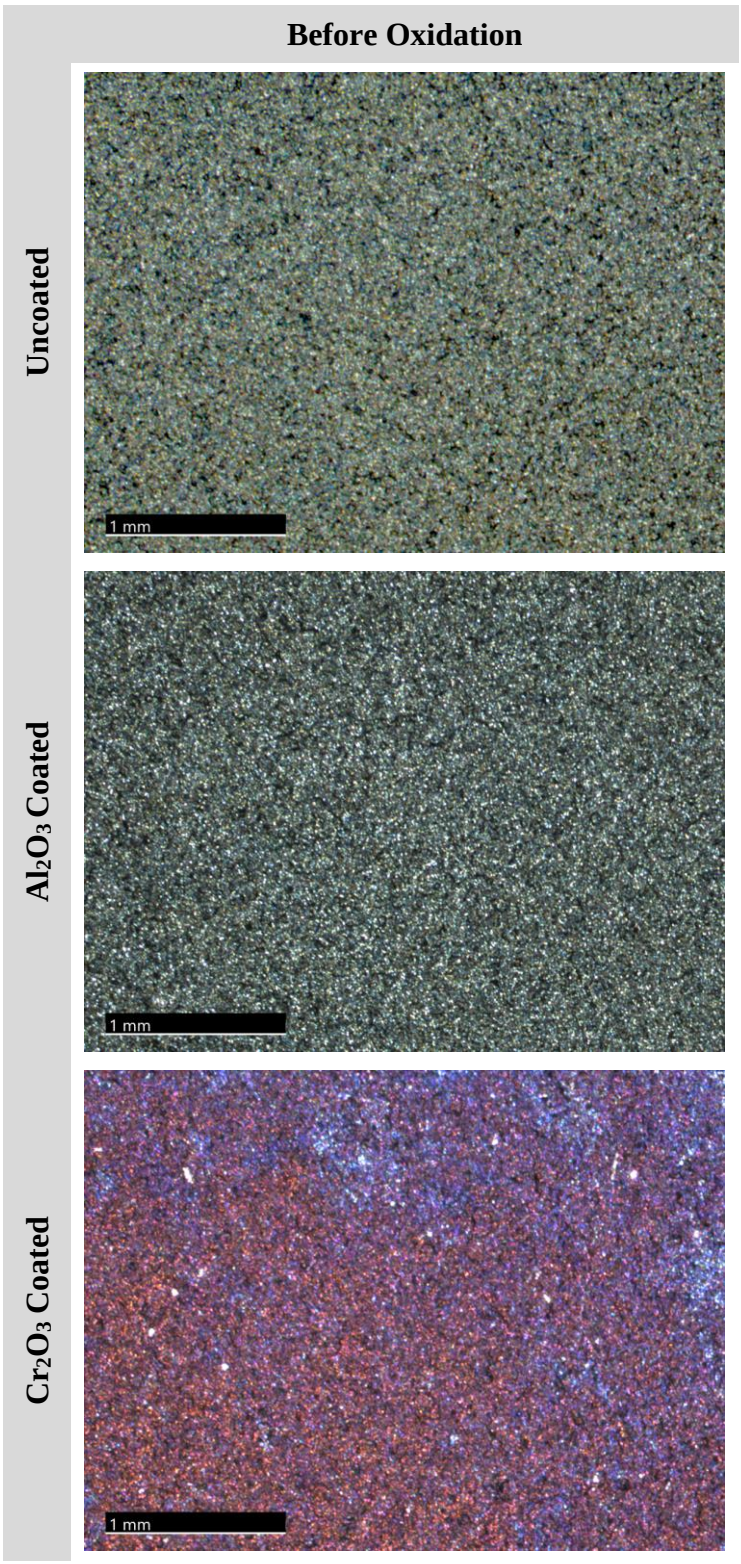

Figure 57: OM Images of the Uncoated, Al_2O_3 Coated, and Cr_2O_3 Coated Vapor Honed HAYNES® 214® Coupons Before Oxidation

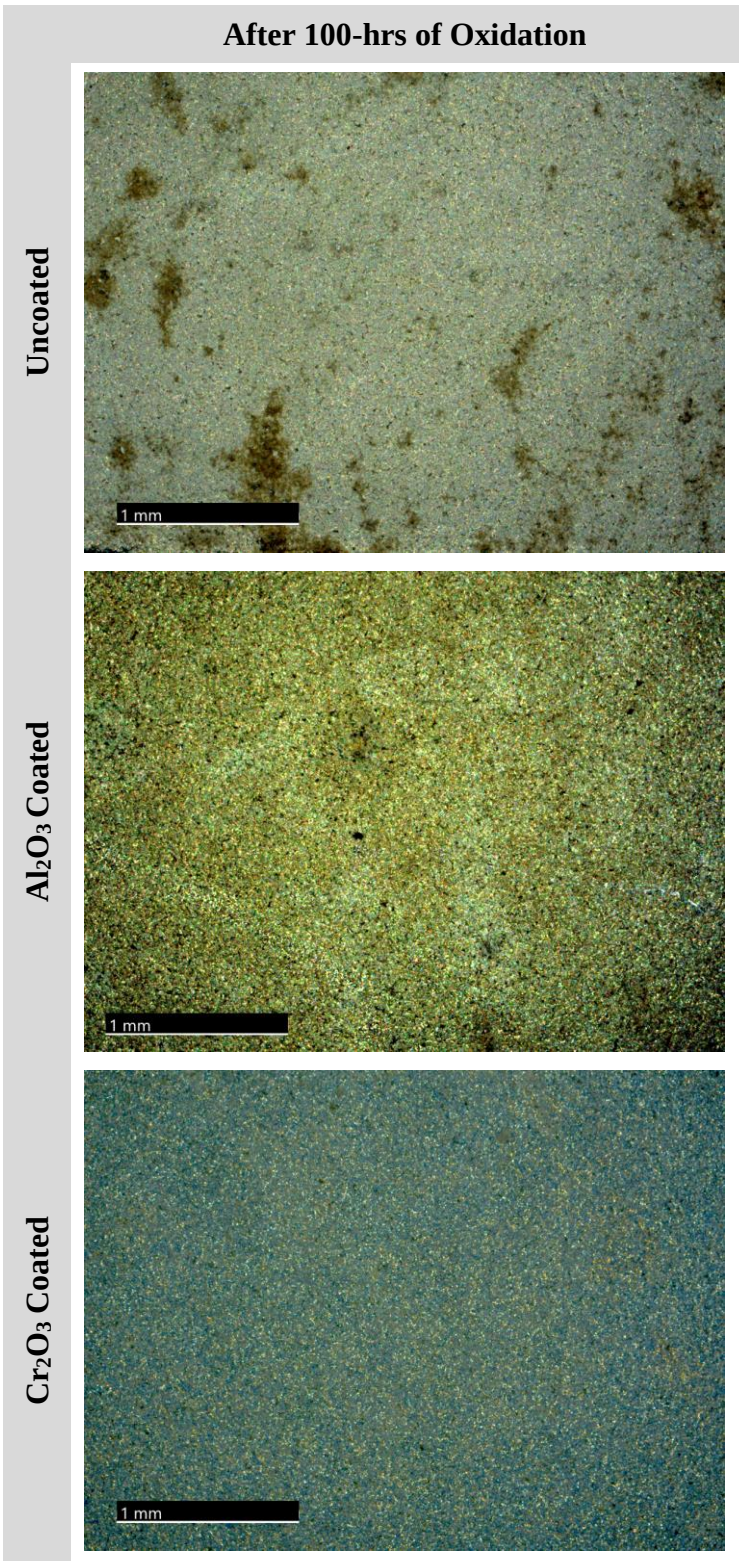

Figure 58: OM Images of the Uncoated, Al_2O_3 Coated, and Cr_2O_3 Coated Vapor Honed HAYNES® 214® Coupons After 100-hrs of Isothermal Oxidation in Air at 800°C

The OM images of the vapor honed alloy coupons closely resemble those from the 1200-grit abraded coupons from Section 5.1.1, aside from the visual differences of the morphology of the coupon surfaces (i.e., abraded coupon surface has grooves whereas the vapor honed coupon surface has dimples). Before oxidation, the uncoated, Al_2O_3 coated, and Cr_2O_3 coated alloys coupon surfaces show a silver, light blue, and red-purple color, respectively, similar to the 1200-grit abraded coupon surfaces that were also unoxidized.

After 100-hrs of oxidation, the colors of the coupon surfaces change indicating that there is a compositional or thickness change of an oxide on the surface. For the uncoated coupon, the surface appears a light blue color with localized regions of the surface containing dark or black areas where the light is being absorbed or scattered. As was the case with the 1200-grit coupons, areas appearing black are indicative of some kind of external oxide growth. However, for the Al_2O_3 coated coupon, the surface appears a yellow-gold color and very few regions of external oxide features were seen. Conversely to both the uncoated and Al_2O_3 coated coupons, the Cr_2O_3 coated surface appears a blue color and no darker regions of external oxide features were found. To get a closer view of the oxidized alloy surfaces, SEM images were taken. Figure 59 and Figure 60 show the surface SEM images of the uncoated, Al_2O_3 coated, and Cr_2O_3 coated coupons before and after 100-hrs of isothermal oxidation in air at 800°C.

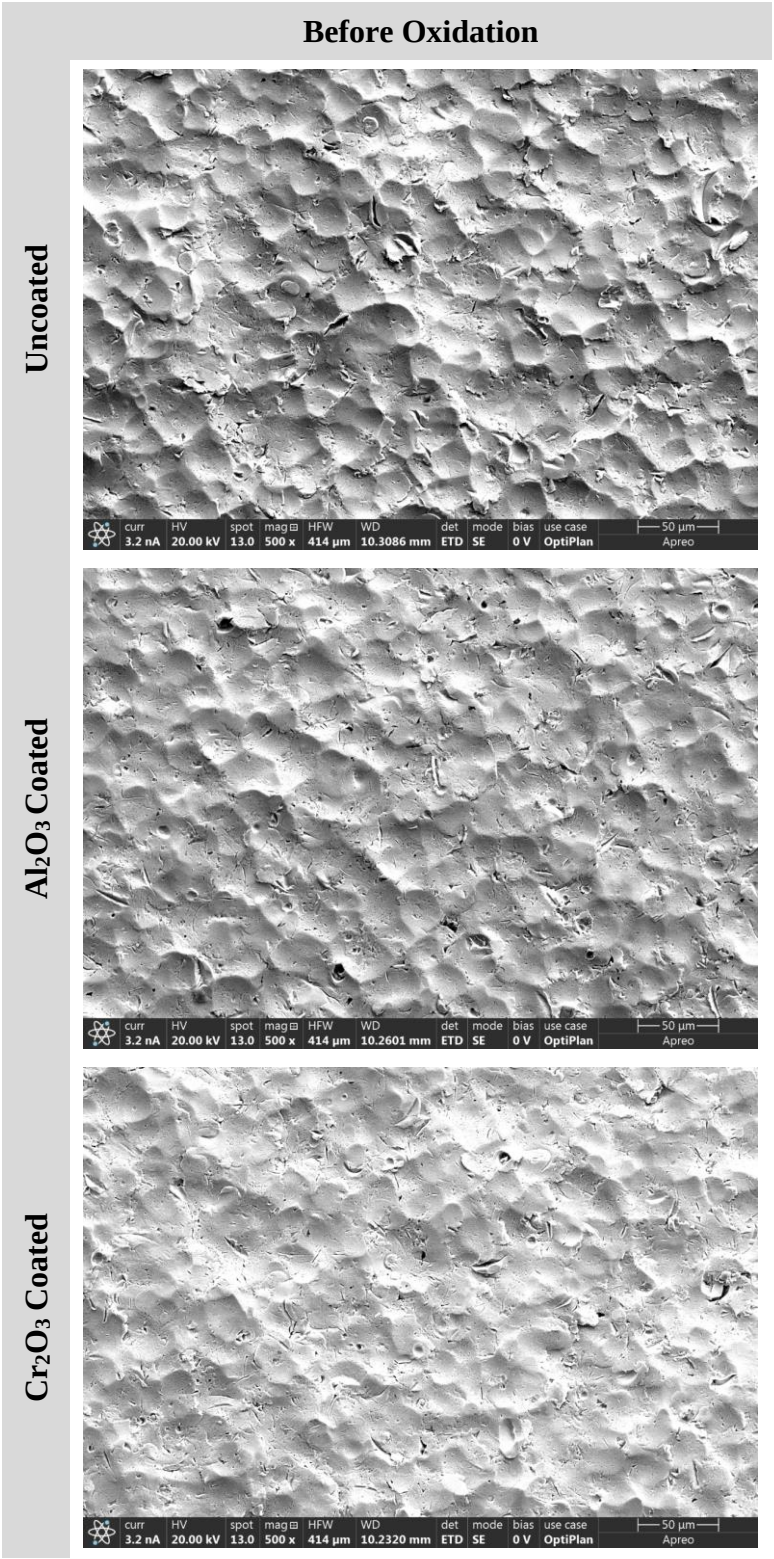

Figure 59: Surface SEM Images of the Uncoated, Al_2O_3 Coated, and Cr_2O_3 Coated Vapor Honed HAYNES® 214® Coupons Before Oxidation

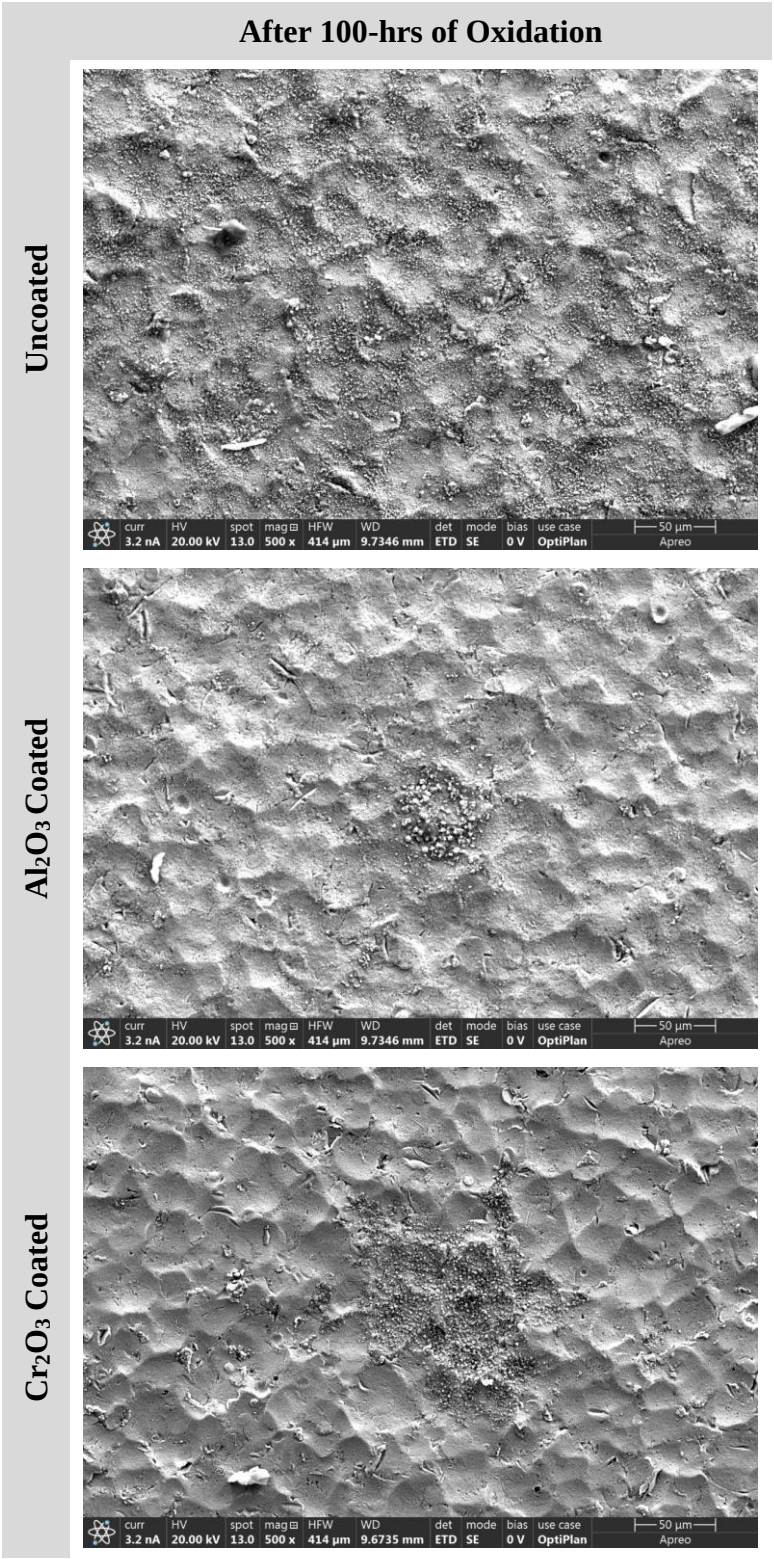

Figure 60: Surface SEM Images of the Uncoated, Al_2O_3 Coated, and Cr_2O_3 Coated Vapor Honed HAYNES® 214® Coupons After 100-hrs of Isothermal Oxidation in Air at 800°C

Before oxidation, the surfaces of the vapor honed coupons look identical where the dimples from the vapor honing process can be easily seen. After 100-hrs of isothermal oxidation, the surfaces of the different coupons look similar but the uncoated coupon shows large regions where small oxide particles or clusters are present and their formation mask the dimples from the vapor honing process. For the Al_2O_3 and Cr_2O_3 coated coupons, the surfaces are completely covered in a continuous and conformal oxide, however very few instances were found where the same small oxide particles or clusters had formed, as seen in the SEM image above.

To determine how the different coupons performed in the longer-term oxidation tests, the cross-sectional SEM images of the uncoated, Al_2O_3 coated, and Cr_2O_3 coated coupons after 100-hrs of isothermal oxidation in air at 800°C are shown in Figure 61, Figure 62, and Figure 63. Accompanying each cross-sectional SEM image is an EDS map showing the compositions of the oxidation products on the alloy surfaces or within the subsurface zone.

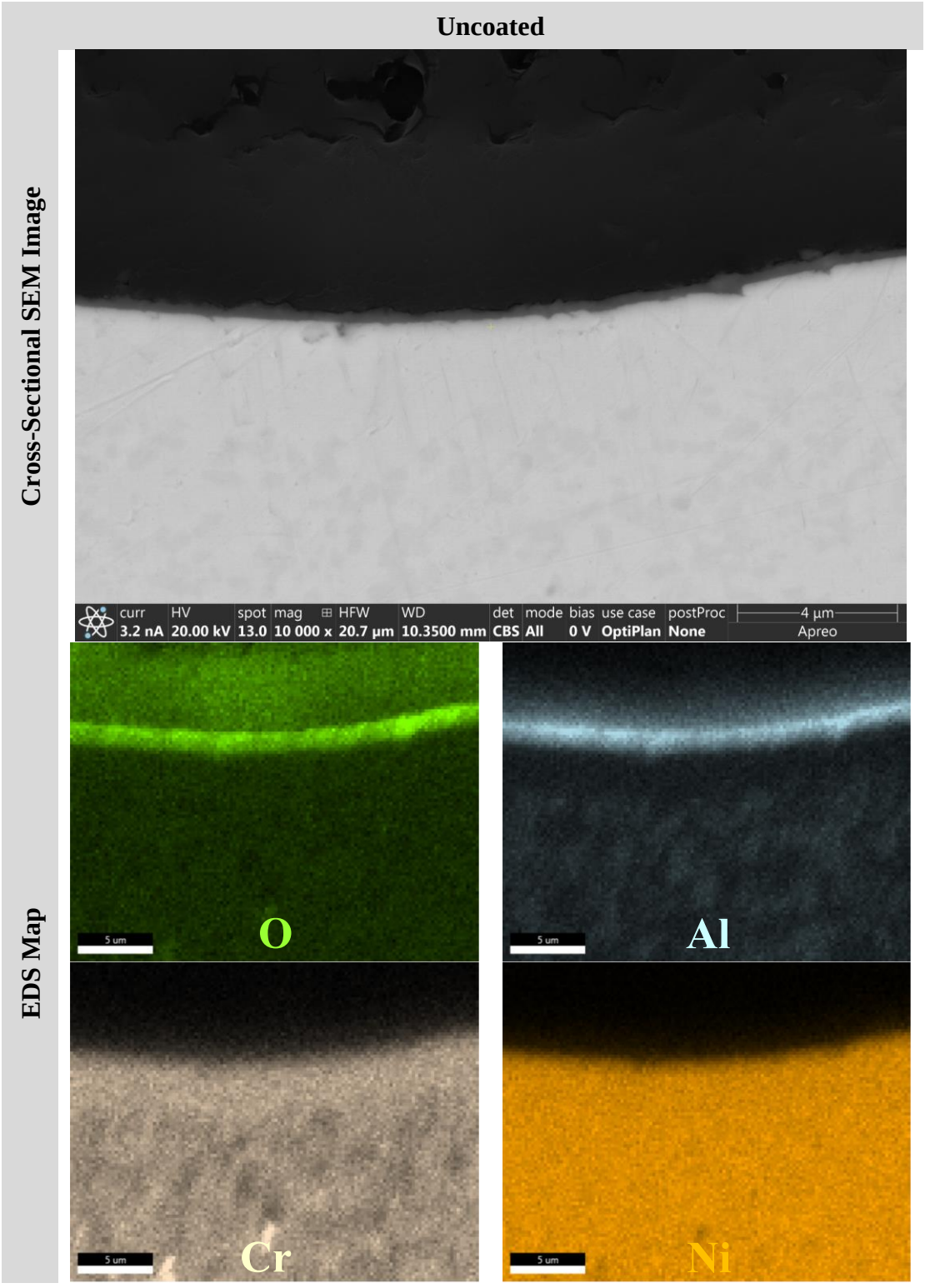

Figure 61: Cross-Sectional SEM Image and EDS Map of the Uncoated Vapor Honed HAYNES® 214® Coupon After 100-hrs of Isothermal Oxidation in Air at 800°C

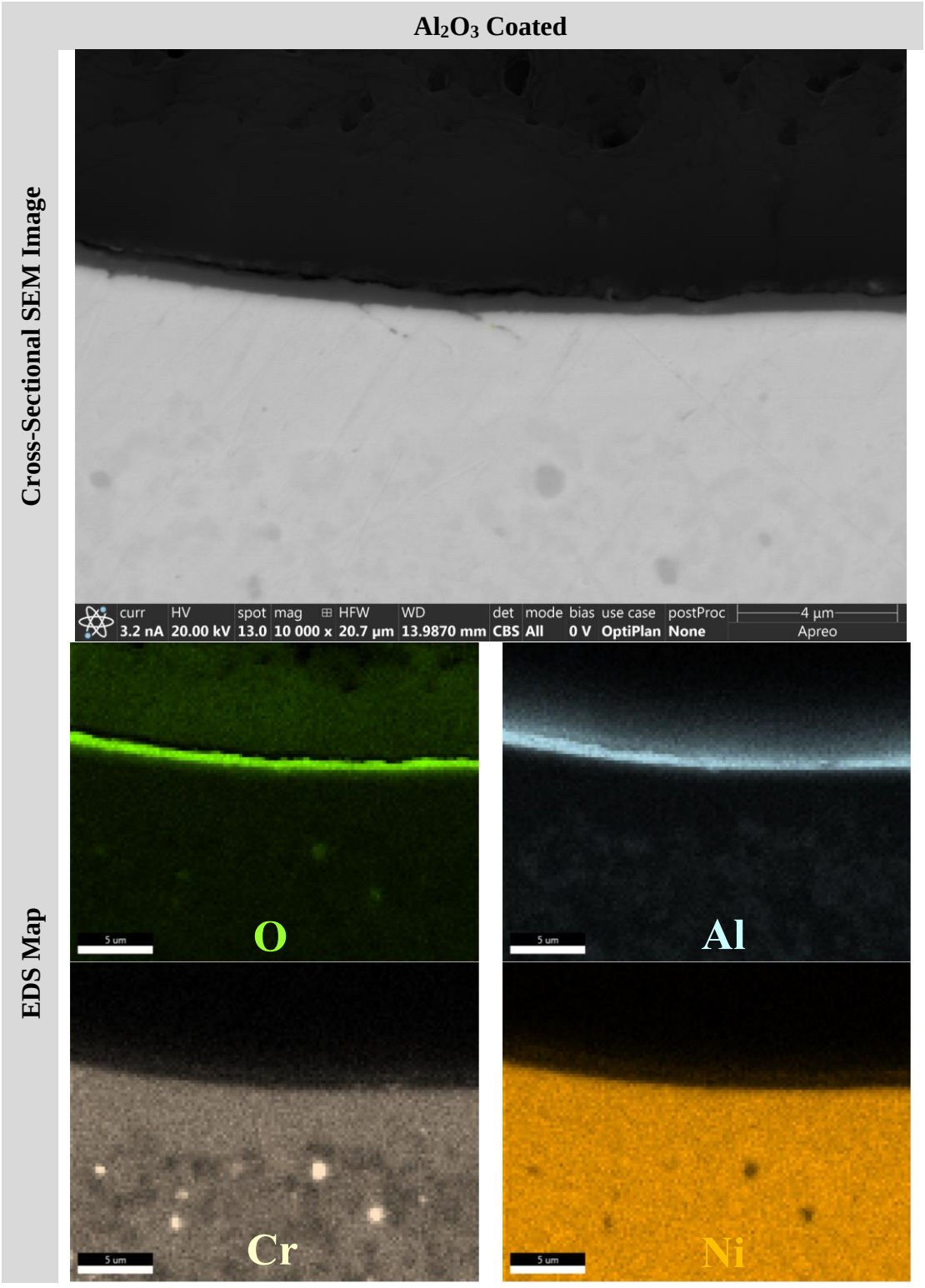

Figure 62: Cross-Sectional SEM Image and EDS Map of the Al_2O_3 Coated Vapor Honed HAYNES® 214® Coupon After 100-hrs of Isothermal Oxidation in Air at 800°C

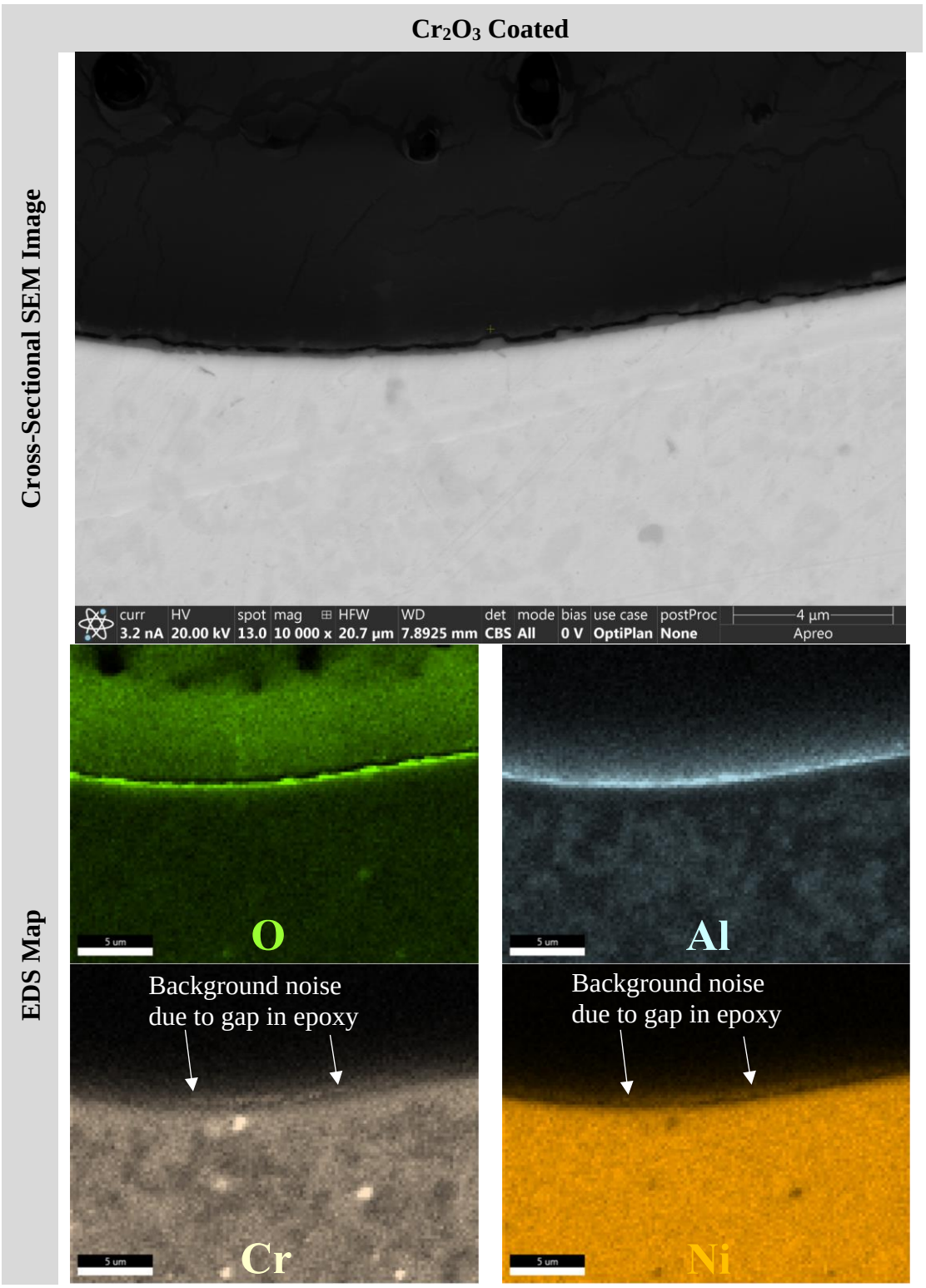

Figure 63: Cross-Sectional SEM Image and EDS Map of the Cr_2O_3 Coated Vapor Honed HAYNES® 214® Coupon After 100-hrs of Isothermal Oxidation in Air at 800°C

After 100-hrs of isothermal oxidation, the oxide growth on the surfaces of the three coupons look identical, with the only difference being the thickness. For the uncoated, Al_2O_3 coated, and Cr_2O_3 coated alloys, the EDS maps show that a continuous and external scale of an Al-rich oxide has formed on all of the surfaces and no internal oxidation is present for any coupon. However, looking at the cross-sectional SEM images, the thicknesses of the Al-rich oxide layers are different for each coupon.

The Al-rich oxide layer on the surface of the uncoated coupon is about 275 nm thick which is about the same thickness as the 1200-grit uncoated coupon. For the Al_2O_3 coated coupon, the Al-rich oxide layer is about 400 nm thick (175 nm thick PLD coating and a 225 nm thermally grown oxide layer) which is comparable to the thickness of the 1200-grit Al_2O_3 coated coupon. Lastly, for the Cr_2O_3 coated coupon, the Al-rich oxide layer is found to be roughly 150 nm thick which is comparable to the 1200 -grit Cr_2O_3 coated coupon.

Since all three coupon types were capable of forming an external Al-rich oxide scale, it can be assumed that the short circuit diffusion phenomenon was critical in the oxidation performance of the vapor honed coupons. Because vapor honing introduces a large amount of surface deformation (more than the 1200-grit abrasion process), the recrystallization that takes place in this region upon initial high temperature exposure was sufficient enough where the grain boundaries facilitated short circuit diffusion pathways for Al to reach the entire alloy surface and form a continuous and external scale. Once this external scale was formed, steady-state, diffusion-controlled growth kinetics were achieved which follow the parabolic rate law described in Section 2.1.2.1.

5.1.3 Surface Effect (Al_2O_3 Coated Alloy Only)

As discussed in Section 2.1.2.5, one way to increase the diffusivity of Al in the bulk alloy (i.e., the most reactive solute metal in the HAYNES® 214® alloy) is to change the surface condition such that a subsurface deformation zone exists. If the subsurface of the alloy is deformed, this region will rapidly recrystallize upon high temperature exposure to relieve the stress and strain. As new crystals nucleate and grow, the recrystallization zone provides significantly more grain boundaries to facilitate the short circuit diffusion of Al. This short circuit diffusion allows Al to reach the alloy surface faster and thus a continuous and external scale of Al_2O_3 is capable of forming.

Therefore, to test the short circuit diffusion phenomena of the Al_2O_3 coated HAYNES® 214® coupons, a separate 100-hr oxidation experiment was performed using three alloy coupons containing three different surface conditions; as-received, abraded to 1200-grit, and vapor honed. The processes for preparing the coupon surfaces that were abraded to 1200-grit and vapor honed are described in Section 4.1.2 and Section 4.1.1, respectively. For the as-received coupon, no surface preparation was done and the surface was left as the wrought alloy received from Haynes International. The intent of using these three different surface conditions is that the as-received alloy coupon would represent a non-surface deformed state, whereas the abraded 1200-grit abraded and vapor honed coupons would represent semi-surface deformed and fully surface deformed states, respectively. Figure 64 below shows the surface SEM images of the Al_2O_3 coated alloy containing the as-received, 1200-grit, and vapor honed surface conditions after 100-hrs of isothermal oxidation in air at 800°C.

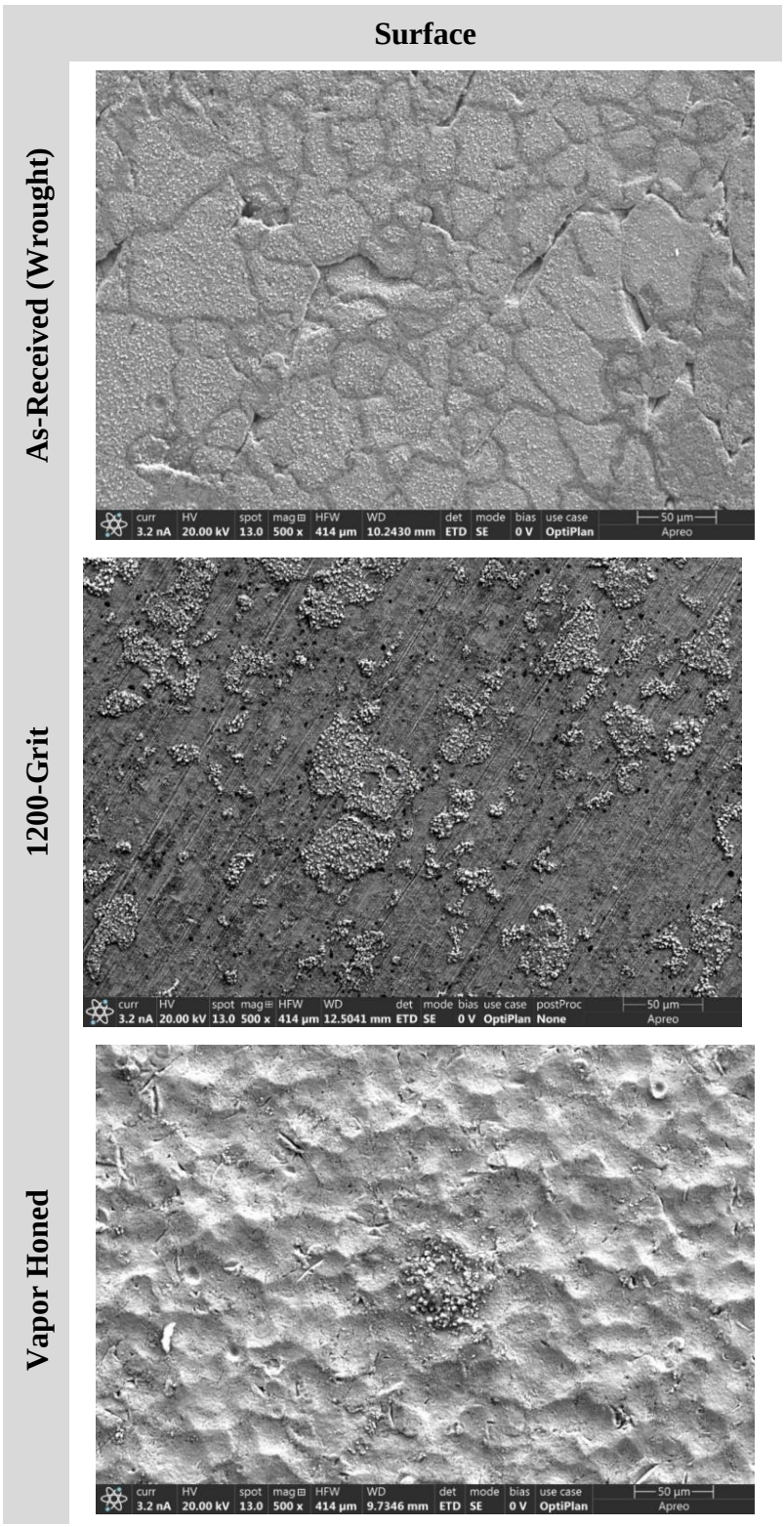

Figure 64: Surface SEM Images of the As-Received, 1200-Grit, and Vapor Honed Al_2O_3 Coated HAYNES® 214® Coupons After 100-hrs of Isothermal Oxidation in Air at 800°C

The oxidation performance of the three Al_2O_3 coated coupons containing different surface conditions, and subsequently differing levels of subsurface deformation zones, was drastically different. The as-received alloy coupon shows large oxide islands on the entire surface of the coupon, and the boundaries between the islands can be distinctly seen. As was described in Section 5.1.1 above, the surface of the 1200-grit alloy shows a dual oxidation growth where about half of the surface area contains a conformal oxide and the remaining surface area shows oxide islands and nodules. Unlike the surfaces of the as-received and 1200-grit alloy coupons, the surface of the vapor honed alloy shows no regions of external oxide growth and is instead completely covered in a conformal oxide. There were, however, a few instances where small oxide particles or clusters had formed, as seen in the SEM image above.

To determine the compositions and morphology of the oxides on the alloy surfaces (and any internal oxidation that may be present), the cross sections of each coupon were analyzed using SEM and EDS. The cross-sectional SEM images of the as-received, 1200-grit, and vapor honed Al_2O_3 coated coupons after 100-hrs of isothermal oxidation in air at 800°C are shown in Figure 65, Figure 66, and Figure 67. Accompanying each cross-sectional SEM image is an EDS map showing the compositions of the oxidation products on the alloy surfaces or within the subsurface zone.

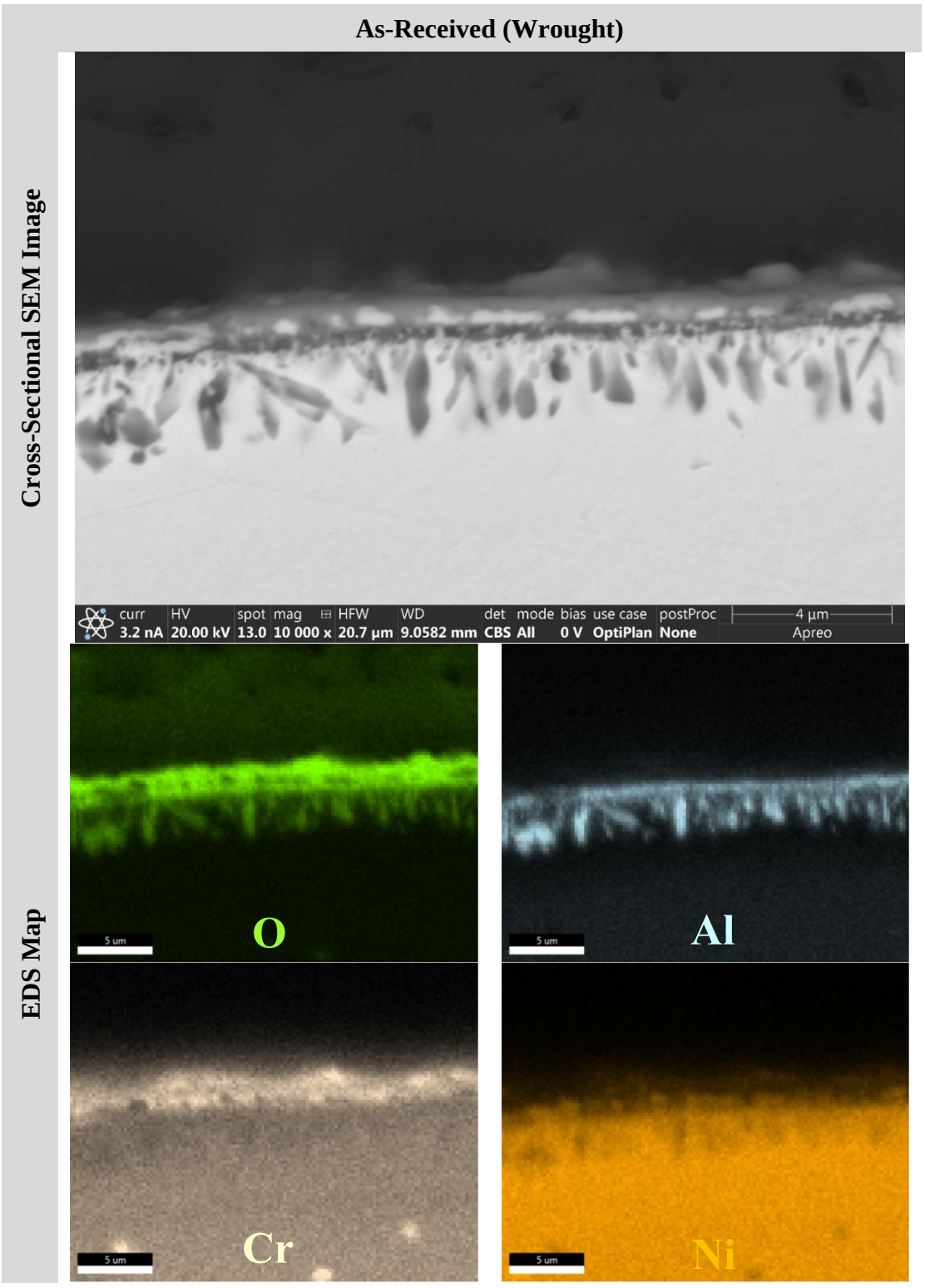

Figure 65: Cross-Sectional SEM Image and EDS Map of the As-Received Al_2O_3 Coated HAYNES® 214® Coupon After 100-hrs of Isothermal Oxidation in Air at 800°C

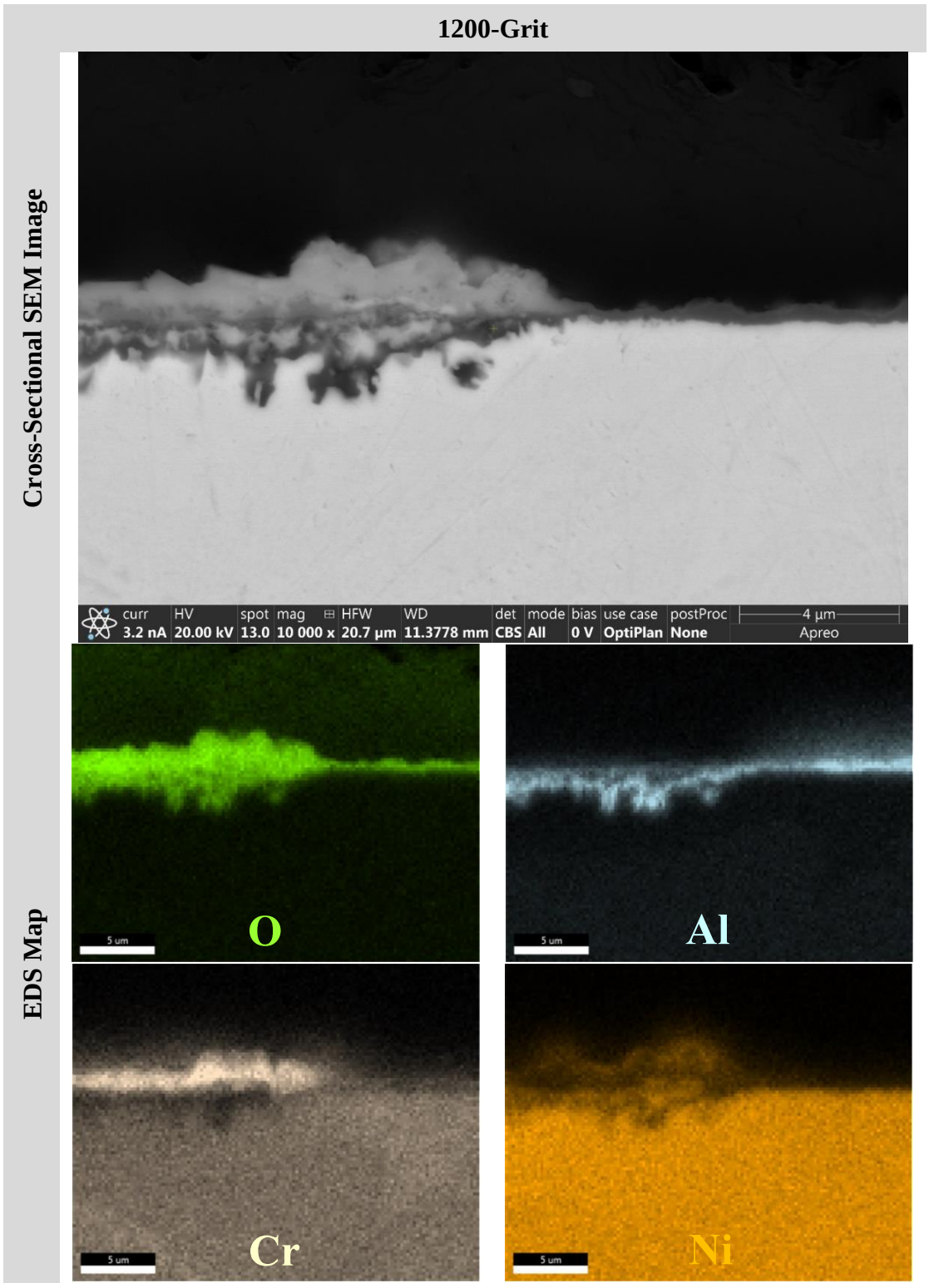

Figure 66: Cross-Sectional SEM Image and EDS Map of the 1200-Grit Al_2O_3 Coated HAYNES® 214® Coupon After 100-hrs of Isothermal Oxidation in Air at 800°C

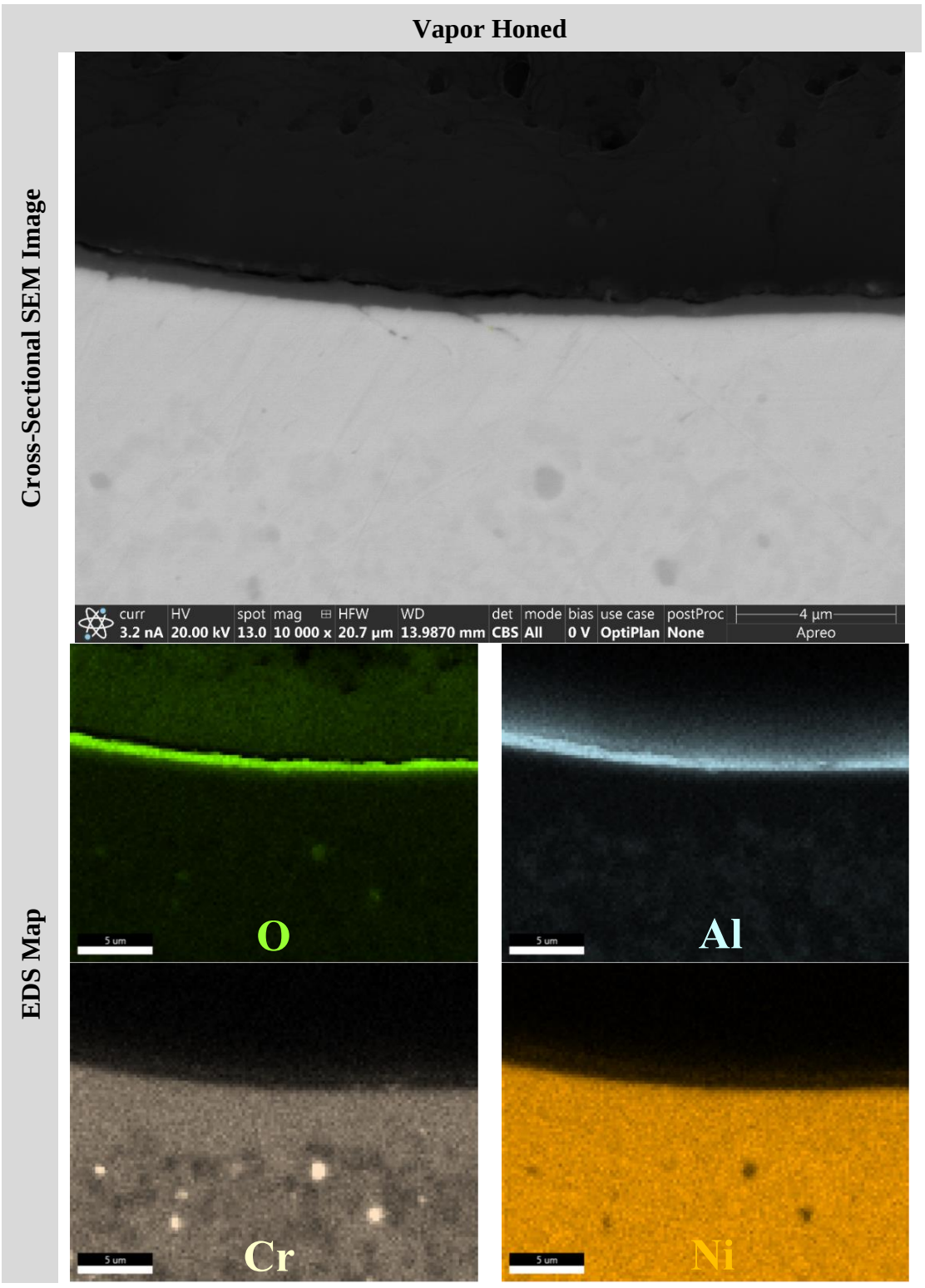

Figure 67: Cross-Sectional SEM Image and EDS Map of the Vapor Honed Al_2O_3 Coated HAYNES® 214® Coupon After 100-hrs of Isothermal Oxidation in Air at 800°C

As expected, based on the surface SEM images of the different alloy coupons, the cross sections are also very different and each coupon shows a different oxide scale growth. In the as-received coupon which had no surface deformation layer, recrystallization in the subsurface zone did not occur which resulted in three distinct oxide formations. As EDS shows, the outer layer is an external Ni/Cr-rich oxide, likely consisting of a combination of NiO, Cr_2O_3, and $NiCr_2O_4$. The middle oxide layer is found to contain Ni, Cr, and Al, which could be a mixed spinel structure of $Ni(Al,Cr)_2O_4$. This middle oxide layer has also formed on the surface of the alloy coupon (i.e., an external scale). Lastly, the inner oxide layer is an internal oxidation zone about 2 μm thick where Al_2O_3 has formed in distinct and individual rod-like precipitates.

In Section 5.1.1, the oxidation performance of the 1200-grit alloy coupon that had been isothermally oxidized in air for 100-hrs at 800°C was discussed extensively. For this surface condition which was intended to represent a semi-surface deformed state, the oxidation results are very different than the as-received coupon. Some regions of the surface show an external Al-rich oxide whereas the remaining areas show a duplex formation of an outer Ni/Cr-rich oxide of NiO, Cr_2O_3, and $NiCr_2O_4$ that has formed on top of an internal oxidation layer of Al_2O_3 which was semi-continuous. Thus, in comparison to the as-received coupon, applying some intermediate level of surface deformation had a pronounced effect on the oxide growth. With surface deformation present and the ability for short circuit diffusion to take place, this diffusion was sufficient for areas of the 1200-grit coupon to form an external Al_2O_3 scale. However, it appears that either the surface deformation in localized areas of the surface or the Al content in these regions was slightly less which resulted slower Al diffusion and the formation of a semi-continuous Al_2O_3 layer within the subsurface region of the alloy coupon.

Section 5.1.2 discussed the isothermal oxidation performance of the Al_2O_3 coated vapor honed coupon. This surface condition represented a fully surface deformed state and EDS shows that the only scale that was formed on the alloy surface was an external Al-rich oxide. When comparing the vapor honed coupon to both the as-received and 1200-grit coupons, it is clear that the surface deformation, recrystallization, and short circuit diffusion process have a direct impact on the ability for the alloy to form an external Al_2O_3 scale. Also, with respect to the 1200-grit coupon, it can be seen that inducing more extensive surface deformation (and possibly more uniform deformation) compared to abrasion provides the needed recrystallization and short circuit diffusion rate required to form a completely external Al_2O_3 scale.

5.1.4 PLD Coating Thickness Effect (Al_2O_3 Coated Coupons Only)

Based on the oxidation performance of the Al_2O_3 coated coupon from Section 5.1.1 which was deposited via PLD for 10 min (having a thickness of about 150 to 175 nm) and showed a dual oxidation mechanism, it was hypothesized that increasing the Al_2O_3 PLD coating thickness could prevent the internal oxidation and subsequent outward oxide growth. This was hypothesized because by increasing the distance that oxygen must diffuse (i.e., through a thicker coating) before reaching the alloy surface and entering the subsurface zone, it may allow additional time for the Al from the bulk alloy to diffuse and subsequently reach the alloy surface in order to form a continuous and external oxide scale on the entire surface. To test this hypothesis, a HAYNES® 214® alloy coupon was coated with Al_2O_3 via PLD for 20 min (i.e., double the deposition duration) which resulted in a coating thickness of about 300 to 350 nm. To determine if increasing the Al_2O_3 PLD coating thickness changed the oxidation performance and mechanism, this coupon was then isothermally oxidized in air for 100-hrs at 800°C. Figure 68 and Figure 69 below shows the surface

SEM images of the 10- and 20-min Al_2O_3 coated coupons that were isothermally oxidized in air for 100-hrs at 800°C.

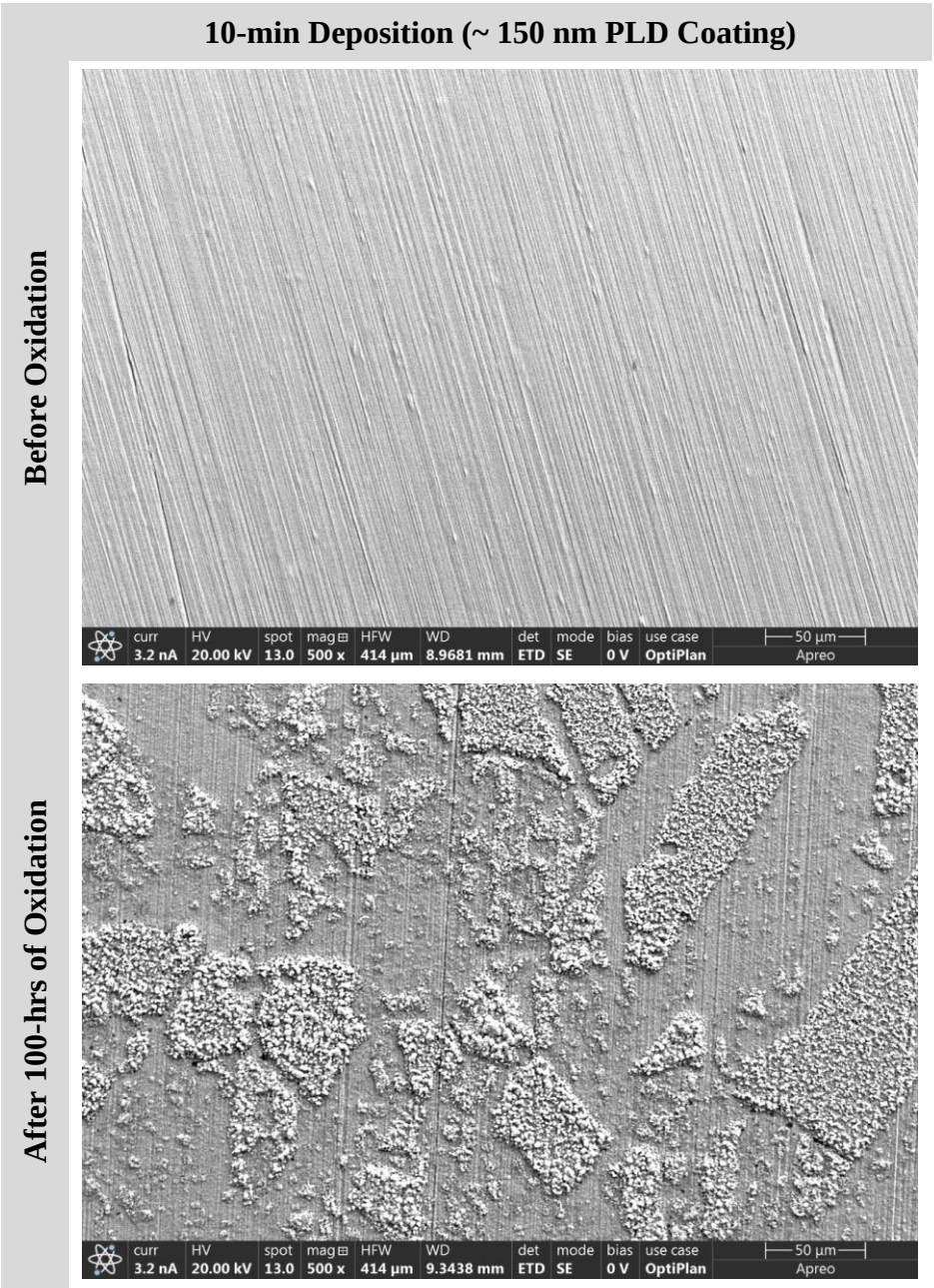

Figure 68: Surface SEM Images of the 10-min Al_2O_3 Coated 1200-Grit HAYNES® 214® Coupon Before and After 100-hrs of Isothermal Oxidation in Air at 800°C

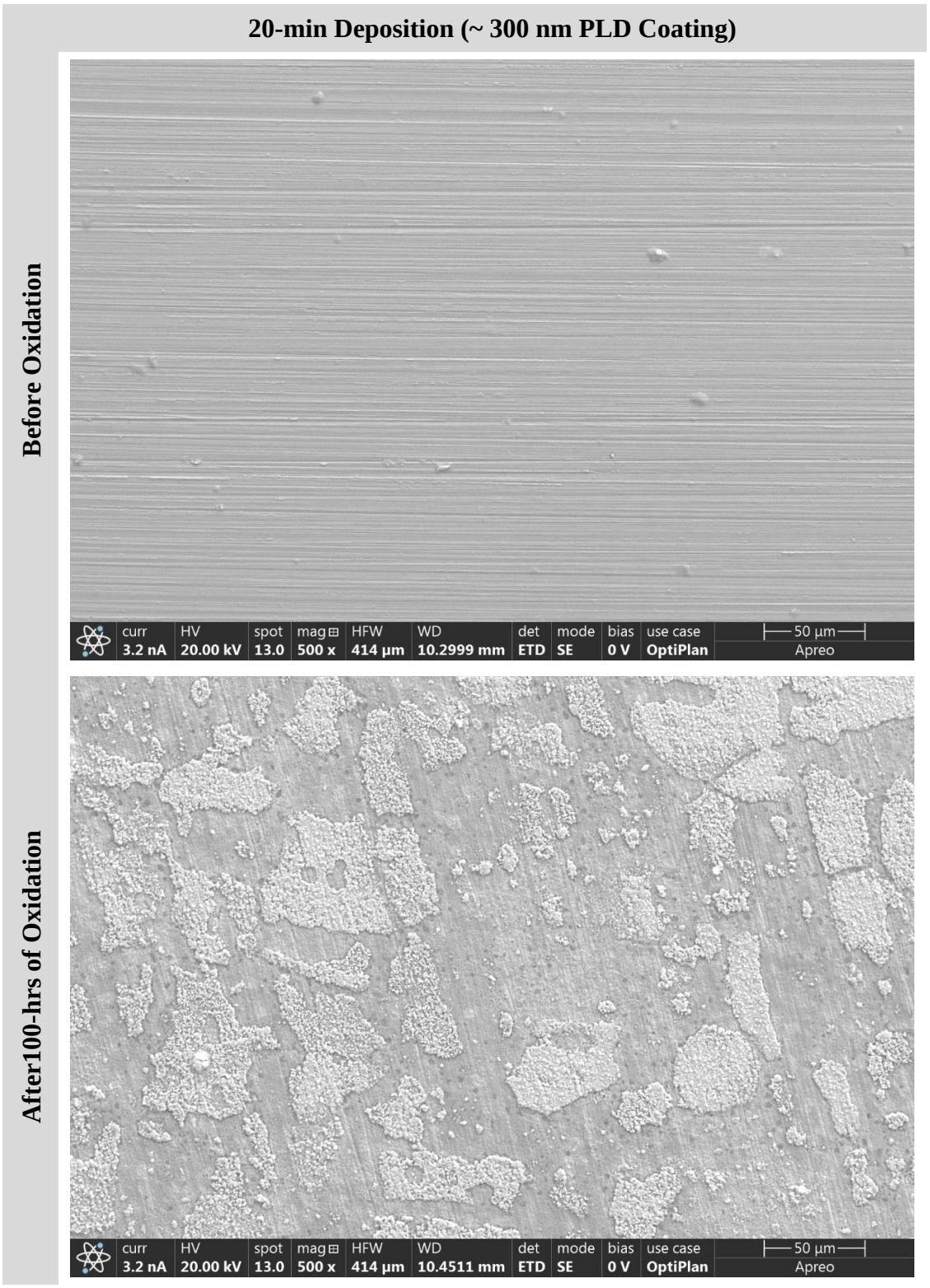

Figure 69: Surface SEM Images of the 20-min Al_2O_3 Coated 1200-Grit HAYNES® 214® Coupon Before and After 100-hrs of Isothermal Oxidation in Air at 800°C

While it was thought that increasing the Al_2O_3 PLD coating thickness would slow down the inward oxygen diffusion as well as prevent the outward oxide growth on the alloy surface, the 20-min coupon surface shows similar results to the 10-min coupon surface. The 20-min coupon surface still shows a dual oxidation growth mechanism where regions of the surface are covered in a smooth, conformal oxide and the other regions show external oxide islands and nodules. It is interesting to note that the sizes (width) of the external oxide islands and nodules on the surfaces of the 10- and 20-min coupons are of the same magnitude (about 50 μm). Although the widths of the oxide islands appear similar, it is obvious to see that the heights (i.e., vertical growth) are not. In the 10-min coupon, the oxide growth on the surface appears to be made up of fine, individual crystals whereas the 20-min coupon shows a flatter, singular oxide growth on the surface.

To determine the compositions and morphology of the oxides on the alloy surfaces (and any internal oxidation that may be present), the cross sections of the 10- and 20-min coupons were analyzed using SEM and EDS. Figure 70 and Figure 71 below shows the cross-sectional SEM images of the 10- and 20-min Al_2O_3 coated coupons that were isothermally oxidized in air for 100-hrs at 800°C. Accompanying each cross-sectional SEM image is an EDS map showing the compositions of the oxidation products on the alloy surfaces or within the subsurface zone.

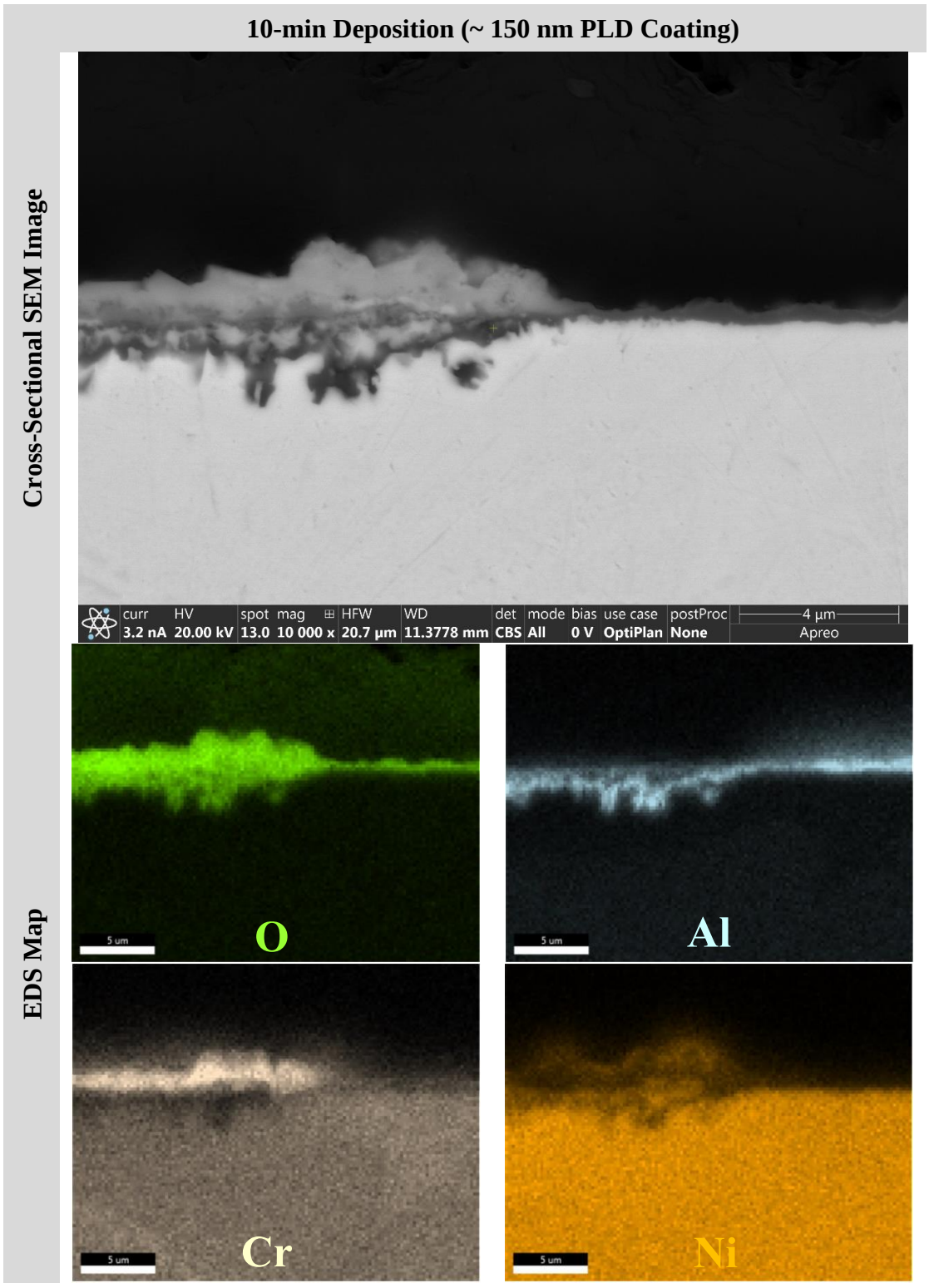

Figure 70: Cross-Sectional SEM Image and EDS Map of the 10-min Al_2O_3 Coated 1200-Grit HAYNES® 214® Coupon After 100-hrs of Isothermal Oxidation in Air at 800°C

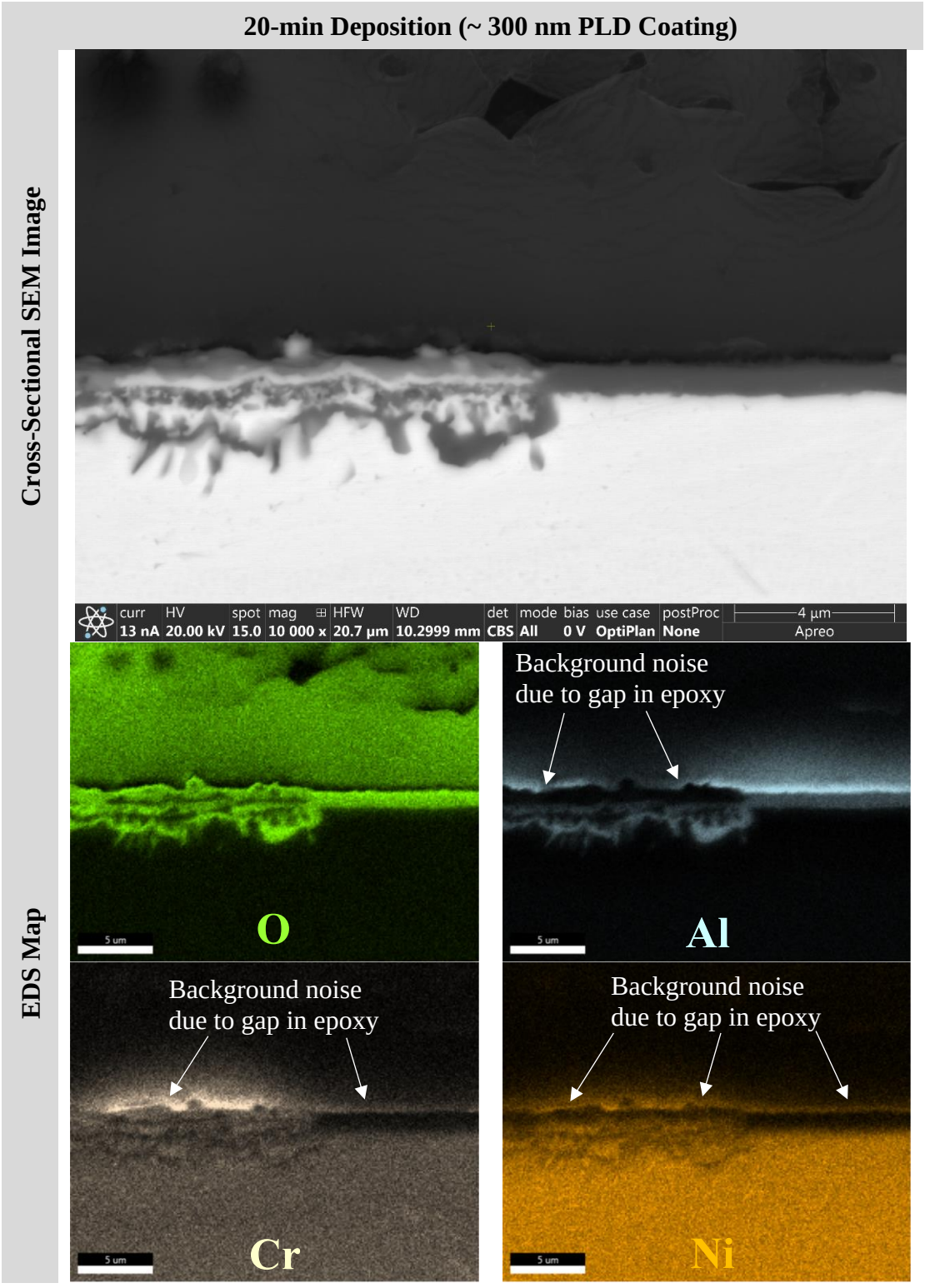

Figure 71: Cross-Sectional SEM Image and EDS Map of the 20-min Al_2O_3 Coated 1200-Grit HAYNES® 214® Coupon After 100-hrs of Isothermal Oxidation in Air at 800°C

The 20-min coupon shows the same type of dual oxidation growth as the 10-min coupon where portions of the surface contain an external scale of an Al-rich oxide and the other portions contain an outer layer of a Ni/Cr-rich oxide on top of a semi-continuous layer of Al_2O_3 precipitates that have formed within the subsurface region of the alloy (i.e., internal oxidation). As expected by increasing the Al_2O_3 PLD coating duration from 10-min to 20-min, the regions where an external Al-rich oxide scale has formed shows different thicknesses. For the 10-min coupon the external Al-rich oxide layer has a thickness of about 350 nm (175 nm Al_2O_3 PLD coating and 175 nm thermally grown Al-rich oxide scale) whereas the 20-min coupon contains a thickness of about 600 nm (350 nm Al_2O_3 PLD coating and 250 nm thermally grown Al-rich oxide scale).

Based on the cross-sectional SEM and EDS results, there are two important differences between the oxidation performance of the 10- and 20-min coupons. The first is that increasing the Al_2O_3 PLD coating thickness does seem to have an effect on the outward diffusion of Ni as the 20-min coupon shows no growth of a Ni-rich oxide and instead the outermost oxide layer is only Cr-rich. This is also evident based on the shape and morphology of the oxide where the oxide on the 10-min coupon that does contain Ni is bumpier and exhibits a more vertical growth whereas the oxide on the 20-min coupon that does not contain Ni is smoother and does not show the same growth height.

Second, when comparing the oxidation performance of the 10- and 20-min alloy coupons, the important takeaway is that increasing the Al_2O_3 PLD coating thickness is still insufficient at slowing down the inward diffusion of oxygen since internal precipitates of Al_2O_3 are still forming into a semi-continuous layer. Based on this result, it is plausible that some kind of structural change is occurring with the Al_2O_3 PLD coating that is still allowing both the outward diffusion of base metal cations as well as a faster inward diffusion of oxygen. One potential explanation would be

that if the Al_2O_3 PLD coating is amorphous in the as-deposited state and thus undergoes crystallization during initial high temperature exposure, the crystallization process would act as a short circuit diffusion path for Ni and Cr cations to diffuse through the Al_2O_3 PLD coating to the surface as well as a short circuit diffusion path for oxygen to diffusion through the Al_2O_3 PLD coating to the alloy-PLD coating interface. This could cause the external Ni/Cr-rich oxide formation that is seen on areas of the surface and the internal Al_2O_3 precipitates that have formed a semi-continuous layer within the subsurface zone of the alloy.

5.2 Thermal Cycling

5.2.1 Abraded Surface Condition

To understand the oxidation performance of the uncoated, Al_2O_3 coated, and Cr_2O_3 coated coupons abraded to 1200-grit in a more representative service environment which experiences fluctuations in temperature as components are heated and cooled, thermal cycling tests were performed. As was the case in the isothermal oxidation tests, the macroscopic oxidation performance of the alloy coupons was first examined using OM. Figure 72 shows the OM images for the uncoated, Al_2O_3 coated, and Cr_2O_3 coated coupons before and after 100-hrs of thermal cycling at 800°C.

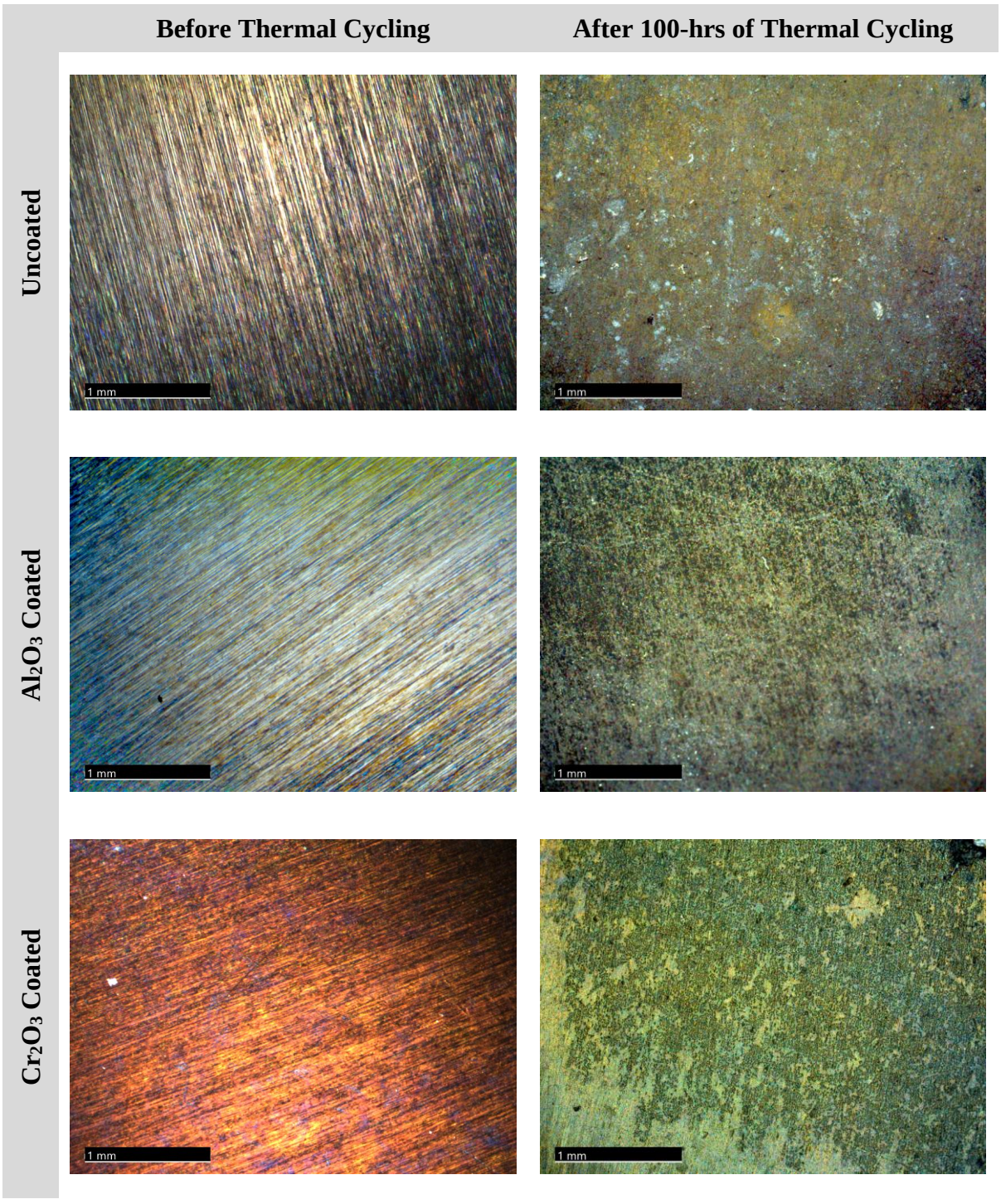

Figure 72: OM Images of the Uncoated, Al_2O_3 Coated, and Cr_2O_3 Coated 1200-Grit HAYNES® 214® Coupons Before and After 100-hrs of Thermal Cycling at 800°C (5 Cycles for 20-hrs)

Macroscopically, it is more difficult to determine which coupon showed better oxidation performance by simply looking at the surfaces using OM. However, Figure 72 does show that the uncoated coupon surface contains a yellow-green hue where traces of the grooves from the 1200-grit abrasion process can be barely seen. Above this, there are larges regions where a black-blue oxide growth has formed. For the Al_2O_3 coated coupon, the surface appears smoother and the grooves from preparing the surface to a 1200-grit can be more clearly seen. A large area of the surface does show the presence of a black oxide which is typically an external growth that is absorbing or scattering the light. However, other regions appear to show a conformal oxide that is a gray-blue color. Lastly, for the Cr_2O_3 coated coupon, the surface shows a smooth conformal oxide that is gold-blue in color, however above this layer is a large area of black oxide growth. Additionally, the grooves from the abrasion process can be easily seen. To get a better understanding of the thermal cycling results between the three coupon types, the total weight gain was plotted. Figure 73 below shows the total weight gain as a function of thermal cycle duration for the uncoated, Al_2O_3 coated, and Cr_2O_3 coated coupons that were thermally cycled for 100-hrs at 800°C.

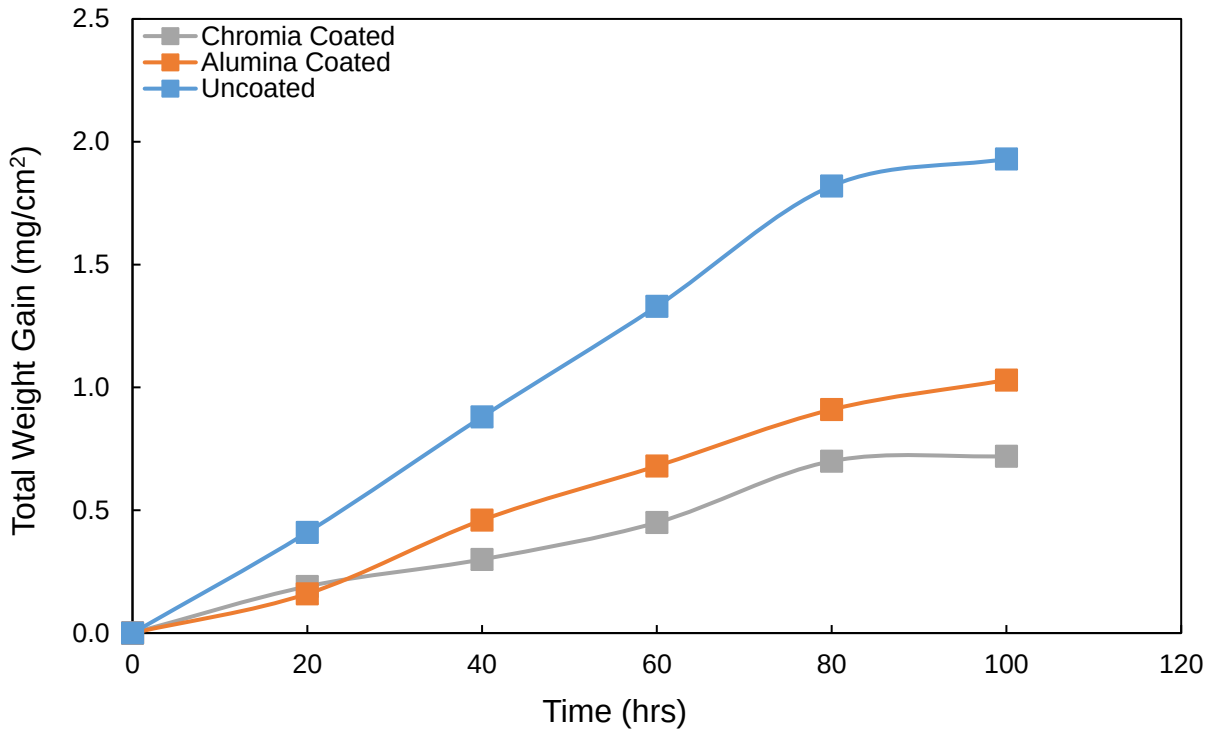

Figure 73: Total Weight Gain of the Uncoated, Al_2O_3 Coated, and Cr_2O_3 Coated 1200-Grit HAYNES® 214® Coupons After 100-hrs of Thermal Cycling at 800°C (5 Cycles for 20-hrs)

As Figure 73 shows, there is a distinct weight gain difference between the three coupon types. The uncoated coupon shows the largest total weight gain but also the interim weight gain measurements were consistently larger than the Al_2O_3 and Cr_2O_3 coated coupons. One interesting trend is that up to 80-hrs of thermal cycling, the total weight gain followed a linear trend. It was not until the last 20-hr cycle where the weight gain appeared to plateau. The total weight gain for the Al_2O_3 coated coupon appears to be about half of the weight gain for the uncoated coupon, and this is also apparent at each interim weight gain measurement. For the Cr_2O_3 coated coupon, the total weight gain, as well as each interim weight gain measurement, appears to be a little more than half that of the Al_2O_3 coated coupon. Based on the weight gain measurements, it would be expected

that the uncoated coupon would show the most oxidation products, followed by the Al_2O_3 and Cr_2O_3 coated coupons.

To determine if the total weight gains correlate to the amount of oxidation products on the alloy surfaces (and any internal oxidation that may be present), the cross sections of the uncoated, Al_2O_3 coated, and Cr_2O_3 coupons were analyzed using SEM and EDS. Figure 74, Figure 75, and Figure 76 below shows the cross-sectional SEM images of the uncoated, Al_2O_3 coated, and Cr_2O_3 coupons that were thermally cycled for 100-hrs at 800°C. Accompanying each cross-sectional SEM image is an EDS map showing the compositions of the oxidation products on the alloy surfaces or within the subsurface zone.

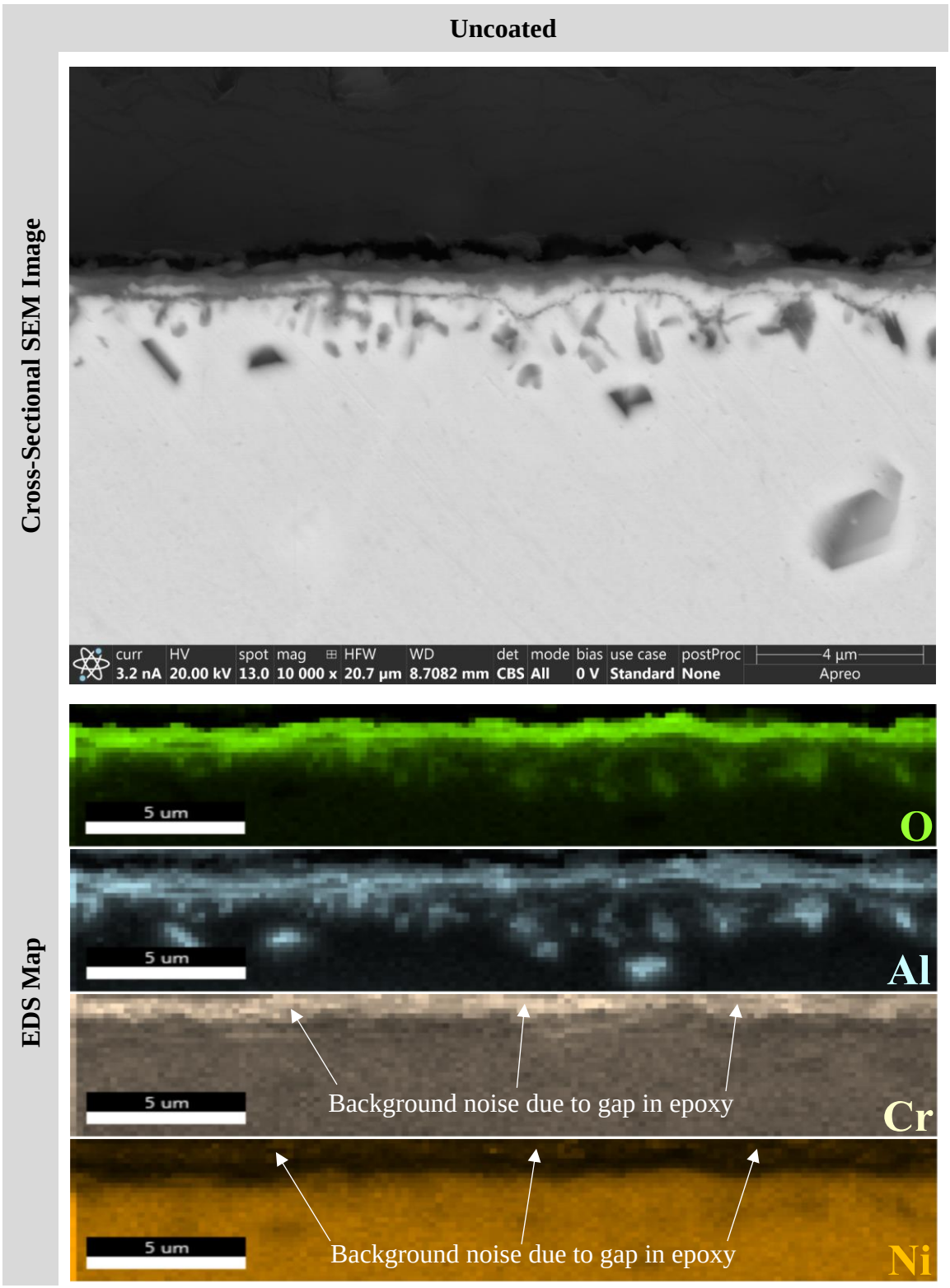

Figure 74: Cross-Sectional SEM Image and EDS Map of the Uncoated 1200-Grit HAYNES® 214® Coupon After 100-hrs of Thermal Cycling at 800°C (5 Cycles for 20-hrs)

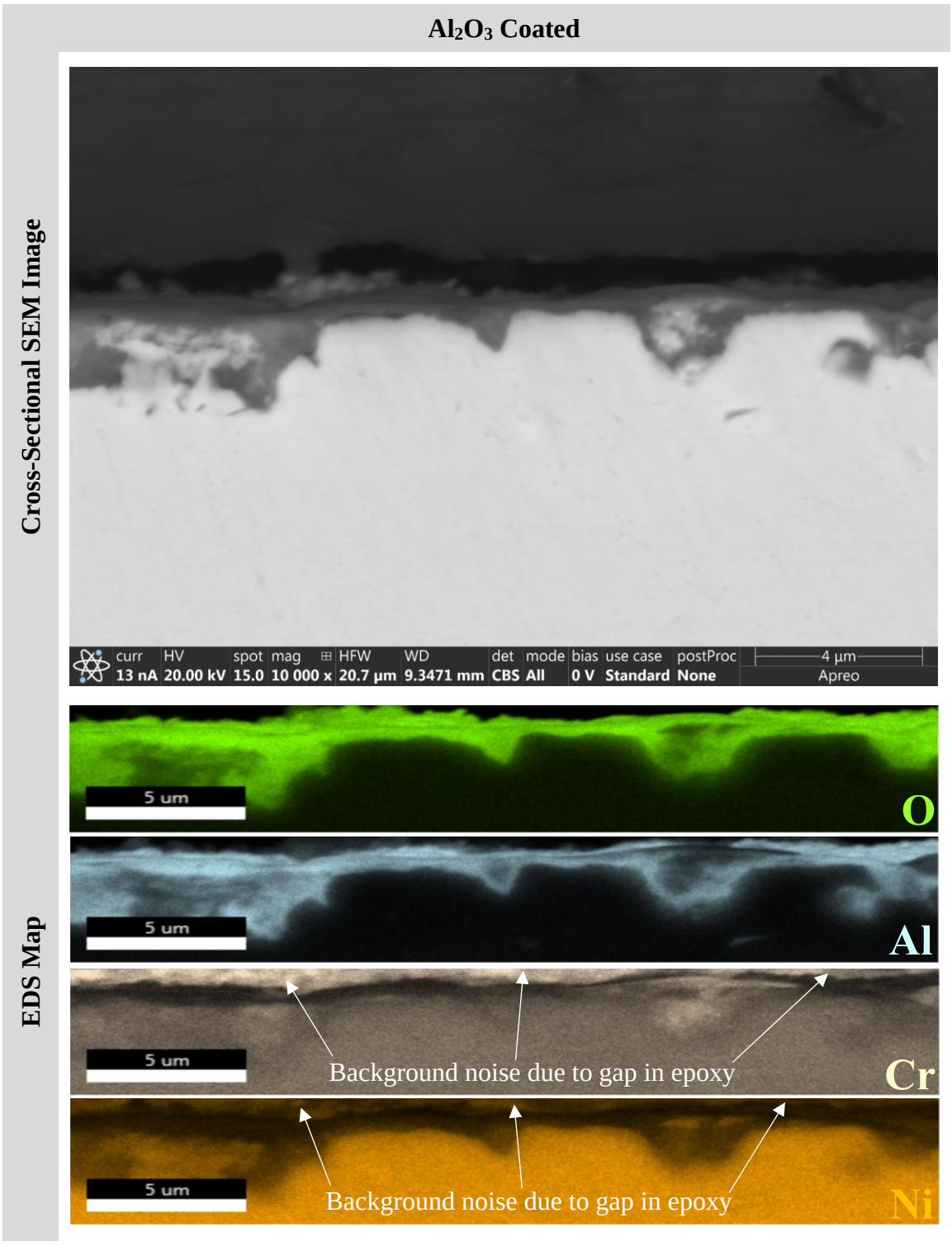

Figure 75: Cross-Sectional SEM Image and EDS Map of the Al_2O_3 Coated 1200-Grit HAYNES® 214® Coupon After 100-hrs of Thermal Cycling at 800°C (5 Cycles for 20-hrs)

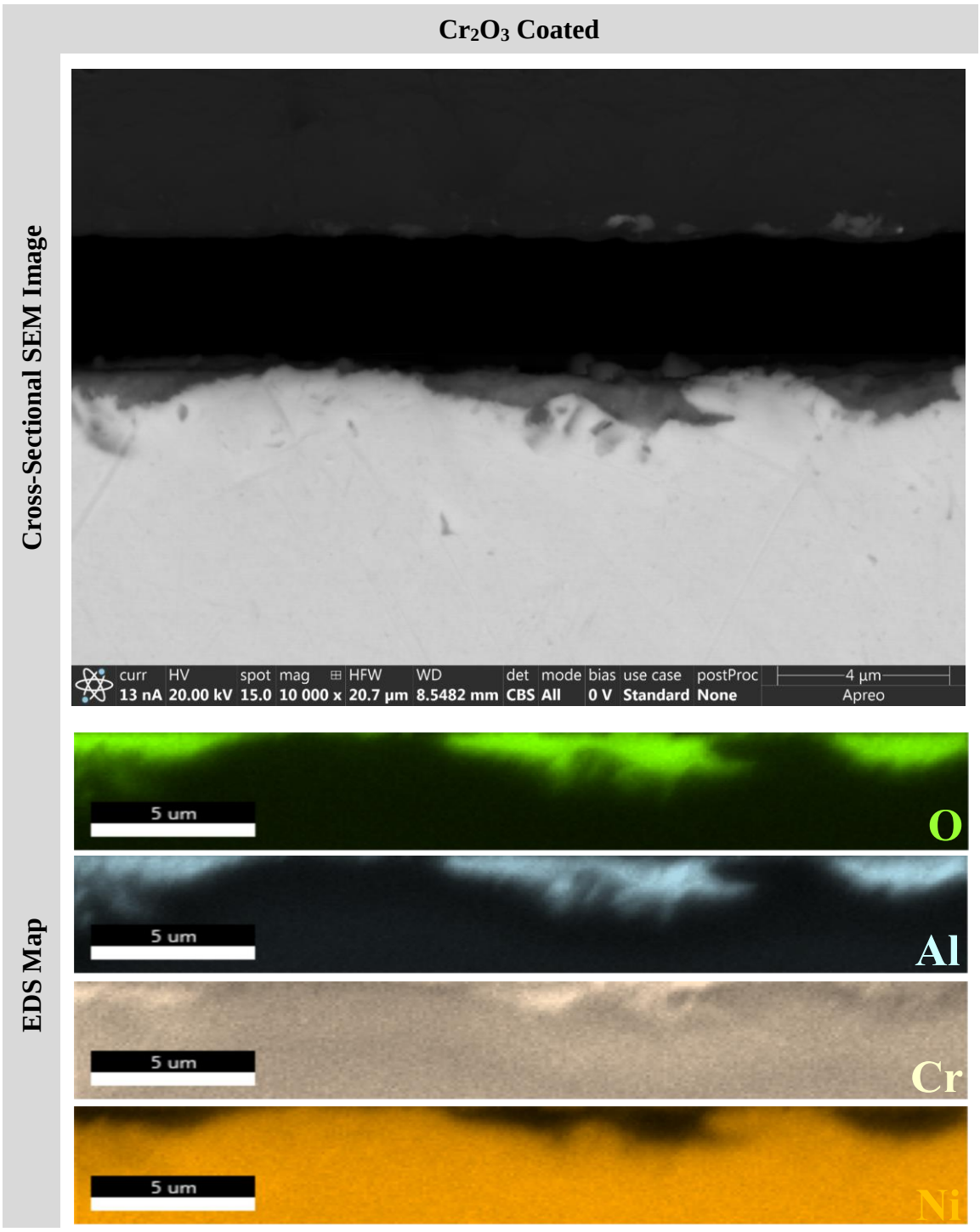

Figure 76: Cross-Sectional SEM Image and EDS Map of the Cr_2O_3 Coated 1200-Grit HAYNES® 214® Coupon After 100-hrs of Thermal Cycling at 800°C (5 Cycles for 20-hrs)

The uncoated coupon shows two distinct oxidation regions, an outer oxide layer and an internal oxidation zone. For the outer oxide scale, EDS shows that this is an Al-rich oxide scale but it also contains a small amount of Cr in the form of a very thin and discontinuous ribbon in the middle. Beneath this outer oxide layer there is roughly a 3 μm internal oxidation zone where relatively coarse precipitates of Al_2O_3 have formed. It is interesting to see that the uncoated coupon formed both an external scale as well as internal oxide precipitates, however this could have occurred if the supply of Al to the alloy-oxide interface was insufficient to sustain the exclusive growth of the external Al_2O_3 scale.

For the Al_2O_3 coated coupon, an internal oxidation zone was not present and the surface shows an external scale. However, in very localized areas, vertical penetrations of the oxide have formed into the alloy surface. EDS shows that the continuous outer scale is an Al-rich oxide and the areas where the oxide has vertically penetrated into the alloy is a mixture of Al, Cr, and Ni. In combination with the cross-sectional SEM image, it appears that these regions contain some Al-rich oxide but also some unoxidized alloy which is where the Ni and Cr would be detected.

Compared to the Al_2O_3 coated coupon, the Cr_2O_3 coated coupon shows a similar oxidation result. A distinct internal oxidation zone was not present and there appears to be a very thin layer of an Al-rich oxide on the surface of the alloy. However, larger and more horizontal oxide formations have penetrated into the alloy similar to what was seen with the Al_2O_3 coated coupon. The EDS maps show that these oxide penetrations are an Al/Cr-rich oxide which likely contain the structure of $(Al,Cr)_2O_3$. Based on these results, it is clear that the use of an Al_2O_3 or Cr_2O_3 PLD coating prevents the formation of internal oxides and thus provides a passivation layer to slow down the inward oxygen diffusion to an extent that allows the bulk Al to diffuse to the alloy surface and form a continuous layer as well as localized oxide regions that have formed into the alloy.

5.3 Hot Corrosion Testing

5.3.1 Single Salt Hot Corrosion of Na_2SO_4

5.3.1.1 Abraded Surface Condition

As described in Section 2.2, hot corrosion is problematic for nickel-base superalloys due to the severe attack or degradation of the protective oxide scale by deposits of salts, most notably Na_2SO_4. Thus, to also test the role of the Al_2O_3 and Cr_2O_3 PLD coatings with respect to hot corrosion, separate hot corrosion tests were performed. The macroscopic hot corrosion performance of the alloy coupons was first examined using OM. Figure 77 below shows the OM images for the uncoated, Al_2O_3 coated, and Cr_2O_3 coated coupons before and after 100-hrs of thermally cycled hot corrosion testing at 900°C.

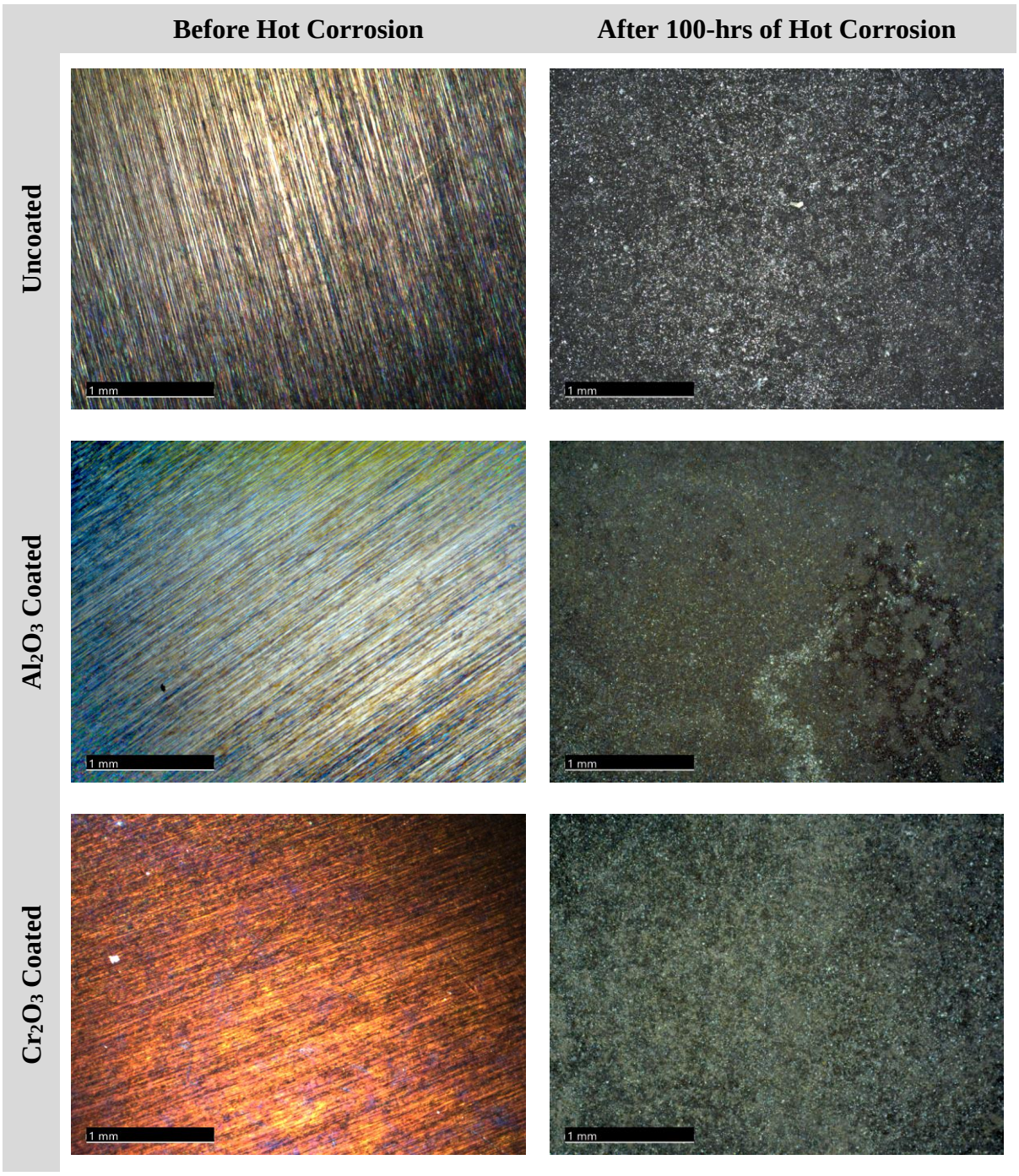

Figure 77: OM Images of the Uncoated, Al_2O_3 Coated, and Cr_2O_3 Coated 1200-Grit HAYNES® 214® Coupons Before and After 100-hrs of Thermally Cycled Hot Corrosion Testing at 900°C (5 Cycles for 20-hrs)

According to the macroscopic images of the alloy coupon surfaces, it is not as obvious as the oxidized coupons relative to which one(s) performed better. For each coupon, the surfaces primarily look black, however it can be seen that the uncoated coupon surface appears blacker than the Al_2O_3 coated coupon surface which in turn looks blacker than the Cr_2O_3 coated coupon surface. For the Al_2O_3 and Cr_2O_3 coated coupon surfaces, a slight greenish hue can also be seen. To get a better understanding of the hot corrosion results between the three coupon types, the total weight gain was plotted. Figure 78 below shows the total weight gain as a function of thermal cycle duration for the uncoated, Al_2O_3 coated, and Cr_2O_3 coated coupons that were hot corrosion tested at 900°C.

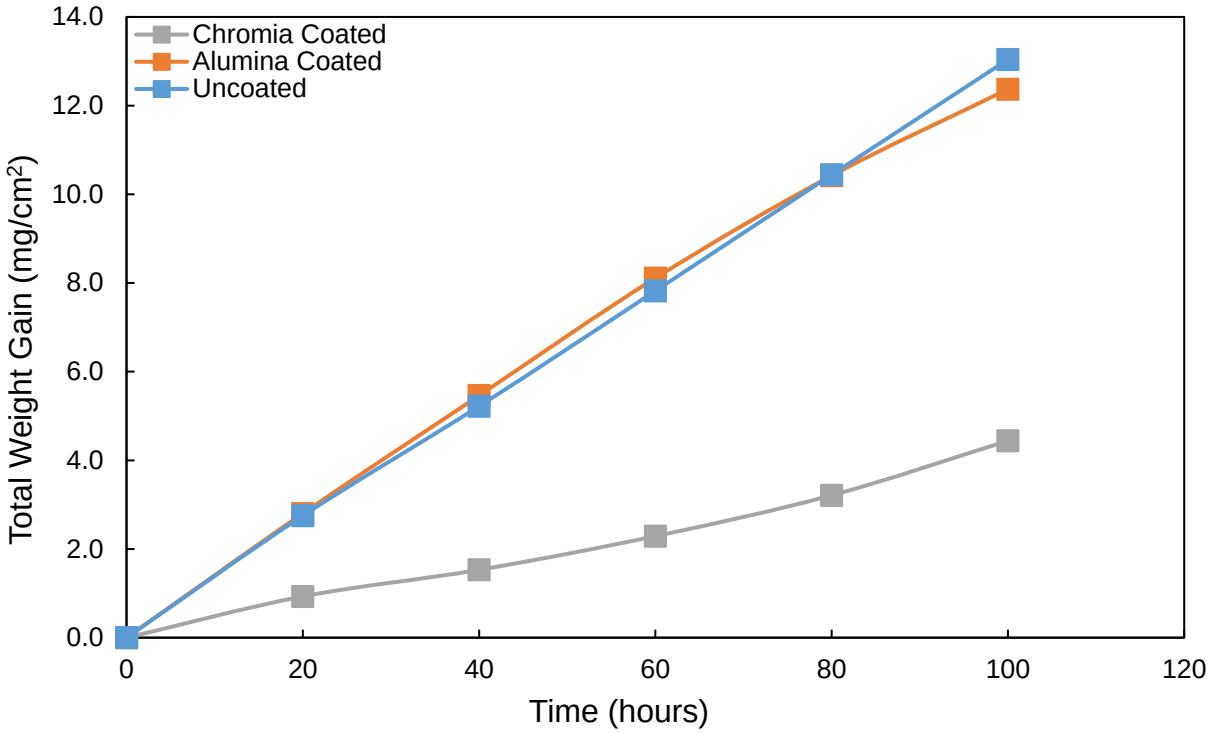

Figure 78: Total Weight Gain of the Uncoated, Al_2O_3 Coated, and Cr_2O_3 Coated 1200-Grit HAYNES® 214® Coupons After 100-hrs of Thermally Cycled Hot Corrosion Testing at 900°C (5 Cycles for 20-hrs)

The total weight gains of the uncoated and Al_2O_3 coated coupons were found to be nearly identical which means that the surfaces and cross sections would be expected to show comparable corrosion products (oxidation and sulfidation) since the weight uptake is the same. Furthermore, it is interesting to see that even after each thermal cycle interval, the weight gains mirror each other. However, the Cr_2O_3 coated coupon had a significantly less total weight gain, even after each thermal cycle interval. Thus, it would be expected that the corrosion products (oxidation and

sulfidation) on the surface and cross section would be considerably less compared to the uncoated and Al_2O_3 coated coupons.

To determine if the total weight gains correlate to the amount of corrosion products on the alloy surfaces (and any sub-surface corrosion products that may be present), the cross sections of the uncoated, Al_2O_3 coated, and Cr_2O_3 coupons were analyzed using SEM and EDS. Figure 79, Figure 80, and Figure 81 shows the cross-sectional SEM images of the uncoated, Al_2O_3 coated, and Cr_2O_3 coupons that were thermal cycle hot corrosion tested at 900°C. Accompanying each cross-sectional SEM image is an EDS map showing the compositions of the corrosion products on the alloy surfaces or within the subsurface zone.

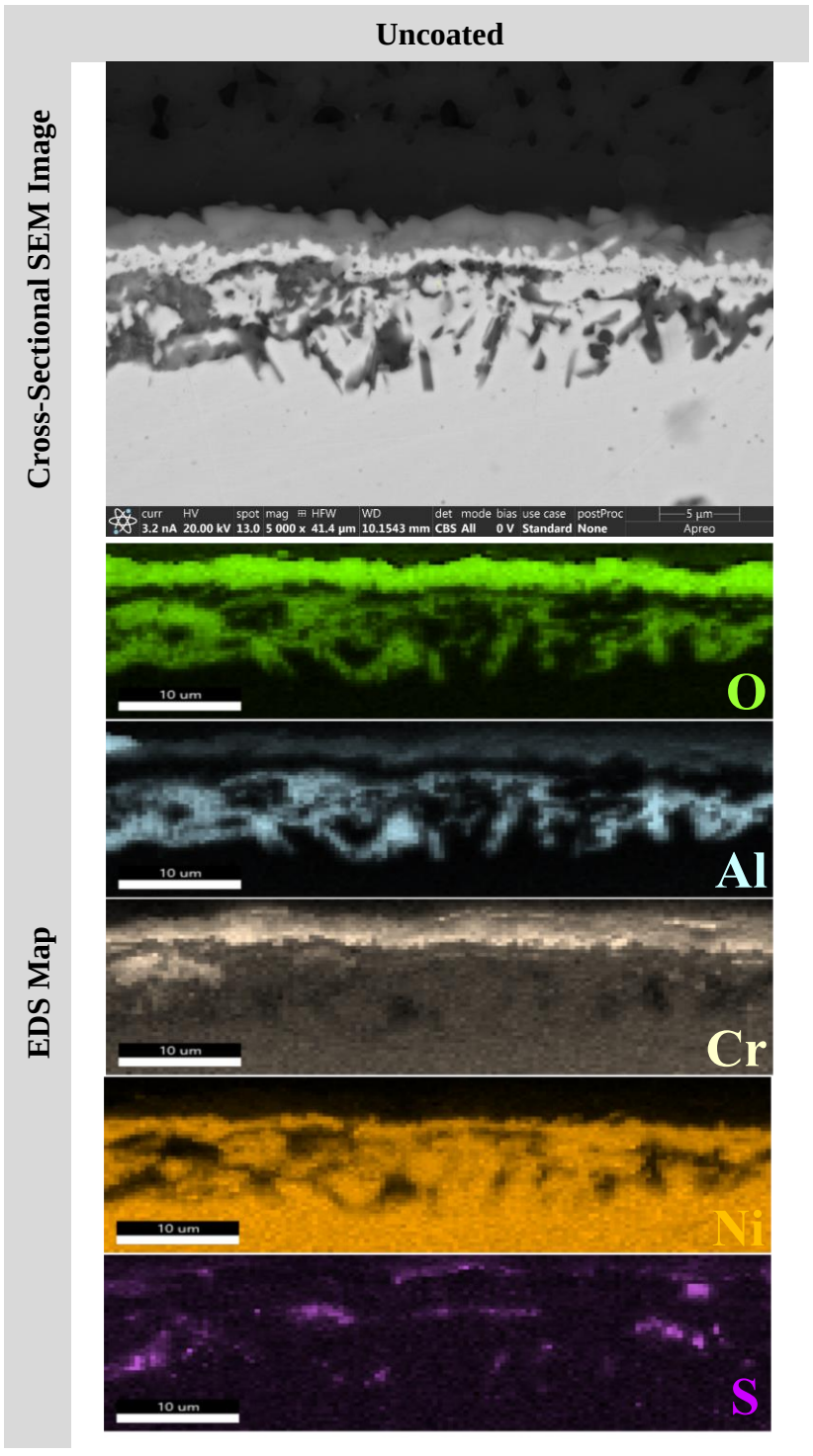

Figure 79: Cross-Sectional SEM Image and EDS Map of the Uncoated 1200-Grit HAYNES® 214® Coupon After 100-hrs of Thermally Cycled Hot Corrosion Testing at 900°C (5 Cycles for 20-hrs)

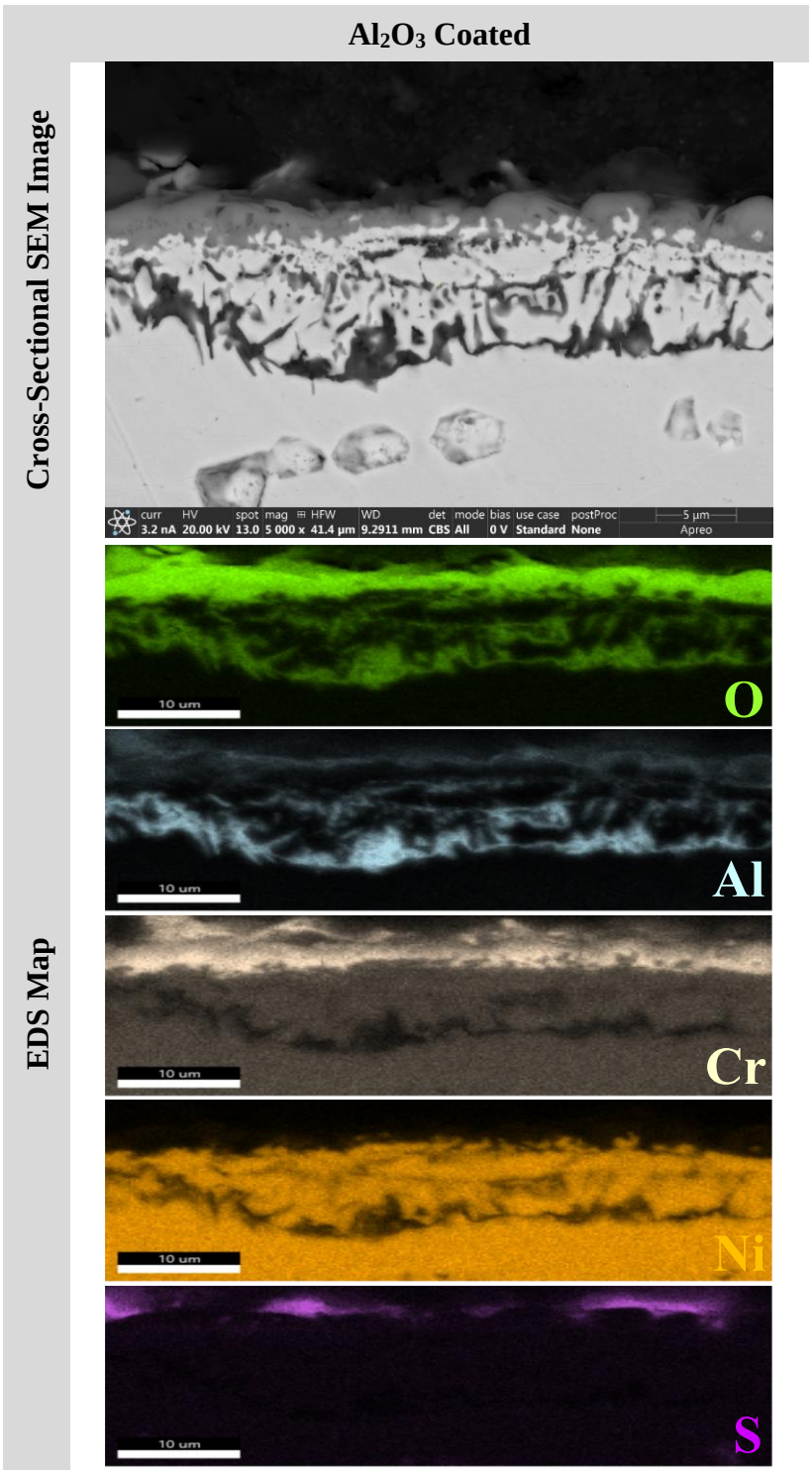

Figure 80: Cross-Sectional SEM Image and EDS Map of the Al_2O_3 Coated 1200-Grit HAYNES® 214® Coupon After 100-hrs of Thermally Cycled Hot Corrosion Testing at 900°C (5 Cycles for 20-hrs)

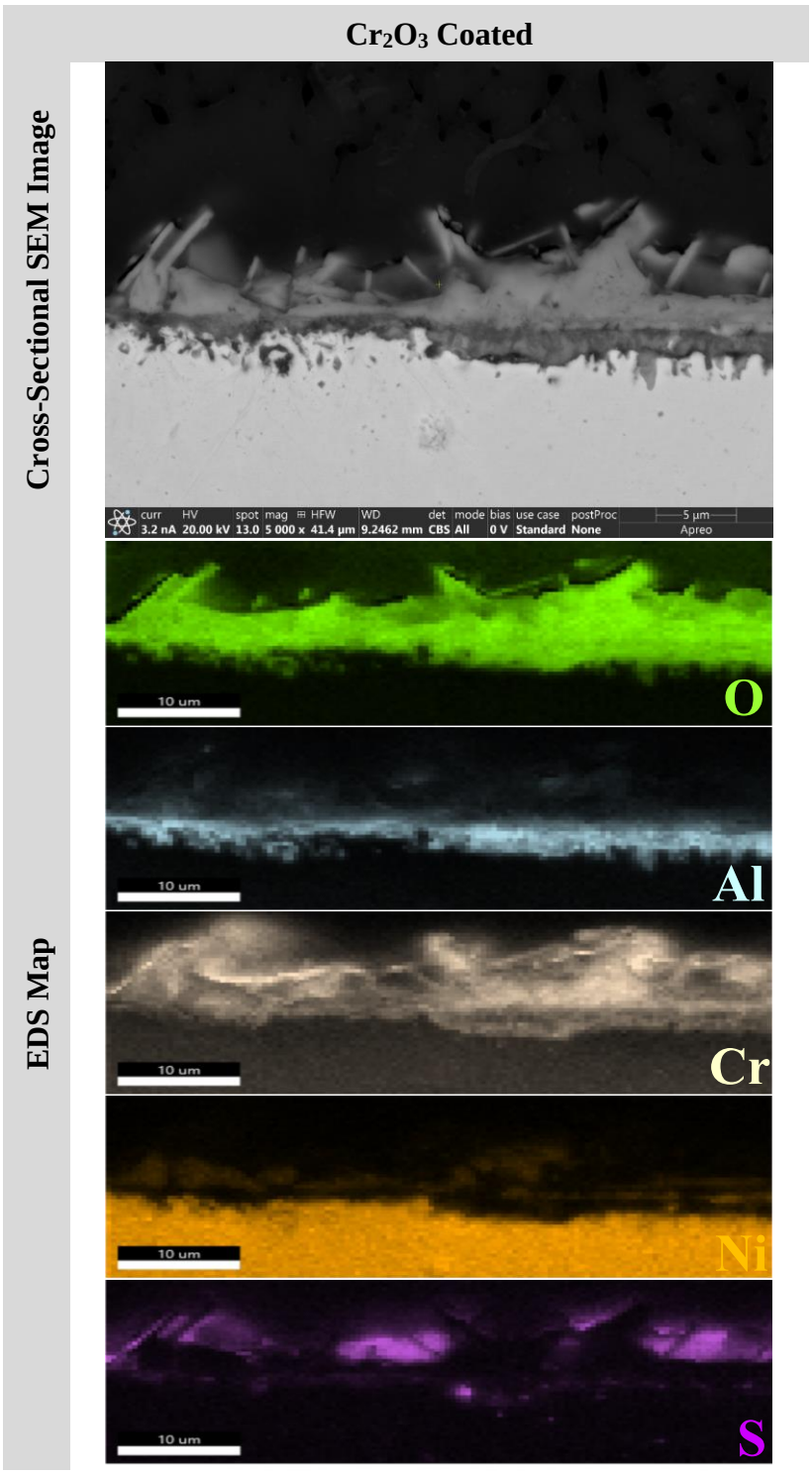

Figure 81: Cross-Sectional SEM Image and EDS Map of the Cr_2O_3 Coated 1200-Grit HAYNES® 214® Coupon After 100-hrs of Thermally Cycled Hot Corrosion Testing at 900°C (5 Cycles for 20-hrs)

The uncoated coupon shows an extensive region of about 10 μm has been affected by the hot corrosion process. EDS shows that there is a thin outer oxide layer consisting of Al and Cr which is likely in the form of $(Al,Cr)_2O_3$. Underneath this Al/Cr oxide layer, there is a thicker layer of a Cr-rich oxide which is assumed to have the structure of Cr_2O_3. In addition to these outer oxide layers, some localized areas show the presence of S which when combined with the EDS map for oxygen, these regions can be deduced as sulfates (SO_4) that remained on the surface after hot corrosion testing. Underneath the thicker layer of the Cr-rich oxide, the subsurface region of the alloy shows a significant area of internal oxidation where rod-like Al_2O_3 precipitates have formed. While the internal oxide precipitates are undesirable, EDS also shows a large amount of S has diffused into the alloy and formed discrete precipitates of Al_2S_3 and Cr_2S_3. The combination of internal oxides and sulfides would explain the large weight gain observed in Figure 78 and also would be detrimental as these consume the reactive metal (Al) which is required to form a continuous protective layer. These internal oxides and sulfides typically form at grain boundaries which can also be initiators for intergranular fracture.

Compared to the uncoated coupon, the Al_2O_3 coated coupon shows a comparable result where a same region of about 10 μm has been affected by hot corrosion. A thin outer layer of an Al/Cr oxide ($(Al,Cr)_2O_3$) has formed on the surface and underneath this layer there is a much thicker scale of a Cr-rich oxide (Cr_2O_3). Like the uncoated coupon, beneath the thick Cr-rich oxide layer, there is a large internal oxidation zone where precipitates of Al_2O_3 have formed. However, one difference between the uncoated and Al_2O_3 coated coupons is the shape of the internal oxide precipitates. In the uncoated coupon, the internal precipitates were shaped like rods whereas in the Al_2O_3 coated coupon they appear to have begun forming a semi-continuous layer. This indicates that the transition between internal and external oxidation could be occurring where the lateral

growth of the Al_2O_3 has become more kinetically favorable. Another key difference between the uncoated and Al_2O_3 coated coupons is the diffusion of S into the alloy. As was seen with the uncoated coupon where extensive internal sulfidation occurred, the Al_2O_3 coated coupon shows no internal sulfide formation. EDS shows that there is sulfur present on the very surface of the alloy, however when combined with the EDS map for oxygen, it can be deduced that these regions are SO_4 that have likely remained on the surface after hot corrosion testing.

Unlike the uncoated and Al_2O_3 coated coupons, the Cr_2O_3 coated coupon shows very different corrosion products. The surface of the alloy shows a very large scale of a Cr-rich oxide which also contains traces of Al and Ni. Beneath this layer, an Al-rich oxide scale has formed which also contains some Cr. As EDS shows, there is some small amount of S that appears to be intermixed with the Al-rich oxide scale. However, no internal sulfidation in the subsurface region of the alloy is observed. It is also important to note that within the thick outer Cr-rich scale, there is a large presence of S, which when combined with the EDS map for oxygen, is likely leftover SO_4 from the hot corrosion testing. Because the Cr_2O_3 coated coupon shows little internal sulfidation and the formation of an external Al-rich oxide scale which appears to have protected the alloy from further oxidation, this likely explains why the total weight gain from Figure 78 is much lower than the uncoated and Al_2O_3 coated coupons (where there was extensive internal oxidation or sulfidation occurring).

6.0 Conclusion and Future Actions

6.1 Conclusion

The results described above show that the use of Al_2O_3 and Cr_2O_3 nanocoatings applied on the surface of the HAYNES® 214® nickel-base superalloy via PLD have an effect on the oxidation and corrosion process. Under isothermal oxidation conditions the Cr_2O_3 coated coupon provided excellent passivation such that the inward oxygen diffusion was slow enough to reduce the oxygen partial pressure at the alloy-PLD coating interface below the value needed to form internal oxide precipitates. This allowed the bulk Al from within the alloy to diffuse to the surface and form a continuous and external scale of α-Al_2O_3. The formation of this α-Al_2O_3 resulted in steady-state, diffusion-controlled kinetics where the α-Al_2O_3 layer was 100 nm thick after 3-hrs and 175 nm thick after 100-hrs. The presence of the α-Al_2O_3 phase was confirmed via XRD, Raman spectroscopy, and PL spectroscopy. Relative to the total weight gain under thermal cycling conditions, the Cr_2O_3 coated coupon also showed the best performance compared to the uncoated and Al_2O_3 coated coupons. Even under more severe hot corrosion conditions, the Cr_2O_3 coated coupon formed a thick outer Cr-rich oxide scale on top of an external scale of an Al-rich oxide, and this combination effectively limited the inward diffusion of both oxygen and S. The formation of the external Al-rich oxide scale provided excellent oxidation and corrosion resistance.

Surprisingly, against expectations, the Al_2O_3 coated coupon showed an intermediate performance and was more closely comparable to the uncoated coupon. Under isothermal oxidation conditions, the Al_2O_3 coating did not provide sufficient passivation to slow down the inward diffusion of oxygen and thus the partial pressure of oxygen below the Al_2O_3 PLD coating

was large enough to form internal precipitates of Al_2O_3. This was perfectly exemplified in Figure 40 where the Al_2O_3 PLD coating could be clearly seen and underneath that layer was small precipitates of Al_2O_3. However, during thermal cycling conditions, the Al_2O_3 coated coupon did appear to perform better than the uncoated coupon due to the formation of a primarily continuous and external scale of Al_2O_3. With respect to hot corrosion tests, the Al_2O_3coated coupon showed nearly identical results compared to the uncoated alloy and an extensive internal oxidation zone containing Al_2O_3 precipitates had formed. However, the Al_2O_3 coated coupon did appear to suppress the inward diffusion of S which prevented the formation of any internal metal sulfides.

6.2 Future Actions

The efforts and results presented in this thesis establish a foundation for the role of using Al_2O_3 and Cr_2O_3 nanocoatings deposited via PLD to affect the oxidation and hot corrosion performance, process, and mechanism of the HAYNES® 214® nickel-base superalloy. Based on the results herein, several future actions have been identified as being valuable to further understand and optimize the role of these nanocoatings with respect to the oxidation and hot corrosion process. The future actions are listed below and a brief description of why this action is valuable is included.

1. Deposit Al_2O_3 coatings via PLD at high temperature (e.g., 800°C) such that crystalline films are grown on the alloy surfaces as opposed to allowing the film to crystallize during the oxidation process.

One possible explanation for the less-than-desirable performance of the Al_2O_3 coating is the possibility of film crystallization. The Al_2O_3 PLD coatings were deposited on the surface of the alloy coupons under room temperature conditions which likely resulted in an amorphous structure as was observed in the literature [31, 32]. Thus, when the alloy coupon was oxidized in a high temperature environment, the Al_2O_3 coating may have undergone crystallization which involves the nucleation and growth of Al_2O_3 crystals. Thus, the film crystallization process could behave in the same manner as the short circuit diffusion phenomena that occurs when the alloy undergoes recrystallization of the surface deformation induced during sample preparation. Essentially, the film crystallization could provide another short circuit pathway for oxygen to diffuse inward and base metal cations to diffuse outwards which may explain the oxidation results seen. This short circuit pathway for oxygen could result in a larger oxygen partial pressure or activity at the alloy-PLD coating interface as well as within the subsurface region of the alloy which is sufficient enough for the precipitation of internal Al_2O_3.

Not only will the short circuit phenomena result in faster inward diffusion of oxygen, but Al_2O_3 has several different types of metastable phases that can be formed prior to the desirable α-Al_2O_3 phase. These phases include the gamma phase (γ-Al_2O_3) and theta phase (θ-Al_2O_3), and both phases have different crystal structures compared to α-Al_2O_3. Compared to the hexagonal close packed (HCP) structure of α-Al_2O_3, the γ-Al_2O_3 has a cubic crystal structure and the θ-Al_2O_3 has a monoclinic structure. Due to the different crystal structures, each lattice has a different size and shape, resulting in a different volume and density. Thus, if the Al_2O_3 PLD coating was amorphous in

the as-deposited state and underwent a crystallization process through these metastable Al_2O_3 phases, there would be a volume or density change associated with the transition. These changes could result in a less dense structure or the formation of pores or cracks could begin in the Al_2O_3 PLD coating. As was the case with grain boundaries facilitating faster oxygen diffusion, the presence of pores, cracks, or a less dense structure could also aid in allowing faster inward oxygen diffusion. If this were the case, the oxygen partial pressure or activity at the alloy-PLD coating interface or within the subsurface of the alloy could be large enough to form the internal Al_2O_3 precipitates that were observed.

To eliminate the film crystallization concerns, one solution would be to deposit the Al_2O_3 PLD coatings at higher temperatures (e.g., 800°C) such that the coatings grown are already crystalline. Thus, when the coupons are oxidized, volume or density changes, as well as short circuit grain boundary diffusion, could be eliminated. This may result in the oxygen partial pressure or activity at the alloy-PLD coating interface and within the alloy subsurface remaining below the value needed for Al_2O_3 precipitation, allowing the Al to diffuse to the surface and form a continuous and external scale.

2. Perform additional oxidation experiments to determine the long-term oxidation performance of the Cr_2O_3 coated alloy.

The Cr_2O_3 coated coupons were found to provide an excellent passivation layer to promote the formation of a continuous and external scale of α-Al_2O_3 for isothermal

oxidation durations of at least 100-hrs. To determine if the growth of this α-Al_2O_3 scale can be sustained for much longer durations, it would be valuable to perform significantly longer oxidation tests (e.g., hundreds or thousands of hours). The long-term performance would provide an insight into whether the Al supply to the alloy surface remains consistent such that the continued growth of the α-Al_2O_3 layer is achievable.

Appendix A Additional Oxidation Figures

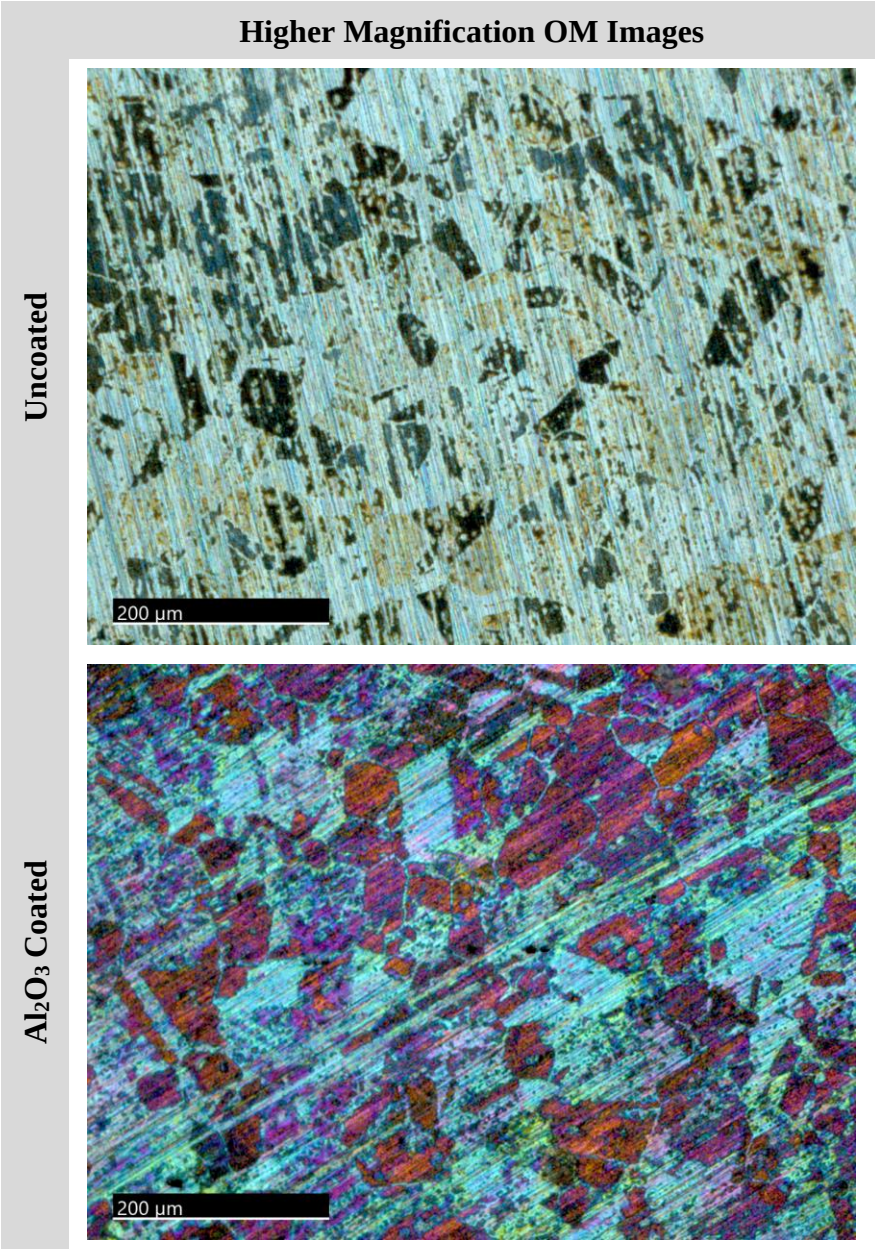

Figure 82: Higher Magnification OM Images of the Uncoated and Al_2O_3 Coated HAYNES® 214® Coupons After 3-hrs of Isothermal Oxidation in Air at 800°C

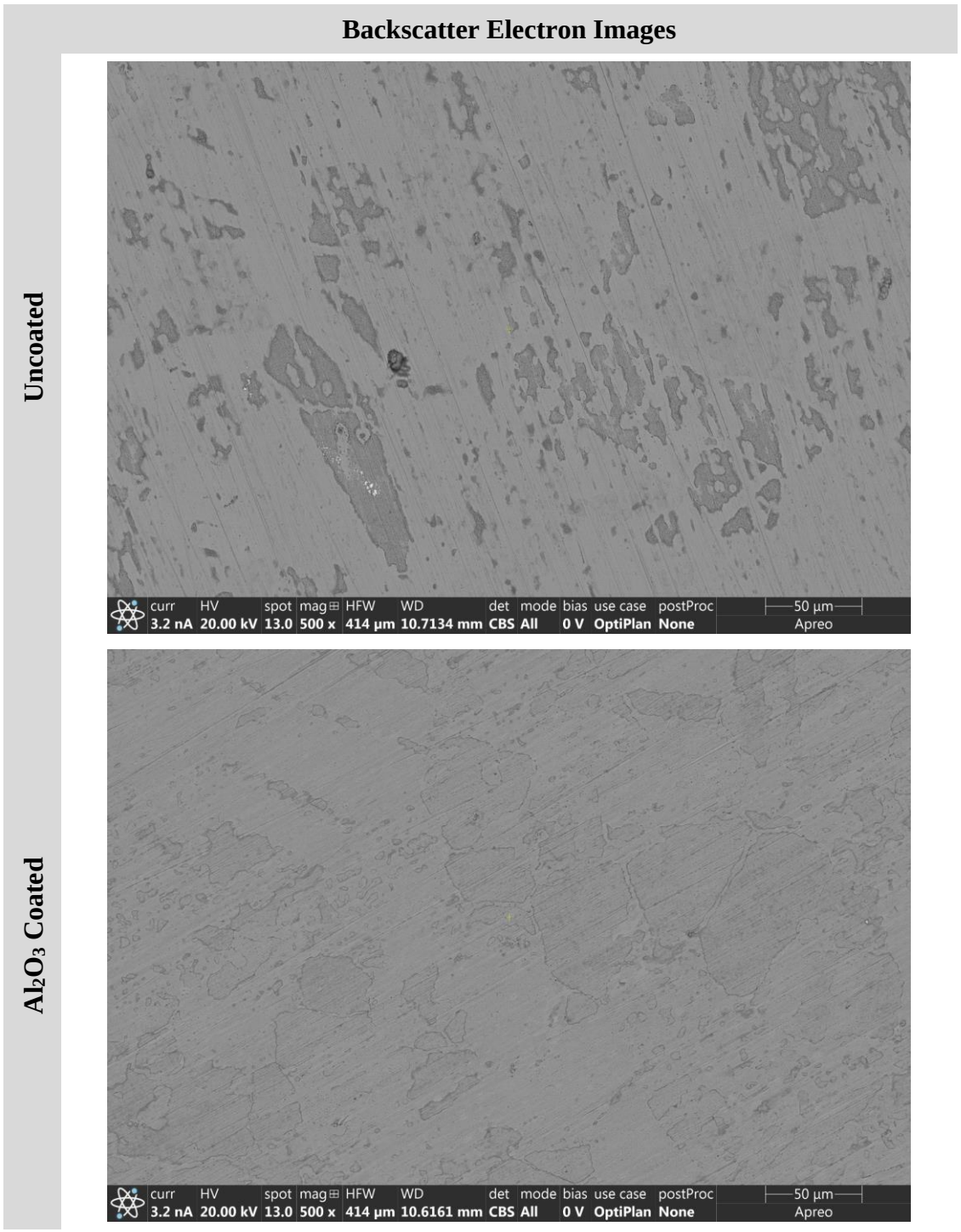

Figure 83: Backscatter Electron Images of the Uncoated and Al_2O_3 Coated HAYNES® 214® Coupons After 3-hrs of Isothermal Oxidation in Air at 800°C

Appendix B Powder XRD Spectra

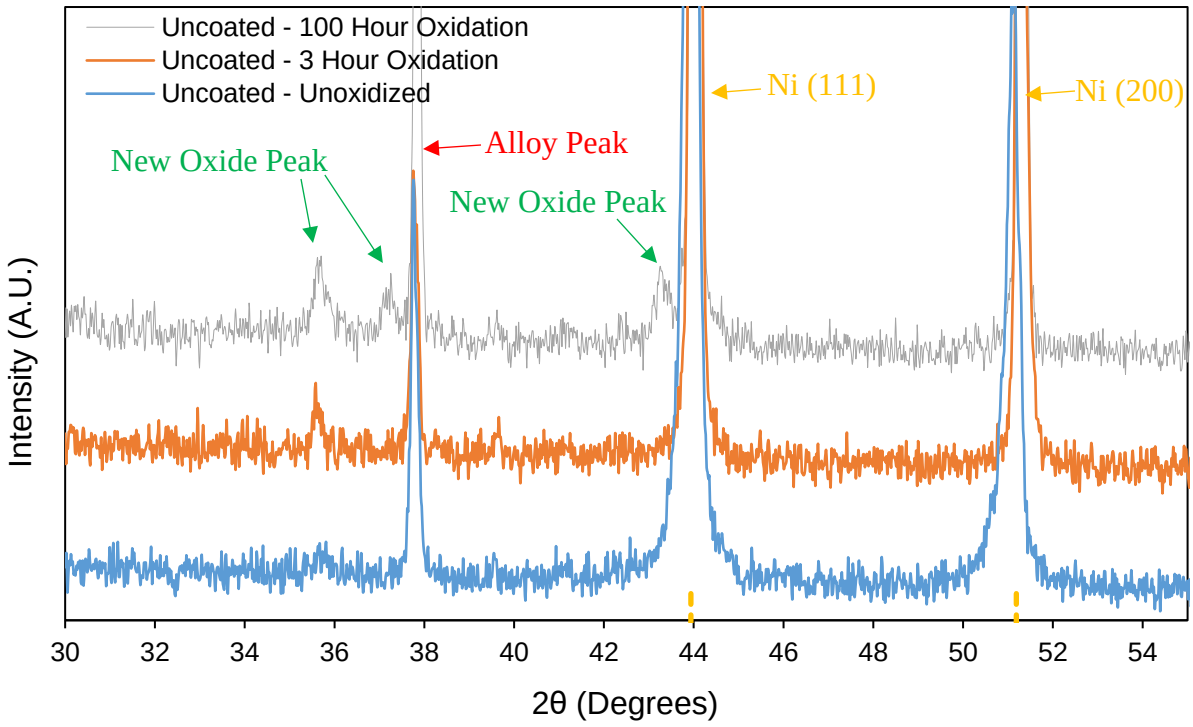

Figure 84: Powder XRD Spectra for the Uncoated HAYNES® 214® Coupon Before, After 3-hrs, and After 100-hrs of Isothermal Oxidation in Air at 800°C

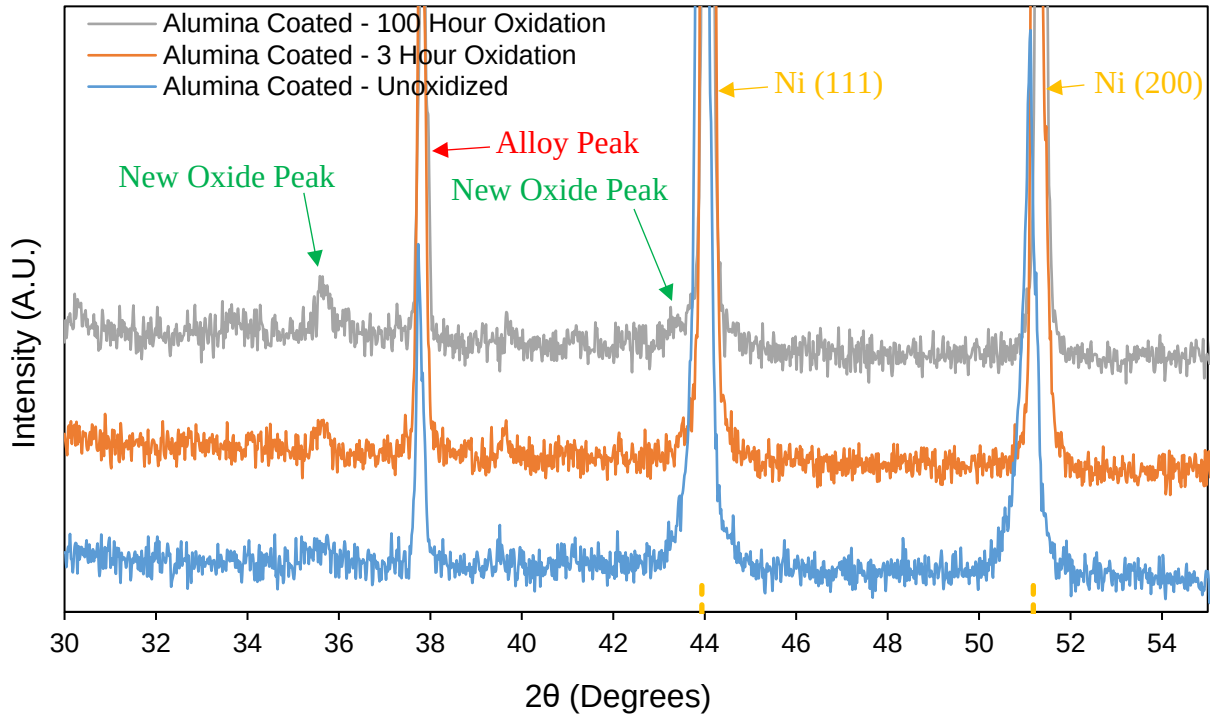

Figure 85: Powder XRD Spectra for the Al_2O_3 Coated HAYNES® 214® Coupon Before, After 3-hrs, and After 100-hrs of Isothermal Oxidation in Air at 800°C

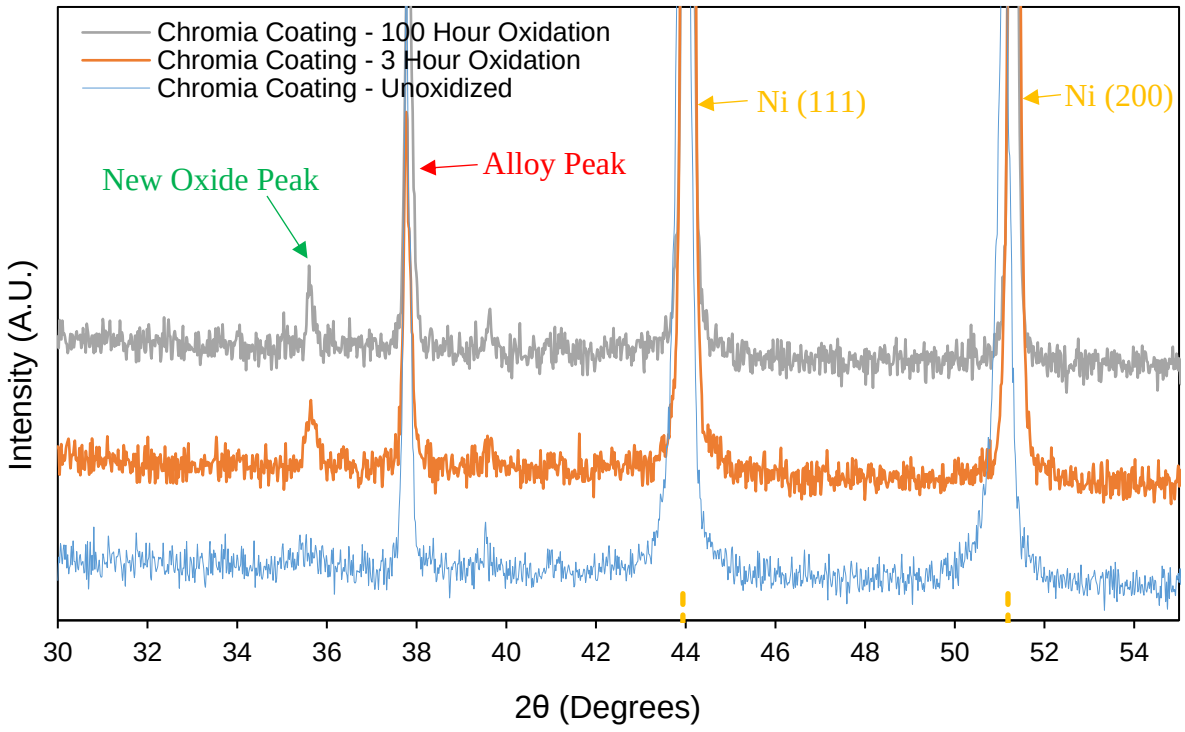

Figure 86: Powder XRD Spectra for the Cr_2O_3 Coated HAYNES® 214® Coupon Before, After 3-hrs, and After 100-hrs of Isothermal Oxidation in Air at 800°C

Bibliography

[1] Darolia, R. (2018). Development of strong, oxidation and corrosion resistant nickel-based superalloys: critical review of challenges, progress and prospects. *International Materials Reviews*, *64*(6), 355–380. https://doi.org/10.1080/09506608.2018.1516713

[2] *HAYNES® 214® alloy*. Principal Features. (n.d.). http://www.haynesintl.com/alloys/alloy-portfolio_/High-temperature-Alloys/haynes-214-alloy/principle-features.

[3] Gleeson, B. (2010). Thermodynamics and Theory of External and Internal Oxidation of Alloys. *Shreir's Corrosion*, 180–194. https://doi.org/10.1016/b978-044452787-5.00012-3

[4] Gaskell, D. R., Laughlin, D. E. (2018). *Introduction to the thermodynamics of materials*. CRC Press, Taylor & Francis Group.

[5] Young, D. J., Chyrkin, A., He, J., Grüner, D., Quadakkers, W. J. (2013). Slow Transition from Protective to Breakaway Oxidation of Haynes 214 Foil at High Temperature. *Oxidation of Metals*, *79*(3-4), 405–427. https://doi.org/10.1007/s11085-013-9364-4

[6] Gleeson, B. (2013). High-Temperature Corrosion of Metallic Alloys and Coatings. *Materials Science and Technology*. https://doi.org/10.1002/9783527603978.mst0407

[7] Giggins, C. S., Pettit, F. S. (1971). Oxidation of Ni-Cr-AI Alloys Between 1000C and 1200C. Journal of The Electrochemical Society, 118(11). https://doi.org/10.1149/1.2407837

[8] Allam, I. M. (2009). Carburization/Oxidation Behavior of Alloy Haynes-214 in Methane–Hydrogen Gas Mixtures. *Oxidation of Metals*, *72*(3-4), 127–144. https://doi.org/10.1007/s11085-009-9151-4

[9] Hayashi, S., Narita, S., Narita, T. (2006). Oxidation Behavior of Ni-3,6, 10 wt.% Al Alloys at 800C. Oxidation of Metals, 66. https://doi.org/10.1007/s11085-006-9034-x

[10] Kvernes, I. A., Kofstad, P. (1972). The oxidation behavior of some Ni-Cr-Al alloys at high temperatures. *Metallurgical Transactions*, *3*(6), 1511–1519. https://doi.org/10.1007/bf02643040

[11] Zhang, X. J., Wang, S. Y., Gesmundo, F., Niu, Y. (2006). The Effect of Cr on the Oxidation of Ni–10 at% Al in 1 atm O2 at 900–1000C. Oxidation of Metals, 65(3/4). https://doi.org/10.1007/s11085-006-9009-y

[12] Niu, Y., Zhang, X. J., Wu, Y., Gesmundo, F. (2006). The third-element effect in the oxidation of Ni–xCr–7Al (x = 0, 5, 10, 15 at.%) alloys in 1 atm O2 at 900–1000C. Corrosion Science, 48, 4020–4036. https://doi.org/10.1016/j.corsci.2006.03.008

[13] Kang, Y. (2016). In-Situ And Ex-Situ Studies On Early-Stage Scale Establishment (dissertation). University of Pittsburgh ETD, Pittsburgh, PA.

[14] House, S. D., Ayoola, H. O., Lyons, J. J., Li, M., Li, B., Yang, J. C., Saidi, W. A., Gleeson, B. M. (2020). The Impact of Surface Treatment on the Structure and Chemistry of Protective Oxide Scale in High-Temperature Oxidation-Resistant Nickel Alloys. Unpublished.

[15] Persechino, I. (2017). Development of a polycrystal plasticity simulation tool including recrystallization (Drx) phenomena (dissertation).

[16] Eliaz, N., Shemesh, G., Latanision, R. M. (2002). Hot corrosion in gas turbine components. Engineering Failure Analysis, 9(1), 31–43. https://doi.org/10.1016/s1350-6307(00)00035-2

[17] Lortrakul, P., Trice, R. W., Trumble, K. P., Dayananda, M. A. (2014). Investigation of the mechanisms of Type-II hot corrosion of superalloy CMSX-4. Corrosion Science, 80, 408–415. https://doi.org/10.1016/j.corsci.2013.11.048

[18] Pettit, F. (2011). Hot Corrosion of Metals and Alloys. Oxidation of Metals, 76(1-2), 1–21. https://doi.org/10.1007/s11085-011-9254-6

[19] Di Fonzo, F., Tonini, D., Li Bassi, A., Casari, C. S., Beghi, M. G., Bottani, C. E., Gastaldi, D., Vena, P., Contro, R. (2008). Growth regimes in pulsed laser deposition of aluminum oxide films. Applied Physics A, 93(3), 765–769. https://doi.org/10.1007/s00339-008-4720-y

[20] Chyrkin, A., Mortazavi, N., Halvarsson, M., Grüner, D., Quadakkers, W. J. (2015). Effect of thermal cycling on protective properties of alumina scale grown on thin Haynes 214 foil. Corrosion Science, 98, 688–698. https://doi.org/10.1016/j.corsci.2015.06.020

[21] Deodeshmukh, V. P., Matthews, S. J., Klarstrom, D. L. (2011). High-temperature oxidation performance of a new alumina-forming Ni–Fe–Cr–Al alloy in flowing air. *International Journal of Hydrogen Energy*, *36*(7), 4580–4587. https://doi.org/10.1016/j.ijhydene.2010.04.099

[22] Singh, A. K., Kaity, S., Singh, K., Thomas, J., Kutty, T. R. G., Sinha, S. (2014). Pulsed laser deposition of alumina coating for corrosion protection against liquid uranium. Materials Chemistry and Physics, 143(3), 1446–1451. https://doi.org/10.1016/j.matchemphys.2013.11.063

[23] García Ferré, F., Ormellese, M., Di Fonzo, F., Beghi, M. G. (2013). Advanced Al2O3 coatings for high temperature operation of steels in heavy liquid metals: a preliminary study. Corrosion Science, 77, 375–378. https://doi.org/10.1016/j.corsci.2013.07.039

[24] PVD Products, I. (n.d.). PLD 2000, PLD 3000 Deposition Systems. http://www.pvdproducts.com/pulsed-laser-deposition-systems/rd-and-pilot-production-tools/pld-systems.

[25] Lucca, D. A., Harriman, T. A., Lee, J.-K., Stowe, E. R. (2021). Raman Spectroscopy and Photoluminescence Spectroscopy of Oxidized HAYNES® 214® Alloy Coupons. Unpublished.

[26] Farrow, R. L., Nagelberg, A. S. (1980). Raman spectroscopy of surface oxides at elevated temperatures. *Applied Physics Letters*, *36*(12), 945–947. https://doi.org/10.1063/1.91659

[27] Hosterman, Brian D., "Raman Spectroscopic Study of Solid Solution Spinel Oxides" (2011). UNLV Theses, Dissertations, Professional Papers, and Capstones. 1087. http://dx.doi.org/10.34917/2476131

[28] Toyoda, T., Obikawa, T., Shigenari, T. (1998). Photoluminescence spectroscopy of Cr3+ in ceramic Al2O3. *Materials Science and Engineering B*, *54*, 33–37. https://doi.org/10.1016/S0921-5107(98)00122-6

[29] Scully, J. R. (2000). Polarization Resistance Method for Determination of Instantaneous Corrosion Rates. CORROSION, 56(2), 199–218. https://doi.org/10.5006/1.3280536

[30] Han, G. S., Yoo, J. S., Yu, F., Duff, M. L., Kang, B. K., Lee, J.-K. (2017). Highly stable perovskite solar cells in humid and hot environment. *Journal of Materials Chemistry A*, *5*(28), 14733–14740. https://doi.org/10.1039/c7ta03881j

[31] Balakrishnan, G., Tripura Sundari, S., Ramaseshan, R., Thirumurugesan, R., Mohandas, E., Sastikumar, D., Kuppusami, P., Kim, T. G., Song, J. I. (2013). Effect of substrate temperature on microstructure and optical properties of nanocrystalline alumina thin films. Ceramics International, 39(8), 9017–9023. https://doi.org/10.1016/j.ceramint.2013.04.104

[32] Boidin, R., Halenkovič, T., Nazabal, V., Beneš, L., Němec, P. (2016). Pulsed laser deposited alumina thin films. Ceramics International, 42, 1177–1182. https://doi.org/10.1016/j.ceramint.2015.09.048